The Dissertation Committee for James Joseph Hermes Jr.
certifies that this is the approved version of the following dissertation:

Gravitational Waves, Pulsations, and More: High-Speed Photometry of Low-Mass, He-Core White Dwarfs

Committee:

D.E. Winget, Supervisor

M.H. Montgomery, Co-Supervisor

E.L. Robinson

Pawan Kumar

S.O. Kepler

Mukremin Kilic

Gravitational Waves, Pulsations, and More: High-Speed Photometry of Low-Mass, He-Core White Dwarfs

by

James Joseph Hermes Jr., B.S.Phy., B.S.Ast., M.A.

DISSERTATION

Presented to the Faculty of the Graduate School of
The University of Texas at Austin
in Partial Fulfillment
of the Requirements
for the Degree of

DOCTOR OF PHILOSOPHY

THE UNIVERSITY OF TEXAS AT AUSTIN
August 2013

Dedicated to the Moon.

Acknowledgments

When I worked at *The Daily Texan* as an undergraduate, there was a tradition in which departing seniors published a long list of shout-outs to their peers in what was called a -30- column, a reference to the old typewritten days of the newspaper industry, in which "-30-" denoted the end of a story. My -30- column in *The Daily Texan* was more polemic than shout-out, a reflection on much of my political paralysis as an undergraduate that in the end mentioned none of my peers by name, since that seemed a vainglorious exercise in favoritism. It is curious that I am afforded the opportunity to repeat the exercise, now as a graduate student at this same great institution. It feels so much more appropriate to reflect on everyone who has helped me as I stand at the precipice of a doctorate in astronomy, and I hope these abbreviated shout-outs can properly convey how essential my professors, advisors, collaborators and friends have been along the way.

First and foremost I have to thank Don Winget, who took me under his tutelage as a directionless and struggling first-year graduate student and imbued in me endless confidence and support in order to transform me into the researcher I am today. Don first introduced me to McDonald Observatory in 2009 August, what is his and now has become my home away from home. He has given me the space to be an independent researcher, but provided the spark of countless ideas and the extensive connections to others in the WD community that have allowed me to be incredibly productive in west Texas.

Don is keen to often mention the academic family tree of himself and his students. So if Don is my academic parent then Mike Montgomery is undoubtedly my other legal guardian; he has been vital in ensuring my progress as a graduate student. Mike is an inspiring researcher and teacher who has the physical insight to calmly explain stellar pulsations, phase transitions, or mixing-length theory to both tenured faculty and first-year undergraduates. I know since I've witnessed him do both with ease. I've been incredibly lucky to share many lunches and international flights with Mike, and am always motivated by our conversations.

I also owe an incredible debt of gratitude to Mukremin Kilic and Warren Brown, who have mentored me as though I were a PhD student of their own. This dissertation would have been incredibly less interesting without their fruitful collaboration and willingness to share the sandbox of extremely low-mass white dwarfs. I was impressed early on, when Mukremin invited me to Norman, OK and we spent an incredibly productive and inspiring 36 hours, so much so that I pulled out my laptop at his home at nearly 11 p.m. in order to keep on working. It will likewise be hard to forget my first visit to Cambridge, MA, when Superstorm Sandy battered trees and dropped limbs onto power lines while Warren and I talked and worked through the madness.

This dissertation would not have been possible without Ed Nather and Anjum Mukadam, who built a most excellent time-series photometer. I never had the pleasure to share my gratitude with Ed, but I hope I have given Anjum her due thanks. Spending a week at Kitt Peak fumbling with an off-the-shelf CCD from Apogee, with minimal real-time reductions and multi-second readout, I owe my PhD to Argos. As Don has often waxed, it's a "great night to be out in West Texas driving Ed's Cadillac down the celestial highway." The thought crosses my mind every night I use Argos.

There were two times, though, that I feared for the health of the instrument. The first came in late 2010, when we began having an intermittent and extremely frustrating grounding problem that would more and more often disrupt our observations with a sudden surge of electricity. I have to profusely thank Dean Chandler for revisiting our best instrument practices in 2011 January and better grounding Argos. The second time came at the end of that year, when Anita Cochran made her way into Don's office one Friday afternoon to deliver the dramatic news that Argos was "dead." Again we were rescued by Dean, who had an exact clone of Argos on loan from Chris Clemens that we have used in Argos's stead at McDonald ever since.

I could hear the distress in the sound of Dave Doss's voice for weeks after he accidentally sent Argos on a collision course with the right pulpit in the 2.1m dome, which is a testament to how much he cares about McDonald and the observers who use it. I was lucky to spend 220 nights at McDonald without once calling Dave after midnight with a problem. But I wouldn't have hesitated to do so at any hour. The same could be said for John Kuehne, who was always tweaking and perfecting the 75-year-old time machine at McDonald. After each nightly visit Dave always joked that I should "call John" if I had any problems, and there were times when I wouldn't even have to — John was watching remotely at 3 a.m., sometimes from out of town. I have thanked Dave and John at the end of every one of my papers, but I absolutely have to do it here again. Thanks again, and the same goes to everyone else who made my 29 trips to McDonald smooth as silk.

The white dwarf community is small but close-knit, and I have thoroughly enjoyed the bi-annual European white dwarf conferences. Don's former students and current collaborators are littered around astronomy, but almost all of them have been marked with a passion for white dwarfs and still work in the sub-field. One of the first white dwarfers I had the pleasure to meet at my first EuroWD meeting in Tübingen, Germany, was S.O. Kepler, who is always a well-spring of ideas and guidance, and who is perennially a pleasure to be around. I also owe an incredible amount to Fergal Mullally, who left behind an excellent data set from his planet search using hot DAVs, as well as an intuitive and excellent suite of software to hasten that investigation. Fergal, I feel like every time we hang out I should buy you at least two beers.

I owe a similar number of future beers to all my fellow UT graduate students, especially those with whom I've shared the benches nearly every Friday afternoon at Crown & Anchor for the last five years. Chalence, John, Paul, Manos, Ross, Gully, Keaton, Rudy, Kevin, Jonathan, Chris, Jacob, Jeremy, Erik, Manuel, Kyle; you guys have been awesome to both work and play with. I'm sure we'll get the opportunity to knock one back every winter at AAS, at least until we all luck our way into tenure-track jobs.

It's rare that I've found myself bored in RLM 15.216; my graduate classes in astronomy were some of the most interesting and compelling hours I've passed. No doubt I've learned an incredible amount about both astronomy and pedagogy from Volker Bromm, Pawan Kumar, Rob Robinson, Dan Jaffe, Don, and Mike. But I owe a special note to Rob, who has literally always had an open door for me. At least a few times a month, often far more regularly, I have popped into Rob's office to test ideas and refine my understanding or presentation of a problem. I can only hope to be such a fair and knowledgeable critic of so many different ideas as I progress through astronomy.

Finally, I have to thank my family for sticking by my side while I go on international adventures on a minimal paycheck while I pursue my hobby in astronomy. The best run I've ever had at McDonald included the few November nights that mom and dad shared with me under the west Texas skies. I can only dream we have more nights like that in the future.

Gravitational Waves, Pulsations, and More: High-Speed Photometry of Low-Mass, He-Core White Dwarfs

James Joseph Hermes Jr., Ph.D.
The University of Texas at Austin, 2013

Supervisors: D.E. Winget
M.H. Montgomery

This dissertation is an observational exploration of the exciting physics that can be enabled by high-speed photometric monitoring of extremely low-mass (ELM, $< 0.25\ M_{\odot}$) white dwarf (WD) stars, which are found in some of the most compact binaries known. It includes the cleanest indirect detection of gravitational waves at visible wavelengths, the discovery of pulsations in He-core WDs, the strongest evidence for excited p-mode pulsations in a WD, the discovery of the first tidally distorted WDs and their use to constrain the low-end of the WD mass-radius relationship, and the strongest cases of Doppler beaming observed in a binary system. It is the result of the more than 220 nights I have spent at McDonald Observatory doing high-speed photometry with the Argos instrument on the 2.1 m Otto Struve telescope, which has led to a number of additional exciting results, including the discovery of an intermediate timescale in the evolution of cooling DA WDs and the discovery of the most massive pulsating WD, which should have an ONe-core and should be highly crystallized.

WDs are the electron degenerate remnants of stars that have exhausted core nuclear burning, and represent the end-points of stellar evolution for all stars with

initial masses below about 8 $M_\odot$, which includes more than 97% of all stars in our Galaxy. About half of stars in the Milky Way go through stellar evolution as single stars and end up as typical Earth-sized, 0.6 $M_\odot$ carbon-oxygen-core WDs. The remaining half evolve in binaries, including short-period systems, where stable or unstable mass transfer can take place in the late stages of their evolution. Many short-period binaries go through one or two common-envelope phases, which efficiently removes enough mass to prevent ignition of helium to carbon and oxygen, leaving an underweight WD with an He core.

The Galaxy is not old enough to produce low-mass ($< 0.4\,M_\odot$) WDs through single-star evolution. ELM WDs are thus excellent signposts for compact binaries, which may be strong sources of gravitational waves and possible supernovae progenitors. Low-mass WDs have been known for some time as pulsar companions, but recently their numbers have grown dramatically as a result of the ELM Survey, a targeted spectroscopic search for low-mass WDs. The results here detail follow-up of many of these exciting new compact systems with time-series photometry.

We present high-speed photometry of 20 low-mass WDs in compact binaries with unseen companions, all of which have orbital periods less than 4 hr. We use the discovery of the first eight tidally distorted WDs to constrain the mass-radius relationship for He-core WDs, and use the Doppler beaming signals observed in 10 of these compact binaries to verify the high-amplitude radial-velocity observations. The shortest-period binaries are strong sources of gravitational waves, and we expect to use the time-of-minimum of those that display ellipsoidal variations to detect orbital decay from this radiation, which carries away orbital angular momentum.

In fact, we have already detected the signature of orbital decay from gravitation wave radiation in the most compact detached WD system ever discov-

ered, J0651+2844. This 12.75-min WD+WD binary exhibits primary and secondary eclipses, since it is inclined nearly edge on with Earth. These eclipses allow us to constrain the radii of both WDs, and provide an excellent clock of the orbital period. By measuring the changing mid-eclipse times we have shown that the orbit is decaying at a rate in line with the expected decay from general relativity, the first such detection at visible wavelengths.

Just as with normal-mass DAs, these hydrogen-atmosphere WDs should develop a hydrogen partial-ionization zone that drives pulsations when they cool to the appropriate effective temperature. Searching a wide parameter space, we have discovered the first five pulsating ELM WDs, which are the coolest and lowest-mass WDs known to pulsate. The observed luminosity variations have relatively long periods and are most likely the result of surface temperature variations caused by global, non-radial g-mode pulsations. In the two lowest-mass pulsating ELM WDs we see significant evidence for shorter-period oscillations that are best explained as acoustic (p-mode) pulsations. Asteroseismology will go a long way in testing that these low-mass WDs indeed have He cores, and can also probe the star's hydrogen layer mass and rotation rate, which in turn constrains hypothesized residual hydrogen burning and tidal synchronization, since we have detected close, unseen companions in three of these systems.

Motivated by the discovery of pulsations in low-mass, He-core WDs and the prospect asteroseismology holds for discerning the interior composition of these stars, we have searched for pulsations in ultramassive WDs, as well. This search has yielded the most massive pulsating WD ever found, GD 518, a 1.2 $M_\odot$ WD which may have a highly crystallized oxygen-neon core. This dissertation has thus uncovered both the lowest- and highest-mass pulsating WDs, objects which will shed considerable light on the late stages of binary and stellar evolution.

Table of Contents

List of Tables

List of Figures

Chapter 1

Introduction and Astrophysical Context

The cloudless sky is wet with stars, silently burning in the distance. Standing on the catwalk, I am surrounded by a soundless cosmic sea. A dry wind shakes noise into the void, joining the quiet hum of gears guiding the 2.1m Otto Struve telescope here at the McDonald Observatory.

But my eyes are fixed on stars a-singing. My ears useless, I see their notes dance on screen, keeping nearly perfect time in the quiet night. They are ringing with their secrets.

This dissertation is about variable white dwarfs, dying stars that can pulse like a heartbeat or whirl like a top. The tones they make are so consistent that we on Earth, dozens to hundreds of light years away, can learn a great deal about them by measuring their notes or detecting any subtle changes in their music.

Watching their brightness change from night to night, year to year, we can explore low-mass white dwarfs in ways that we otherwise couldn't. Most of these low-mass white dwarfs have nearby companions, and we can infer their physical extent if these stars eclipse or are tidally distorted. Some are speeding around their binary companions so quickly that Einstein's special relativity is relevant, beaming a large bit of light toward Earth as the stars approach on every orbit. With luck, we can watch the most compact of these systems spiral into one another as they lose orbital energy from the emission of gravitational waves. Most uniquely, we can investigate the internal constitution, among other things, of these dying stars using pulsations, global starquakes that can reveal the secrets of a star's interior.

This dissertation applies the tools of time-series photometry to understand the properties and future of low-mass white dwarf stars. It is the result of an extensive observing campaign from several optical telescopes, but the vast majority of data were taken with the Argos instrument on the 2.1 Otto Struve telescope at McDonald Observatory, where I have had the pleasure to spend 220 nights on 29 different observing runs from 2009 August to 2013 April. Having spent the equivalent of more than seven months at the telescope, I've had the fortune to find many other exciting and interesting things along the way.

This chapter serves as a basic introduction to the concepts that will be discussed and applied throughout this dissertation. I have written it at a level that I hope my parents can understand, neither of whom have an advanced degree in astrophysics, in the hopes that they can fully appreciate why I've spent nearly one in five nights over the last three years in west Texas. However, it will also have information that even a seasoned reader may find useful.

1.1 White Dwarfs: The Impossible Stars

In many ways, I owe this dissertation to Sirius, the brightest star in the northern hemisphere, located very near the recognizable constellation of Orion. This is in part because Orion and its neighbors have kept me company in the sky, the spot where I rest my gaze for much of a long winter's night. More specifically, though, I should honor Sirius B, the companion to Sirius A that is $10{,}000$ times fainter and can only be seen through a telescope. It was one of the first white dwarf stars discovered, and posed a rigorous challenge to early physicists.

As with many discoveries in astronomy, Sirius B was first inferred before directly observed, when Friedrich Wilhelm Bessel detected a wobble in the position of the bright Sirius A in the 1840s. This wobble was caused by the then-unseen white dwarf, which astronomers were eventually able to directly observe by the end of that century. There are many objects in this dissertation that are still merely wobbles, unwilling to share enough light for our Earthly detectors. For now, we are forced to only infer their existence.

By the 1920s, astronomers had a good grasp of some fundamental properties of Sirius B, but the results were unsettling. The object had a mass comparable to that of the Sun, packed into a volume roughly the size of Earth. Such a result required an immensely dense star, a million times more dense than the Sun. There was simply no way to imagine a Sun's mass worth of even the smallest atom, hydrogen, packing into such a small volume without being ionized. Sir Arthur Eddington was especially troubled at what would happen if such an ionized star cooled and the energy to keep the atoms ionized was no longer there; he famously referred to white dwarfs as "impossible" stars in his seminal work on the stellar mass-luminosity relation (Eddington 1924).

Fortunately, physicists like Eddington pondered impossible stars at the time of the quantum revolution, which provided a way to reach such high densities via the uncertainty principle. This was first shown by R. H. Fowler, who posited in 1926 that quantum mechanics could indeed pack material into such a compact state (Fowler 1926). Specifically, Fowler showed that the degenerate electrons could have a pressure much higher than the ions. We now refer to this as electron degeneracy pressure: As the space between free electrons gets smaller the average momentum of the electrons gets higher, providing a powerful source of pressure, enough to hold up a star a hundred thousand times denser than lead.

For a stable star to exist it must satisfy hydrostatic equilibrium and maintain a steady balance between the strong gravity pulling inward and the internal pressure pushing outward. A main-sequence star like the Sun is able to support itself by fusing hydrogen to helium, which releases enough energy to hold a solar mass of material (1 $M_{\odot}$) at bay. Electron degeneracy pressure is at work to hold up the white dwarf stars.

We know now that a white dwarf star is a star at the end of its life cycle, and it is essentially the burnt-out core of a star like the Sun, the ashy byproduct of previous epochs of nuclear fusion. White dwarf stars no longer fuse elements in their interior to generate energy; for the significant majority of a white dwarf's existence it is simply cooling, like a coal ember removed from a fire (Mestel 1952).

These stars are deeply personal, since we expect our Sun will become a white dwarf when it exhausts its internal energy generation in a bit more than five billion years. They are also excellent tools to understanding stellar evolution for stars of all masses below about eight times the mass of our Sun. Stars in binary systems will also evolve into white dwarfs, and slower-evolving companions can strongly influence the fate of these stars, as we will soon see.

1.2 Extremely Low-Mass White Dwarfs

Thanks mostly to the Sloan Digital Sky Survey (SDSS), we now know of more than $25{,}000$ spectroscopically identified white dwarf stars. The vast majority, more than 80%, have outer atmospheres composed entirely of hydrogen, as their strong surface gravities have caused the heavier elements to sink down out of visibility (Kleinman et al. 2013). All of the objects in this dissertation are such hydrogen-atmosphere white dwarfs, belonging to the spectral class DA.

The SDSS has also given us an opportunity to take census of the range of white dwarfs masses. This mass distribution peaks at about 0.6 $M_{\odot}$ (where $M_{\odot}$ is the mass of the Sun), and the mean mass for white dwarfs has been determined by multiple methods to fall near this value (Falcon et al. 2010, Tremblay et al. 2011, Kleinman et al. 2013). It is likely that the progenitor of a typical 0.6 $M_{\odot}$ white dwarf was a roughly 2.5 $M_{\odot}$ star that sustained an epoch of fusion from hydrogen to helium, exhausted that core hydrogen, then expanded into a red giant, and finally fused that remnant helium to carbon and oxygen. Along the way it lost a majority of its initial mass, eventually leaving behind its remnant, exposed core: a white dwarf.

However, we also observe white dwarfs in nature with considerably higher and lower masses. These low-mass white dwarfs are interesting for a number of reasons, and make up the central focus of this dissertation.

For one, an isolated low-mass white dwarf stars cannot be formed within the finite age of the Universe, about 13.8 billion years. Since white dwarfs are the endpoints of stellar evolution, a star must go through its other phases, all of which take some amount of time. More massive stars live fast and die young, and shine bright enough to burn through their fuel quickly. But low-mass stars burn through their fuel much more slowly; a main-sequence star with an initial mass of 0.5 $M_{\odot}$ burns its hydrogen to helium for more than 50 billion years before it evolves its way down to its final white dwarf cooling stage.

Such is the fate for a single star burning on its lonesome, like our Sun. But the Universe has a trick up its sleeve: Binary systems composed of at least two stars orbiting relatively closely to each other. More than half the stars in our Galaxy form in such binary systems, so they are quite common. The gravitational pull from a binary companion is often responsible for stripping stars of more mass than otherwise would be removed, leaving behind underweight white dwarfs. Often a companion can strip the now-low-mass white dwarf of enough mass to prevent the ignition of helium in its core, and the lowest-mass white dwarfs likely harbor cores of degenerate helium. The star was unable to fuse its core helium into any heavier elements.

These low-mass white dwarfs are therefore excellent signposts for close binary systems. As Tom Marsh has suggested, low-mass white dwarfs need friends (Marsh et al. 1995).

The first extremely low-mass white dwarfs ($\leq 0.25\ M_{\odot}$) were initially inferred (and later directly observed) as companions to millisecond pulsars. However, thanks to an extensive spectroscopic search using color selection from the SDSS known as the ELM Survey, we now know of several dozens of low-mass white dwarfs in nature. All of the low-mass white dwarfs discussed in this dissertation were discovered through the ELM Survey (Brown et al. 2010, Kilic et al. 2011a, Brown et al. 2012, Kilic et al. 2012, Brown et al. 2013).

1.3 Time-Series Photometry

Having identified the targets of this dissertation, I should now briefly introduce the means to the end of studying these stars. Fortunately, time-series photometry is one of the simplest ways to observe an astrophysical object. The concept is startling simple: Time-series photometry is essentially a time-lapse movie of how the brightness of an object changes with time. We draw a circle (aperture) around some target, count up all the photons we detect from the source, and see how each subsequent exposure compares to the mean number of photons from that source over a few hours of observations. Our light-counting device is a high-grade charge-coupled device (CCD), a more expensive version of the chip used in modern cellphone cameras.

White dwarf stars are intrinsically faint; the brightest we ever discuss in this dissertation is still more than a million times fainter than faintest star visible to the naked eye. Thus we require a moderate 2-meter-class telescope for our observations. Fortunately, the Argos instrument, which sits at the prime focus of the 2.1m Otto Struve telescope at McDonald Observatory, gathers enough light to make the measurements we require (Nather & Mukadam 2004). In most cases, we can reliably detect at least 0.1% brightness variations with timescales of a few hours or less over a few nights worth of observations. There are very few objects in the sky that change in brightness with such high amplitudes over such short periods, but some of our white dwarf targets do just that.

However, things are never so simple as point-and-shoot. We must keep meticulous record of the absolute times of our observations, so that we can reliably compare our brightness changes in 2010 with those in 2013. We accomplish this using a GPS-conditioned trigger for our camera. The Earth's atmosphere, which we must peer through from the ground, is variable on all number of timescales, especially on the order of a few hours. We must be careful to distinguish the signals in our data caused by Earth's sky from those truly in the star. And the harsh environment of the observatory, from strong winds to temperatures well below freezing, can challenge our equipment.

For example, on the second night of our original discovery of the pulsations in extremely low-mass white dwarfs (J1840, see Chapter 4), the serial cable running from the camera to our data acquisition computer actually failed, and required a soldering the next morning. An exciting discovery of arguably a new class of pulsating stars was almost postponed due to a loose wire! Additionally, we were frustrated for months by a bad ground in the Argos instrument, which would intermittently (and often repeatedly) overwhelm our observations with static electric noise. Only when a creative colleague isolated the problem in 2011 January were we offered some relief.

More detailed information about our observational setup can be found in Appendix A. While at times simple, this dissertation makes clear the many opportunities for cutting-edge discovery that remain possible using a simple camera mounted on a 75-year-old telescope.

1.4 Seeing Einstein's Effects in White Dwarfs

There is rarely a month that goes by without a popular science article screaming in a headline about "Einstein proved right" or "was Einstein right?" In fact, the results in Chapter 3 of this dissertation were picked up in some highly circulated news outlets under a similar heading. This is due to the fact that Einstein's ideas still have the staying power to captivate modern audiences, and the extreme environments of white dwarf stars offer two tangible ways in which humans can directly observe both special and general relativity.

Special relativity introduced the concept that an observer's frame of reference compared to a source must be considered; it decoupled the notion that time and space were the same for all observers, and gave us situations where time and space can dilate or contract depending on an observer's motion relative to a source.

Doppler beaming is an excellent and specific example of special relativity in action; it is a measurable effect for many compact binaries composed of at least one low-mass white dwarf (see Chapter 2). Doppler beaming essentially derives its amplitude from a Lorentz transformation of the opening angle of radiation from an object, which causes an increase in observed flux from a rapidly moving source toward our line of sight.

Imagine an object that is radiating away energy equally in all directions. If we fully account for special relativity in our treatment of the angle of how such light is emitted from a source, we find that the angle of the emission depends slightly on the velocity of the source. If the motion is fast enough in the direction of an observer, the radiation can be "beamed" toward that observer. Mathematically, if the source is at rest, the angle of emission is simply $\cos\alpha' = \cos\alpha$. However, if the source is in motion then

$$\cos\alpha' = \frac{\cos\alpha + V}{1 + V\cos\alpha}$$

where $V = v/c$ is the dimensionless radial velocity of the source (its motion toward or away from an observer). There is a similar dependence on the frequency of the emitted radiation with the source velocity, but the dominant factor contributing to Doppler beaming of a $\sim 10{,}000$ K white dwarf comes from the beaming of the opening angle of the radiation (Zucker et al. 2007).

This Doppler beaming introduces a detectable modulation in the flux of a source that is approaching or receding. In fact, we see this effect in half of the 20 compact, low-mass white dwarf binaries discussed in Chapter 2, since many of these stars are orbiting so rapidly. Thanks to the ELM Survey, we typically know the radial-velocity amplitude of these systems from spectroscopy, and Doppler beaming yields little new information about our binaries. Still, it is an exciting confirmation of special relativity we can see in the white dwarf stars. Up until the start of this decade, Doppler beaming had never been observed from the ground (Shporer et al. 2010); it's now something we do routinely with low-mass white dwarfs.

Additionally, low-mass white dwarfs can say something profound about the general theory of relativity. In so many words, Einstein's general relativity holds that gravity is a manifestation of the consequence that mass bends space. A popular visualization involves imagining a heavy object like a bowling ball resting atop a sheet of spandex, stretching the surface of the spandex into a ball-shaped indention. The amount of stretching an object imparts on space is directly proportional to that object's mass.

This warping of space can have interesting consequences. In the case that two objects are in close orbit around each other, they often perturb each other just via gravity; they are forced to bob up and down in the wake of each other's mass-bent space. This bobbing accelerates each object, which in turn causes the emission of gravitational waves, subtle ripples in the fabric of space-time.

These ripples carry energy and angular momentum; subtle as they are they can carry away enough energy to cause the orbits of two stars to decay quite rapidly, especially if those stars are close together. Gravitational waves cause such a minute effect on space-time that humans have never directly detected them, despite hundreds of millions of dollars spent over decades trying. Humanity's first confirmation of these subtle waves came in the mid-1970s when radio astronomers measured the orbital decay of a merging binary system containing a pulsar, a rapidly spinning neutron star that keeps exceptionally precise time due to its millisecond spin period. It turns out that low-mass white dwarfs can also contain accurate clocks, and we have used the eclipses from an exceptional 12.75-min WD+WD binary to detect and measure the orbital decay of this system, due mostly to gravitational radiation (see Chapter 3). This is the first time that gravitation waves have been indirectly detected using visible light.

1.5 O−C Diagrams

In order to fully understand our detection of gravitational waves using the 75-year-old Otto Struve telescope we should take a step back into the methods used in this dissertation. I make frequent use of $(O - C)$ diagrams, which compares the timing of an event (say the mid-point of an eclipse or the peak of a pulsation cycle) to when we expect such an event if it occurred at an exactly constant periodicity. It may help to visualize an example:

Imagine a leaky faucet that keeps exceptionally precise time, left unattended for many decades. Its drip rate is very slow — every 12 minutes a drop of water falls to a basin below, and we can measure the time these drips hit the basic with good precision, to better than a little less than a second.

Now imagine the water isn't perfectly pure, and these impurities build up as sediment slowly but in a constant way. This sediment very slowly lengthens the period between drips, causing them to occur less and less frequently. In this case, let's imagine the buildup is incredibly gradual, and that the original drip period of exactly 12 minutes is changing by just 0.5 milliseconds every year (0.5 ms yr^{-1}).

By building an $(O - C)$ diagram we can measure such a sub-millisecond change in the drip period over a year, even if we can only measure each drip to an accuracy of about 1 second. Our leverage comes from the first observation, and the fact that the change from our first observation caused by the period change piles up the longer we observe our leaky sink. This change from the original observations — what we observe (O) versus what we calculate (C) given a perfectly constant period — is at the heart of the $(O - C)$ diagram.

For simplicity sake, let's say that we measured a drip to occur at exactly midnight on 1 January 2014, at UT 00:00:00[1]. We observe a drip around midnight on the first of every month and record the absolute time that drip hit the basin. If there were no sediment buildup, the time of the drip would be perfectly constant, always separated by exactly 12 minutes. After a year, the 43800th drip would occur

---

[1] The UTC midnight on 1 Jan 2014 corresponds to a Julian date of 2456658.5, which is a natural unit of absolute time for astronomers.

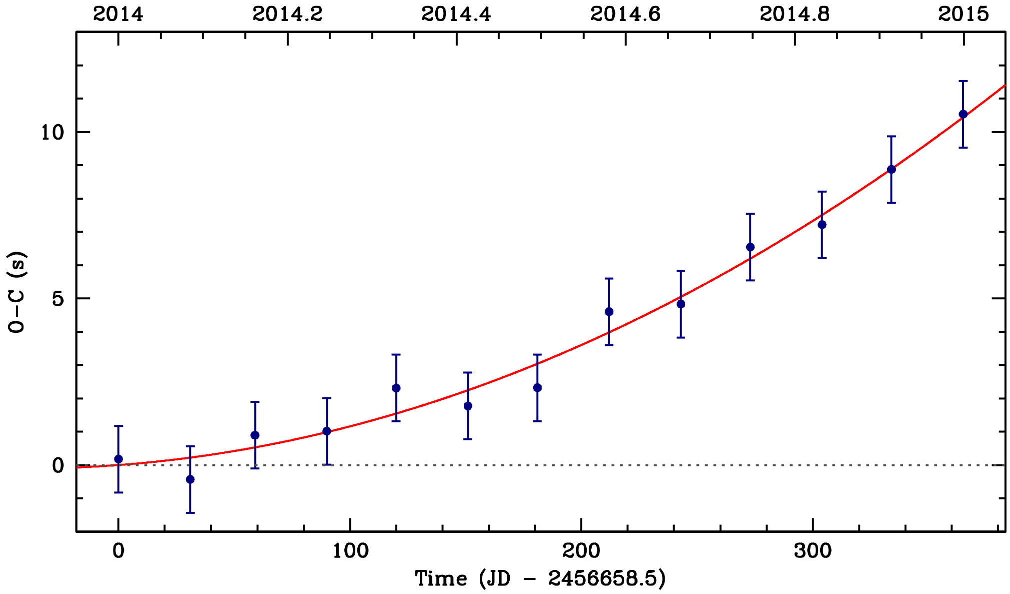

Figure 1.1 An $(O - C)$ diagram for our thought experiment of a leaky faucet that keeps excellent time but which has a drip period that is lengthening slightly, by 0.5 ms each year from an initial drip period of 12 minutes. Our first observation occurred exactly at midnight on 1 Jan 2014, and we subsequently show here how much time has elapsed after midnight before we observed a drip on the first of every month. The best-fit red parabola to the observations corresponds to the rate of period change, as described in the text.

exactly at midnight on 1 January 2015. Instead, we have stated that the drip period is increasing by half a millisecond every year.

It's natural to expect that when we go and look on 1 January 2015 we'd see a drip occur 0.5 ms after midnight. Instead, we would measure that drip to occur at about UT 00:00:11 on 1 January 2015; the drip would occur nearly 11 s after midnight! Sure enough, the time between drips has only changed by half a millisecond in the year between 1 January 2014 and 1 January 2015, so that the period after one year would be $P = 12.00000833$ min (720.0005 s). But the drip itself would be delayed by more than 10 s.

Figure 1.1 illustrates this thought experiment, showing the $(O-C)$ diagram of when we observe the drips versus when we'd expect them given an exactly constant drip period. The grey dotted line shows the line of $(O-C) = 0$ s; what we would "expect" for a perfectly constant period. Our "observations" are shown in dark blue and have been perturbed by random Gaussian noise assuming 1 s uncertainties for each observation. These "observations" essentially correspond to how much time after midnight we observe the drip at the beginning of each month.

A more detailed derivation of the $(O-C)$ equations are found in Chapter 6, but the key is that the effect increases with time squared. We write this mathematically as $O-C \propto \frac{1}{2} P_0 \dot{P} E^2$, where P_0 is the period at the time of the first measurement, $\dot{P}$ is the rate of period change, and E is the ephemeris such that $E = t/P_0$, where t is the elapsed time since the first observation. This means that the second-order polynomial fit, shown as a solid red parabola in Figure 1.1, constrains the rate of period change from an $(O-C)$ diagram. In our example, we would be able to measure a rate of period change of $dP/dt = (1.24 \pm 0.47) \times 10^{-11}$ s s^{-1} (or 0.39 ± 0.15 ms yr^{-1}) from the best-fit parabola.

Even though the period change is quite slow (0.5 ms yr^{-1}), we would have a nearly 3-sigma measurement of the rate of period change, accurate to a fraction of a millisecond per year, after just 13 "measurements" over one year of monitoring! This thought experiment illustrates the power of constructing a long-term $(O-C)$ diagram in measuring very small rates of period change.

1.6 Pulsations

When we observe a white dwarf in space, it is true that we are seeing it as it was tens or hundreds of years ago, since it took light that long to reach our eyes here on Earth. It is also true that we are only seeing light from a thin layer right at the surface, since the light will have scattered many times off the deeper material before it can escape.

In some ways this makes our understanding of the composition and internal constituency of stars superficial. However, just as we can explore the interior of the Earth using seismology, the propagation of waves from earthquakes, we can unravel the inner secrets of stars using stellar pulsations, global stellar oscillations that respond differently depending on the internal composition of these objects. This affords us a unique window into the inside of stars otherwise inaccessible.

Fortunately, white dwarf stars have been known to pulsate for more than 45 years, and the theory behind their pulsations is relatively well understood. Due to their strong surface gravities, white dwarfs generally have highly stratified atmospheres, differentiated by lighter elements that rise to the top and heavier elements that sink down. We focus here on the subset of white dwarfs with only a thin veil of hydrogen at their surface belonging to the spectral class DA.

Since they are essentially the bared cores of stars, typical white dwarfs begin their lives with very high temperatures. If the surface temperature of a white dwarf exceeds roughly $12{,}500$ K, the hydrogen at the surface of such a hot star is completely ionized — the negatively charged electrons move too quickly to be bound to the positively charged protons, and the atoms at the surface are in an ionized state. Light escaping from the interior of the star passes easily through these ions and free electrons.

However, white dwarfs evolve by cooling, and as the surface reaches lower temperatures these hydrogen atoms can begin to recombine (the electrons can begin to rejoin and orbit the protons). These atoms with now-bound electrons form a partial-ionization zone and can begin to effectively absorb radiation leaving the center of the white dwarf. This partial-ionization zone can now efficiently store and release large amounts of energy, which provides the sufficient conditions to drive global pulsations. Such a pulsating white dwarf is now located inside the so-called DAV instability strip, and the global pulsations are manifest as periodic brightness changes, caused by temperature changes on the surface of the star that keep a regular tune. These are the stars a-singing.

We can then match the notes from these pulsating stars to detailed models in order to infer the interior properties of these stars. This is just like using the app Shazam to identify a song on the radio; a computer algorithm Fourier transforms the music, which determines the dominant frequencies in the song, which the app then matches to a database of processed songs to make an identification. For white dwarf stars we are instead using the periods of gravity-mode (g-mode) pulsations that have been excited, the periods of which we match to detailed theoretical models[2].

However, the first step in this process is to actually identify the pulsating stars and their pulsation periods, which has been a large part of the discovery component of this dissertation. Since pulsations are extremely useful in probing the interior composition of stars, we have systematically searched for pulsations in white dwarfs at both mass extremes, in the hopes of finding low-mass pulsators (which should have He-cores, see Chapter 4) and ultramassive pulsators (which should have ONe-cores, see Chapter 5). While we have yet to build a sufficient grid of models with which to fully exploit the asteroseismic inferences from these newfound pulsating white dwarfs, we have already been able to prove some funda-

---

[2] Please note: There is a sharp distinction between gravitational waves, the subtle ripples in spacetime predicted by Einstein's general theory of relativity mentioned before, and gravity waves, g-mode pulsations that can be excited inside a star. Often these words are muddled and used interchangeably, but they should not be. This dissertation actually includes the detection of both gravitational waves and gravity waves in low-mass white dwarfs, but their usage should not be confused!

mental aspects of these objects. More detailed modeling is certainly forthcoming.

1.7 Overview of this Dissertation

This dissertation attempts to weave a linear story anchored on time-series photometric observations of white dwarf stars, with a large emphasis on low-mass white dwarfs. Each chapter is based on at least one (and as many as three) accepted peer-reviewed publications.

Chapter 2 highlights the many types of optical variability visible in compact binaries containing at least one low-mass white dwarf, and is a photometric survey of the 20 shortest-period low-mass white dwarf binaries known, all with orbital periods less than 4 hr (Hermes et al. 2012a). We find excellent examples of ellipsoidal variations (which we use to constrain the low-end of the white dwarf mass-radius relationship), Doppler beaming, and one system that shows eclipses, the 12.75-min WD+WD binary J0651+2844. Chapter 3 continues our investigation of J0651+2844 by monitoring the mid-eclipse times of the system over more than two years. We detect rapid orbital decay in line with expectations from the emission of gravitational waves, and begin to constrain the tidal effects on the rate of period change of this merging binary (Hermes et al. 2012b).

Chapter 4 outlines our discovery of the first five pulsating extremely low-mass white dwarfs, all of which should have He-cores and are observed to pulsate at exceptionally cooler effective temperatures than any previously known pulsating white dwarf (Hermes et al. 2012c, 2013d,b). These mark the five lowest-mass pulsating white dwarfs ever found. Chapter 5 continues this exploration of extreme-mass pulsating white dwarfs, but instead extends to the high-mass regime. We describe in Chapter 5 our discovery of pulsations in GD 518, which at 1.2 $M_{\odot}$ makes it the highest-mass white dwarf ever discovered to pulsate (Hermes et al. 2013a). In addition, we spent considerable time searching for pulsating white dwarfs in the *Kepler* field, and include as Appendix B our discovery of the first DAV in the *Kepler* field (Hermes et al. 2011), which was observed from space for roughly 1.5 years before the mission lost fine pointing ability in 2013 May.

Discovering pulsations is sometimes a relatively simple task; we detect significant variability, attempt to disentangle the periods present, and await further modeling before drawing deep conclusions. This can feel thin, short on a full asterosismic treatment. As a counterweight, I conclude with Chapter 6, which outlines more than nine years of observations of the pulsating CO-core white dwarf WD0111+0018. By monitoring the pulse arrival times of the four main periodicities present in this 0.71 $M_{\odot}$ DAV we have shown that the rate of period change is several orders of magnitude faster than expected from cooling alone, and outline our explanations for this new intermediate timescale in pulsation behavior, which likely signifies a new physical effect in the evolution of pulsating white dwarf stars (Hermes et al. 2013c).

Chapter 2

High-Speed Photometry of 20 Merging Low-Mass White Dwarf Binaries

There are a number of physical effects that can induce photometric variability in close binary systems: eclipses, ellipsoidal variations (tidal deformations of the visible primary), reflection, and Doppler beaming. We have searched for these signals by carrying out high-speed photometry on 20 of the shortest-period extremely low-mass (ELM) white dwarf (WD) binaries known, all of which have orbital periods less than 4 hr. Doing so, we have identified the first eight tidally distorted WDs, which can put constraints on the mass-radius relationship for ELM WDs. In half of these binaries we have also detected Doppler beaming, which we can use to confirm the high amplitude of the system's radial-velocity variability. Only one of our ELM WD binaries shows detectable eclipses, J0651+2844, the remarkable 12.75-min WD+WD binary we will discuss in Chapter 3. All of these systems are strong gravitational wave sources, and the time-of-minimum of those that show ellipsoidal variations can be used to detect the orbital period decay, which for some systems will be possible on a timescale of a decade or less.[1]

---

[1] *Significant portions of this chapter have been previously published as:* J. J. Hermes, Mukremin Kilic, Warren R. Brown, M. H. Montgomery, and D. E. Winget, *The Astrophysical Journal*, **749**, 42 (2012) & J. J. Hermes, Warren R. Brown, Mukremin Kilic, Paul Chote, Denis Sullivan, Keaton J. Bell, K. I. Winget, Samuel T. Harrold, E. L. Robinson, Paul Mason, M. H. Montgomery, and D. E. Winget, *The Astrophysical Journal*, in preparation (2013)

2.1 Introduction

White dwarfs (WDs) are the remnant, degenerate cores of stars. About one-third of the stars in the galaxy go through stellar evolution as single stars and end up as typical Earth-sized 0.6 $M_\odot$ CO-core WDs. The remaining two-thirds evolve in binary systems, including short-period systems where stable or unstable mass transfer can take place in the late stages of their stellar evolution. Many short-period systems go through one or two common-envelope phases and evolve into systems containing low-mass WDs. Indeed, radial velocity surveys of low-mass, putatively He-core WDs ($M < 0.45 M_\odot$) indicate that most form in binary systems (Marsh et al. 1995, Brown et al. 2011a). The lower mass WDs are predicted to be larger in radius than their more massive counterparts. However, observational data for radius measurements for low-mass WDs are scarce.

Eclipsing binaries are important laboratories for constraining the mass-radius relation for WDs, but only a handful of direct radius measurements for low-mass, He-core WDs exist. Observations using the *Kepler* spacecraft have so far found four A-stars with bloated $\sim 0.2 - 0.4 M_\odot$ WD companions. The radius measurements for these four WDs range from 0.04 to 0.15 $R_\odot$ (van Kerkwijk et al. 2010, Carter et al. 2011, Breton et al. 2012). However, these four WDs are likely the product of a previous epoch of stable mass transfer (not a common envelope scenario), which suggests that all four of these WDs may be larger than a normal degenerate He star of the same mass (see Section 5.1 of Carter et al. 2011). Hence, they provide only an upper limit for the mass-radius relation for low-mass WDs. In addition, there have been four eclipsing low-mass WD systems detected from the ground (Steinfadt et al. 2010b, Parsons et al. 2011, Vennes et al. 2011, Brown et al. 2011c). Maxted et al. (2011) recently identified a $0.23 M_\odot$ stripped core of a red giant star, a pre-He WD. They measure a radius of 0.33 $R_\odot$ from the eclipse observations, providing an estimate for the radii of an extremely low mass (ELM) WD progenitor.

Tidally distorted WDs in (non-)eclipsing systems also provide reliable constraints on WD radii. The amplitude of the flux variation from ellipsoidal variations goes roughly as $\delta f_{EV} \approx (m_2/m_1)(r_1/a)^3$, where a is the orbital semi-major axis and r_1 is the radius of the primary (e.g., Mazeh & Faigler 2010). Hence, this effect is most important for short-period systems with extreme mass ratios and more importantly with relatively large (radius) WDs, i.e., systems containing ELM WDs. Not surprisingly, the first and second direct detection of tidally distorted WDs occurred in the $P < 1$ h orbital period ELM WD systems J0106-1000 (Kilic et al. 2011c) and J0651+2844 (Brown et al. 2011c). J0651+2844, a 12.75-minute orbital period detached eclipsing double WD system, illustrates the wealth of photometric information that can be present in an ELM WD system: there are primary and secondary eclipses, ellipsoidal variations, and a strong Doppler beaming signal.

The ELM Survey (Brown et al. 2010, Kilic et al. 2011a, Brown et al. 2012, Kilic et al. 2012, Brown et al. 2013) continues to discover a large number of short-period systems containing low-mass WDs. This survey has uncovered more than 30 double-degenerate binaries with < 10 Gyr merger times (Brown et al. 2013) and the only known detached binary WDs with <1 h orbital periods: two 39-minute orbital period binaries, J0106-1000 and J1630+4233 (Kilic et al. 2011c,b), and the 12.75-minute system, J0651+2844 (Brown et al. 2011c). Based on the probability of eclipses and other photometric variability at the timescale of the orbital period, we have established a follow-up program to observe the shortest-period binaries found in the ELM Survey. These time-series photometric observations have been carried out at the McDonald Observatory using the Argos instrument, a frame-transfer CCD mounted at the prime focus of the 2.1m Otto Struve telescope (Nather & Mukadam 2004).

Observations of tidal distortions in these short-period systems can provide important constraints on the physical parameters of the binary. Any mis-alignment between the tidal bulge and the binary orbital period can be measured using the ellipsoidal variations; a mis-alignment will result in tidal heating of the ELM WD (e.g., Fuller & Lai 2012). If the radius of the WD is known, ellipsoidal variations can also be used to constrain the mass of the unseen companion and the inclination angle. This has strong implications for understanding the future evolution of these systems, which depends on the mass ratio of the two stars (Marsh et al. 2004).

2.2 Characterizing Binary Variability

There are five major effects that can cause photometric variability in the primary of a binary system: Doppler beaming, reprocessed light from the secondary (reflection), ellipsoidal variations, eclipses, and pulsations (which we will save for more extensive discussion in Chapter 4). Here, and throughout, we will consider the ELM WD to be the primary, as it is the only visible component of the single-lined spectroscopic binary.

Given a high enough radial velocity variation, Doppler beaming (also referred to as Doppler boosting or relativistic beaming) will act to modulate stellar flux upon approach or recession (see, e.g., Zucker et al. 2007). We treat this as a $\sin\phi$ modulation at the orbital period, where $\phi = 0$ is defined by the spectroscopic conjunction (the point at which the primary is farthest away from Earth). When present, this signal is usually evident as a strong asymmetry in the maxima of ellipsoidal variations, peaking at $\phi = 0.25$.

We follow the formalism of Shporer et al. (2010) and approximate this modulation as dependent on only the effective temperature of the primary ($T_{\mathrm{eff},1}$) and

RV amplitude of the primary (K_1) in the following form:

$$A_{DB} \approx \alpha_1^{'} \frac{K_1}{c} \tag{2.1}$$

where c is the speed of light and $\alpha_1^{'}$ relates to the spectral index $\alpha_1 \equiv \frac{d\log(F_{\nu,1})}{d\log(\nu)}$ as:

$$\alpha_1^{'} = 3 - \alpha_1 = \frac{x_1\, e^{x_1}}{e^{x_1} - 1} \tag{2.2}$$

where $x_1 = h\nu/kT_{\mathrm{eff},1} = \frac{31621}{T_{\mathrm{eff},1}}$ for our blue-bandpass BG40 filter centered at roughly 4550 Å.

Irradiation of the primary by the secondary can cause a reflection effect, which will also sample the orbital period, with a maximum at $\phi = 0$. We treat the reflection effect as a $\cos\phi$ modulation at the orbital period.

Finally, tidal distortions of the primary will cause ellipsoidal variations. The dominant modulation occurs when the larger face comes into view twice per rotation, effectively a $\cos 2\phi$ modulation of the spin period, which would be the orbital period for a synchronized system. However, since tidal distortions do not cause a perfectly ellipsoidal shape, we treat the ellipsoidal variations as harmonics to the first four $\cos\phi$ terms, as derived in Morris & Naftilan (1993). Equation (1) in that work yields a theoretical prediction for the ellipsoidal variation amplitude dominated by

$$L(\phi)/L_0 = \frac{-3(15+u_1)(1+\tau_1)(r_1/a)^3 q \sin^2 i}{20(3-u_1)} \cos(2\phi) \tag{2.3}$$

based on the mass function $q = m_2/m_1$, the limb-darkening (u_1) and gravity-darkening (τ_1) coefficients for the primary, the semimajor axis of the system a, the orbital inclination i, and the radius of the primary r_1. Here we will assume a linear limb darkening law and use the coefficients for u_1 calculated by Gianninas et al. (2013). Since we are most interested in setting a lower limit on the radius of the

ELM WD, we assume that the stellar flux from the surface is purely radiative and assume $\tau_1 = 1.0$. This should be valid for our ELM WDs with $T_{\rm eff} > 10{,}000$ K, justified by our theoretical (and growingly empirical) blue edge for pulsating ELM WDs found in Figure 4.14 in Chapter 4.

To best characterize the variability in the light curve, we perform a Monte Carlo analysis. We create 10^5 synthetic light curves by replacing the measured flux f with $f + g\,\delta f$, where δf is the error in flux and g is a Gaussian deviate with zero mean and unit variance. We then fit each light curve with a five-parameter model that includes an offset, and the (co)sine terms for Doppler beaming, ellipsoidal variations, reflection, and the first harmonic of the orbital period (e.g., Sirko & Paczyński 2003, Shporer et al. 2010, Mazeh & Faigler 2010).

Additionally, we have computed a Fourier transform of our time-series photometry. In some cases, this Fourier analysis has allowed us to refine the orbital period of the system from the less-sampled radial-velocity observations. Usually, though, the periods are so long and the data coverage so sparse that there is much alias structure around the peaks of interest. Since we have signals that may occur at $\cos\phi$ and $\sin\phi$, our Monte Carlo analysis yields a more reliable estimate for the amplitude of the relevant effects.

2.3 Target Selection and Observations

All compact binaries discussed in this work have been discovered through the ELM Survey, a targeted spectroscopic search for ELM WDs using color selection from the Sloan Digital Sky Survey (SDSS). This has been a highly successful survey for short-period compact binaries: The ELM Survey has increased the number of detached, double degenerate binaries known to 54, roughly 30 of which will merge within a Hubble time (Brown et al. 2013).

Table 2.1. Atmospheric and Binary Parameters of our Low-Mass WD Targets

Object	$T_{\rm eff}$ (K)	$\log g$ (cm s^{-2})	$P_{\rm orb}$ (days)	K_1 km s^{-1}	M_1 $M_\odot$	M_2 $M_\odot$	$M_2(60^\circ)$ $M_\odot$	$\tau_{\rm merge}$ Gyr	g_0 (mag)	Ref
J0651+2844	16530	6.76	0.00886	616.9	0.26	0.50	$\cdots$	0.0011	19.1	1,2
J0106−1000	16960	6.10	0.02715	395.2	0.17	≥ 0.37	0.49	≤ 0.039	19.8	3
J1630+4233	14670	7.05	0.02766	295.9	0.30	≥ 0.30	0.37	≤ 0.031	19.0	4
J1053+5200	15180	6.55	0.04256	264.0	0.20	≥ 0.26	0.33	≤ 0.16	18.9	5,6
J0056−0611	12210	6.17	0.04338	376.9	0.17	≥ 0.46	0.61	≤ 0.12	17.2	7
J1056+6536	20470	7.13	0.04351	267.5	0.34	≥ 0.34	0.43	≤ 0.085	19.8	8
J0923+3028	18350	6.63	0.04495	296.0	0.23	≥ 0.34	0.44	≤ 0.13	15.6	9
J1436+5010	16550	6.69	0.04580	347.4	0.24	≥ 0.46	0.60	≤ 0.10	18.2	5,6
J0825+1152	24830	6.61	0.05819	319.4	0.26	≥ 0.47	0.61	≤ 0.18	18.6	8
J1741+6526	10540	6.01	0.06111	508.0	0.16	≥ 1.10	1.55	≤ 0.17	18.4	10
J0755+4906	13160	5.84	0.06302	438.0	0.17	≥ 0.81	1.12	≤ 0.22	20.1	9
J2338−2052	16630	6.87	0.07644	133.4	0.27	≥ 0.15	0.18	≤ 0.95	19.6	7
J0849+0445	10290	6.23	0.07870	366.9	0.17	≥ 0.64	0.88	≤ 0.47	19.1	5
J0022−1014	18980	7.15	0.07989	145.6	0.33	≥ 0.19	0.23	≤ 0.73	19.6	11
J0751−0141	15660	5.43	0.08001	432.6	0.17	≥ 0.94	1.32	≤ 0.37	17.4	7
J2119−0018	10360	5.36	0.08677	383.0	0.17	≥ 0.75	1.04	≤ 0.54	20.0	2
J1234−0228	18000	6.64	0.09143	94.0	0.23	≥ 0.09	0.11	≤ 2.7	17.7	11
J0745+1949	8190	5.70	0.11240	109.0	0.16	≥ 0.46	0.60	≤ 2.4	16.3	10
J0112+1835	10020	5.76	0.14698	295.3	0.16	≥ 0.62	0.85	≤ 2.7	17.1	10
J1233+1602	10920	5.12	0.15090	336.0	0.17	≥ 0.86	1.20	≤ 2.1	19.8	9

References. — (1) Brown et al. (2011c); (2) Hermes et al. (2012b); (3) Kilic et al. (2011c); (4) Kilic et al. (2011b); (5) Kilic et al. (2010); (6) Mullally et al. (2009); (7) Brown et al. (2013); (8) Kilic et al. (2012); (9) Brown et al. (2010); (10) Brown et al. (2012); (11) Kilic et al. (2011a)

We adopt the atmospheric and binary parameters from the ELM Survey; these parameters and their individual references are found in Table 2.1, in order of increasing orbital period. These are all single-lined spectroscopic binaries, so K_1 refers to the radial velocity amplitude of the visible primary. We adopt the convention that the primary is the star that is visible, even though the primary is usually the lowest-mass component.

The targets in this sample range in de-reddened SDSS-g magnitude (g_0) from $15.6 - 20.1$ mag. They are strong sources of gravitational wave radiation, as all of them will merge within 3 Gyr.

2.4 Individual Results

Our photometric observations constrain the 20 shortest-period ELM WD binaries, all with orbital periods < 4 hr. Unless otherwise stated, our observations were obtained at the McDonald Observatory. Our reduction techniques are described in Appendix A. We detail our results in relative order of orbital period, from shortest to longest, and visually represent the results in Figures $2.1 - 2.5$. We include the orbital periods we have used to fold the light curves in Table 2.2. The dashed green and blue lines show the $4\langle\mathrm{A}\rangle$ and $3\langle\mathrm{A}\rangle$ significance level, respectively.

2.4.1 SDSS J065133.34+284423.4

J0651+2844 is the quintessential compact low-mass WD binary, deserving of its own chapter in this dissertation given its extreme nature. Still, it is worth mentioning in this context since it evidences the three main ways compact WD binaries can show photometric variations.

The system is the shortest orbital-period detached binary known: It has an orbital period of 12.7534 ± 0.0033 min with an RV semi-amplitude of $K_1 = 616.9 \pm 5.0$ km s^{-1}, but we can use the photometry to better constrain the orbital period to $12.75344238 \pm 0.00000092$ min, as we will discuss in in Chapter 3. The primary is a $T_{\mathrm{eff}} = 16{,}530 \pm 200$ K, $\log g = 6.76 \pm 0.04$ WD, which corresponds to a mass of $M_1 = 0.26 \pm 0.04\ M_{\odot}$ (Hermes et al. 2012b, Brown et al. 2011c).

We have amassed more than 320 hr of photometry of this system from multiple sites in order to monitor the rate of change of the orbital period. For this chapter, we display here in Figure 2.1 only our data from 2012 January, 60.4 hr of coverage. Our journal of these observations is found in Table 5.1.

This ultra-compact binary system shows deep primary eclipses at $\phi = 0$,

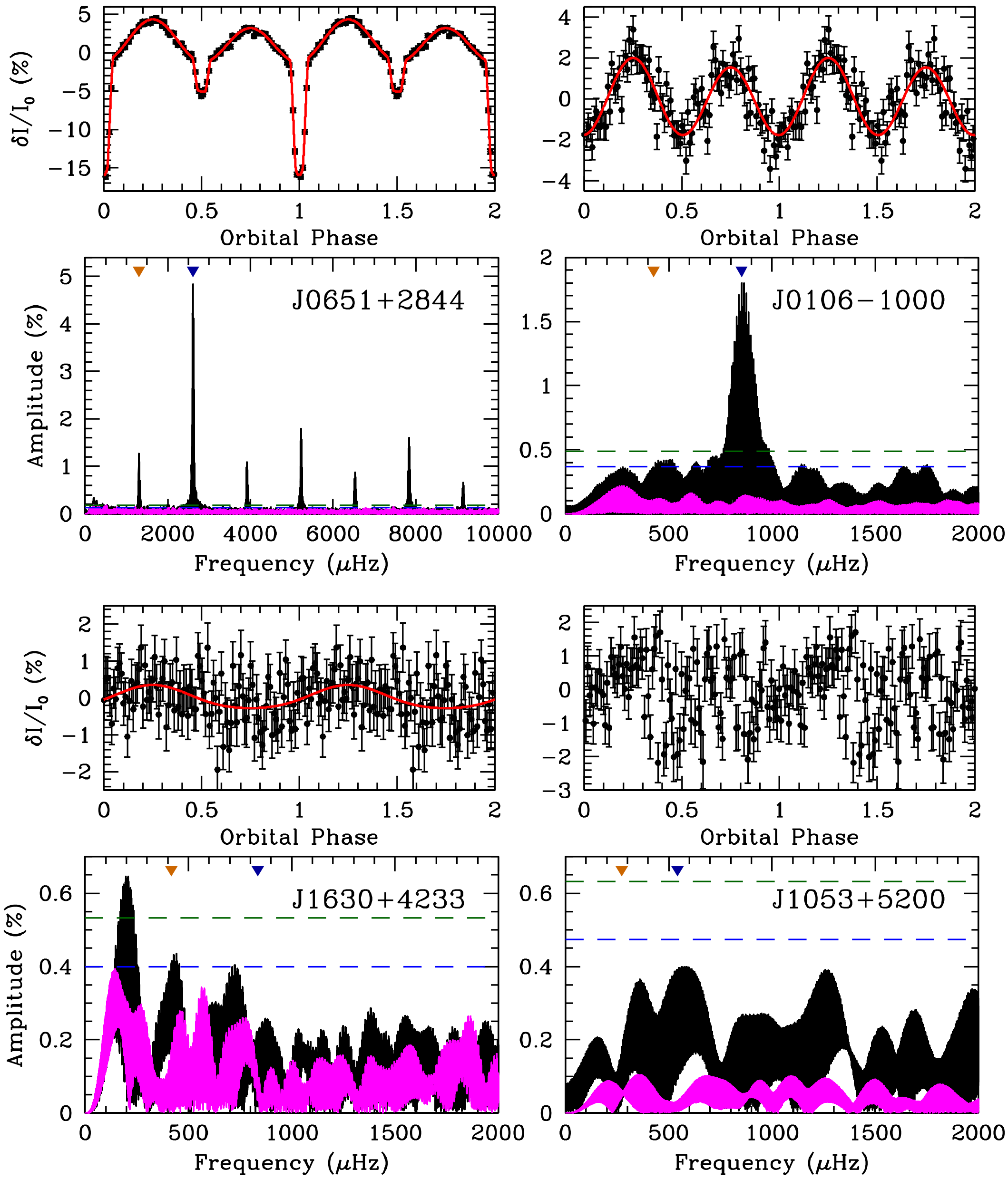

Figure 2.1 High-speed photometry of four ELM WDs in short-period binaries. The top panel for each shows the optical light curve, folded at the orbital period and repeated for clarity. The bottom panel for each shows an FT of the target (black) and brightest comparison star (magenta). The orange and blue triangles show the orbital period and half-orbital period, respectively. These binaries have orbital periods of 12.8 min (J0651+2844), 39.1 min (J0106-1000), 39.8 min (J1630+4233), and 61.3 min (J1053+5200), respectively.

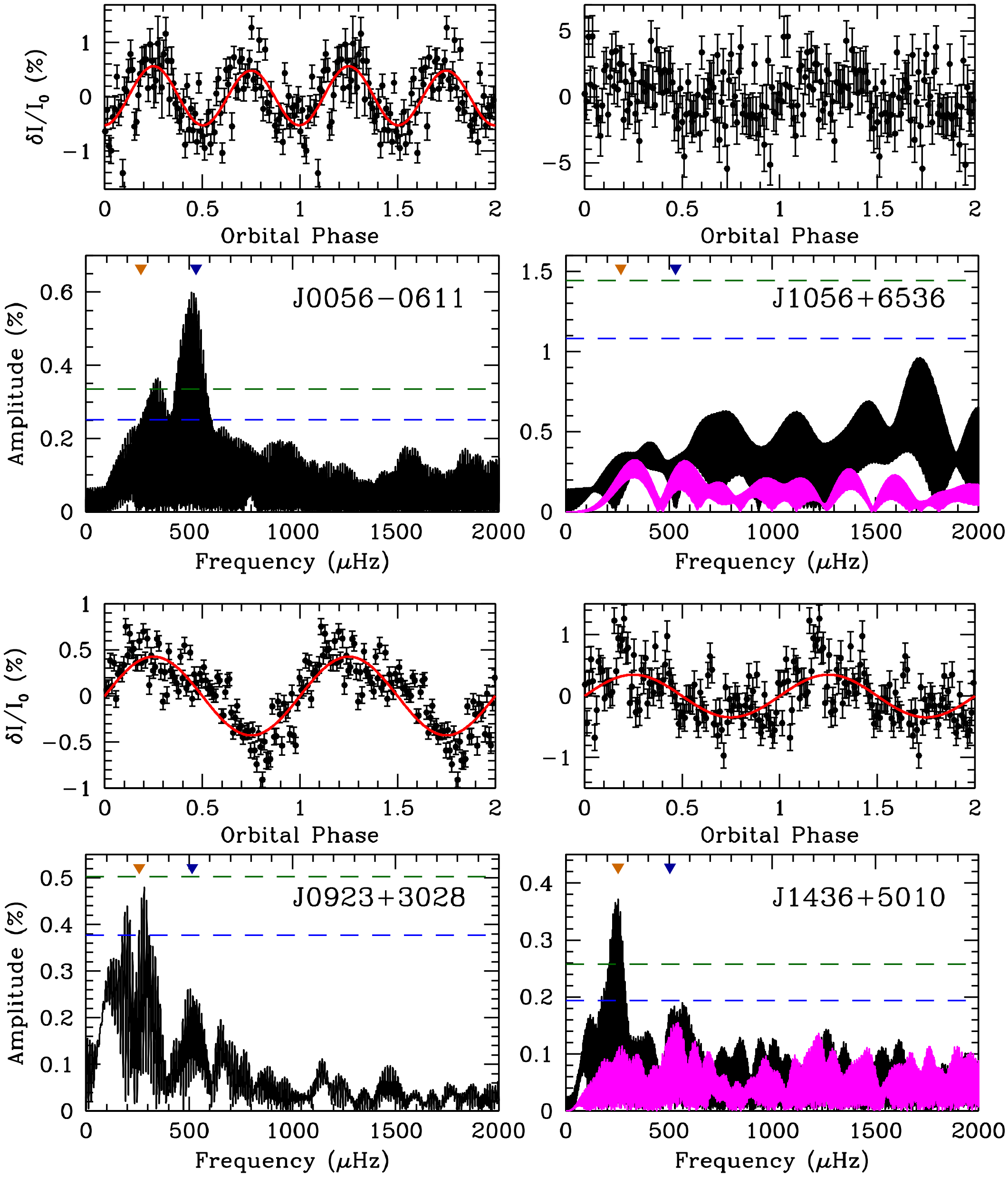

Figure 2.2 The same as Figure 2.1 but for four additional ELM WD binaries. These binaries have orbital periods of 62.5 min (J0056-0611), 62.5 min (J1056+6536), 64.7 min (J0923+3028), and 66.0 min (J1436+5010), respectively. There was only one comparison star in the field for J0056-0611 and J0923+3028.

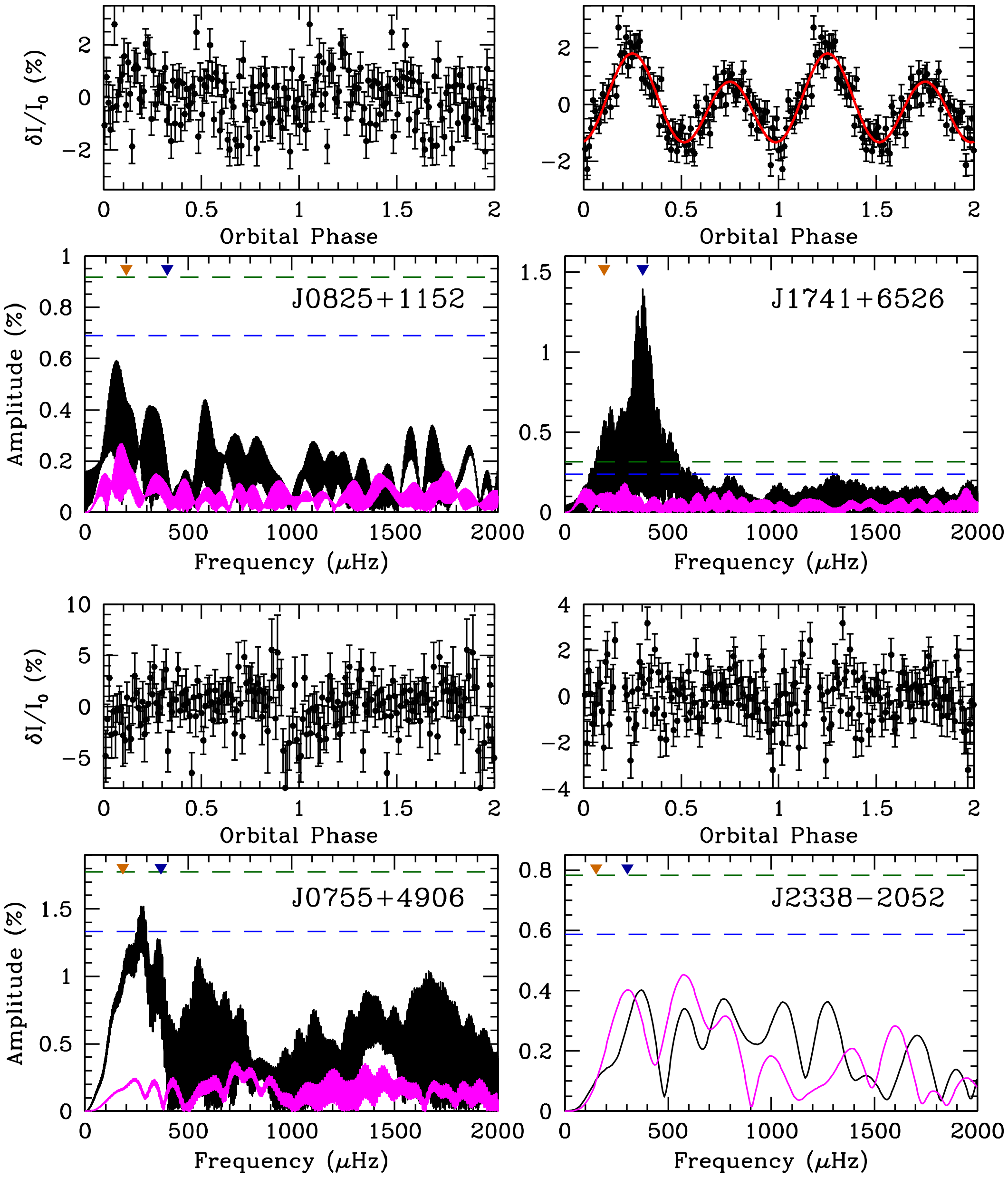

Figure 2.3 The same as Figure 2.1 but for four additional ELM WD binaries. These binaries have orbital periods of 83.8 min (J0825+1152), 88.0 min (J1741+6526), 90.7 min (J0755+4906), and 110.1 min (J2338-2052), respectively.

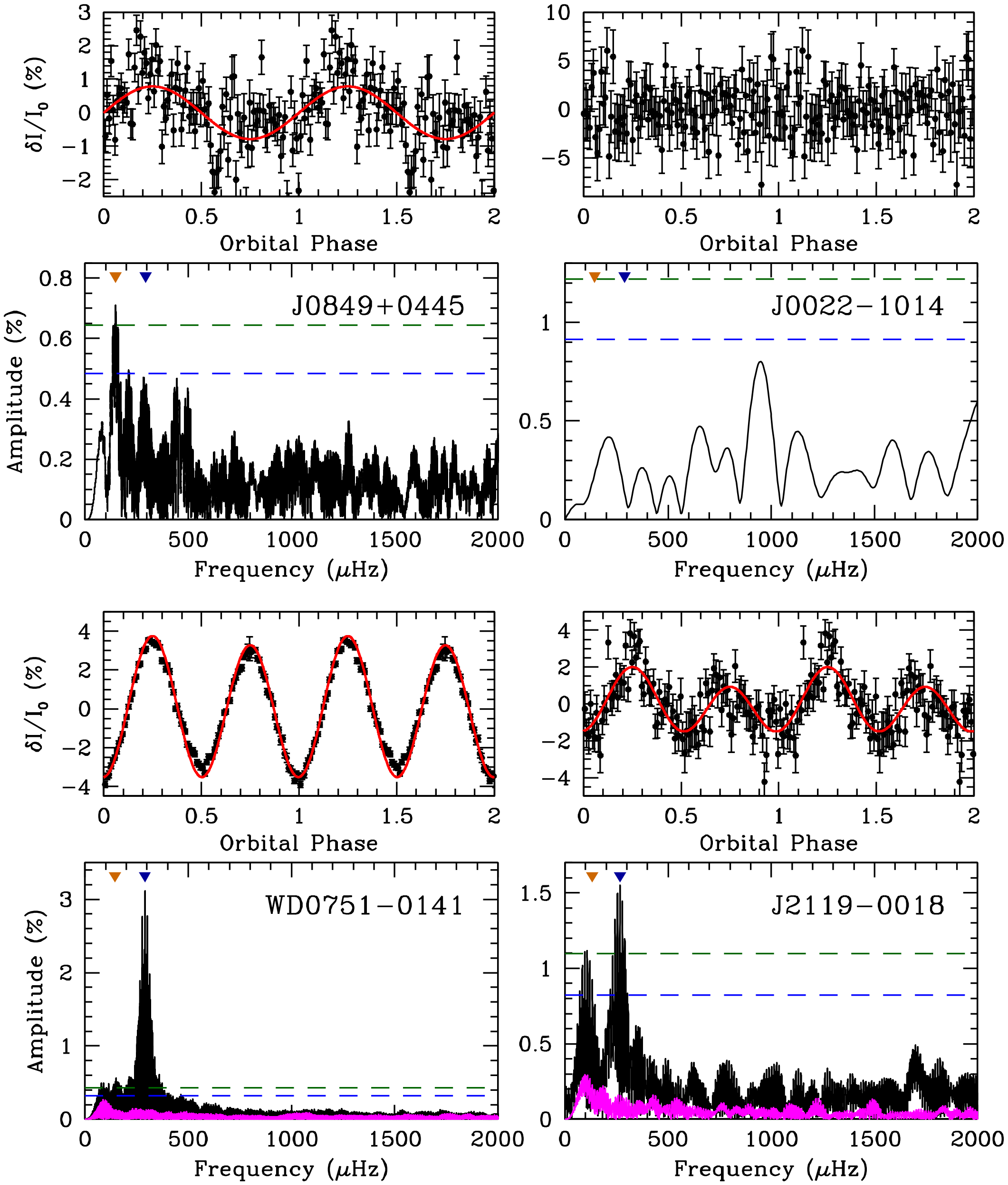

Figure 2.4 The same as Figure 2.1 but for four additional ELM WD binaries. These binaries have orbital periods of 113.3 min (J0849+0445), 115.0 min (J0022-1014), 117.2 min (WD0751-0141), and 124.9 min (J2119-0018), respectively. There was only one comparison star in the field for J0849+0445 and J0022-1014.

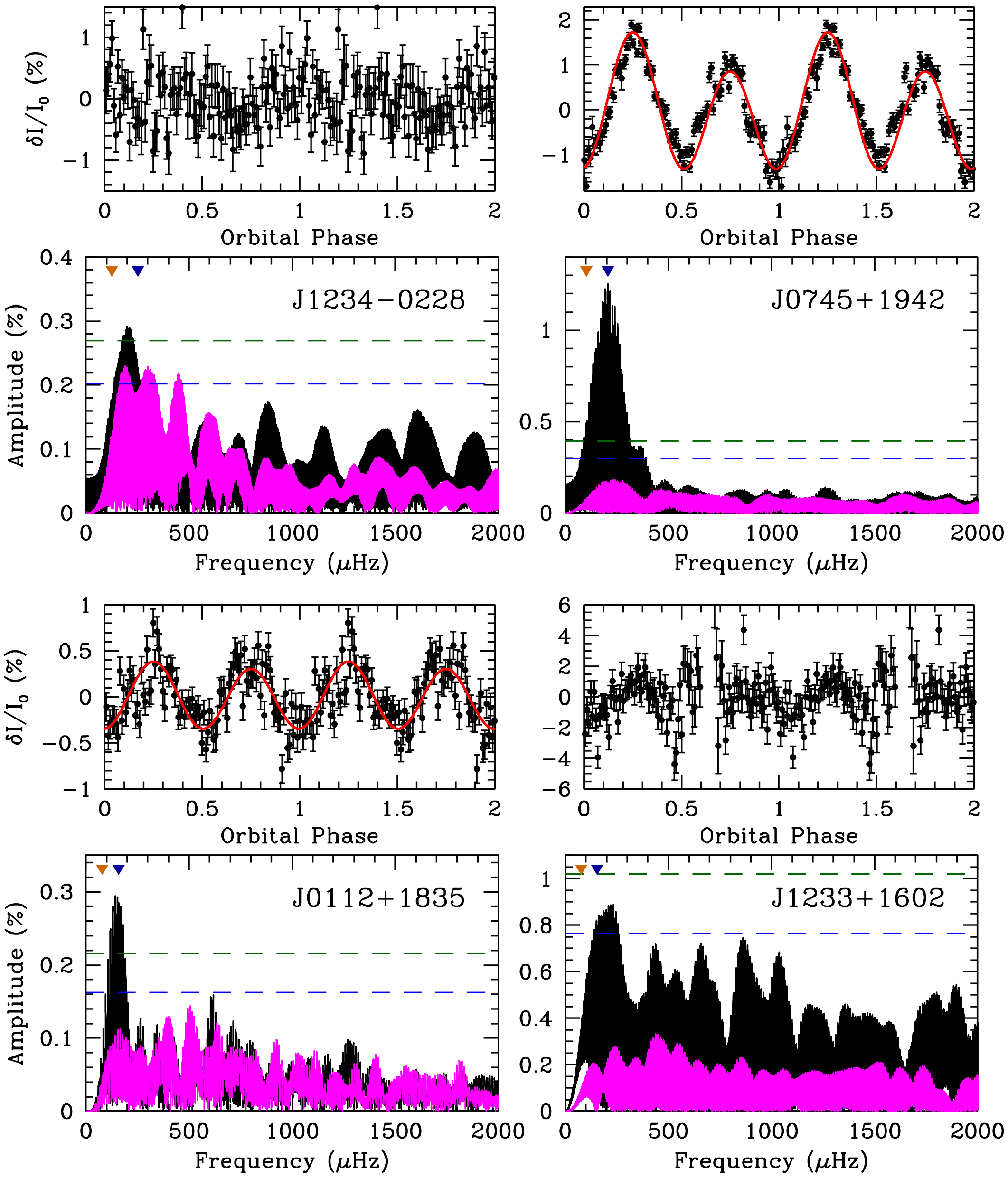

Figure 2.5 The same as Figure 2.1 but for four additional ELM WD binaries. These binaries have orbital periods of 131.7 min (J1234-0228), 161.9 min (J0745+1949), 211.7 min (J0112+1835), and 217.3 min (J1233+1602), respectively.

secondary eclipses at $\phi = 0.5$, ellipsoidal variations from tidal distortion of the primary WD peaking twice each orbit, and Doppler beaming at the orbital period, manifest as the higher asymmetry in the ellipsoidal variations at $\phi = 0.25$. The red curve over the folded light curve is a model fit to the data, described in Chapter 3.

The Fourier transform of this data orients us for the other systems. The highest peak in the FT occurs at the half-orbital period, denoted by the dark blue inverted triangle, which serves to reproduce the high-amplitude ellipsoidal variations. There is also a significant peak at the orbital period, denoted by the orange inverted triangle, primarily corresponding to the Doppler beaming signal. Finally, the comb of peaks at harmonics of the orbital period are a Fourier series reproducing the deep eclipses.

There is a considerable amount we can measure from the light curve of this compact binary; most notably, we have used the changing mid-eclipse times to detect the rapid orbital decay from gravitational radiation (Hermes et al. 2012b). For now we save further discussion of this exciting system for Chapter 3.

2.4.2 SDSS J010657.39-100003.3

Our original photometric observations of J0106-1000 were published in Kilic et al. (2011c), announcing what was then the most compact detached WD binary ever known (J0651+2844 was discovered within days of this binary going to press). Radial velocity observations show this ELM WD is in a 39.100 ± 0.028 min orbit with $K_1 = 395.2 \pm 3.6$ km s^{-1}. With just 2.6 hr of Argos photometry on this $g = 19.8$ mag WD we found 1.7 ± 0.3 percent ellipsoidal variations.

We have followed up those discovery observations with an additional 12.3 hr of photometry using Argos, as well as 4.3 hr using GMOS-S on the 8.1m Gemini-South telescope at Cerro Pachón. This new data confirms the high-amplitude ellipsoidal variations, and we have measured these variations with three different filters. We refine our original measurement through our typical, broad-bandpass BG40 filter, finding a $1.77 \pm 0.12\%$ amplitude. Using our GMOS-S observations we find a $1.82 \pm 0.18\%$ ellipsoidal variation amplitude through a Sloan-g filter and a $1.78 \pm 0.28\%$ amplitude through a Sloan-r filter. There is an additional small signal at the orbital period at 0.23 ± 0.12 percent amplitude (using our Argos observations through a BG40 filter) that may correspond to Doppler beaming of the primary, however it is not yet statistically significant (we expect Doppler beaming at 0.30% amplitude given K_1). The amplitude of the ellipsoidal variations help us constrain the radius of this ELM WD to $R_1 > 0.05\ R_\odot$, which we discuss in Section 2.5.1.2.

The system is a strong source of gravitational wave radiation, and it is possible also to use the ellipsoidal variations to constrain any changes in the system as a result of the emission of gravitational wave radiation. This is discussed in Section 2.5.3.

In addition to our follow-up photometry, we have revisited the spectroscopic parameters of the the visible primary so that the atmospheric parameters for all of our systems that display ellipsoidal variations have been reduced in an identical manner. Detailed description of our fits to low-surface-gravity ELM WD models can be found in Hermes et al. (2013d). From our new fits we adopt values of $T_{\rm eff} = 16960 \pm 400$ K and $\log g = 6.10 \pm 0.06$ for this ELM WD.

2.4.3 SDSS J163030.58+423305.8

J1630+4233 is the third-most-compact low-mass WD binary known, with an orbital period of 39.8 ± 0.1 min and an RV semi-amplitude of $K_1 = 295.9 \pm 4.9$ km s^{-1}. Our 7.8 hr of high-speed photometry was analyzed for the discovery paper on this object, Kilic et al. (2011b). A full journal of observations is listed in Table 5.1.

There is no evidence for ellipsoidal variations of the primary in J1630+4233, which is expected given its relatively higher surface gravity and thus smaller radius. Even though J0106-1000 and J1630+4233 have almost the same orbital period, J1630+4233 is comparatively about a factor of two more massive and nearly a factor of two smaller in radius. Therefore, the expected amplitude of the ellipsoidal variations is $< 0.1\%$, consistent with the observations.

We expect to see roughly 0.24% amplitude sinusoidal variations due to the Doppler beaming effect. Fitting a sinusoid to the folded light curve, it is best explained by $0.31 \pm 0.13\%$ variations at the orbital period. These variations are consistent with the expected beaming signal, however, they do not provide any new physical constraints on the properties of this binary. Using the highest alias in the FT near the RV variability, we can refine the orbital period to 39.833 ± 0.066 min.

2.4.4 SDSS J105353.89+520031.0

J1053+5200 is in a 61.34 ± 0.14 min orbital period binary with $K_1 = 264.8 \pm 15.0$ km s^{-1} (Mullally et al. 2009, Kilic et al. 2010). We obtained 4.7 hr of photometric observations on J1053+5200 and do not detect any significant variability, to a limit of 0.6% amplitude. This is not surprising: The system has a relatively small mass function of $0.082 \pm 0.014\ M_\odot$, and with a 0.20 $M_\odot$ primary, we do not expect a signal from ellipsoidal variations or Doppler beaming much above 0.2% amplitude.

2.4.5 SDSS J005648.23-061141.6

Previous radial-velocity observations show that J0056-0611 has a 62.467 ± 0.029 min orbit with $K_1 = 376.9 \pm 2.4$ km s^{-1} (Brown et al. 2013). Our 12.2 hr of photometric observations span less than 3 months, but the aliasing remains difficult to parse. However, we see good evidence for ellipsoidal variations in this system.

We have folded our light curve on the highest alias peak closest to the half-orbital-period informed by the RV variability, 62.4456 ± 0.0014 min, shown in the FT in Figure 2.2.

There is only one bright comparison star in our field-of-view for these observations, so we cannot fully assess the atmospheric contribution to the low-frequency end of the Fourier transform. Given K_1 we expect a 0.35% amplitude Doppler beaming signal; our Monte Carlo analysis instead finds a corresponding signal with $0.04 \pm 0.08\%$ amplitude. The FT shows stronger evidence, with a peak of 0.19 ± 0.09 amplitude at the orbital period. However, we cannot claim to detect Doppler beaming in this system with any significance.

We have put constraints on both the radius of the primary ($0.055 < R_1 < 0.07\ R_\odot$) and the inclination of the system ($i < 40°$), which constrains the mass of the secondary ($1.3 < M_2 < 1.9\ M_\odot$), using the observed ellipsoidal variations and spectroscopically derived surface gravity, as we will show in Section 2.5.1.1.

2.4.6 SDSS J105611.03+653631.5

J1056+6536 is a compact binary with a 62.7 ± 1.5 min orbital period (Kilic et al. 2012). We obtained 3.0 hr of photometry on this faint $g = 19.8$ WD, covering less than three full cycles of the orbit, so our limits are not very stringent. We do not detect any significant photometric variability in this system.

2.4.7 SDSS J092345.60+302805.0

J0923+3028 is the brightest target in our sample, and is a 64.73 ± 0.71 min orbital period binary with $K_1 = 296 \pm 3$ km s^{-1} (Brown et al. 2010). We observed J0923+3028 for 10.8 hr over three consecutive nights in 2010 December and detect a modest signal near the orbital period, corresponding to Doppler beaming of the primary.

As seen in Figure 2.2, the highest peak in the FT does not line up exactly with the RV-determined orbital period. However, the third-highest alias peak falls very close, at 64.848 ± 0.036 min. We have used this period for the folded light curve, which yields a Doppler beaming amplitude of 0.43 ± 0.13 percent (we expect 0.21% amplitude given the temperature and radial velocity). We do not detect any other significant photometric variability in this system.

2.4.8 SDSS J143633.29+501026.8

J1436+5010 has an orbital period of 65.95 ± 0.14 min with $K_1 = 347.4 \pm 8.9$ km s^{-1} (Mullally et al. 2009, Kilic et al. 2010). We obtained 12.5 hr of photometry spanning nearly three years, from 2010 June to 2013 March. There is a significant peak in the FT at the orbital period, but it suffers from considerable aliasing, so we have folded the data on the best period determined from the RV variability. Our analysis finds a $0.35 \pm 0.08\%$ amplitude signal from Doppler beaming, in line with the expectation of 0.26% from T_1 and K_1. We see no evidence for tidal distortions of this 0.24 $M_\odot$ WD.

2.4.9 SDSS J082511.90+115236.4

J0825+1152 has the hottest WD primary in our sample, at $24{,}830 \pm 740$ K, and has an RV period of 83.794 ± 0.014 min with a $K_1 = 319.4 \pm 2.7$ km s^{-1} (Kilic et al. 2012). We obtained 7.2 hr of photometry in mediocre conditions, spanning 2011 November to 2012 December; we do not detect variability to a limit of 0.9% amplitude.

2.4.10 SDSS J174140.49+652638.7

J1741+6526 has an RV period of 83.794 ± 0.014 min with a mass function of 0.830 ± 0.018 $M_{\odot}$ (Brown et al. 2012). It has the second-highest radial velocity amplitude in our sample, $K_1 = 508 \pm 4$ km s^{-1}, behind only the 12.75-min WD+WD binary J0651+2844. Given the spectroscopically determined mass of the primary, the minimum mass of the unseen companion is 1.09 $M_{\odot}$, and there is a 57% chance that the inclination is such that its companion is more massive than 1.4 $M_{\odot}$. We obtained 9.5 hr of photometry in 2011 May and September, which was analyzed in Hermes et al. (2012a). Our results here include 3.5 hr of additional coverage in 2012 June and July.

The system exhibits significant evidence for both Doppler beaming (at $0.50 \pm 0.08\%$ amplitude) and ellipsoidal variations (at $1.31 \pm 0.08\%$ amplitude). Given the system's high RV amplitude, we expect a 0.57% amplitude signal from Doppler beaming, which is within the errors what we observe. This is to date the highest-amplitude Doppler beaming signal ever observed for a binary system. Additionally, we can use the high-amplitude ellipsoidal variations to constrain the radius of the ELM WD in this system, as we discuss in Section 2.5.1.3.

J1741+6526 was originally found to be one of the lowest surface gravity WDs known, with a spectroscopically determined $\log g < 5.20$ (Brown et al. 2012). However, this low surface gravity is incompatible with the relatively small inferred radius of the ELM WD determined from the ellipsoidal variations. We have used the extended model atmospheres described at length in Hermes et al. (2013d) and Brown et al. (2013) to re-fit the observed optical spectrum of this low-mass WD. Our new fits find that this is a $T_{\rm eff} = 10540 \pm 100$ K, $\log g = 6.00 \pm 0.04$ WD, as discussed in Section 2.5.1.3.

2.4.11 SDSS J075552.40+490627.9

Previous radial-velocity observations show that J0755+4906 has a 90.7 ± 3.1 min orbit with $K_1 = 438 \pm 5$ km s^{-1} (Brown et al. 2010). This is the faintest target in our sample, with $g = 20.1$ mag. We obtained 1.6 hr of photometry with Argos in good conditions, but the faintness of our target introduced an r.m.s. scatter greater than 2.3 percent relative amplitude. We therefore obtained additional time-series photometry from larger facilities. Our journal of observations can be found in Table 5.1.

We obtained 1.6 hr of photometry over two consecutive nights in 2012 November using the DIAFI instrument mounted on the 2.7 Harlan J. Smith telescope at McDonald Observatory. Additionally, we obtained 2.3 hr in 2012 December using a CCD mounted at the f/5 wavefront sensor of the 6.5m MMT telescope. Using standard IRAF routines we dark-subtracted and flat-fielded our raw science frames, and applied a barycentric correction to this data using the IDL code of Eastman et al. (2010).

Our 5.5 hr of data is spread over more than two years; we covered less than four of the more than $12{,}000$ orbital cycles that elapsed from the beginning to end of our observations. We do not detect any significant photometric variability in J0755+4906, although our limits are not very stringent, to 1.77% relative amplitude.

2.4.12 SDSS J233821.51-205222.8

J2338-2052 is another relatively faint binary ($g = 19.6$ mag) in our sample, and has RV period of 110.1 ± 10.3 min (Brown et al. 2013). Using the same f/5 science camera on the 6.5m MMT as used with J0755+4906, we obtained 1.8 hr of photometry on the J2338-2052 system. We do not detect significant photometric variability, to a limit of 0.6% relative amplitude.

2.4.13 SDSS J084910.13+044528.7

J0849+0445 is a 113.33 ± 0.14 min binary with a relatively high RV semi-amplitude, $K_1 = 366.9 \pm 14.7$ km s^{-1}(Kilic et al. 2010). We obtained 11.7 hr of photometry in 2013 March and April and detect variability at the orbital period with $0.78 \pm 0.16\%$ amplitude corresponding to Doppler beaming. There are likely some atmospheric effects contributing to inflating this variability — we expect Doppler beaming should induce a 0.40% amplitude signal given the RV semi-amplitude — but we have only one bright comparison star in the Argos field-of-view, so we have a more difficult time constraining the atmospheric contribution to our target light curve. We do not detect any other significant photometric variability.

2.4.14 SDSS J002207.65-101423.5

J0022-1014 has RV period 115.1 ± 4.3 min with $K_1 = 145.6 \pm 5.6$ (Kilic et al. 2011a). We do not detect any significant photometric variability, to a limit of 0.9% amplitude, in the 2.2 hr of observations obtained over one night in 2010 October.

2.4.15 WD J075141.18-014120.9

WD0751-0141 contains an ELM WD in a 115.2 ± 4.0 min binary with a massive unseen companion, which induces RV variability of $K_1 = 432.6 \pm 2.3$ km s^{-1} on the primary (Brown et al. 2013). The companion has a minimum mass of 0.94 $M_{\odot}$; assuming a random inclination, there is a nearly 50% chance the companion is more massive than 1.4 $M_{\odot}$.

We originally had a difficult time phasing the photometry using the orbital period derived from the RV observations. We therefore obtained 63.2 hr of photometric observations, spread from 2012 February to 2013 April. Much of this data was obtained using the Puoko-Nui instrument mounted on the 1.0 m telescope at

Mt. John Observatory, through the same BG40 filter as the McDonald observations. An FT of all 63.2 hr of data shows a well-resolved peak at 57.60907 ± 0.00003 min, which is nearly half the RV-determined orbital period. We thus refined the orbital period to 115.21814 ± 0.00006 min, which provides for a much more coherent folded light curve, shown in Figure 2.4.

Our time-series photometry reveals high-amplitude ($3.20 \pm 0.11\%$ amplitude) ellipsoidal variations of the ELM WD primary by the massive companion, which constrains the radius of the ELM WD primary, as discussed in Section 2.5.1.7. We also detect a slight asymmetry in these tidal distortions best explained by a $0.24 \pm 0.11\%$ Doppler beaming signal; we expect a 0.33% amplitude effect given K_1.

2.4.16 SDSS J211921.96-001825.8

The ELM WD J2119$-$0018 is in a binary with a 124.95 ± 0.06 min orbital period and a $K_1 = 383 \pm 4$ km s^{-1}, yielding a minimum mass for the unseen companion of 0.75 $M_\odot$ (Brown et al. 2010). Observations of J2119$-$0018 were carried out using over three nights in 2011 July, yielding 11.8 hr of coverage. Figure 2.4 shows the Argos light curve folded over the best-fit orbital period from the radial velocity variations, 124.95 min, binned into 100 orbital phase bins.

Only the $\cos 2\phi$ term for ellipsoidal variations appears with any statistical significance in the Monte Carlo analysis of the folded light curve; our results were first reported in Hermes et al. (2012a). This analysis yields an estimate for the observed amplitude of the ellipsoidal variations of 1.45 ± 0.27 percent, which can constrain the radius of the ELM WD primary, as discussed in Section 2.5.1.4. We also see slight evidence for the $\sin \phi$ term corresponding to Doppler beaming at $0.70 \pm 0.27\%$ amplitude; we expect a 0.42% amplitude signal given K_1 and $T_{\mathrm{eff},1}$.

2.4.17 SDSS J123410.36-022802.8

The 131.6 ± 5.8 min binary system J1234-0228 has the smallest RV semi-amplitude in our sample, with $K_1 = 94.0 \pm 2.3$ km s^{-1} (Kilic et al. 2011a). We obtained more than 8.4 hr of photometry in 2011 January and April. In an FT of all our data we see evidence for variability at 76.861 ± 0.004 min with 0.30% relative amplitude, which is close to but not exactly at the half-orbital period. However, we also see a formally significant alias in the brightest comparison star at 76.824 ± 0.002 min with 0.22% relative amplitude, so this signal is very likely an artifact from atmospheric variability. Our Monte Carlo analysis does not reveal any significant signals corresponding to Doppler beaming or ellipsoidal variations; we expect such signals to have $< 0.1\%$ amplitude given that $K_1 = 94$ km s^{-1} and $M_1 \sim 0.23\ M_\odot$.

2.4.18 SDSS J074511.56+194926.5

J0745+1949 is a heretofore unpublished binary containing an ELM WD with a 161.850 ± 0.014 min orbital period and $K_1 = 109 \pm 3$ km s^{-1}; the atmospheric parameters were outlined in Brown et al. (2012) and the orbital solution is in preparation (Gianninas et al. 2013, in prep.). We obtained 10.9 hr of photometry in 2012 November and December and 2013 March, and fold the data using the alias in the FT closest to the half-orbital period, 161.84375 ± 0.00005 min.

We see high-amplitude ellipsoidal variations, with $1.07 \pm 0.10\%$ amplitude, which can help us constrain the radius of the ELM WD primary, as discussed in Section 2.5.1.6. We also see evidence for Doppler beaming at $0.30 \pm 0.10\%$ amplitude; we expect a 0.15% amplitude signal given K_1.

The low surface gravity and 8190 K temperature of J0745+1949 put it near the instability strip for pulsations in ELM WDs (see Chapter 4). However, we see no evidence for variability at timescales other than the orbital- and half-orbital periods, to a limit of 0.4% amplitude, and include this star as an NOV4 in our search for pulsations in He-core WDs (see Chapter 4). This star also happens to be one of the most heavily polluted WDs known, with deep absorption lines of several different metals that corresponds to some of the highest metal abundances observed in any WD; analysis of these abundances is in preparation.

2.4.19 SDSS J011210.25+183503.74

The 211.651 ± 0.043 min binary J0112+1835 is composed of an ELM WD and an unseen companion; the RV semi-amplitude of 295 ± 2 km s^{-1} suggests the unseen companion is at least 0.62 $M_{\odot}$ (Brown et al. 2012). We obtained 12.8 hr of photometry in 2011 September with Argos, which yield a formally significant detection of ellipsoidal variations with $0.31 \pm 0.06\%$ amplitude. We will use this signal to constrain the radius of this ELM WD in Section 2.5.1.5. We expect a 0.34% amplitude variation at the orbital period corresponding to Doppler beaming; however, we see no evidence for this effect. Our three observations are 4.1 hr, 4.0 hr, and 4.8 hr in length, respectively, which make detecting a 3.5 hr signal more difficult.

2.4.19.1 Narrow-Band Photometry of a Compact Binary

We have also used J0112+1835 as a proof of concept to show that radial-velocity variations in compact ELM WD binaries are detectable through narrow-band photometry. Motivated by the observational technique of Robinson & Shafter (1987), we used a custom narrow-band filter with a bandpass centered in the wing of a hydrogen Balmer line to observe this compact binary, with the expectation that radial-velocity variations would be manifest as periodic variations in the light curve through this narrow-band filter. Figure 2.6 shows our result, comparing light curves of J0112+1835 through two different filters. Spectroscopy shows J0112 is in

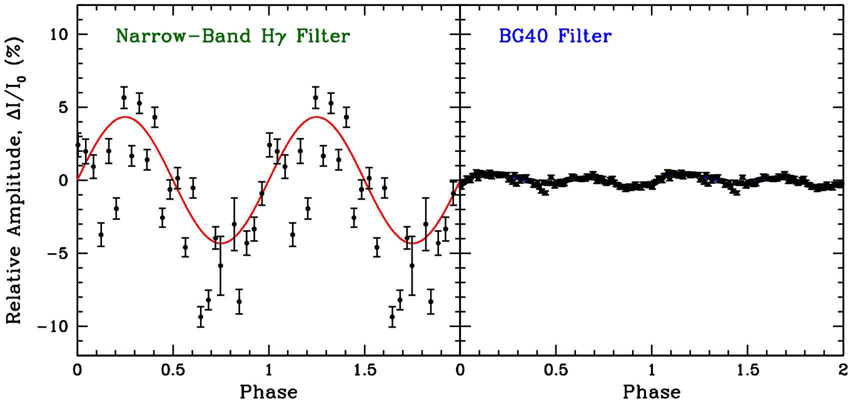

Figure 2.6 Proof of concept for a narrow-band photometric technique to discover radial velocity variations in ELM WDs. The left panel shows a light curve of J0112+1835 through a narrow-band filter centered in the blue wing of the Hγ line, and confirms that this method will detect RV variability. The right panel shows the same star through a broader BG40 filter; only low-amplitude ellipsoidal variations twice per orbit are visible. Both light curves are folded at the previously known orbital period of 3.5275 hr and duplicated for clarity.

a 3.5275 hr orbit with $K_1 = 295 \pm 2$ km s^{-1} (Brown et al. 2012). The left panel of Figure 2.6 shows 5.2 hr of observations in 2012 October of J0112+1835 taken with Argos using a custom interference filter centered at 4322 Å, in the blue wing of the Hγ absorption line, with a FWHM of 45 Å. The right panel shows 12.8 hr of observations in 2011 September on the same telescope and instrument through a much broader BG40 filter. Both light curves have been folded at the orbital period and binned into 25 and 100 points, respectively. Observing less than two orbits with narrow-band photometry confirms the RV variability, as well as the orbital period, to the 3-σ level. This approach is limited to the brightest systems, since the interference filter scatters a significant amount of light, but it affords the opportunity to further broaden the search for additional ultra-compact systems using photometry instead of spectroscopy.

2.4.20 SDSS J123316.20+160204.6

J1233+1602 is composed of a faint ($g = 19.8$ mag) ELM WD in a 217.30 ± 0.13 min orbital period with $K_1 = 336 \pm 4$ km s^{-1} (Brown et al. 2010). We obtained 5.6 hr of photometry using Argos; our first 2.9 hr run in 2011 May is separated by more than two years from our three runs in 2013 May. Unfortunately we have not covered a complete 3.6-hr orbit, but we have more than 88% of phase coverage. We see some evidence for a signal corresponding to ellipsoidal variations in this system, but our detection ($0.60 \pm 0.26\%$ amplitude) is not yet formally significant.

2.5 Light Curve Analysis

We feature in Table 2.2 the full results from our Monte Carlo analysis of our high-speed photometry of 20 merging low-mass WD binaries.

2.5.1 Inferred System Parameters from Ellipsoidal Variations

We have used the amplitudes of the observed $\cos(2\phi)$ variations in the light curve, which we interpret as ellipsoidal variations of the primary by the unseen companion, in order to constrain the radius of the ELM WD primary in seven of our systems. In each case, we can put an observed lower-limit on the radius of the ELM WD (the inclination is not known, which effectively increases the inferred ELM WD radius) using Equation 2.3. For the binaries with a primary with $T_{\rm eff}$ $>$ 10,000 K, we assume all energy transport at the surface is radiative and thus the gravity darkening coefficient is $\tau_1 = 1.0$. We assume linear limb-darkening coefficients using the atmosphere models of Gianninas et al. (2013). In some cases, we use the spectroscopically determined surface gravity to constrain the inclination of the system, and thus the companion mass. While we see ellipsoidal variations in the J0651+2844, the eclipses provide a much more robust measurement of the

Table 2.2. Light Curve Analysis of 20 Merging Low-Mass WD Binaries

Object	$P_{\rm orb,spec}$ (min)	$P_{\rm orb,fold}$ (min)	$\sin(\phi)$ (%)	$\cos(2\phi)$ (%)	$\cos(\phi)$ (%)	$\sin(2\phi)$ (%)	M_1 ($M_\odot$)	r_1 ($R_\odot$)
J0651+2844	12.75(1)	12.7534424	0.56(07)	4.01(07)	0.02(07)	0.01(07)	0.26	0.0371(12)[1]
J0106−1000	39.10(3)	39.10406	0.23(12)	1.77(12)	0.00(12)	0.01(12)	0.17	$0.05-0.075$
J1630+4233	39.8(1)	39.830	0.31(13)	0.04(13)	0.05(13)	0.04(13)	0.30	$\cdots$
J1053+5200	61.3(1)	61.286	0.23(16)	0.36(16)	0.04(16)	0.24(16)	0.20	$\cdots$
J0056−0611	62.47(3)	62.466700	0.04(08)	0.52(08)	0.02(08)	0.05(08)	0.17	$0.045-0.0675$
J1056+6536	62.7(2)	62.654	0.69(29)	0.34(29)	0.09(29)	0.20(29)	0.34	$\cdots$
J0923+3028	64.7(7)	64.8482	0.43(13)	0.00(13)	0.00(13)	0.16(13)	0.23	$\cdots$
J1436+5010	66.0(1)	65.95	0.35(08)	0.12(08)	0.01(08)	0.07(08)	0.24	$\cdots$
J0825+1152	83.79(1)	83.7936	0.42(19)	0.01(19)	0.02(19)	0.19(19)	0.26	$\cdots$
J1741+6526	87.996(6)	87.9984	0.50(08)	1.30(08)	0.11(08)	0.03(08)	0.16	$0.067-0.085$
J0755+4906	91(3)	90.749	0.03(44)	0.94(44)	0.00(44)	0.00(44)	0.17	$\cdots$
J2338−2052	110(10)	110.07	0.05(20)	0.28(20)	0.00(20)	0.05(20)	0.27	$\cdots$
J0849+0445	113.3(1)	113.2013	0.78(16)	0.41(16)	0.03(16)	0.05(16)	0.17	$\cdots$
J0022−1014	115(4)	115.04	0.10(30)	0.16(30)	0.07(30)	0.10(30)	0.33	$\cdots$
J0751−0141	115(4)	115.21814	0.24(11)	3.20(11)	0.00(11)	0.00(11)	0.16	$0.115-0.158$
J2119−0018	124.95(6)	124.949	0.70(27)	1.45(27)	0.01(27)	0.12(27)	0.17	$0.089-0.134$
J1234−0228	132(6)	131.66	0.07(08)	0.00(08)	0.10(08)	0.00(08)	0.23	$\cdots$
J0745+1949	161.8(1)	161.84375	0.30(10)	1.07(10)	0.00(10)	0.16(10)	0.17	>0.12
J0112+1835	211.65(4)	211.55545	0.01(06)	0.31(06)	0.00(06)	0.01(06)	0.16	$0.075-0.125$
J1233+1602	217.3(1)	217.30	0.01(26)	0.60(26)	0.00(26)	0.00(26)	0.17	$\cdots$

Note. — (1) Radius measured from eclipses (see Chapter 3) inferred low-mass WD radius, so we do not include its analysis here. We present our results here in order of decreasing surface gravity, which should roughly be in order of increasing inferred ELM WD radius, since models predict these low surface-gravity WDs have masses $0.16 - 0.17\ M_{\odot}$ for their given temperatures.

2.5.1.1 J0056-0611

We use the $0.52 \pm 0.08\%$ amplitude ellipsoidal variations to constrain the radius of the ELM WD in J0056$-$0611 utilizing Equation 2.3, assuming a linear limb-darkening coefficient of $u_1 = 0.46$, and present the results graphically in the top panel of Figure 2.7. Regardless of any other assumptions, we show that $R_1 > 0.04\ R_{\odot}$. However, we can constrain our system further by using the spectroscopically determined surface gravity.

We show in the top panel of Figure 2.7 the location of the radius we would infer for this ELM WD given its surface gravity, $R_1 = (GM/g)^{1/2}$, and include the 1-σ uncertainties that would result from the uncertainties on both the measured surface gravity (in dark red) and also including the uncertainties in the derived mass (in dark green). We use the region where both radius estimates intersect, within the 1-σ uncertainties, to constrain the inclination of the system to $32 < i < 64$ degrees. This then constrains the companion mass to $0.6 < M_2 < 1.9\ M_{\odot}$, as shown in the bottom panel of Figure 2.7.

The best match to the observed surface gravity occurs for $i = 42°$, which would imply that the unseen companion is a roughly $1\ M_{\odot}$ WD. If we use the surface gravity constraint on the inclination angle, we can constrain the primary radius to $0.045 < R_1 < 0.0675\ R_{\odot}$.

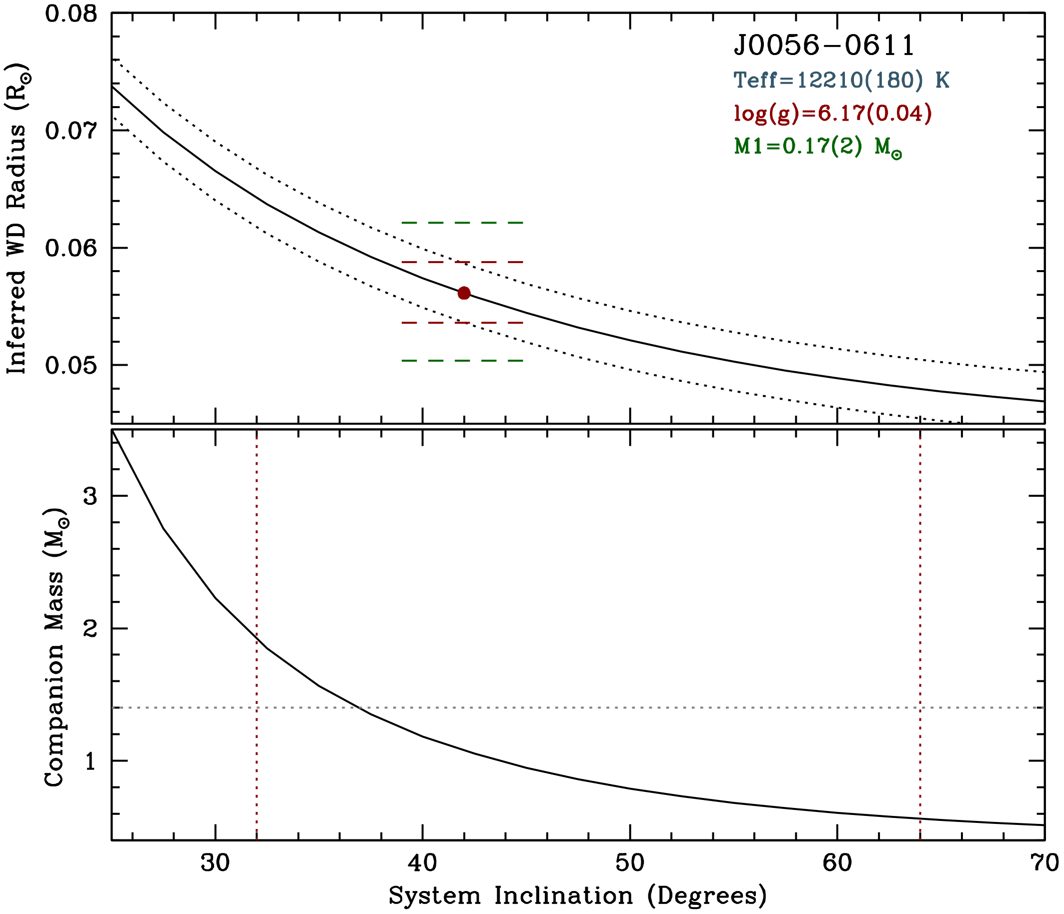

Figure 2.7 The top panel shows allowed values for the radius, modulo the system inclination, to explain the $0.52 \pm 0.08\%$ amplitude ellipsoidal variations observed in J0056−0611, and includes 1-σ uncertainties. We can also use the determined surface gravity and mass to predict an expected ELM WD radius; this is plotted as a dark red dot, with dashed lines showing the 1-σ uncertainties from the surface gravity alone (dark red) and the surface gravity and the inferred mass (dark green). This constrains the inclination to $32 < i < 64$ degrees, which we use in the bottom panel to constrain the companion mass to $0.6 < M_2 < 1.9\ M_\odot$.

2.5.1.2 J0106-1000

J0106-1000 is another system in which we can use the $1.77 \pm 0.12\%$ amplitude ellipsoidal variations to constrain the radius of the ELM WD primary. The top panel of Figure 2.8 shows the run of the inferred radius modulo the system inclination, assuming $u_1 = 0.40$. We find that $R_1 > 0.05\ R_\odot$.

We have again used the spectroscopically derived surface gravity of this ELM WD to put constraints on the inclination, and find that $i > 32$, which indicates that the companion mass should be $0.4 < M_2 < 1.45\ M_\odot$, making the unseen companion very likely another WD. For this run of inclinations, we infer $0.05 < R_1 < 0.075\ R_\odot$ for the visible ELM WD primary.

2.5.1.3 J1741+6526

Our original results using the observed ellipsoidal variations of J1741+6526 to infer the radius of the primary ELM WD in that system were originally reported in Hermes et al. (2012a). We have obtained an additional 3.5 hr of coverage, which refines the observed ellipsoidal variations to $1.30 \pm 0.08\%$ amplitude. Assuming a linear limb-darkening coefficient of $u_1 = 0.54$, we plot a run of the inferred radius versus inclination in the top panel of Figure 2.9.

Our photometry rules out 2% or deeper primary eclipses, which constrains the system inclination to be less than 85°. The minimum radius of the ELM WD in J1741+6526 is thus 0.067 $R_\odot$. This also implies that the mass of the unseen companion exceeds 1.11 $M_\odot$.

The original atmospheric parameters for this ELM WD were reported in (Brown et al. 2012). However, we fit the observations to a grid of model atmospheres that only extended to $\log g = 5.0$, and many of those fits bottomed out at

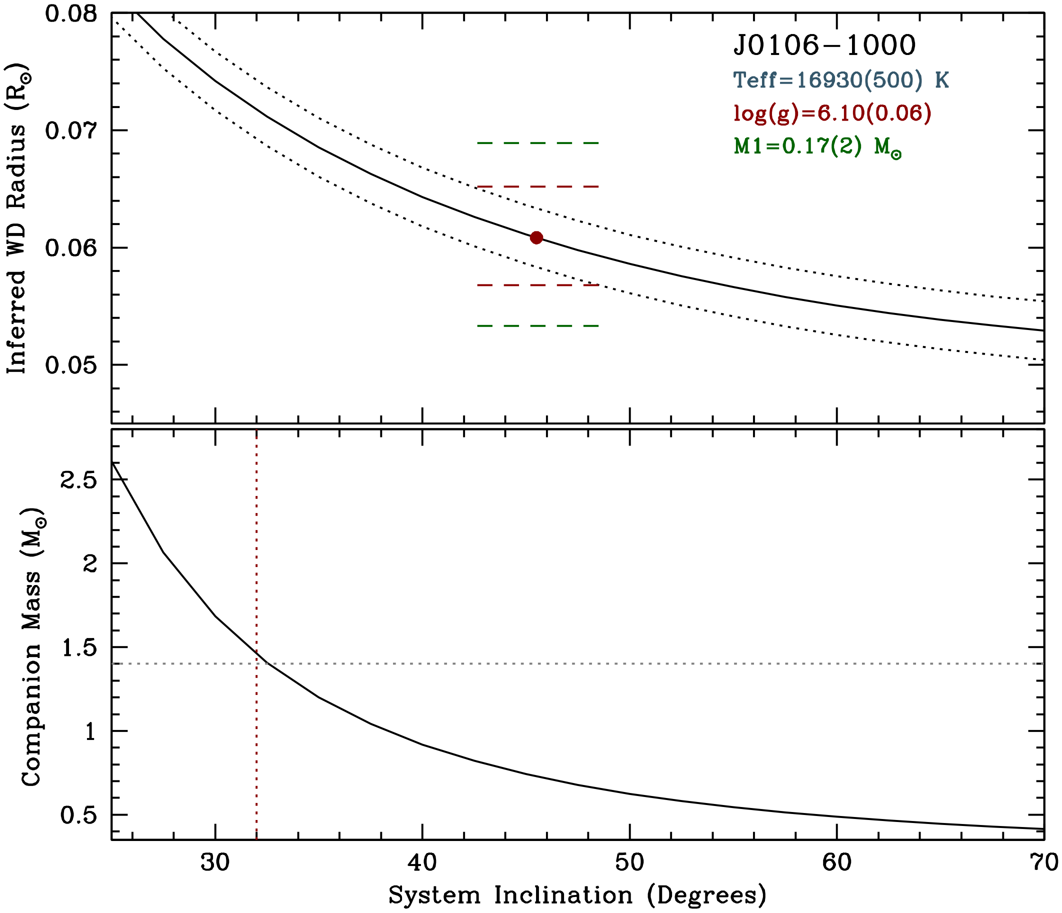

Figure 2.8 The top panel shows allowed values for the radius, modulo the system inclination, to explain the $1.77 \pm 0.12\%$ amplitude ellipsoidal variations observed in J0106−1000, and includes 1-σ uncertainties. We can also use the determined surface gravity and mass to predict an expected ELM WD radius; this is plotted as a dark red dot, with dashed lines showing the 1-σ uncertainties from the surface gravity (dark red) and surface gravity and inferred mass (dark green). This constrains the inclination to $i > 32$ degrees, which we use in the bottom panel to constrain the companion mass to $0.4 < M_2 < 1.45\ M_\odot$.

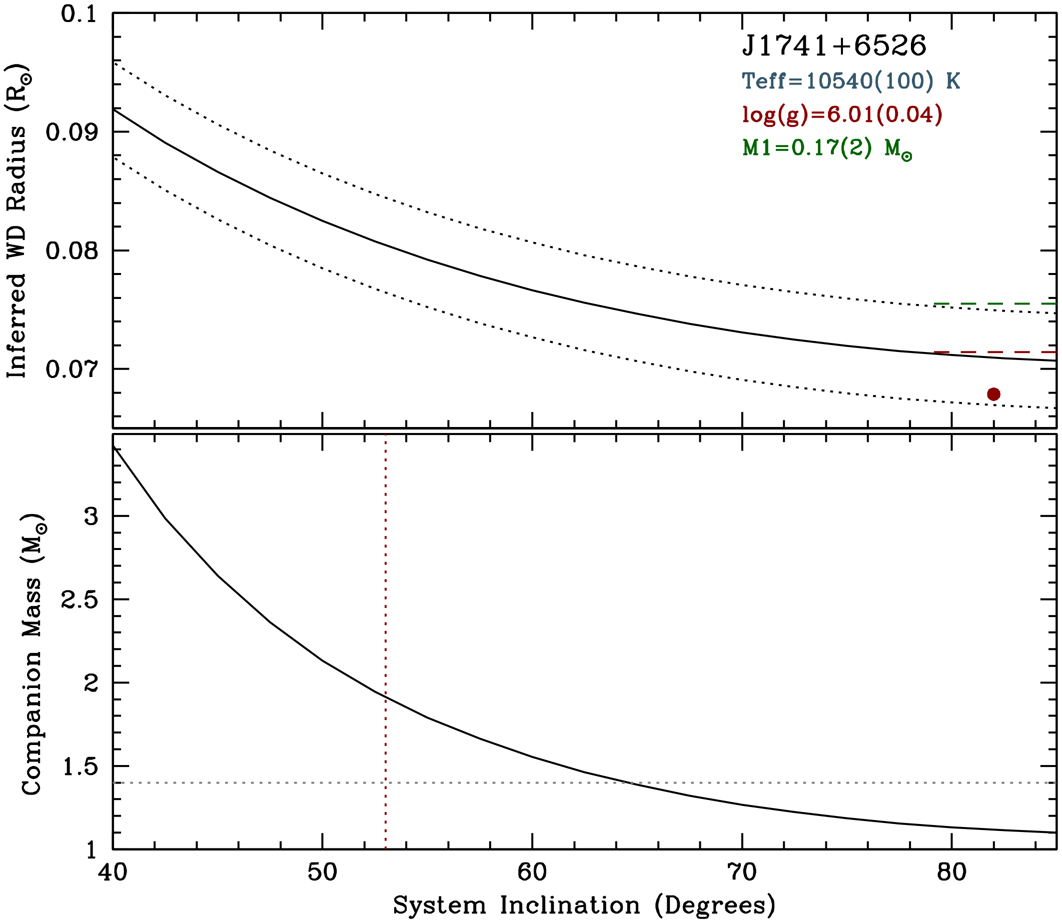

Figure 2.9 The top panel shows allowed values for the radius, modulo the system inclination, to explain the $1.30 \pm 0.08\%$ amplitude ellipsoidal variations observed in J1741+6526, and includes 1-σ uncertainties. As described previously, we can use the determined surface gravity and mass to predict an expected ELM WD radius, marked as a dark red dot. This constrains the inclination to $i > 53°$, which constrains the companion mass to $1.1 < M_2 < 1.9\ M_\odot$.

5.0, deriving an extremely low surface gravity, $\log g = 5.19 \pm 0.06$. This would correspond to a $0.16 \pm 0.02\ M_{\odot}$ ELM WD, which would infer a radius of roughly 0.168 $R_{\odot}$. This is in contradiction with the allowed radius of the ELM WD primary, which runs from $0.067 - 0.095\ R_{\odot}$ for all system inclinations above $40°$ (for inclinations below this amount, the unseen companion would have a mass in excess of 4 $M_{\odot}$).

We have used the extended model atmospheres described at length in Hermes et al. (2013d) and Brown et al. (2013) to re-fit the observed optical spectrum of this low-mass WD. Our new fits find that this is a $T_{\rm eff} = 10540 \pm 100$ K, $\log g$ $= 6.00 \pm 0.04$ WD, which suggest a 0.068 $R_{\odot}$ WD, consistent with our inferred radius from the ellipsoidal variations. The uncertainties on this expected ELM WD radius constrains the inclination to $i > 53°$, which in turn implies the companion mass should be between $1.1 < M_2 < 1.9\ M_{\odot}$. The ellipsoidal variations and surface gravity combine to show that the radius of the ELM WD is likely between $0.067 - 0.085\ R_{\odot}$.

2.5.1.4 J2119-0018

Our original result for J2119−0018 was outlined in Hermes et al. (2012a), but we have refined the analysis slightly to be more in line with the other systems that evidence tidal distortions. We have used the observed $1.45 \pm 0.27\%$ amplitude ellipsoidal variations and assumed $u_1 = 0.52$ to constrain the radius of the ELM WD primary visible in the system, and display the results as a function of inclination in the top panel of Figure 2.10.

Given the observed surface gravity, we expect a 0.17 $M_{\odot}$ ELM WD to have a radius no larger than about 0.09 $R_{\odot}$. This is slightly smaller than the lower-limit we measure from the amplitude of the ellipsoidal variations, which suggests this

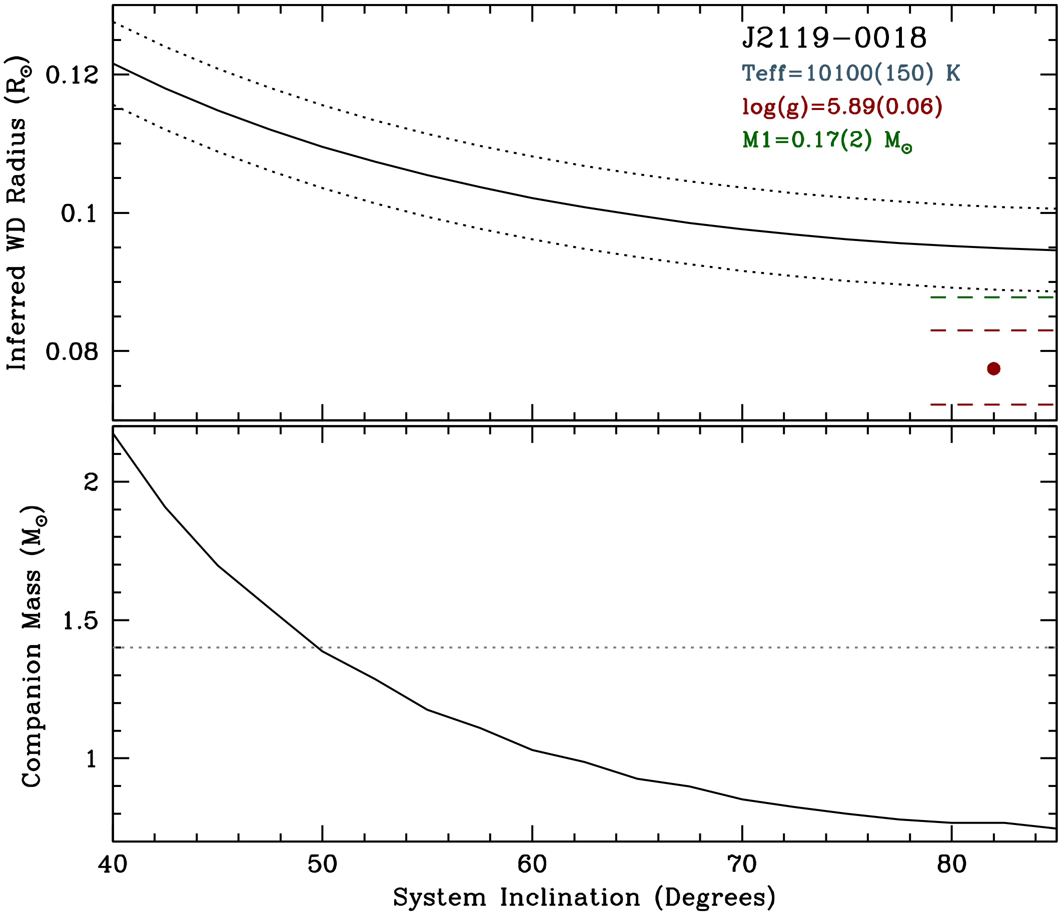

Figure 2.10 The top panel shows allowed values for the radius, modulo the system inclination, to explain the $1.45 \pm 0.27\%$ amplitude ellipsoidal variations observed in J2119−0018, and includes 1-σ uncertainties. If we use the determined surface gravity and mass to predict an expected ELM WD radius, we do not expect an ELM WD with a radius larger than 0.09 $R_{\odot}$, which is slightly smaller than the lower-limit we measure from the ellipsoidal variations. This suggests the system might be at relatively high inclination, which would indicate that the unseen companion is a $\sim 0.8\ M_{\odot}$ WD.

system might be at relatively high inclination, near $80°$. We choose to only put limits on the primary radius and companion mass: $M_2 > 0.75\ M_\odot$ and $R_1 > 0.089\ R_\odot$.

2.5.1.5 J0112+1835

J0112+1835 appears to be another ELM WD for which the tidal distortions can put reasonable constraints on the nature of both the ELM WD primary and the unseen companion. Assuming $u_1 = 0.51$, we have used the observed $0.31 \pm 0.06\%$ amplitude ellipsoidal variations to infer the radius of the ELM WD primary, as seen in Figure 2.11. This is the lowest-amplitude detection of ellipsoidal variations in our sample, but our detection is significant to better than 5-σ and is clearly visible in the folded light curve found in Figure 2.5.

We pair the inferred ELM WD radius range with the expected radius of such a star given the surface gravity in order to estimate the inclination of this compact binary. This moderately constrains the inclination to be between $i > 37$ degrees, which in turn constrains the unseen companion to a mass between $0.6 < M_2 < 2.0\ M_\odot$. For this run of inclinations we infer $0.075 < R_1 < 0.0125\ R_\odot$.

Our surface gravity estimate suggests an inclination of $i \sim 60°$, for which the unseen companion is a relatively massive $M_2 \sim 0.85\ M_\odot$ WD.

2.5.1.6 J0745+1949

We have computed a range of inferred radii for J0745+1949, assuming $u_1 = 0.58$ for this relatively cool ELM WD, shown in the top panel of Figure 2.12. The radius inferred from the ellipsoidal variations of the primary appears somewhat larger that we would expect given its surface gravity; we expect a radius around 0.10 $R_\odot$, but observe a minimum radius at high inclinations of about 0.12 $R_\odot$.

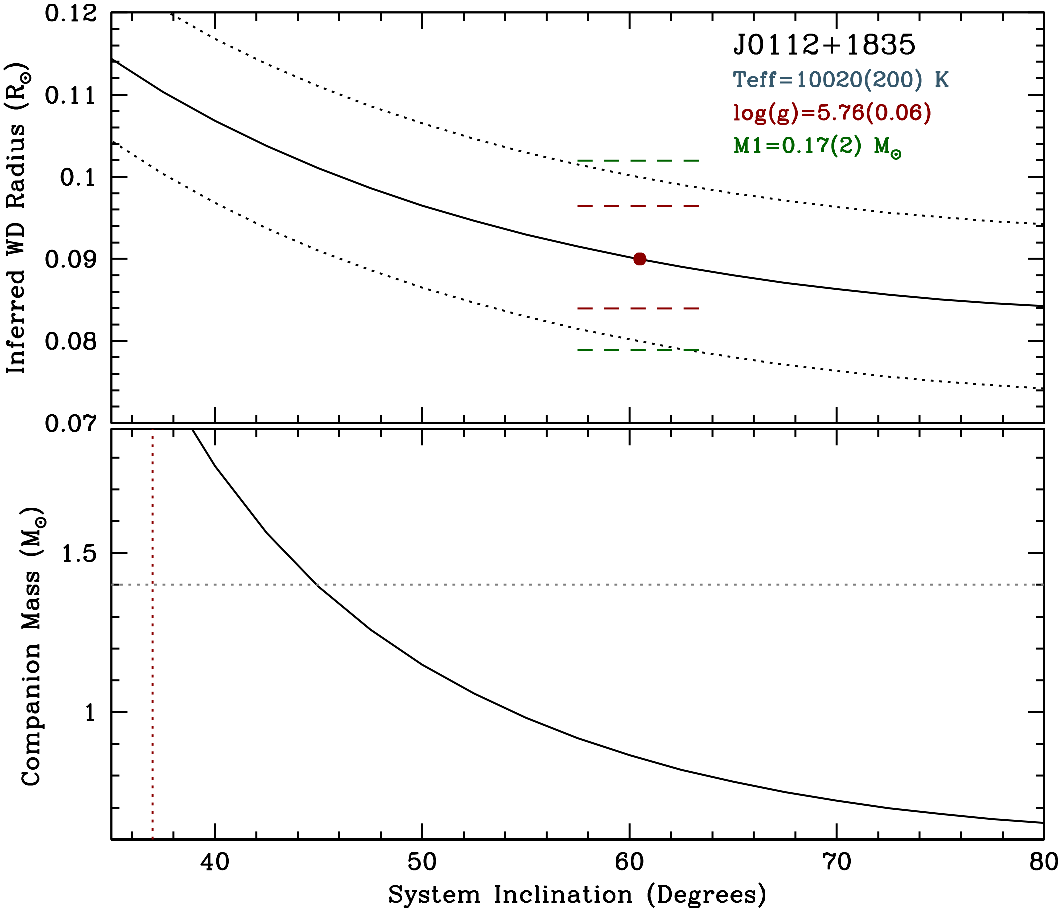

Figure 2.11 The top panel shows allowed values for the radius, modulo the system inclination, to explain the $0.31 \pm 0.06\%$ amplitude ellipsoidal variations observed in J0112+1835, and includes 1-σ uncertainties. As before, we use the determined surface gravity and mass to predict an expected ELM WD radius. This constrains the inclination to $i > 37$ degrees, which we use in the middle panel to constrain the companion mass to $0.6 < M_2 < 2.0\ M_\odot$.

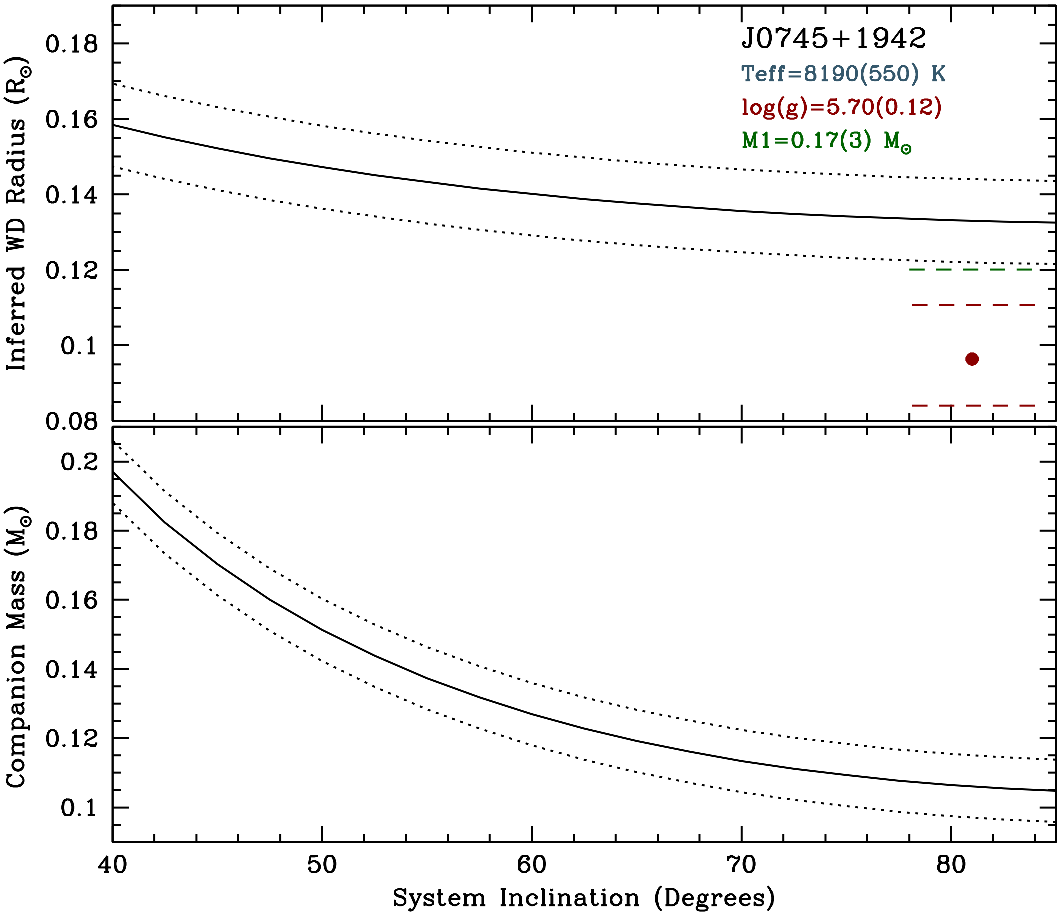

Figure 2.12 The top panel shows allowed values for the radius, modulo the system inclination, to explain the $1.07 \pm 0.10\%$ amplitude ellipsoidal variations observed in J0745+1949, and includes 1-σ uncertainties. If we use the determined surface gravity and mass to predict an expected ELM WD radius, we do not expect an ELM WD with a radius larger than 0.12 $R_{\odot}$, which is slightly smaller than the lower-limit we measure from the ellipsoidal variations. The unseen companion is most likely a cooler ELM WD.

This 8190 K WD is the coolest in our sample with ellipsoidal variations, and the assumption of a radiative atmosphere may not be valid. However, changing the gravity darkening coefficient from 1.0 to 0.36 only serves to increase the inferred ELM WD radius, by about 15% for each inclination angle. Decreasing the observed surface gravity by about 0.20 dex allows for overlap between the two observations, which would continue to suggest a relatively high inclination. However, due to this ambiguity, we cannot put good constraints on the system inclination. Regardless, the unseen companion is likely a cooler ELM WD with $M_2 < 0.2\ M_\odot$ for all inclinations $i > 40°$, which appears likely given that the radius we infer from the surface gravity comes closest to the observations for $i \sim 80°$.

2.5.1.7 WD0751-0141

We observe the highest-amplitude ellipsoidal variations in our sample in the system WD0751$-$0141, which we measure to have $3.20 \pm 0.11\%$ amplitude. Assuming a linear limb-darkening coefficient of $u_1 = 0.41$, we can use these tidal distortions to infer the radius of this ELM WD, shown in the top panel of Figure 2.13.

Given the observed surface gravity and the uncertainty on the mass of the primary, we expect a radius of $0.128^{+0.016}_{-0.011}\ R_\odot$, which is marked in Figure 2.13. Our observed ellipsoidal variations could be explained by a 0.128 $R_\odot$ ELM WD for a system inclination of $63°$, which when paired with the RV mass function would imply that the unseen companion is a 1.24 $M_\odot$ compact object. However, in order to more fully accommodate all the uncertainties in the inferred observed WD radius, surface gravity and mass, a more conservative estimate on the constraint on the inclination runs from $42 < i < 85$ degrees, which implies that the companion mass is $1.0 < M_2 < 2.5\ M_\odot$. This suggests the ELM WD primary has a radius between $0.115 - 0.158\ R_\odot$.

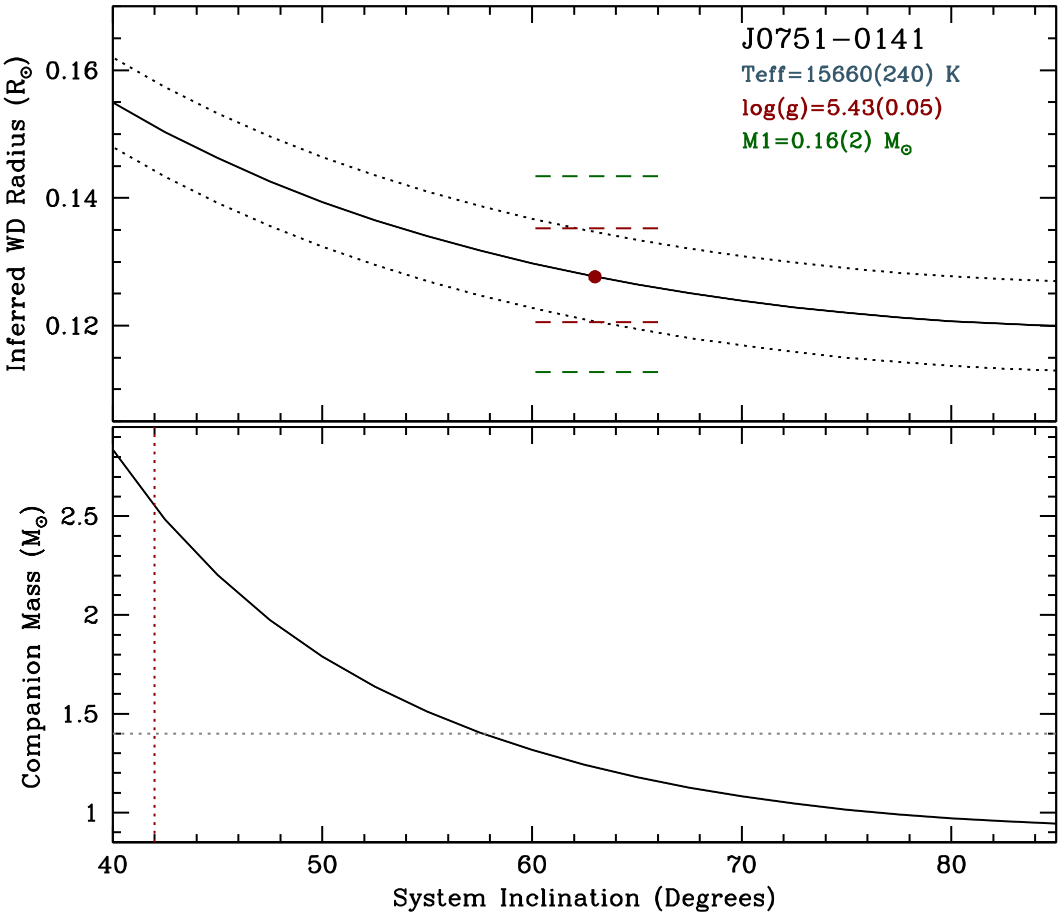

Figure 2.13 The top panel shows allowed values for the radius, modulo the system inclination, to explain the $3.20 \pm 0.11\%$ amplitude ellipsoidal variations observed in WD0751−0141, and includes 1-σ uncertainties. We also use the determined surface gravity and mass to predict an expected ELM WD radius. This constrains the inclination to $i > 42$ degrees, which we use in the bottom panel to constrain the companion mass to $1.0 < M_2 < 2.5\ M_{\odot}$.

2.5.2 Constraining the Low-Mass WD Mass-Radius Relation

Now that we have inferred constraints on the radii of seven ELM WDs using the amplitudes of their ellipsoidal variations, we can put them into context by comparing the theoretical and observational mass-radius relationship, shown in Figure 2.14. These seven tidally distorted ELM WDs are the lowest-mass WDs with radius constraints, so our observational results fill an important and relatively untested part of the picture.

The most precise constraints on the radius of low-mass WDs comes from detached eclipsing systems. Fortunately, there are now five known low-mass WDs in eclipsing binaries: NLTT 11748, CSS 41177 A&B, GALEX J1717, and J0651+2844 (Steinfadt et al. 2010b, Parsons et al. 2011, Vennes et al. 2011, Brown et al. 2011c). Our measurements for J0651+2844 are discussed in more detail in Chapter 3. We include these objects as black squares in Figure 2.14.

Additionally, there are four known low-mass WDs in eclipsing binaries with A-star companions, all recently discovered in the *Kepler* field. The radii of the low-mass WDs in these systems can provide a useful context for the least-massive tail of the WD mass-radius relationship. These WDs are KOI81B, KOI74B, KHWD3, and KHWD4 (van Kerkwijk et al. 2010, Rowe et al. 2010, Carter et al. 2011, Breton et al. 2012). We mark these low-mass WDs as green squares in Figure 2.14, and differentiate between the other WDs because the A-star companions may provide a different environment for the low-mass WDs, and could contribute to inflating the radius of the WD (Carter et al. 2011).

Our work with tidally distorted ELM WDs in compact binaries nearly doubles the number of systems in which we can constrain the radius of an ELM WD, adding seven new measurements to the nine previously reported nine in the literature. We mark these objects as blue points in Figure 2.14. These results greatly extend our understanding of the observational mass-radius relationship for He-core WDs, and as expected, these lower surface gravity (and lower mass) WDs have larger radii than typical 0.6 $M_{\odot}$ Earth-sized WDs.

Interpolating the model atmosphere grids to derive a mass for a given surface gravity still requires considerable guesswork (see Figure 4.14 and its discussion in Chapter 4 of this dissertation). Therefore, in order for us not to have multiple overlapping 0.16 and 0.17 $M_{\odot}$ WDs, the masses for these seven tidally distorted WDs have been slightly scaled by surface gravity, so that the lowest surface gravity objects are staggered and have slightly lower masses plotted in Figure 2.14.

For J0056−0611, J0106−1000, J0112+1835, and WD0751−0141, the value dotted for the radius corresponds to the value expected for the observed surface gravity. For the other three systems the dot corresponds to the radius for which $i = 80^{\circ}$, since the surface gravity suggests a radius at the low end of the ELM WD radii inferred from the ellipsoidal variations. This plot is most useful in displaying the maximum and minimum radius allowed by the observed ellipsoidal variations; this forms the upper and lower limits of the y-axis errors for each tidally distorted WD. Since no system is observed to eclipse to at least 2% amplitude, the lower limit of the inferred radius is the radius at the highest allowable inclination, usually around $i = 85^{\circ}$. The upper limit on the inferred radius occurs at the inclination for which the unseen companion would exceed 3 $M_{\odot}$, a relatively arbitrary but solid constraint from ELM WD formation scenarios. This gives us the radius limits shown, which are also described in Table 2.2.

2.5.3 Monitoring for the Effects of Gravitational Waves

Finally, the ellipsoidal variations in the shortest-period systems in our sample provide a unique opportunity to act as a stable clock which can be used to

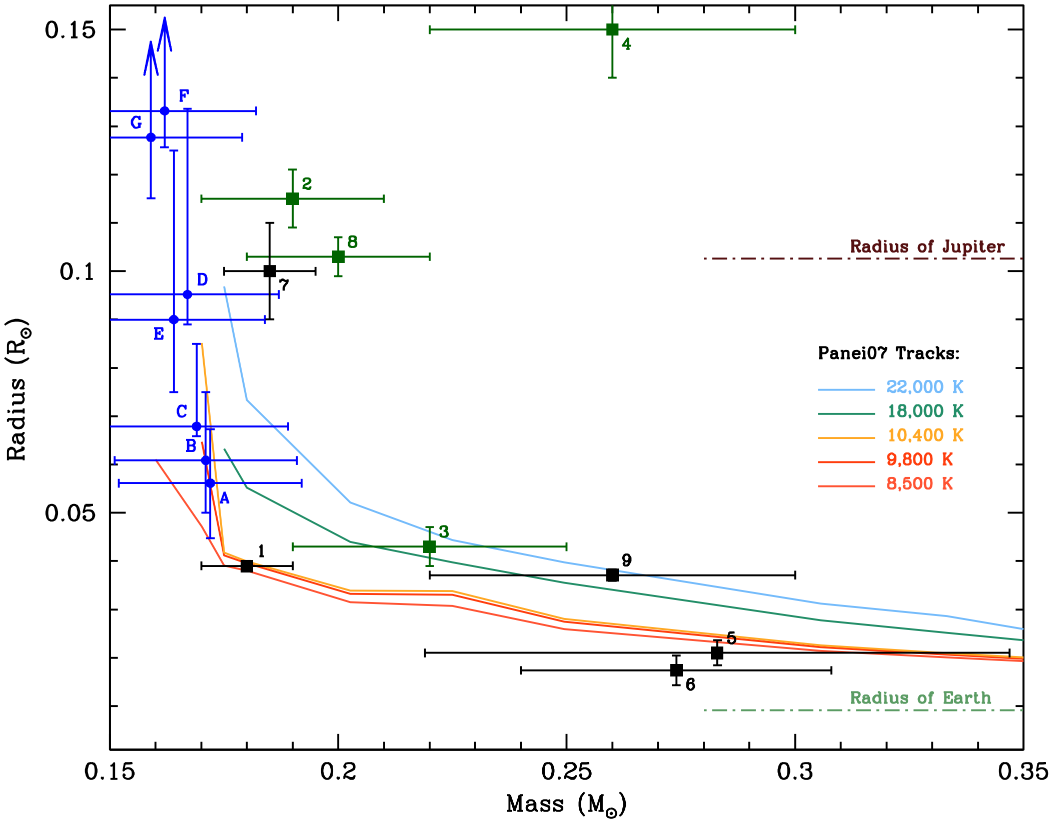

Figure 2.14 Observed mass and radius determinations for low-mass (He-core) WDs. The radius measurements for points marked by squares came from eclipsing systems and the blue dots from the amplitude of ellipsoidal variations, as in this work. The seven systems for which we can use the ellipsoidal variations to constrain the ELM WD radius are, in decreasing order of surface gravity: (A) J0056−0611; (B) J0106−1000; (C) J1741+6526; (D) J2119−0018; (E) J0112+1835; (F) J0745+1942; (G) WD0751−0141. The mass-radius determinations from eclipsing systems come from several references: (1) NLTT 11748 (Steinfadt et al. 2010b, Kilic et al. 2010); (2) KOI81B (van Kerkwijk et al. 2010, Rowe et al. 2010); (3) KOI74B (van Kerkwijk et al. 2010); (4) KHWD3 (Carter et al. 2011); (5 and 6) CSS 41177 A and B (Parsons et al. 2011); (7) GALEX J1717 (Vennes et al. 2011); (8) KHWD4 (Breton et al. 2012); and (9) J0651+2844 (Hermes et al. 2012b). We mark those systems which may be bloated because their companions are A stars in dark green. To guide the eye we include the theoretical mass-radius tracks for He-core WDs from Panei et al. (2007), which cover a range of temperatures. We have also marked the radii of Earth and Jupiter for reference.

monitor any changes to the system as a result of orbital decay from the emission of gravitational wave radiation. In each case, the ellipsoidal variations show that the tidal bulge of the primary is synchronized with the orbital period. As that orbital period shrinks with the emission of gravitational waves, the primary will be spun up, and the period of the ellipsoidal variations should decrease, which we can detect by monitoring the arrival times of the ellipsoidal variations. Some of these systems are so compact that it is possible to detect the influence of such gravitational waves on multiple systems within a decade or less.

We have already seen that such a monitoring campaign is possible: We have used the time-of-minima of the ellipsoidal variations in the 12.75-min WD+WD binary J0651+2844 to detect the rapid orbital decay due to gravitational wave radiation. More on that system will be discussed in Chapter 3.

The most compact binary in our sample that displays ellipsoidal variations, aside from J0651+2844, is the 39.1-min J0106−1000. The system is a strong source of gravitational wave radiation; assuming an inclination of 60°, the system will merge within 40 Myr. We expect the emission of gravitational waves to cause the orbit to decay at roughly $dP/dt = -1.1 \times 10^{-12}$ s s^{-1}, which will produce a change in the half-orbital period of $dP/dt = -5.5 \times 10^{-13}$ s s^{-1}. We have constructed an $(O - C)$ diagram of the time-of-minima of the ellipsoidal variations, guided by the period of the highest peak in the FT of our Argos dataset, 39.104063 min. We find $dP/dt = (0.3 \pm 6.4) \times 10^{-10}$ s s^{-1}, consistent with flat, as we'd expect with less than a single year of coverage. However, this effect piles up with time-squared, so we expect this time of minima to change by more nearly 35 s within 12 years of our initial observations. Our 2011 phase measurements have an r.m.s. scatter of roughly 11 s, comparable to the formal uncertainty in phase for that whole year's worth of data, making this detection of orbital period decay a relatively simple

Table 2.3. Expected Rates of Period Change from Gravitational Waves

Object	$P_{\rm orb}$ (min)	M_1 ($M_\odot$)	M_2 ($M_\odot$)	$dP/dt_{\rm GR}$ (10^{-13} s s^{-1})	$\tau_{\rm detect}$ (yr)	$T_{0,\rm ELV}$ (BJD$_{\rm TDB}$)
J0651+2844	12.7534424	0.26	0.50 ± 0.04	-82 ± 17	< 1	2455652.5980910(84)[1]
J0106−1000	39.10406	0.17	$0.7^{+0.8}_{-0.4}$	-6^{+3}_{-4}	12	2455533.56210(11)
J0056−0611	62.466700	0.17	$1.1^{+0.8}_{-0.5}$	-4^{+3}_{-7}	25	2455891.60676(42)
J1741+6526	87.9984	0.17	$1.1^{+0.8}_{-0.1}$	-2^{+1}_{-1}	28	2455686.76149(21)
J0751−0141	115.21814	0.16	$1.2^{+1.5}_{-0.3}$	-2^{+1}_{-5}	17	2455960.700532(54)
J2119−0018	124.949	0.17	$0.8^{+0.2}_{-0.1}$	-1^{+1}_{-1}	49	2455769.84049(61)
J0745+1949	161.84375	0.17	$0.11^{+0.10}_{-0.02}$	$-0.12^{+0.01}_{-0.03}$	109	2456245.89337(33)
J0112+1835	211.55545	0.17	$0.8^{+1.3}_{-0.2}$	$-0.4^{+0.2}_{-1.8}$	134	2455808.79083(91)

Note. — (1) See Chapter 3

measurement to make given a long enough baseline. With comparable coverage roughly every other year, we can expect a 3-σ detection of the spin-up of the tidal bulge due to the emission of gravitational waves by 2023.

We have made a similar set of calculations for the six other systems with ellipsoidal variations, and include the information in Table 2.3. We have calculated here for these other systems the time it would take to make a 3-σ detection of the period change given the phase uncertainty of our best subset, listed as $\tau_{\rm detect}$. This value is an upper limit, since more observations can greatly increase the accuracy with which we can measure the minima of the ellipsoidal variations. We also include the T_0 from the first epoch of observations, which can be used in the future to construct an updated $(O-C)$ diagram with more coverage. Additionally, we show the $(O-C)$ diagrams for the systems for which we have more than one epoch of observations in Figure 2.15.

Continued observations of these tidally distorted systems holds the exciting prospect of monitoring, on relatively accessible timescales, the evolution of these

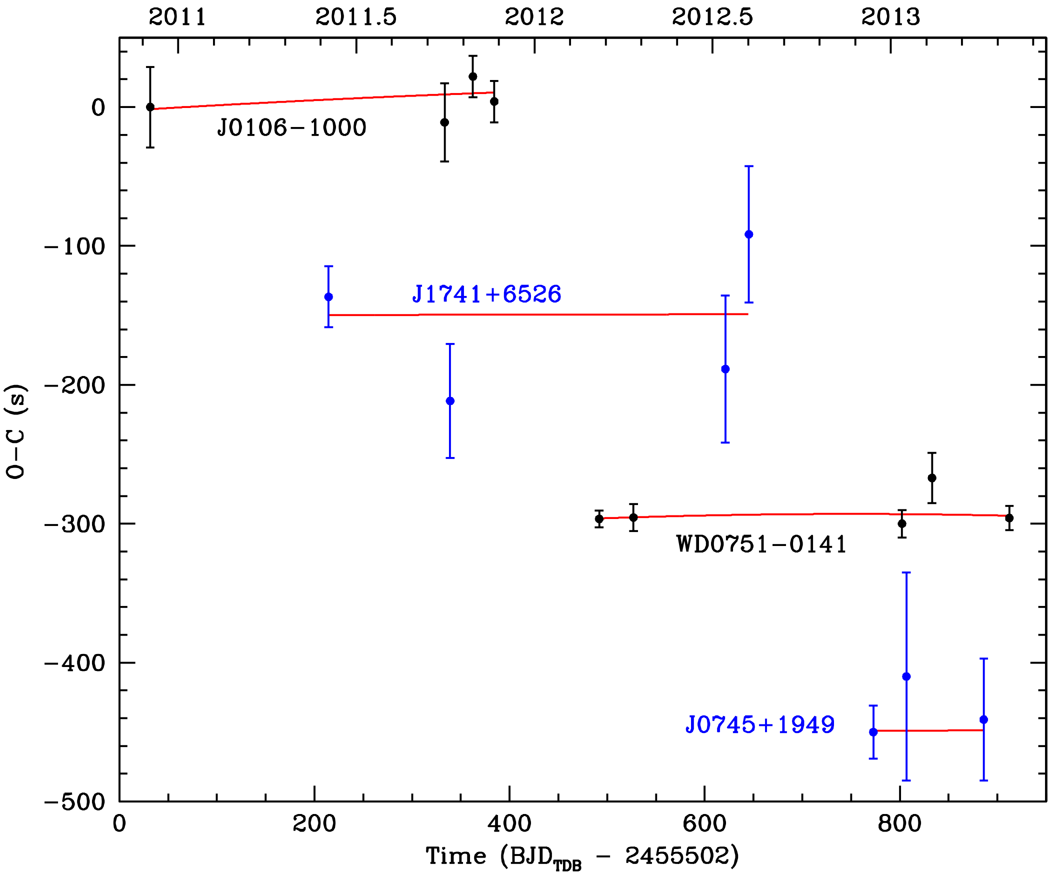

Figure 2.15 Observed $(O - C)$ diagrams for the tidally distorted systems in our sample with multiple epochs of observations. We plot here the times-of-minima of the ellipsoidal variations observed from season-to-season. At top is J0106−1000, followed by J1741+6526 offset by -150 s, followed by WD0751−0141 offset by -300 s, and finally J0745+1942 offset by -450 s. The ephemeris times for these observations can be found in Table 2.3. The best-fit parabola is shown for each system, but so far the observations are consistent with flat $(O-C)$ diagrams, with no significant rate of period change detected.

binaries as a result of the emission of gravitational wave radiation.

2.6 Conclusions

We present the discovery of eight new low-mass WDs that display ellipsoidal variations, the first detached tidally distorted white dwarf stars ever found. We use the amplitude of the observed ellipsoidal variations to constrain the radius of this rare, fluffy class of WDs. These new measurements, plus *Kepler* Hot White Dwarf 3 ($R \sim 0.15 R_{\odot}$ Carter et al. 2011) and GALEX J171708.5+675712 ($R \sim 0.1 R_{\odot}$ Vennes et al. 2011), are the largest radii WDs ever observed. Unlike the typical Earth-sized 0.6 $M_{\odot}$ CO-core WDs, these <0.20 $M_{\odot}$ He-core WDs are similar in size to (some even larger than) a giant planet such as Jupiter. There are less than a dozen other empirical mass-radius determinations for low-mass (presumably He-core) WDs, and we plot our results with the theoretical mass-radius relations from evolutionary models by Panei et al. (2007) in Figure 2.14. Evolution models predict that He-core WDs with masses less than about 0.18 $M_{\odot}$ should sustain substantial hydrogen shell burning (Serenelli et al. 2002, Panei et al. 2007, Steinfadt et al. 2010a). In fact, a majority of the flux from these ≤ 0.18 $M_{\odot}$ WDs comes from this residual burning. This should in turn cause a considerable increase in their radius, which has so far been borne out in our empirical mass-radius determinations. In addition, unless the systems are perfectly synchronized, tidal heating may also occur, which acts to heat the primary low-mass WD, effectively inflating it (Fuller & Lai 2012).

We have detected the strongest Doppler beaming signals ever measured for binary systems, as a result of the high-amplitude radial-velocity variations. The signals observed from Doppler beaming generally confirm previously published measurements of the radial velocity variations in these systems.

The orbital periods in these systems are decaying due to the emission of gravitational radiation; all will merge within 3 Gyr. It is possible to use the time-of-minimum of the ellipsoidal variations in the objects that display ellipsoidal variations to detect this orbital period decay. This rate of the orbital period change is sensitive to the mass of the unseen secondary, but we have used the inferred radius from the ellipsoidal variations with the spectroscopically determined surface gravity to constrain the inclination of the system with respect to Earth and thus constrain the companion mass. It will be possible to detect the spin-up of the tidal bulge due to gravitational wave radiation for at least two of our compact binaries within two decades, even with sparse observations every few years.

Table 2.4. Journal of photometric observations.

Run	UT Date	Length (hr)	Seeing (″)	Exp. (s)
	J0651+2844			
A2567	2012 Jan 21	5.9	1.9	15
A2569	2012 Jan 22	1.9	2.2	10
A2573	2012 Jan 23	6.6	2.0	15
A2576	2012 Jan 24	5.8	1.3	10
A2579	2012 Jan 26	4.5	2.5	15
A2582	2012 Jan 28	3.5	1.7	10
A2585	2012 Jan 29	5.9	2.0	10
A2587	2012 Jan 30	8.0	1.6	10
A2589	2012 Jan 31	8.2	1.5	5
A2592	2012 Feb 01	4.5	1.4	10
A2596	2012 Feb 02	5.6	1.7	10
	Overall	60.4	1.8	
	J0106-1000			
A2259	2010 Dec 03	2.6	1.4	30
A2444	2011 Sep 02	2.2	1.3	30
GMOSg	2011 Sep 23	2.1	1.4	30
A2463	2011 Sep 29	2.3	1.1	20
GMOSr	2011 Oct 02	2.2	1.2	30
A2478	2011 Oct 04	2.4	1.4	30
A2480	2011 Oct 22	2.7	1.5	30
A2487	2011 Oct 24	2.8	1.1	20
	Overall	14.9	1.3	
	J1630+4233			
A2404	2011 May 07	2.8	1.4	15
A2429	2011 Jul 27	2.9	1.5	15
A2434	2011 Jul 28	2.2	1.3	30
	Overall	7.8	1.4	
	J1053+5200			
A1849	2009 Mar 24	1.5	1.7	15
A2629	2012 Mar 16	1.0	1.3	15
A2863	2013 May 13	2.2	1.4	10
	Overall	4.7	1.5	
	J0056-0611			
A2515	2011 Nov 26	2.4	2.3	15
A2522	2011 Nov 28	1.2	2.3	15
A2529	2011 Nov 30	2.5	1.7	15
A2532	2011 Dec 01	2.6	2.3	15
A2572	2012 Jan 23	2.5	2.0	15
A2575	2012 Jan 24	0.9	1.3	10
	Overall	12.2	2.0	
	J1056+6536			
A2593	2012 Feb 01	1.8	1.8	15
A2652	2012 Apr 18	1.2	2.0	15
	Overall	3.0	1.9	

Table 2.4—Continued

Run	UT Date	Length (hr)	Seeing ($''$)	Exp. (s)
		J0923+3028		
A2292	2010 Dec 08	1.5	2.5	5
A2297	2010 Dec 09	4.8	3.0	5
A2302	2010 Dec 10	4.5	1.9	5
	Overall	10.8	2.5	
		J1436+5010		
A2141	2010 Jun 06	1.6	1.6	15
A2670	2012 Apr 23	2.5	1.4	15
A2805	2013 Mar 11	4.9	1.6	15
A2829	2013 Mar 19	3.5	1.6	15
	Overall	12.5	1.6	
		J0825+1152		
A2502	2011 Nov 22	2.6	2.6	15
A2773	2012 Dec 17	4.6	3.5	30
	Overall	7.2	3.2	
		J1741+6526		
A2400	2011 May 05	4.6	1.8	15
A2406	2011 May 08	2.8	1.6	15
A2457	2011 Sep 08	2.3	1.4	20
A2680	2012 Jun 16	1.6	1.7	15
A2702	2012 Jul 10	1.8	1.6	30
	Overall	13.0	1.6	
		J0755+4906		
A2247	2010 Nov 13	1.6	1.5	30
Diafe1	2012 Nov 14	0.9	1.3	60
Diafe2	2012 Nov 15	0.7	1.5	60
MMT1	2012 Dec 12	2.3	1.4	120
	Overall	5.5	1.4	
		J2338-2052		
MMT2	2012 Nov 03	1.8	1.7	30
		J0849+0445		
A2821	2013 Mar 16	6.7	1.7	15
A2823	2013 Mar 17	3.3	1.5	30
A2848	2013 Apr 08	1.7	1.6	15
	Overall	11.7	1.6	
		J0022-1014		
A2201	2010 Oct 08	2.2	1.7	30
		WD0751-0141		
A2599	2012 Feb 03	5.4	1.8	5
A2604	2012 Feb 15	1.9	2.5	15
A2613	2012 Feb 20	3.3	1.9	10
A2617	2012 Mar 13	0.9	1.7	15
A2620	2012 Mar 14	4.2	1.8	15
A2765	2012 Dec 11	5.4	3.0	10
MJ001	2012 Dec 12	4.1	3.6	30
MJ002	2012 Dec 14	2.5	3.8	45
MJ003	2012 Dec 15	3.9	3.1	45

Table 2.4—Continued

Run	UT Date	Length (hr)	Seeing ($''$)	Exp. (s)
A2771	2012 Dec 16	3.6	2.5	30
MJ004	2012 Dec 16	3.6	4.1	45
A2781	2012 Dec 20	6.0	4.6	30
A2783	2013 Jan 13	3.4	7.1	15
A2787	2013 Jan 14	3.9	2.9	15
MJ008	2013 Jan 15	3.8	3.6	45
A2832	2013 Apr 02	2.0	2.9	15
A2834	2013 Apr 03	2.0	3.1	15
A2836	2013 Apr 04	3.2	2.2	15
	Overall	63.2	3.2	
	J2119-0018			
A2430	2011 Jul 27	2.8	1.3	30
A2435	2011 Jul 28	3.9	1.1	30
A2438	2011 Jul 30	5.1	1.3	30
	Overall	11.8	1.2	
	J1234-0228			
A2343	2011 Jan 08	2.8	1.3	10
A2348	2011 Jan 10	3.0	3.1	15
A2374	2011 Apr 06	2.7	1.9	10
	Overall	8.4	2.1	
	J0745+1949			
A2749	2012 Nov 14	2.8	1.3	15
A2753	2012 Nov 15	2.3	1.9	15
A2770	2012 Dec 15	2.3	3.0	30
A2780	2012 Dec 19	1.9	2.3	5
A2797	2013 Mar 08	1.7	1.5	10
	Overall	10.9	2.0	
	J0112+1835			
A2450	2011 Sep 04	4.1	1.2	10
A2453	2011 Sep 06	4.0	1.6	10
A2456	2011 Sep 07	4.8	1.5	15
	Overall	12.8	1.4	
	J1233+1602			
A2396	2011 May 04	2.9	1.5	30
A2856	2013 May 07	1.8	1.7	30
A2858	2013 May 08	2.0	1.2	30
A2870	2013 May 17	1.8	1.2	20
	Overall	5.6	1.3	

Chapter 3

Gravitational Waves from a 12.75-min WD+WD Binary

We report the detection of orbital decay in the 12.75-min, detached binary white dwarf (WD) SDSS J065133.338+284423.37 (hereafter J0651). Our photometric observations over a 13-month baseline constrain the orbital period to $765.206543(55)$ s and indicate the orbit is decreasing at a rate of $(-8.9{\pm}1.0){\times}10^{-12}$ s s^{-1} (or $-0.28\pm$ 0.03 ms yr^{-1}). We revise the system parameters based on our new photometric and spectroscopic observations: J0651 contains two WDs with $M_1 = 0.26{\pm}0.04\ M_\odot$ and $M_2 = 0.50 \pm 0.04\ M_\odot$. General relativity predicts orbital decay due to gravitational wave radiation of $(-8.2 \pm 1.7) \times 10^{-12}$ s s^{-1} (or -0.26 ± 0.05 ms yr^{-1}). Our observed rate of orbital decay is consistent with this expectation. J0651 is currently the second-loudest gravitational wave source known in the milli-Hertz range and the loudest non-interacting binary, which makes it an excellent verification source for future missions aimed at directly detecting gravitational waves. Our work establishes the feasibility of monitoring this system's orbital period decay at optical wavelengths.[1]

3.1 Introduction

The 12.75-minute orbital period detached binary WD system J0651+2844 was discovered by Brown et al. (2011c) as part of the extremely low mass (ELM,

---

[1] *Significant portions of this chapter have been previously published as:* J. J. Hermes, Mukremin Kilic, Warren R. Brown, D. E. Winget, Carlos Allende Prieto, A. Gianninas, Anjum S. Mukadam, Antonio Cabrera-Lavers, and Scott J. Kenyon, *The Astrophysical Journal*, **757**, L21 (2012)

$\leq 0.25\ M_\odot$) WD Survey, a targeted spectroscopic search for ELM WDs. While that survey has yielded dozens of merger systems, with orbital periods of tens of minutes to hours (Brown et al. 2013), none are as compact as J0651+2844.

In addition to a large radial-velocity amplitude, this double degenerate system is oriented in such a way that it yields a wealth of photometric information: eclipses of each star by the other, ellipsoidal variations and Doppler boosting (see Chapter 2). While photometric observations engender an accurate way to measure the orbital and system parameters, they also provide multiple clocks with which to monitor the orbital evolution of the system.

The orbital decay of compact binary systems is currently the best method to detect the influence (and existence) of gravitational waves, and few known systems are radiating as strongly or decaying as rapidly as J0651+2844. There are presently just five binaries known with orbital periods less than 15 minutes, and the other four are interacting: three are the AM CVn systems HM Cnc, V407 Vul, and ES Cet, and the other is the low-mass X-ray binary 4U 1820-30 (Israel et al. 1999, Haberl & Motch 1995, Steeghs et al. 2006, Warner & Woudt 2002, Stella et al. 1987). After the 5.4-minute HM Cnc (Israel et al. 2002, Roelofs et al. 2010), J0651+2844 is the second-loudest gravitational wave source known in the milli-Hertz frequency range (Amaro-Seoane et al. 2012). J0651 is thus the shortest-period detached compact binary known and the cleanest system to observe at optical wavelengths for orbital decay due to gravitational wave radiation.

Here we present follow-up photometric and spectroscopic observations of J0651+2844, refine orbital and system parameters, and report the detection of rapid orbital decay in the system, predominantly due to the emission of gravitational radiation. We discuss the orbital period change in the context of expectations from general relativity, as well as deviations expected due to tidal interactions. Since the publication of this discovery in Hermes et al. (2012b) after 2012 May, we have obtained an additional 104 hr of photometry, bringing our total baseline of observations to more than two years. We first present our published result, and update our analysis with our additional year of observations.

3.2 Initial Detection of Rapid Orbital Decay

3.2.1 Photometric Observations

The majority of our photometric observations were carried out in an identical manner to the discovery observations described in Brown et al. (2011c), with the Argos instrument, through a 3 mm BG40 filter to reduce sky noise. We obtained $5-30$ s exposures of the target, with a typical exposure time of 10 s, depending on the observing conditions. Additionally, we obtained nearly 3 hr of data in December 2011 using the Agile instrument (Mukadam et al. 2011) mounted on the 3.5 m telescope at Apache Point Observatory (APO), using a 1 mm *BG40* filter and $10-15$ s exposures. In January and March 2012, we obtained 6.8 hr of data with 20 s exposures using GMOS (Hook et al. 2004) on the 8.1 m Gemini North telescope as part of the queue programs GN-2011B-Q-95 and GN-2012A-Q-29. Most of the Gemini data were taken using a Sloan-g filter, but we obtained nearly 2 hr of data using a Sloan-r filter to constrain the luminosity of the secondary WD (see Section 3.2.3). Additionally, we obtained 1.5 hr of data using 10 s exposures in March 2012 and 1.0 hr of data using 5 s exposures in 2012 April using the OSIRIS instrument (Cepa et al. 2000, 2003) through a Sloan-g filter and in fast photometry mode, mounted on the Gran Telescopio Canarias (GTC) 10.4 m telescope. Our high-quality light curves from Gemini and GTC are shown in Figure 3.1.

We bias- and flat-field correct the raw science frames using standard IRAF routines. For Argos and Agile, we perform weighted, circular, fixed-aperture pho-

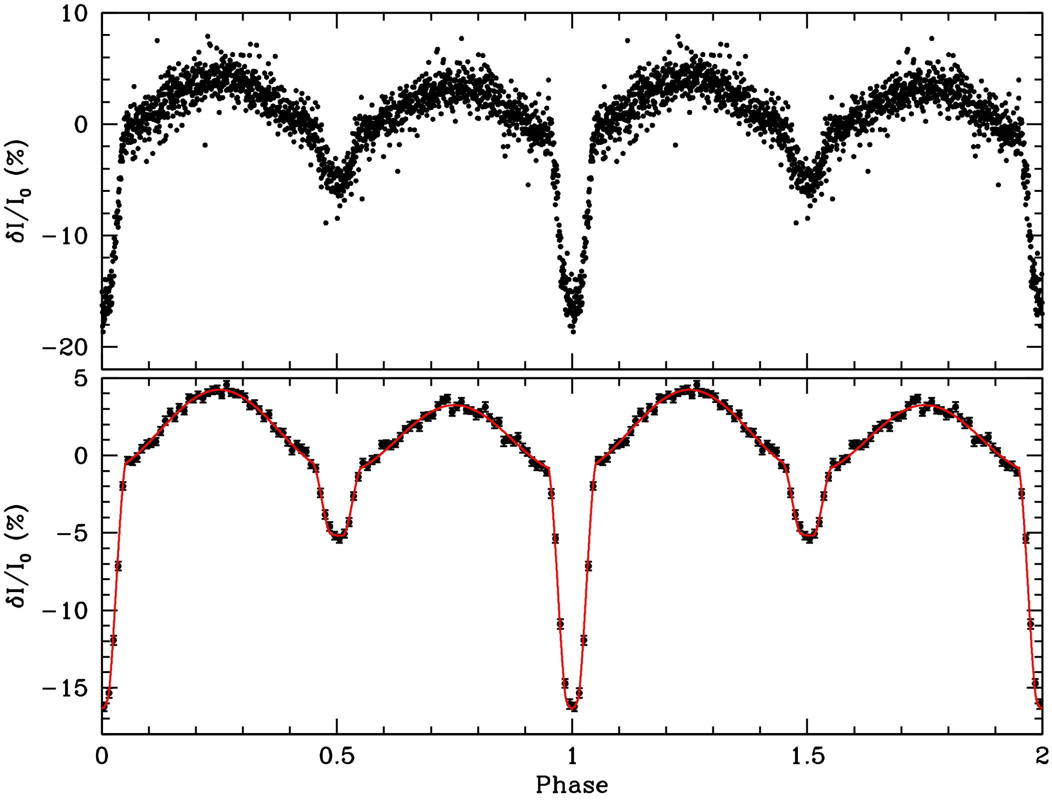

Figure 3.1 Time-series photometry of J0651+2844 through a *g*-band filter from the 8.1 m Gemini North telescope and the GTC 10.4 m telescope, folded at the orbital period and duplicated for clarity. Directly below is the same data binned into 100 phase bins, with error bars, and over-plotted with our best-fit model.

tometry on the calibrated frames using the external IRAF package *ccd_hsp* (see Appendix A). We divide the sky-subtracted light curves using five brighter comparison stars in the field to remove transparency variations. To remove any long-term trends caused by differential atmospheric extinction, we fit a low-order polynomial to observing runs exceeding 2 hr using the WQED software suite (Thompson & Mullally 2009), which we also use to apply a timing correction to each observation to account for the motion of the Earth around the barycenter of the solar system (Stumpff 1980). We use the formalism described in Everett & Howell (2001) to derive average point-by-point photometric errors of 1.0 mmag for GMOS and OSIRIS, and 2.8 mmag for Argos observations. We calibrate these errors using the $g = 19.1$ mag, photometrically constant star SDSS J065132.86+284408.4, within 20″ of our target.

For the GMOS and OSIRIS data, we use DAOPHOT (Stetson 1987) to perform aperture photometry on our target and a dozen photometrically constant SDSS point sources in our images for calibration. We use a script by Eastman et al. (2010) to apply a barycentric timing correction and check it against the timings based on WQED.

3.2.2 Spectroscopic Observations

To obtain higher signal-to-noise-ratio spectroscopy and better phase coverage, we obtained additional time-series spectroscopy of J0651+2844 at the 6.5m MMT telescope in 2011 October and 2012 April. All 79 spectra were taken using the Blue Channel Spectrograph (Schmidt et al. 1989) with a 800 l mm^{-1} grating and a 1″ slit. This set-up provides 2.1 Å resolution and a spectral coverage from 3550—5450 Å. The lower resolution compared to the discovery observations presented by Brown et al. (2011c) enabled us to decrease the exposure time to 90 s, providing

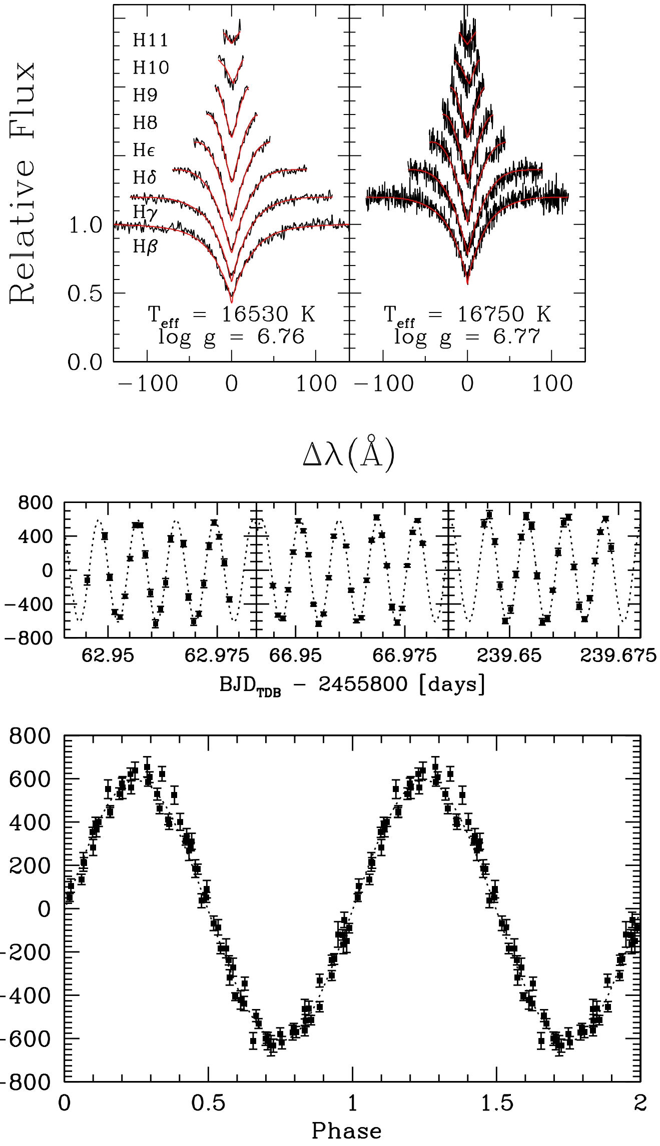

Figure 3.2 Spectroscopic observations of J0651+2844. The top left panel shows the summed spectra from our 2011 October and 2012 April observations, with model fits to the Hβ to H11 lines, which we use to derive the primary parameters in Section 3.2.3. The top right panel shows fits to the lower S/N, summed spectra from 2011 March from Brown et al. (2011c). The middle panel shows our new radial velocity observations of J0651+2844 from three new epochs, and the bottom panel shows those data phased to the orbital period.

a radial velocity curve with better phase coverage (see Figure 3.2). The reduced spectra have an average radial velocity error of ± 31 km s^{-1}.

3.2.3 Updated System Parameters

We compute the orbital elements using the code of Kenyon & Garcia (1986), which weights each velocity measurements by its associated error. However, the observed velocity amplitude is an underestimate because our 90 s exposures span 12% of the orbital phase, and because the radial velocity curve is not linear. By integrating a sine curve at the phase covered by our exposures, we determine that the velocity amplitude correction is 2.3%. The resultant best-fit, corrected velocity semi-amplitude is $K = 616.9 \pm 3.5$ km s^{-1}. This is significantly lower than our original value, 657.3 ± 2.4 km s^{-1}, computed in the same way.

Given that the original radial velocity semi-amplitude depended on a dozen measurements at quadrature with 30 km s^{-1} errors, the formal error was an underestimate. A Monte Carlo calculation indicates that the true uncertainty in K using our original 27 spectra was actually 14 km s^{-1}. The same calculation with the new data yields an uncertainty in K of 5 km s^{-1}. This implies that the companion is less massive than originally predicted by Brown et al. (2011c).

We refine the physical parameters of the primary[2] WD using the summed spectrum, which has S/N=78 per resolution element. Fitting our new spectra with the stellar atmosphere models of **?**, which include improved Stark broadening profiles with non-ideal gas effects, formally yields $T_{\rm eff} = 16530 \pm 105$ K and $\log g = 6.76 \pm 0.02$. This result is nearly identical to our original measurements ($T_{\rm eff} = 16400 \pm 300$ K and $\log g = 6.79 \pm 0.04$, Brown et al. 2011c). A direct comparison

---

[2] Following (Brown et al. 2011c) we refer to the low-mass WD as the primary since it contributes >95% of optical light.

of the difference in the models can be found in the upper right panel of Figure 3.2: Fits of the discovery data to the new models of **?** formally yield $T_{\rm eff} = 16750 \pm 200$ K and $\log g = 6.77 \pm 0.04$.

Additionally, we investigate the effect of velocity smearing on the derived atmospheric parameters by analyzing the spectra obtained at quadrature ($|v| > 500$ km s^{-1}, when velocity smearing should be at its minimum). For these spectra at quadrature, we find that $T_{\rm eff}$ is 500 K lower and $\log g$ is 0.07 dex higher. These differences reflect our systematic error, and also indicate how the parameters of the tidally distorted primary depend on phase, but the parameters remain consistent with the higher S/N summed and phased spectrum. Thus we adopt a mean $T_{\rm eff}$ $= 16530 \pm 200$ K and $\log g = 6.76 \pm 0.04$, implying a $0.25\ M_{\odot}$ primary (Panei et al. 2007).

We use our high-quality g-band Gemini and GTC photometry to refine the system parameters using the light curve fitting code JKTEBOP (Southworth et al. 2004). We supply the limb-darkening coefficients from WD atmosphere models appropriate for the J0651 system using $I(\mu)/I(1) = 1 - c_1(1-\mu) - c_2(1-\sqrt{\mu})$, where $\mu = \cos\theta$ (P. Bergeron 2012, private communication). These coefficients are included in Table 3.1; their uncertainties are negligible given our observed $T_{\rm eff}$ and $\log g$ uncertainties. Additionally, we have adopted gravity-darkening coefficients of $\beta_1 = \beta_2 = 0.36$ for both the primary and secondary, where $F \propto T_{\rm eff}^4 \propto g^{\beta}$. We expect convection to be present in both stars, and our light curve fits do poorly for $\beta = 1.0$, as expected for a purely radiative atmosphere, so adopting $\beta = 0.36$ is reasonable.

We fix the limb- and gravity-darkening coefficients and fit for the inclination and component radii, and our error estimates result from 10,000 Monte Carlo simulations, as described in Southworth et al. (2005). Gravitational lensing should minimally affect the derived radius of the primary and secondary, by roughly 0.1% and 0.7%, respectively (Marsh 2001), and have not been included in the fits. The primary radius is a volume-average; the tidal distortions make the star 3.3% oblate.

The photometry allows us to test the ELM WD models by providing an independent estimate on the mass of the primary. To do so, we hold fixed a series of different mass ratios in our light curve fits, and in each case use the resultant secondary radius in combination with the tested mass-radius relation of Wood (1995) in order to back out the mass of the primary. Consistently, this method finds $M_1 = 0.26 \pm 0.04\ M_{\odot}$, which we adopt.

Taking $M_1 = 0.26 \pm 0.04\ M_{\odot}$ and $K = 616.9 \pm 5.0$ km s^{-1}, the secondary mass is thus $M_2 = 0.50 \pm 0.04\ M_{\odot}$ for the best-fit inclination of 84.4 ± 2.3 deg. Table 3.1 shows our final light curve results found by fixing $q = 1.92$. The resulting radius of the secondary, $R_2 = 0.0142 \pm 0.0010\ R_{\odot}$, implies $M_2 = 0.50 \pm 0.04\ M_{\odot}$ (Wood 1995), in good agreement. Pairing the volume-averaged primary radius $R_1 = 0.0371 \pm 0.0012\ R_{\odot}$ with the observed surface gravity yields $M_1 = 0.29 \pm 0.05$ $M_{\odot}$, somewhat larger but consistent with our adopted value, as well as with the result using the Panei et al. (2007) models.

Finally, we use our Gemini *r*-band data to constrain the luminosity and temperature of the secondary. Fixing the limb- and gravity-darkening coefficients, and adopting the inclination and component radii from the *g*-band fits, we find the secondary contributes 3.7 ± 0.2% of light in the *g*-band and 4.6 ± 0.6% of light in the *r*-band. This difference, especially in the depth of the primary and secondary eclipses, can be seen in Figure 3.3.

Adopting $M_g = 8.9 \pm 0.1$ mag and $M_r = 9.2 \pm 0.1$ mag for the 0.26 $M_{\odot}$ primary (Panei et al. 2007), the secondary thus has $M_g = M_r = 12.5 \pm 0.2$ mag.

Table 3.1. System parameters.

Parameter [method used to derive parameter]	Value
Orbital Period [phot.]	$765.206543(55)$ s
K_1 (corrected for smearing) [spec.]	616.9 ± 5.0 km s^{-1}
γ_{vel} [spec.]	-7.7 ± 4.5 km s^{-1}
Primary $T_{\rm eff}$ [spec.]	16530 ± 200 K
Primary $\log g$ [spec.]	6.76 ± 0.04
Primary Mass (M_1) [spec.]	$0.26 \pm 0.04\ M_{\odot}$
Primary Radius (R_1) [phot.]	$0.0371 \pm 0.0012\ R_{\odot}$
Inclination (i) [phot.]	84.4 ± 2.3 degrees
Mass Ratio (q) [spec.]	1.92 ± 0.46
Secondary Mass (M_2) [spec.]	$0.50 \pm 0.04\ M_{\odot}$
Secondary $T_{\rm eff}$ [phot.]	8700 ± 500 K
Secondary Radius (R_2) [phot.]	$0.0142 \pm 0.0010\ R_{\odot}$
Limb Darkening, Primary, g-band	$c_1 = -0.106$, $c_2 = 0.730$
Limb Darkening, Secondary, g-band	$c_1 = -0.128$, $c_2 = 0.898$
Limb Darkening, Primary, r-band	$c_1 = -0.076$, $c_2 = 0.562$
Limb Darkening, Secondary, r-band	$c_1 = -0.099$, $c_2 = 0.735$

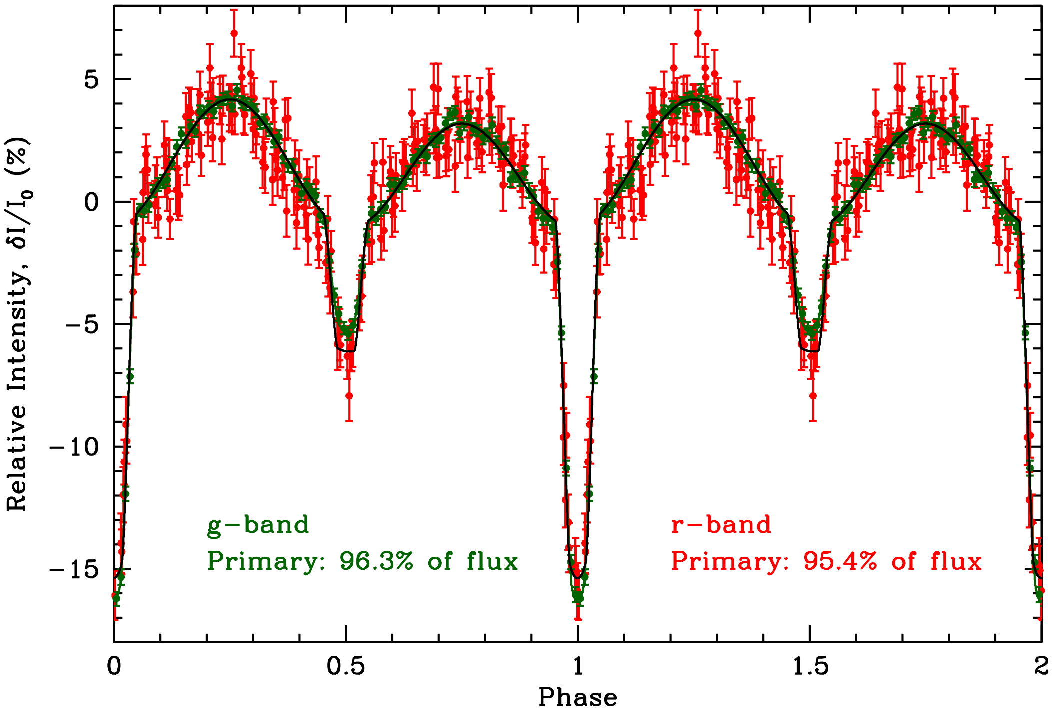

Figure 3.3 We display time-series photometry of J0651+2844 through a g-band filter from the 8.1 m Gemini North telescope in green points, and through an r-band filter on the same telescope with red points. These light curves are folded at the orbital period and duplicated for clarity. We over-plot our best-fit model for the g-band data with a solid green line, and the r-band data with a solid black line.

For a 0.5 $M_{\odot}$ WD, cooling models[3] suggest a temperature of 8700 ± 500 K for the secondary, which corresponds to a cooling age of roughly 700 Myr (Holberg & Bergeron 2006, Kowalski & Saumon 2006, Tremblay et al. 2011, Bergeron et al. 2011).

3.2.4 Detection of Orbital Period Decay

We demonstrate a secular change in the orbital period of J0651+2844 by constructing an $(O - C)$ diagram, where we compare the observed mid-eclipse times (O) to expected mid-eclipse times computed from the assumption of a fixed orbital period (C) for future epochs ($E = t/P$). To estimate the mid-eclipse times, we fix the best-fit model parameters from our analysis in Section 3.2.3 and fit each subset of observations only for the mid-eclipse time nearest the mean time of the observations.

Following Kepler et al. (1991), if the orbital period is changing slowly with time, we can expand the observed mid-time of the Eth eclipse, t_E, in a Taylor series around E_0 to arrive at the classic $(O - C)$ equation

$$O \ - \ C = \Delta T_0 + \ \Delta P_0 \, E + \frac{1}{2} P_0 \dot{P} E^2 + ...$$

where T_0 is the mid-time of the first eclipse, ΔT_0 is the uncertainty in this mid-point, P_0 is the orbital period at the first eclipse and ΔP_0 is the uncertainty in this period. Any secular change in the period, dP/dt, will cause a parabolic curvature in an $(O - C)$ diagram. Currently, the acceleration in the period change, $d(dP/dt)/dt$, is negligible, and we will limit our discussion to a second-order polynomial fit.

To construct an $(O - C)$ diagram, we must first determine T_0 and P_0. A preliminary estimate comes from a simple Fourier transform of our whole data

---

[3] http://www.astro.umontreal.ca/ bergeron/CoolingModels

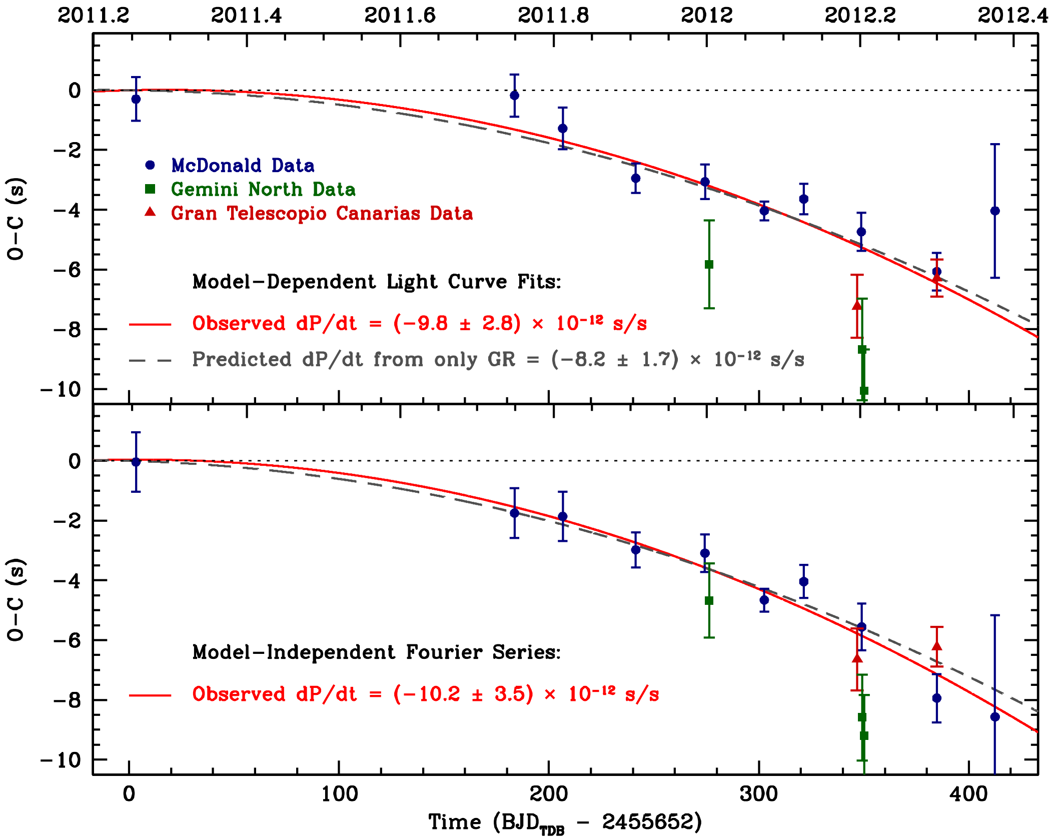

Figure 3.4 $(O - C)$ diagrams of the orbital evolution in J0651+2844 from 2011 April to 2012 May; blue dots represent data from McDonald Observatory and APO, green squares from Gemini-North, and maroon triangles from GTC. The top panel shows the change in mid-eclipse times as determined by light curve modeling, and the best-fit parabola yields an estimate for the observed rate of orbital period change. Complimentarily, the bottom panel shows the results from a model-independent, linear least-squares fit using the orbital period and higher harmonics. The dotted line at $(O - C) = 0$ shows the line of zero orbital decay, while the grey dashed line shows the predicted orbital decay expected solely from gravitational wave radiation. Using both methods, our early results match the GR prediction to the 1-σ level.

set, which we use to create an initial $(O - C)$ diagram. We then iteratively adjust T_0 and P_0 by the zeroth- and first-order terms from our best-fit parabola until the adjustments are smaller than the error in these terms; these errors result from the covariance matrix. Our recomputed, final $(O{-}C)$ diagram uses this new ephemeris and period and is shown in Figure 3.4. We find:

$$T_0 = 2455652.5980910 \pm 0.0000084 \ \mathrm{BJD_{TDB}}$$

$$P_0 = 765.206543 \pm 0.000055 \ \mathrm{s}$$

Table 3.2 presents the mid-eclipse times from each subset of our observations. Each night of observing from Gemini and GTC have been given their own subset, as have each month of data from McDonald. Since ΔT_0 and ΔP_0 are nonzero, the zeroth- and first-order terms of the parabola indicating the predicted dP/dt in Figure 3.4 have been allowed to vary within the current constraints on these terms.

A weighted, second-order, least-squares fit to the mid-eclipse times yields a rate of period change of $(-9.8 \pm 2.8) \times 10^{-12}$ s s^{-1} (or -0.31 ± 0.09 ms yr^{-1}). This value includes our May 2012 data point, which has just 3.4 hr of data spread over four nights at a minimum airmass of 2.0. If we do not include this last point, the inferred rate of period change differs slightly, yielding $(-10.6 \pm 2.9) \times 10^{-12}$ s s^{-1} (or -0.33 ± 0.09 ms yr^{-1}). A parabola is needed to best represent the data: The best second-order fit has $\chi^2 = 33.0$ (12 d.o.f.), whereas the best first-order fit has $\chi^2 = 44.9$ (13 d.o.f.).

As a sanity check, we also construct an $(O - C)$ diagram using a model-independent approach. Here we perform a simultaneous least-squares fit to each subset of data using a series of sine curves at the orbital period (P_0) up to the last

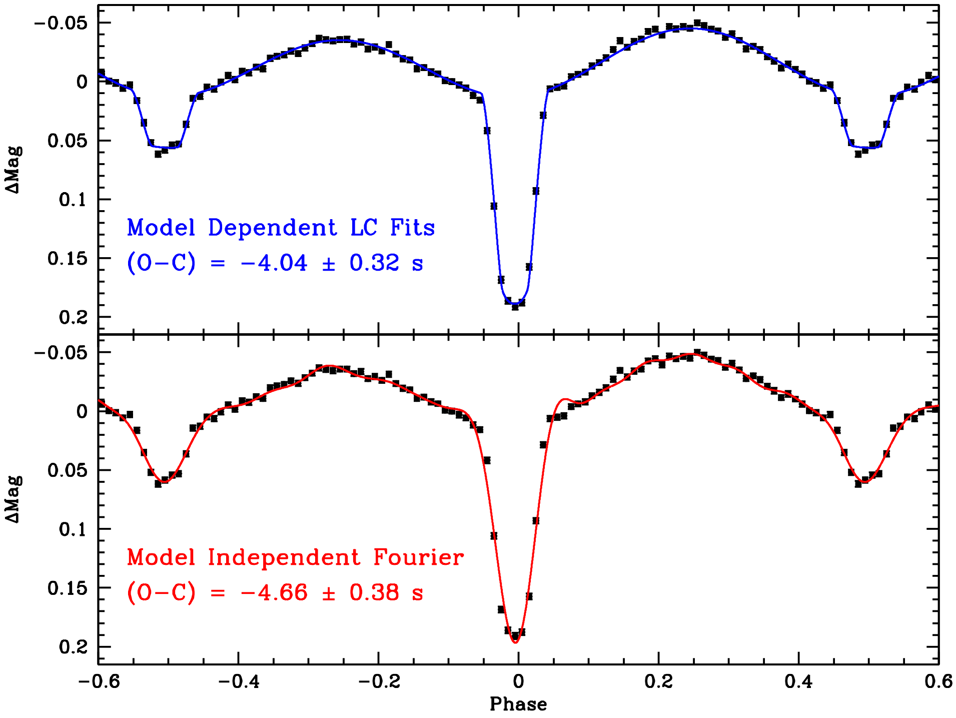

Figure 3.5 A comparison of the model-dependent light curve fits (top panel, in blue) and the model-independent Fourier method (bottom panel, in red) in reproducing the 2012 January folded data set. The results are comparable, but the Fourier series does a poor job of representing the eclipse profiles, and thus retains larger uncertainties.

harmonic before the Nyquist frequency of that subset. This effectively uses the high-amplitude ellipsoidal variations at half the orbital period as our clock, with a Fourier series of the orbital harmonics to reproduce the eclipses. A best-fit parabola to the observed minima of the ellipsoidal variations is shown in the bottom panel of Figure 3.4 and yields $dP/dt = (-5.1 \pm 1.8) \times 10^{-12}$ s s^{-1}. In order to compare this to the mid-eclipse times at the orbital period, we must multiply this result by a factor of two, which yields $dP/dt = (-10.2 \pm 3.5) \times 10^{-12}$ s s^{-1} (or -0.32 ± 0.11 ms yr^{-1}).

We can visualize how these two methods compare in fitting the observations in Figure 3.5 by displaying our best data set, the folded light curve from 2012 January. The top panel shows in blue the result from the model-dependent light curve fitting by JKTEBOP, and the associated uncertainties on the derived mid-eclipse time. Complimentary, the bottom panel shows in red the fit derived from the model-independent Fourier series (a Fourier transform of this same data set is shown in Figure 2.1 in Chapter 2).

The model-independent $(O - C)$ method retains larger uncertainties because the harmonics are inevitably truncated by the Nyquist frequency in the observations and so are only roughly capable of replicating the deep primary eclipses. Our results from this method are not orthogonal to the model-dependent light curve fitting, as both fit the eclipses and ellipsoidal variations. Therefore, both results cannot be averaged, and we emphasize the results from the model-dependent approach.

Thus, our best estimate for the rate of orbital period change in J0651 after 13 months is $(-9.8 \pm 2.8) \times 10^{-12}$ s s^{-1} (or -0.31 ± 0.09 ms yr^{-1}), a 3-σ detection. This yields a timescale for period change, $P/\dot{P} = 2.5 \pm 0.8$ Myr.

3.3 Refining the Measurement of Orbital Decay

3.3.1 Photometric Observations

Subsequent to our 2011 April to 2012 May observations of J0651+2844 published in Hermes et al. (2012b), we have continued to photometrically monitor the eclipses of this exceptional 12.75-min WD+WD binary. A detailed journal of these new observations is found in Table 3.3.

Our observations from McDonald Observatory were obtained and reduced in an identical manner to those described in Section 3.3. However we have added new observations from the commissioning of a rapid deployment science camera (an Apogee photometer with an e2v 2048x2048 CCD) mounted at the f/5 wavefront sensor of the 6.5m MMT. These observations in 2012 November were flat-fielded and dark-subtracted using standard IRAF routines, and aperture photometry was performed using the external IRAF package *ccd_hsp*. We use a script by Eastman et al. (2010) to apply a barycentric timing correction.

3.3.2 Refining Our Measurement of Orbital Period Decay

As in Section 3.2.4, we demonstrate a secular change in the orbital period by constructing an $(O - C)$ diagram of the mid-eclipse times of each subset of our new observations. We have used the system parameters derived in Section 3.2.3 in our light-curve fitting routines, which derive the mid-eclipse times.

We display these updated $(O-C)$ diagrams, using both the model-dependent light curve fits from JKTEBOP and the model-independent Fourier method, in Figure 3.6. Our observations continue to match the prediction of orbital decay due solely to the emission of gravitational radiation from two point masses, within the uncertainties. After the first two full years of observations we adopt a rate of period change of $(-8.9 \pm 1.0) \times 10^{-12}$ s s^{-1} (or -0.28 ± 0.03 ms yr^{-1}), a highly significant detection of orbital decay.

We can also use only our McDonald Observatory observations to obtain a similarly significant measure of the rate of orbital decay, with the added benefit that these Argos observations were all obtained in an identical manner and with high time precision. This measurement yields $dP/dt = (-9.2 \pm 1.0) \times 10^{-12}$ s s^{-1} (or -0.29 ± 0.03 ms yr^{-1}), which is in good agreement with our adopted value.

Finally, we have included an intuitive visualization of our detection of orbital decay in J0651+2844, shown in Figure 3.7. Here we can see, by eye, the de-

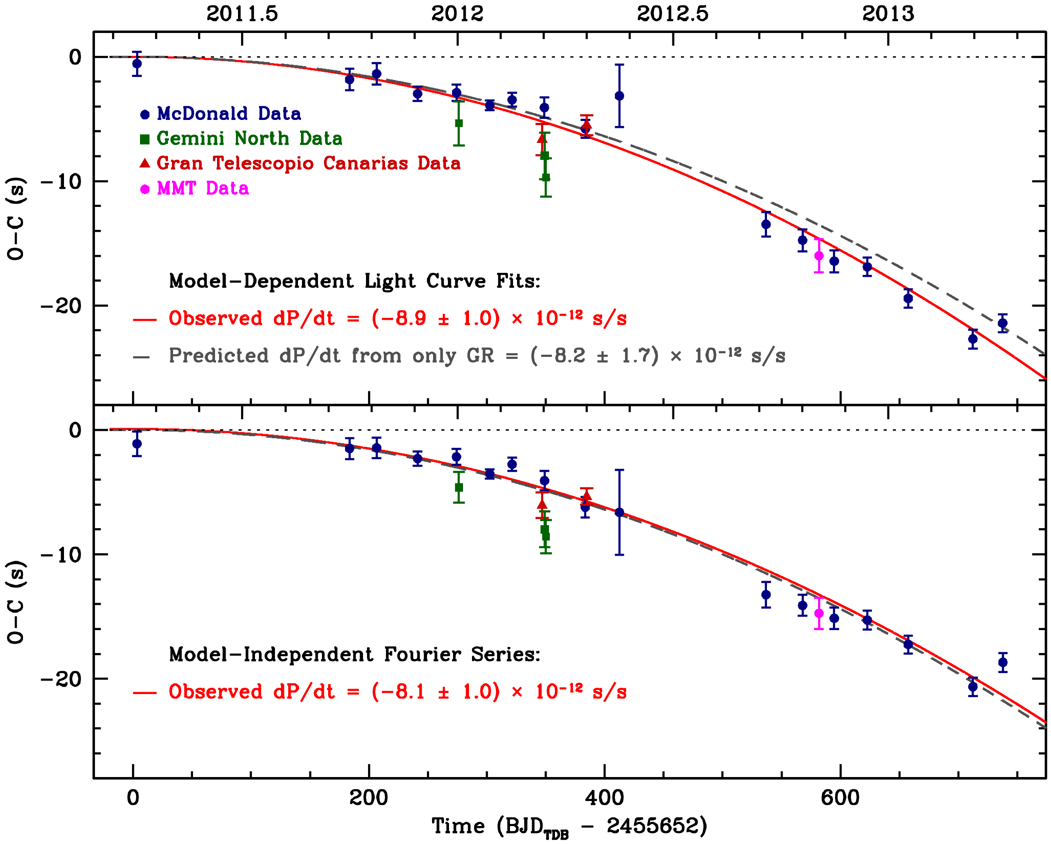

Figure 3.6 Updated $(O - C)$ diagrams of the orbital evolution in J0651+2844 from 2011 April to 2013 April. Dark blue dots represent data from McDonald Observatory and APO, green squares from Gemini-North, maroon triangles from GTC, and magenta dots from the MMT. The top panel shows the change in mid-eclipse times as determined by light curve modeling, and the best-fit parabola yields an estimate for the observed rate of orbital period change. Complimentarily, the bottom panel shows the results from a model-independent, linear least-squares fit using the orbital period and higher harmonics. The dotted line at $(O - C) = 0$ shows the line of zero orbital decay, while the grey dashed line shows the predicted orbital decay expected solely from gravitational wave radiation.

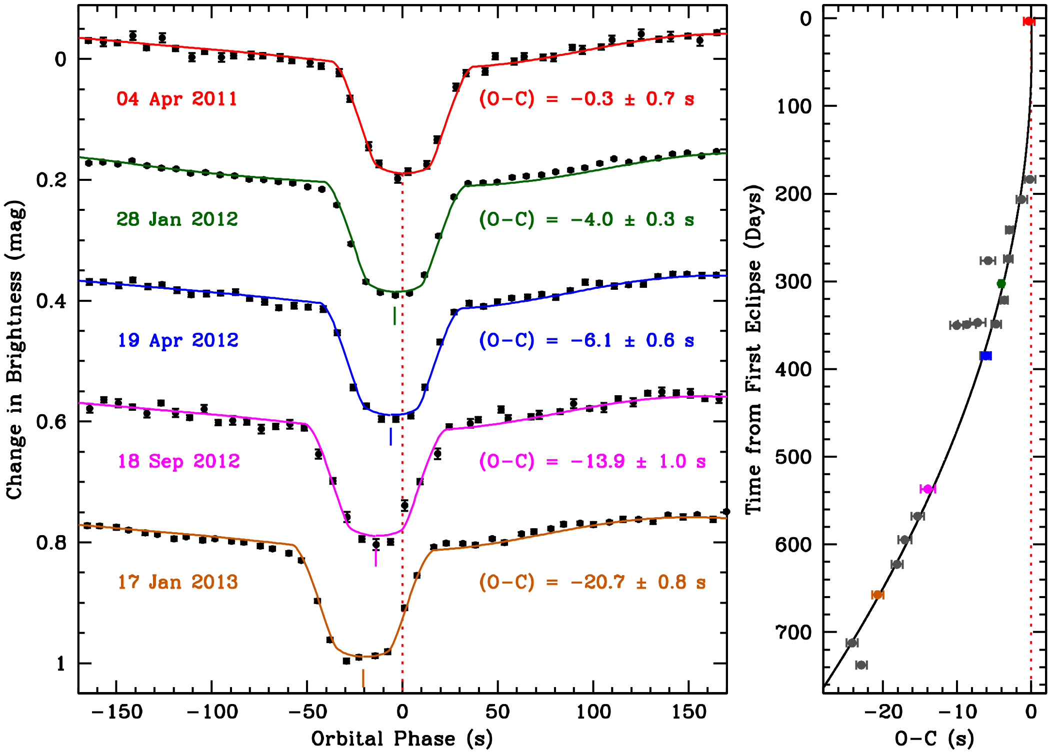

Figure 3.7 Another way to visualize the $(O - C)$ diagram for the orbital evolution in J0651+2844, from 2011 April to 2013 April. The left panel shows five different monthly subsets of observations binned into 100 phase bins, with error bars, and overplotted with our best-fit model. The decreasing orbital period is evident as the primary eclipses, centered around the Orbital Phase $= 0$ s in 2011 April, shift sooner and sooner, to the left. The right panel shows the same information as a classical $(O - C)$ diagram, and color codes each subset.

creasing orbital period by watching the mid-point of the primary eclipses for different subsets shift to sooner and sooner times. The mid-point of each eclipse is marked with a solid line. Comparison of this mid-point to the mid-point of the first subset in 2011 April, shown as a dotted red line, corresponds to the $(O - C)$ points shown in the right panel of this figure.

3.4 Discussion and Conclusions

Based on the refined parameters for the J0651+2844 system (see Section 3.2.3) and treating each WD as a point mass in a non-relativistic circular orbit, general relativity predicts an orbital period decay in this system of $(-8.2 \pm 1.7) \times 10^{-12}$ s s^{-1} (or -0.26 ± 0.05 ms yr^{-1}) (Landau & Lifshitz 1975). Recently, van den Broek et al. (2012) demonstrated that the point mass approximation is valid to better than 1% in cases such as J0651+2844, so our uncertainty in the orbital decay from gravitational wave radiation is dominated by the uncertainty in the component masses. Additional effects that could modulate the mid-eclipse times are unlikely to explain the observed shift: For example, given the estimated distance of 1.0 kpc (Brown et al. 2011c), we expect the proper motion to change the period by no more than 5×10^{-16} s s^{-1} (Shklovskii 1970).

It is evident from the high-amplitude ellipsoidal variations of the primary that strong tidal forces are also present. These tides will act as a torque to spin-up the WDs if the system is synchronized, further robbing the orbit of angular momentum and increasing the rate of orbital period decay. The degree to which this tidal torquing influences the orbital evolution depends on the effective tidal locking, which is in many ways determined by the physical structure of the ELM WD. This effect could increase the rate of period decay by at least 5% if the system is synchronized (Piro 2011, Benacquista 2011, Fuller & Lai 2012). After two years of monitoring, our sensitivity in the observed rate of orbital decay is not yet sufficient to detect a significant deviation from pure gravitational wave losses. However, future observations should constrain this discrepancy, providing an excellent probe of the interior of ELM WDs, in addition to the possibilities opened through asteroseismology (Steinfadt et al. 2010a, Hermes et al. 2012c).

The short period of J0651+2844 makes it one of the loudest known sources of gravitational wave radiation, and continued monitoring of orbital decay in the system will provide strong constraints on the gravitational wave strain of J0651. This is important for future gravitational wave missions, like the evolved Laser Interferometry Space Antenna (*eLISA*). Critical to that success is disentangling the contributions of tidal torques on the orbital decay, an effort worthy of further photometric observations and modeling.

Table 3.2. Journal of J0651+2844 mid-eclipse times.

Facility	Epoch (E)	No. Eclipses	Mid-Eclipse Time ($\mathrm{BJD_{TDB}} - 2450000$)
McD	373	59	5655.9015834(85)
McD	20735	41	5836.2388027(83)
McD	23327	52	5859.1949862(81)
McD	27251	146	5893.9480974(57)
APO,McD	30981	110	5926.9830544(67)
Gem-N	31207	5	5928.984604(17)
McD	34164	284	5955.1734648(37)
McD	36291	80	5974.0113666(59)
GTC	39171	7	5999.518210(12)
McD	39383	53	6001.3958287(75)
Gem-N	39426	6	6001.776615(20)
Gem-N	39542	10	6002.803960(16)
McD	43317	89	6036.2375095(72)
GTC	43446	5	6037.3800027(72)
McD	46578	16	6065.118766(26)

Note. — While the instruments used to take data at McD, APO and GTC are conditioned with a GPS receiver and thus have absolute time stamps accurate to a few ms, the mid-exposure times for our GMOS-N data all end in .2 or .7 s, suggesting a rounding error of up to 0.25 s; the uncertainties in our Gemini mid-eclipse times have thus been enlarged by 0.25 s. We may remove any potential systematic time offsets by computing the period change using only the points from McDonald Observatory, which yields $(-9.2 \pm 1.0) \times 10^{-12}$ s s^{-1}.

Table 3.3. Journal of J0651+2844 photometric observations.

Subgroup	Run	UT Date	Length (hr)	Seeing ($''$)	Exp. (s)
2011 04 McD	A2364	2011 Apr 01	2.2	1.7	15
	A2365	2011 Apr 02	3.0	1.7	15
	A2366	2011 Apr 03	2.8	1.4	10
	A2376	2011 Apr 08	2.2	1.1	15
	A2383	2011 Apr 13	2.5	1.8	30
2011 09 McD	A2464	2011 Sep 29	1.8	1.5	15
	A2469	2011 Oct 01	2.3	1.5	15
	A2472	2011 Oct 02	2.2	1.1	15
	A2476	2011 Oct 03	2.5	1.3	20
2011 10 McD	A2484	2011 Oct 23	3.2	1.3	15
	A2489	2011 Oct 24	3.9	1.3	15
	A2496	2011 Oct 26	4.0	1.3	20
2011 11 McD	A2505	2011 Nov 23	5.3	1.4	15
	A2518	2011 Nov 26	3.2	2.9	15
	A2523	2011 Nov 28	6.6	2.0	15
	A2526	2011 Nov 29	3.7	2.1	15
	A2530	2011 Nov 30	6.5	2.3	15
	A2533	2011 Dec 01	6.1	2.4	15
2011 12 APO/McD	Agile89	2011 Dec 25	2.6	···	15
	A2553	2011 Dec 26	1.3	2.0	30
	A2555	2011 Dec 30	8.9	1.9	15
	A2558	2012 Jan 01	3.8	2.0	10
	A2565	2012 Jan 03	6.7	1.6	10
2012 01 Gem-N	GMOSg-1	2012 Jan 02	1.1	···	20
	GMOSr-1	2012 Jan 02	1.1	···	20
2012 01 McD	A2567	2012 Jan 21	5.9	1.9	15
	A2569	2012 Jan 22	1.9	2.2	10
	A2573	2012 Jan 23	6.6	2.0	15
	A2576	2012 Jan 24	5.8	1.3	10
	A2579	2012 Jan 26	4.5	2.5	15
	A2582	2012 Jan 28	3.5	1.7	10
	A2585	2012 Jan 29	5.9	2.0	10
	A2587	2012 Jan 30	8.0	1.6	10
	A2589	2012 Jan 31	8.2	1.5	5
	A2592	2012 Feb 01	4.5	1.4	10
	A2596	2012 Feb 02	5.6	1.7	10
2012 02 McD	A2601	2012 Feb 14	6.0	1.5	10
	A2606	2012 Feb 16	5.3	1.5	10
	A2609	2012 Feb 19	5.8	1.2	10
2012 03 GTC	GTC-1	2012 Mar 12	1.5	···	10
2012 03 McD	A2615	2012 Mar 12	3.5	2.1	15
	A2623	2012 Mar 15	3.3	1.4	15
	A2628	2012 Mar 16	2.2	1.6	15
	A2637	2012 Mar 17	2.4	1.8	10
2012 03 Gem-N	GMOSg-2	2012 Mar 15	1.4	···	20
	GMOSr-2	2012 Mar 15	1.0	···	20
	GMOSg-3	2012 Mar 16	2.3	···	20

Table 3.3—Continued

Subgroup	Run	UT Date	Length (hr)	Seeing (″)	Exp. (s)
2012 04 McD	A2640	2012 Apr 14	1.8	1.9	10
	A2644	2012 Apr 15	1.1	2.0	15
	A2645	2012 Apr 16	2.6	1.4	10
	A2648	2012 Apr 17	2.7	1.8	10
	A2651	2012 Apr 18	2.1	2.2	15
	A2655	2012 Apr 19	2.1	1.9	10
	A2661	2012 Apr 21	2.4	1.6	10
	A2668	2012 Apr 23	2.0	1.7	15
	A2674	2012 Apr 24	2.3	1.7	15
2012 04 GTC	GTC-2	2012 Apr 19	1.0	· · ·	5
2012 05 McD	J0651-1	2012 May 16	0.9	2.1	10
	J0651-2	2012 May 17	0.9	2.2	10
	J0651-3	2012 May 18	0.6	2.4	10
	J0651-4	2012 May 19	1.0	2.1	10
2012 09 McD	A2709	2012 Sep 16	1.2	1.5	15
	A2712	2012 Sep 17	1.7	2.1	30
	A2715	2012 Sep 18	1.8	2.3	30
	A2718	2012 Sep 19	1.9	1.6	15
	A2720	2012 Sep 20	2.2	1.3	15
	A2722	2012 Sep 21	0.0	1.8	15
2012 10 McD	A2729	2012 Oct 18	3.2	2.1	15
	A2732	2012 Oct 19	3.1	1.4	10
	A2734	2012 Oct 20	2.6	1.4	15
	A2736	2012 Oct 21	2.5	1.2	10
2012 10 MMT	MMT-1	2012 Nov 02	2.3	· · ·	11
	MMT-2	2012 Nov 03	1.9	· · ·	11
2012 11 McD	A2740	2012 Nov 10	3.6	2.2	15
	A2748	2012 Nov 14	1.8	1.3	10
	A2761	2012 Nov 20	5.0	1.2	15
2012 12 McD	A2767	2012 Dec 12	6.1	2.1	15
	A2769	2012 Dec 13	7.8	1.7	15
	A2779	2012 Dec 19	4.6	2.5	30
2013 01 McD	A2789	2013 Jan 16	5.3	2.4	15
	A2792	2013 Jan 17	4.0	1.7	15
	A2795	2013 Jan 18	7.3	1.4	10
2013 03 McD	A2804	2013 Mar 11	4.9	2.3	30
	A2806	2013 Mar 12	4.1	2.1	15
	A2810	2013 Mar 13	3.9	2.2	15
	A2813	2013 Mar 14	4.2	1.6	10
	A2817	2013 Mar 15	3.4	1.6	15
2013 04 McD	A2839	2013 Apr 05	3.5	1.4	10
	A2841	2013 Apr 06	2.7	1.8	15
	A2844	2013 Apr 07	3.1	1.4	10
	A2847	2013 Apr 08	2.6	1.3	10
	A2850	2013 Apr 09	3.1	1.6	15
	A2853	2013 Apr 12	2.7	1.1	10

Chapter 4

Discovery of Pulsations in Extremely Low-Mass WDs

We report the discovery of the first five pulsating extremely low mass (ELM) white dwarfs. Spectral fits indicate these are both the coolest and lowest-mass pulsating WDs ever found; all have effective temperatures below $10{,}000$ K and masses $< 0.25\ M_\odot$, establishing these putatively helium-core WDs as a cooler class of pulsating hydrogen-atmosphere WDs (DAVs). These stars exhibit long-period variability consistent with non-radial g-mode pulsations; these are not tidally induced pulsations and are so far best explained by the same hydrogen partial-ionization driving mechanism at work in classic C/O-core DAVs. The two lowest-mass ELM WDs also evidence lower-amplitude, short-period variability that may be evidence for hybrid acoustic (p-mode) pulsations, which provide an exciting opportunity to probe this WD in a complimentary way. Consistent with the expectation that ELM WDs must be formed in binaries, three of these pulsating ELM WDs have detected nearby companions.[1]

---

[1] *Significant portions of this chapter have been previously published as:* J. J. Hermes, M. H. Montgomery, D. E. Winget, Warren R. Brown, Mukremin Kilic and Scott J. Kenyon, *The Astrophysical Journal*, **750**, L28 (2012) & J. J. Hermes, M. H. Montgomery, D. E. Winget, Warren R. Brown, A. Gianninas, Mukremin Kilic, Scott J. Kenyon, Keaton J. Bell, and Samuel T. Harrold, *The Astrophysical Journal*, **765**, 102 (2013) & J. J. Hermes, M. H. Montgomery, A. Gianninas, S. T. Harrold, D. E. Winget, Warren R. Brown, Keaton J. Bell, Scott J. Kenyon, and Mukremin Kilic, *Monthly Notices of the Royal Astronomical Society*, submitted (2013)

4.1 Introduction

Asteroseismology allows us to probe below the photosphere and into the interiors of stars. There are many pulsation instability strips on the Hertzsprung-Russell diagram, including the DAV (or ZZ Ceti) instability strip, driven by a hydrogen partial ionization zone in the cool, hydrogen atmosphere (DA) white dwarfs (WDs). Seismology using the non-radial gravity-mode (g-mode) pulsations of DAVs has enabled us to constrain the mass, core and envelope composition, rotation rate, and the behavior of convection in these objects (see reviews by Winget & Kepler 2008, Fontaine & Brassard 2008 and Althaus et al. 2010).

The mass distribution of DA WDs in the SDSS shows a strong peak at 0.6 $M_{\odot}$with tails toward higher and lower masses (Tremblay et al. 2011, Kleinman et al. 2013); masses of individual WDs range from about 0.2 $M_{\odot}$ to 1.3 $M_{\odot}$. The roughly 150 DAVs known to date have masses $0.5-1.1$ $M_{\odot}$, implying they all likely contain C/O-cores. Lower mass WDs are likely to pulsate as well (Steinfadt et al. 2010a).

The galaxy is not old enough to produce low mass (< 0.5 $M_{\odot}$) WDs through single-star evolution; these WDs are believed to be the product of binary evolution. Indeed, radial velocity surveys of low-mass WDs indicate that most form in binary systems (Marsh et al. 1995, Brown et al. 2011a). Mass loss during at least one common-envelope phase has precluded the ELM WD from igniting helium in its core, and the result is an underweight WD with a core devoid of C/O. These WDs have been known for some time as companions to pulsars, but recently their numbers have grown dramatically as a result of the ELM Survey, a targeted spectroscopic search for ELM WDs (Brown et al. 2010, Kilic et al. 2011a, Brown et al. 2012, Kilic et al. 2012, Brown et al. 2013). However, there is little direct evidence that low-mass WDs have He-cores. But if they pulsate, as do their C/O-core brethren, we may differentiate their interior structure.

We have been engaged in an ongoing search for low-mass DAVs for many years at McDonald Observatory. The benefits of a search for a low-mass (and putatively He-core) DAV were recently emphasized by Steinfadt et al. (2010a). Should they pulsate in g-modes like the C/O-core DAVs, the eigenfunctions of ELM WDs would globally sample the interior, making the pulsations sensitive to core composition. Seismology may also allow us to constrain the hydrogen layer mass; this is vitally important since hydrogen burning is expected to be a major or even dominant component of the luminosity of these stars (e.g., Panei et al. 2007).

Steinfadt et al. (2012) outlined the null results of a search for pulsations in 12 low-mass WDs. We have extended a similar, systematic search for variable He-core WDs, armed with the many dozens of new extremely low-mass (ELM, ~ 0.2 $M_{\odot}$) WDs catalogued by the ELM Survey. That search has yielded the first five pulsating ELM WDs, which were announced in three separate discovery papers (Hermes et al. 2012c, 2013d,b). The discovery of pulsating ELM WDs provides the first chance to apply the tools of asteroseismology to these low-mass, putatively He-core WDs (Córsico et al. 2012b, Van Grootel et al. 2013). These objects belong to an extension of the instability strip from the C/O-core DAVs, and are most likely driven by the same mechanism acting in the classical ZZ Ceti stars.

Here we chronologically outline the discovery of each new pulsating ELM WD, and populate the empirical instability strip with ELM WDs that vary and more than a dozen that do not vary to a limit of at least 1% relative amplitude.

4.2 SDSS J184037.78+642312.3 (J1840)

4.2.1 Observations

Brown et al. (2012) present the spectroscopic discovery data for J1840 from the Blue Channel spectrograph on the 6.5m MMT. They use 37 separate spectra over more than a year to determine the system parameters. Brown et al. (2012) find that J1840 is in a 4.5912 ± 0.0012 hr (16528.32 ± 4.32 s) orbital period binary with a $K = 272 \pm 2$ km s^{-1} radial velocity semi-amplitude. However, a significant alias exists at 3.85 hr.

Model fits to the co-added spectra for J1840 yield $T_{\rm eff} = 9390 \pm 140$ K and $\log g = 6.49 \pm 0.06$, which correspond to a mass of roughly 0.17 $M_{\odot}$. Given the mass function of the system, $f = 0.399 \pm 0.009$ $M_{\odot}$, the minimum mass of the unseen companion is 0.64 $M_{\odot}$; if the orbital inclination is random, there is a 70% probability that the companion is a WD with < 1.4 $M_{\odot}$. We note, however, that the nature of the unseen companion has no bearing on the impact of the discovery of pulsations in this WD, although it may contaminate the spectra.

We obtained high-speed photometric observations of J1840 at the McDonald Observatory over three consecutive nights in 2011 October, for a total of more than 5.5 hr of coverage. Using the Argos instrument (see Appendix A), we obtained 15 s exposures on this $g = 18.8$ mag WD. The seeing averaged 1.5″ and transparency variations were low, although our second and third nights were cut short by clouds. Figure 4.1 shows all 1365 Argos light curve points obtained for J1840 from 25 Oct 2011 to 27 Oct 2011. We also include the light curve of the brightest comparison star in the field, SDSS J184043.21+642351.8, for reference.

4.2.2 Analysis

Our original photometric data set analyzed in Hermes et al. (2012c) is relatively short, as we caught J1840 just before it went behind the Sun. This limited the significance of the detected periods. Still, we had sufficient data to show convincingly that this low-mass WD is a multi-periodic variable star.

The high-amplitude variability is easy to distinguish in the raw light curve

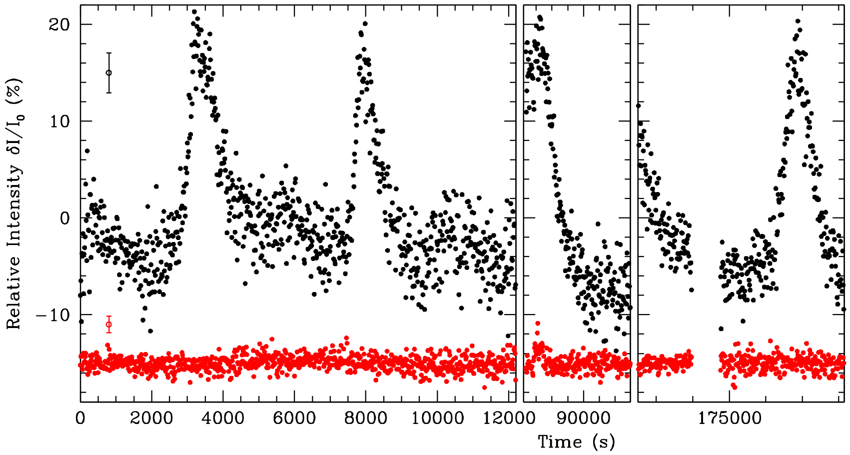

Figure 4.1 The discovery light curves of J1840 (in black) over three consecutive nights in 2011 October, representing the first pulsating ELM WD found. The gap in the third night was caused by a passing cloud. The bottom red light curve, offset by -15%, shows the brightest comparison star in the field over the same period. Average 2σ errors are shown offset with error bars.

(Figure 4.1), with more than 25% peak-to-peak variability. The highest peak in a Fourier transform (FT) of the brightest companion star in the field yields only a small signal (0.24% amplitude) at 7340 ± 15 s, consistent with low-frequency noise from atmospheric variability. Our apertures and sky annuli have been chosen to ensure there is no significant contamination from the nearby star SDSS J184038.73+642315.6, which is $7.0''$ away from our target. Thus the signal we are observing is intrinsic to the WD. Without evidence for a companion star or accretion from the spectra, the light curves, or existing broadband photometry, we are confident that the photometric variability are pulsations on the surface of the ELM WD.

The pulse shape appears non-sinusoidal, with a steep rise and decline. We first test whether a single mode (f_1) and its harmonics ($2f_1 + 3f_1 + ...$) could reproduce the observed light curve. A nonlinear least squares fit with the highest peak in the FT and its fixed harmonics converges on 225.03 μHz (4444 s) as the best

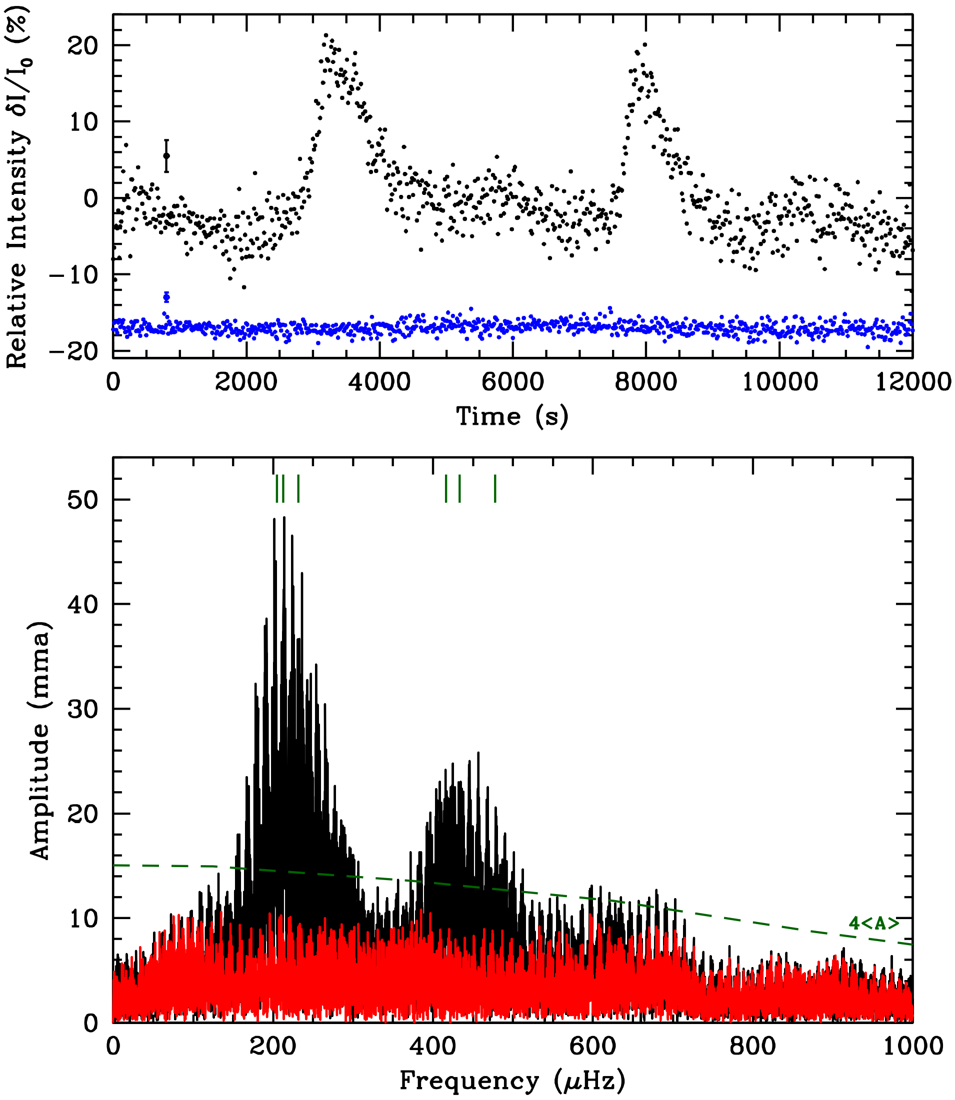

Figure 4.2 The top panel shows high-speed photometry of J1840 from a representative run on 2012 February 1. The brightest comparison star is shown in blue, offset by −8%. Average point-by-point photometric errors are also shown. The bottom panel shows a Fourier transform of our entire data set to date, some 70.2 hr of observations from 2012 January to 2012 April. We also display in red the Fourier transform of the residuals after prewhitening by the five highest-amplitude periods listed in Table 4.2 and mark those periods with green tick marks at the top of the panel. We mark the 4⟨A⟩ significance level as a dashed green line.

parent mode. However, our data from multiple nights rule out this scenario. The single-mode harmonic solution fits the two peaks during the first night well, but it fails to match the peak in our second night of data, predicting a maximum in the light curve more than 500 s too soon.

A multi-mode solution (see Table 4.1) where the frequencies are determined from the highest amplitudes in an FT of the entire dataset (see Figure 4.2) improves the residuals by more than 20%. For more realistic estimates, the cited errors are not formal least-squares errors to the data but rather the product of 10^5 Monte Carlo simulations of perturbed data using the software package Period04 (Lenz & Breger 2005). The signal-to-noise calculation is based on the average amplitude of a 1000 μHz box after pre-whitening by the three significant, highest-amplitude frequencies. This set of period solutions is by no means exhaustive, but it establishes that this ELM WD is variable and multi-periodic.

We have completed a reanalysis of the periods detected in J1840 using nearly 33.0 hr of photometric observation from October 2011 to July 2012, as outlined in (Córsico et al. 2012b). Our observing and reduction techniques are identical to those described in Hermes et al. (2012c), but include more than 27.0 hr of additional observations. Aliasing of the data has made determining the periods especially difficult, so we have made every attempt to be as conservative as possible in our error estimates. We include in Figure 4.2 a representative light curve and Fourier transform of this entire data set.

The highest-amplitude mode excited in the star occurs at 4697.8 ± 4.3 s (51 ± 5 mma); this periodicity appears in the 5.5 hr of October 2011 discovery data, but was the second-highest alias of the 4445 s mode quoted by Hermes et al. (2012c). Additionally, we see evidence of variability at the following periods (we have made very conservative estimates on the uncertainties, mindful of possible

Table 4.1. Frequency solution for SDSS J1840+6423

ID	Period (s)	Frequency (μHz)	Amplitude (mma)	S/N
f_1	4697.831 ± 0.006	212.8642 ± 0.0003	50.7 ± 0.8	13.4
f_2	4697.831 ± 0.012	231.8435 ± 0.0007	27.8 ± 0.8	7.4
f_3	2308.94 ± 0.37	433.099 ± 0.070	25.2 ± 1.9	7.4
f_4	2403.416 ± 0.008	416.0745 ± 0.0014	21.9 ± 1.0	6.3
f_5	4887.943 ± 0.018	204.5851 ± 0.0008	21.5 ± 0.7	5.7
f_6	2094.246 ± 0.004	477.4989 ± 0.0010	17.1 ± 1.8	5.1

Note. — 1 mma = 0.1% relative amplitude

aliasing): 4310 ± 200 s (28 ± 3 mma), 2309 ± 60 s (25 ± 3 mma), 2400 ± 120 s (21 ± 3 mma), 4890 ± 270 s (21 ± 3 mma), and 2094 ± 50 s (17 ± 3 mma). These periodicities may be independently excited modes, but it is possible that the shorter-period modes are nonlinear combination frequencies of the longer modes (Brickhill 1992). If the ELM white dwarf is synchronized (or nearly synchronized) with the orbital period, it is possible that the modes just short and long of the 4697.8 s mode may be rotationally split components rather than independent modes.

4.3 SDSS J111215.82+111745.0 (J1112)

4.3.1 Spectroscopic Observations

Brown et al. (2012) presented a preliminary fit of $T_{\rm eff} = 9400 \pm 490$ K and $\log g = 5.81 \pm 0.12$ based on a single spectrum of this $g = 16.2$ mag WD from the FLWO 1.5 m telescope using the FAST spectrograph (Fabricant et al. 1998). We have obtained an additional 26 spectra using the FLWO 1.5 m telescope and an additional 6 spectra using the Blue Channel Spectrograph (Schmidt et al. 1989) on the 6.5m MMT. The time-series spectroscopy reveals that J1112 is short-period binary, as described below.

4.3.1.1 Atmospheric Parameters

We have phased (see Section 4.3.1.2) and co-added our new spectroscopic observations to determine the atmospheric parameters of the primary ELM WD visible in J1112. Our observations cover a wavelength range from $3700 - 4500$ Å. The model atmospheres used for this analysis are described at length in Gianninas et al. (2011) and employ the new Stark broadening profiles from Tremblay & Bergeron (2009). Models where convective energy transport becomes important are computed using the ML2/α = 0.8 prescription of the mixing-length theory (see Tremblay et al. 2010). However, since we are dealing with ELM WDs, the model grid needed to be extended down to lower surface gravities. Thus the model grid used in this analysis covers the ranges in $T_{\rm eff}$ from 4000 to 30,000 K in steps ranging from 250 to 5000 K and $\log g$ from 5.0 to 8.0 in steps of 0.25 dex.

The method used for fitting the observations relies on the so-called spectroscopic technique, described in Gianninas et al. (2011) and references therein. The main difference here is that we fit the Balmer lines we observe up to and including H12, as the considerably lower surface gravity means that these higher Balmer lines are still observed. Since the higher Balmer lines are sensitive mostly to $\log g$ (see Figure 2 of Tremblay & Bergeron 2009), the inclusion of these extra lines further constrains our measurement of the surface gravity.

The uncertainty for each parameter is calculated by combining the internal error, which is the dominant source of uncertainty, obtained from the covariance matrix of the fitting algorithm with the external error, obtained from multiple observations of the same object, estimated for DA stars at 1.2% in $T_{\rm eff}$ and 0.038 dex in $\log g$ (see Liebert et al. 2005 for details). The effect on the uncertainties caused by different values of S/N are included in the internal error.

Our final fit to the phased and co-added spectra of J1112 is shown in the top panel of Figure 4.3 and yield $T_{\rm eff} = 9590 \pm 140$ K and $\log g = 6.36 \pm 0.06$. This corresponds to a mass of $\sim$0.17 $M_{\odot}$ using the He-core models of Panei et al. (2007).

In addition to the Balmer series, the Ca II K line at 3933 Å is also observed in the spectra of J1112. For the purposes of this analysis, we simply exclude the wavelength range where that metal line is present so that it does not affect either the normalization of the individual Balmer lines nor the actual fits themselves. This Ca feature phases with the radial velocity variations of the Balmer lines, and is thus not interstellar but rather in the photosphere of the WD. We will not discuss this Ca feature further.

4.3.1.2 Radial Velocity Observations

The bottom two panels of Figure 4.3 show the radial velocity curve of the 32 spectra we have obtained of J1112. We compute the orbital elements of this single-lined binary using the code of Kenyon & Garcia (1986), which weights each velocity measurements by its associated error. Our spectroscopic observations find that J1112 is in a 4.13952 ± 0.00024 hr orbital period binary with a $K = 116.2 \pm 2.8$ km s^{-1} radial velocity semi-amplitude.

This yields a mass function of $f = 0.028 \pm 0.003$ $M_{\odot}$, which constrains the minimum mass of the unseen companion to $M_2 > 0.14$ $M_{\odot}$ assuming a 0.17 $M_{\odot}$ primary. The nature of this companion has no direct bearing on the discovery of pulsations in the primary ELM WD, but it may be contribute enough flux to partially contaminate the spectral fits of the primary. It also suggests that unless

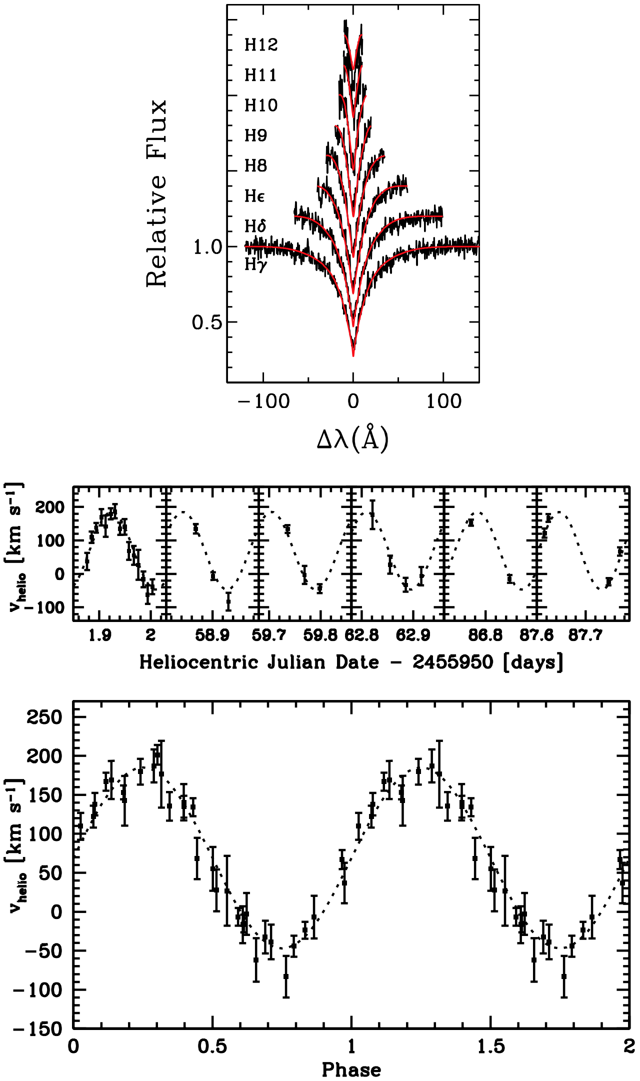

Figure 4.3 Spectroscopic observations of J1112. The top panel shows the summed and phased spectra, with a model fit to the $H\gamma$–H12 lines of the Balmer series. This model derives the primary parameters in Section 4.3.1.1. The middle panel shows our new radial velocity observations of J1112 over six epochs, and the bottom panel shows those data phased to the orbital period of 4.13952 hr.

the system is inclined to less than 30 degrees (which would happen at random less than 15% of the time), the companion is most likely another He-core WD with a mass below 0.45 $M_{\odot}$. Similar single-lined ELM WDs with likely He-core WD companions have been found in the ELM Survey (i.e., SDSS J1005+3550 in Kilic et al. 2012).

We have folded our photometric observations on this orbital period and do not see evidence of eclipses, at a limit of 0.5%. This suggests that the inclination of the system is $i < 80$ degrees, although this does not significantly constrain the nature of the unseen companion.

4.3.2 Photometric Observations

We obtained high-speed photometric observations of J1112 at the McDonald Observatory over four months, from 2012 January to 2012 April, for a total of more than 70.2 hr of coverage using the Argos instrument; a full journal of observations can be found in Table 4.8.

The top panel of Figure 4.4 shows a portion of a typical light curve for J1112, obtained on 2012 February 1, and includes the brightest comparison star in the field over the same period (the scatter is large because the other comparison stars in the field used to construct this divided light curve are all fainter than $g = 16.9$ mag). The bottom panel of this figure shows a Fourier transform (FT) utilizing all $38{,}863$ light curve points collected thus far. We display the 4$\langle\mathrm{A}\rangle$ significance line at the bottom of Figure 4.4, calculated from the average amplitude, $\langle\mathrm{A}\rangle$, of an FT within a 1000 μHz region in steps of 200 μHz, after pre-whitening by the five highest-amplitude periodicities.

The pulse shape of J1112 appears quite sinusoidal, and is nearly solved with five independent periodicities. Those periods have been identified in decreasing

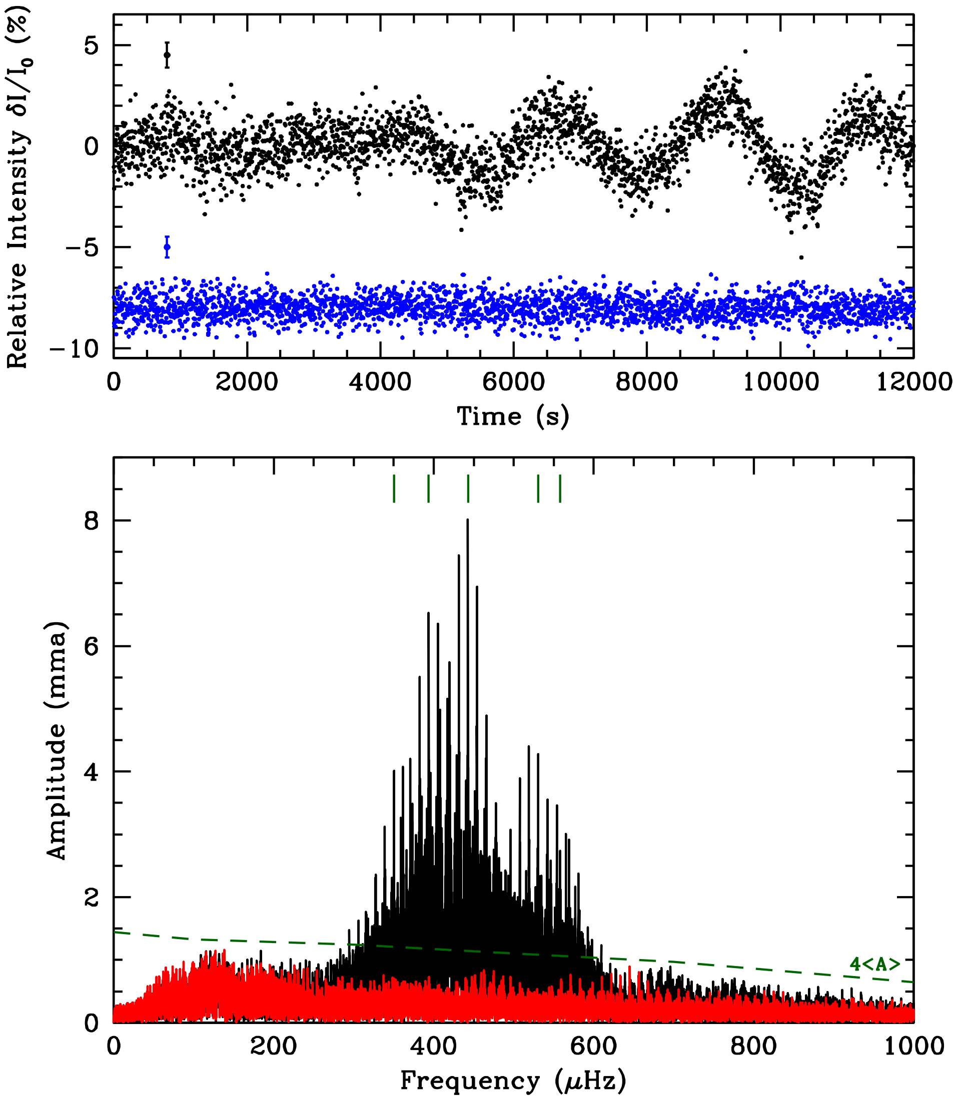

Figure 4.4 The top panel shows high-speed photometry of J1112 from a representative run on 2012 February 1. The brightest comparison star is shown in blue, offset by −8%. Average point-by-point photometric errors are also shown. The bottom panel shows a Fourier transform of our entire data set to date, some 70.2 hr of observations from 2012 January to 2012 April. We also display in red the Fourier transform of the residuals after prewhitening by the five highest-amplitude periods listed in Table 4.2 and mark those periods with green tick marks at the top of the panel. We mark the $4\langle A\rangle$ significance level as a dashed green line.

order of amplitude in Table 4.2. For more realistic estimates, the cited errors are not formal least-squares errors to the data but rather the product of 10^5 Monte Carlo simulations of perturbed data using the software package Period04 (Lenz & Breger 2005). The signal-to-noise calculation is based on the amplitude of the variability as compared to the average amplitude of a 1000 μHz box centered around that variability, after pre-whitening by the five highest-amplitude periodicities.

A simultaneous linear least-squares fit, fixing these five periods, shows that this variability is quite stable in both amplitude and phase. The f_1 periodicity is especially stable in phase, with an r.m.s. scatter less than 7 s between our four months of data—better than 3% of the 2258.5 s period. The phase stability of J1112 is reminiscent of hot DAVs such as G117-B15A (Kepler et al. 2005), and could be monitored long-term for periodic deviations in arrival times to constrain any possible circumbinary planets (Mullally et al. 2008). There is slightly more scatter about the amplitudes measured from month to month, which are more sensitive to variations in photometric conditions. The only periodicity with a consistently decreasing amplitude is f_2, which showed an amplitude of 0.7184% ± 0.0098% in 2012 January decrease to 0.573% ± 0.016% in 2012 April.

None of these periods are an integer harmonic of the 4.13952 hr (14902.27 ± 0.86 s) orbital period. Given our cited uncertainties, f_3, the closest, is more than 8-σ from $8 \times f_{orb}$. Thus, tidally induced pulsations cannot properly explain the observed multi-periodic variability. Instead, we conclude that these are global, nonradial g-mode pulsations driven to observability by the same mechanism at work in classical DAVs (Brickhill 1991). The timescale of this variability is considerably longer than for the pulsations seen in C/O-core DAVs. However, it is consistent with the expectation that the periods of pulsation modes roughly scale with the dynamical timescale for the whole star, $\Pi \propto \rho^{-1/2}$, and are thus much longer for

Table 4.2. Frequency solution for SDSS J1112+1117

ID	Period (s)	Frequency (μHz)	Amplitude (mma)	S/N
f_1	2258.528 ± 0.003	442.7662 ± 0.0007	7.49 ± 0.08	26.5
f_2	2539.695 ± 0.005	393.7480 ± 0.0007	6.77 ± 0.09	23.0
f_3	1884.599 ± 0.004	530.6170 ± 0.0011	4.73 ± 0.08	16.9
f_4	2855.728 ± 0.010	350.1734 ± 0.0013	3.63 ± 0.09	11.5
f_5	1792.905 ± 0.005	557.7542 ± 0.0017	3.31 ± 0.08	11.9
f_6	134.275 ± 0.001	7447.388 ± 0.010	0.44 ± 0.08	*4.4*
f_7	107.56 ± 0.04	9297.4 ± 3.6	0.38 ± 0.14	*4.1*

the low-surface-gravity ELM WDs.

4.3.3 Potential p-mode Pulsations

In addition to the relatively high-amplitude, long-period variability observed in J1112, we see evidence for low-amplitude variability on much shorter timescales. These periodicities are included at the bottom of Table 4.2 in decreasing order of S/N. This S/N value is conservative: We have not pre-whitened by the variability in question for this calculation, which effectively considers some signal as noise in this estimate. We have identified all periodicities with S/N > 4.0, and italicize these S/N values to indicate they were calculated in a different way.

We have also computed the probability that each of the short-period detections is real by computing the false alarm probability (FAP), using the formalism described in Kepler (1993). We find that f_6 and f_7 have a FAP $> 99.9\%$. (There is an additional peak at 119.552 s with S/N = 3.7 and a FAP of 99.8%. However, this periodicity is sufficiently close to the 119.667 s periodic drive error of the 2.1 m

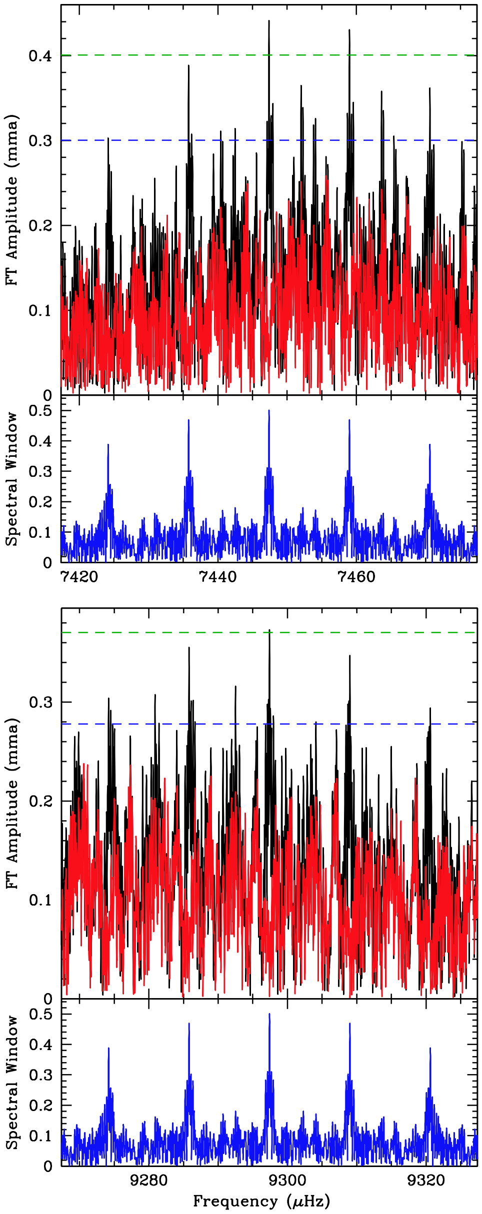

Figure 4.5 A zoom of the high-frequency regions in the FT of the entire J1112 data set that display evidence for short-period variability, potential p-mode pulsations at 134.3 s (top) and 107.6 s (bottom). The original FT is shown in black, and the red shows the residuals after pre-whitening by the highest-amplitude peak. The dashed blue and green lines show the $3\langle A\rangle$ and $4\langle A\rangle$ lines, respectively. The lower panel shows the spectral window in blue centered around each periodicity.

Otto Struve telescope that we will not include it in our formal frequency solution.) Figure 4.5 shows a zoomed-in portion of the FT around 134.3 s and 107.6 s using our entire data set.

This variability is coherent enough to reach significant amplitude over four months of observations. Some of our longest individual runs also evidence this variability, such as the 6.5 hr run on 2012 Jan 27 (with a 1.24 ± 0.36 mma signal at 134.2 ± 2.2 s) and the 3.5 hr run on 2012 Feb 1 (with a 1.17 ± 0.40 mma signal at 107.9 ± 1.8 s). These two peaks are also fairly significant if we use just our 2012 January data: The 134.275 s mode has 0.55 ± 0.17 mma amplitude ($> 99.9\%$ FAP) while the 107.557 s mode has 0.46 ± 0.14 mma amplitude (98.2% FAP).

This variability is too short to be explained as g-mode pulsations without invoking implausibly high values of the spherical harmonic degree. A recent non-adiabatic pulsation analysis relevant to low-mass WDs by Córsico et al. (2012b) found that g-modes of low radial order (and thus the shortest period) are stable to pulsations and should not be driven to observability. Their calculations found that unstable g-modes in a 0.17 $M_{\odot}$ WD have radial orders $k \geq 9$ and periods longer than 1100 s. Even if we ignore their conclusion that an $\ell = 1$, $k = 1$ mode is stable, they find this lowest radial order mode has a period ~249.5 s. Similarly, Steinfadt et al. (2010a) also found that an $\ell = 1$, $k = 1$ g-mode for a 0.17 $M_{\odot}$ WD has a ~245 s period.

The short-period variability seen in J1112 is also inconsistent with nonlinear combination frequencies present in the non-sinusoidal light curves of many classical DAVs (Brickhill 1992). For one, the light curve of J1112 is extremely sinusoidal. Additionally, the short-period variability is not a multiple of any of the five low-frequency modes, nor is it a combination of different modes.

Instead, we propose that this variability is caused by acoustic or pressure

(p-mode) pulsations driven to observability in J1112. Córsico et al. (2012b) find that low-order p-modes are pulsationally unstable, and have periods ranging from $109 - 7.5$ s for their $1 < k < 29$ models of a 0.17 $M_{\odot}$ He-core WD. The 134.3 s period we observe in J1112 is slightly longer than this predicted range, which suggests some uncertainty in identifying the true nature of these instabilities. Still, should these hold up as acoustic modes, this would mark the first detection of p-mode pulsations in any WD. We discuss the impact of this discovery in Section 4.7.3.

4.4 SDSS J151826.68+065813.2 (J1518)

4.4.1 Spectroscopic Observations

Brown et al. (2012) present the spectroscopic discovery data for this $g = 17.5$ mag WD from the Blue Channel spectrograph on the 6.5m MMT. They use 41 separate spectra over more than a year to determine the system parameters, and find that J1518 is in a 14.624 ± 0.001 hr (52646.4 ± 3.6 s) orbital period binary with a $K = 172 \pm 2$ km s^{-1} radial velocity semi-amplitude.

We have fit their 41 phased and co-added spectra with the extended stellar atmosphere models of Tremblay & Bergeron (2009), as described in Section 4.3.1.1. This fit formally yields $T_{\rm eff} = 9900 \pm 140$ K and $\log g = 6.80 \pm 0.05$ for J1518, which corresponds to a mass of ∼0.23 $M_{\odot}$ (Panei et al. 2007). Given the mass function ($f = 0.322 \pm 0.005$ $M_{\odot}$), the minimum mass of the unseen companion is $M_2 > 0.61$ $M_{\odot}$, making it most likely another WD. As with J1112, the nature of the companion has no direct bearing on pulsations in the primary, but it may partially contaminate the spectral fits. Unlike J1112, no metal lines are detected in the spectrum of J1518.

4.4.2 Photometric Observations

We obtained photometric observations of J1518 from 2012 March to 2012 July for more than 32.2 hr of coverage; a full journal of observations can be found in Table 4.8. We divided the sky-subtracted light curves by the two brightest comparison stars in the field, SDSS J151824.11+065723.2 ($g = 14.0$ mag) and SDSS J151828.78+065928.9 ($g = 14.3$ mag), to allow for fluctuations in seeing and cloud cover.

The top panel of Figure 4.6 shows a portion of a typical light curve for J1518, obtained in 2012 April, and includes the brightest comparison star in the field over the same period. High-amplitude, multi-periodic, highly non-sinusoidal variability is evident. The bottom panel of this figure shows an FT utilizing all $16{,}522$ light curve points collected thus far.

Given the relatively sparse coverage over four months ($< 1.2\%$ duty cycle), the spectral window for our observations of J1518 is quite messy, and aliasing from gaps in the data makes identifying the underlying periods of variability especially difficult. As such, we have provided two families of solutions in Table 4.3.

The highest peak in the FT occurs at $\sim$357 μHz. However, after pre-whitening by this frequency, there is considerable ambiguity as to the next highest peak. There are two peaks with nearly the same amplitude, one slightly higher at 452.4895 μHz than the other split apart by the daily alias at 440.8777 μHz. Our two families of solutions are based on which of these aliases we pick. We note that the top family of solutions holds up more robustly to a Monte Carlo simulation of the associated frequency and amplitude uncertainties, but the bottom family does a marginally better job of reproducing the data (the residuals after fitting this solution have a 3.27% total amplitude, while the residuals after fitting the top family have 3.32% total amplitude). In both cases, the fits do a poor job of reproducing the non-linear

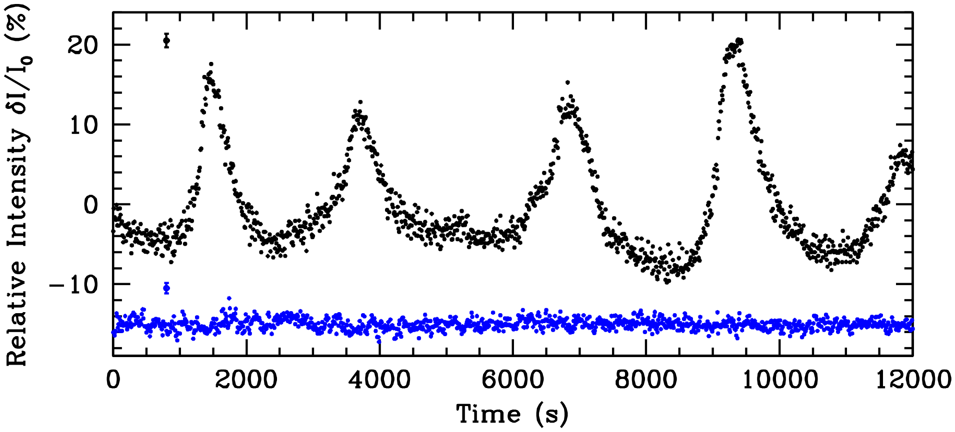

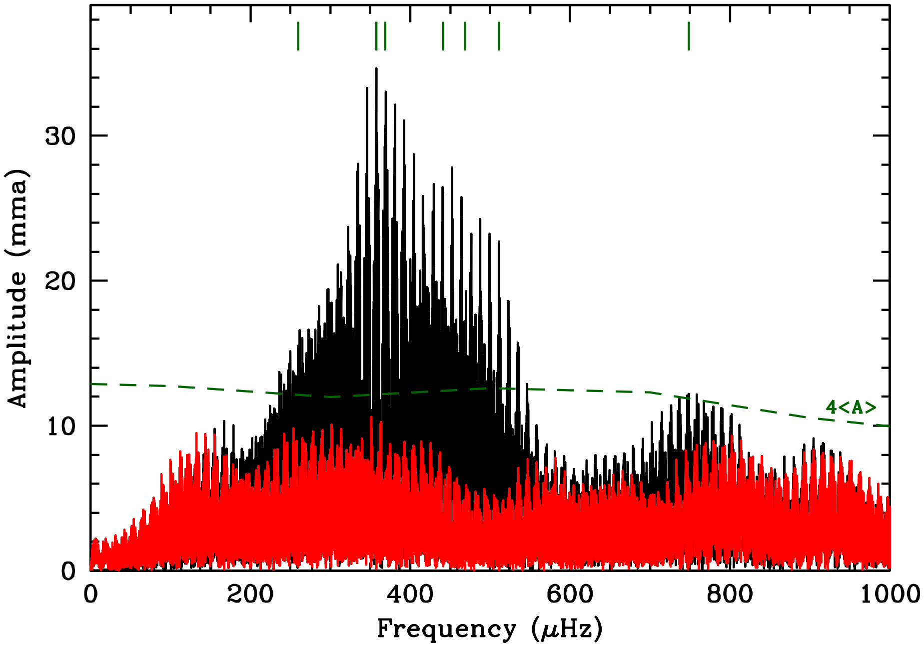

Figure 4.6 The top panel shows high-speed photometry of J1518 from a representative run, this a portion from 2012 April 16. The brightest comparison star is shown in blue, offset by −15%. Average point-by-point photometric errors are shown. The bottom panel shows a Fourier transform of our entire data set to date, more than 32 hr of observations from 2012 March to 2012 July. We also display in red the Fourier transform of the residuals after pre-whitening by the seven periods listed in the top portion of Table 4.3 and mark those periods with green tick marks at the top of the panel. We mark the 4⟨A⟩ significance line as a dashed green line.

Table 4.3. Frequency Solutions for SDSS J1518+0658

ID	Period (s)	Frequency (μHz)	Amplitude (mma)	S/N
		Family I		
f_1	2799.087 ± 0.005	357.2593 ± 0.0007	35.4 ± 0.6	11.8
f_2	2268.203 ± 0.004	440.8777 ± 0.0007	21.6 ± 0.2	7.1
f_3	2714.306 ± 0.003	368.4183 ± 0.0005	21.6 ± 0.9	7.1
f_4	1956.361 ± 0.003	511.1532 ± 0.0007	18.1 ± 0.3	5.7
f_5	3848.201 ± 0.009	259.8617 ± 0.0006	15.7 ± 0.3	5.3
f_6	1335.318 ± 0.003	748.8855 ± 0.0015	13.6 ± 0.6	4.5
f_7	2134.027 ± 0.004	468.5976 ± 0.0008	14.2 ± 0.4	4.5
		Family II		
f_1	2796.048 ± 0.022	357.6476 ± 0.0028	41.1 ± 4.8	13.5
f_2	2209.996 ± 0.024	452.4895 ± 0.0049	19.9 ± 1.4	6.5
f_3	2802.769 ± 2.6	356.79 ± 0.33	26.4 ± 3.9	8.7
f_4	1956.331 ± 0.008	511.1609 ± 0.0020	18.1 ± 0.8	5.7
f_5	3683.703 ± 7.7	271.47 ± 0.57	17.7 ± 3.2	5.7
f_6	2413.091 ± 29.5	414.41 ± 5.07	15.6 ± 4.0	5.2
f_7	1318.847 ± 0.004	758.2382 ± 0.0021	12.9 ± 0.4	4.4

peakiness manifest as the sharp rises and falls in the light curve. However, the fits do a decent job of predicting when these features occur.

The seven significant periodicities we identify in J1518 are by no means exhaustive; we note the significant residual power left over after pre-whitening by these periods shown as the red FT at the bottom of Figure 4.6. In the range between $200 - 800$ μHz ($1250 - 5000$ s), the average amplitude of the original FT is 6.4 mma, and after pre-whitening it remains above 3.4 mma. A coordinated campaign of near-continuous observations of this relatively bright WD has been undertaken to help resolve the periods present in this pulsating WD.

4.5 SDSS J161431.28+191219.4 (J1614)

4.5.1 Spectroscopic Observations

Brown et al. (2012) found that J1614 had $T_{\rm eff} = 8590 \pm 540$ K and $\log g = 5.64 \pm 0.12$, based on a single spectrum of this $g = 16.4$ mag WD from the FLWO 1.5 m telescope using the FAST spectrograph (Fabricant et al. 1998). We have obtained an additional 51 spectra using the same instrument and setup.

4.5.1.1 Atmospheric Parameters

We have co-added our spectroscopic observations to determine the atmospheric parameters of the ELM WD J1614 (Figure 4.7). Our observations cover a wavelength range from $3550 - 5450$ Å. The model atmospheres used for this analysis are described at length in Gianninas et al. (2011) and employ the new Stark broadening profiles from Tremblay & Bergeron (2009). Models where convective energy transport becomes important are computed using the ML2/α = 0.8 prescription of the mixing-length theory (see Tremblay et al. 2010). A discussion of our extension of these models to lower surface gravities and more details of our fitting method can be found in Section 4.3.1.1.

Our final fit to the phased and co-added spectrum of J1614 is shown in the top panel of Figure 4.7 and yields $T_{\rm eff} = 8880 \pm 170$ K and $\log g = 6.66 \pm 0.14$. This corresponds to a mass of ~0.20 $M_{\odot}$ using the He-core WD models of Panei et al. (2007).

We have also performed our fit without using the low S/N lines H11$-$H12, but this marginally affects our solution: Using only the H$\gamma$$-$H10 lines of the Balmer series, we find $T_{\rm eff} = 8830 \pm 160$ K and $\log g = 6.54 \pm 0.16$. To remain self-consistent with our previous pulsating ELM WD atmospheric determinations (Hermes et al. 2012c, 2013d), we will include the H11$-$H12 lines in our adopted solution for J1614.

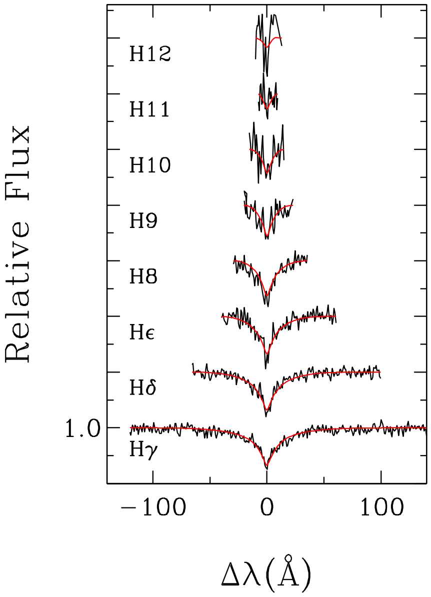

Figure 4.7 The summed spectra of J1614, with a model fit to the $\mathrm{H}\gamma - \mathrm{H}12$ lines of the Balmer series. This model derives the primary parameters in Section 4.5.1.1.

4.5.1.2 Radial Velocity Observations

ELM WDs are typically found in close binary systems; these companions are necessary to strip the progenitor of enough mass to form such a low-mass WD within the age of the universe (Kilic et al. 2011a). However, using the code of Kenyon & Garcia (1986), we do not detect any significant radial velocity variability in our observations of J1614. The r.m.s. scatter gives us an upper limit on the RV semi-amplitude: $K < 56$ km s^{-1}. The systemic velocity is $\gamma = -148.7 \pm 7.6$ km s^{-1}.

We note that this non-detection does not indicate the lack of a companion to the ELM WD in J1614. Rather, the system may be inclined nearly face-on to our line of sight, or the companion may be a much cooler low-mass WD. If the inclination is $i > 30°$, which is more than 85% likely if the orientation to the system is randomly inclined, the companion has $M_2 < 0.17\ M_{\odot}$if the system has a 7 hr orbital period, the median for ELM WD binaries in the ELM Survey (Brown et al. 2013). Empirically, there are similarly low-mass WDs in the ELM Survey with no significant radial velocity variability (e.g. SDSS J0900+0234, Brown et al. 2012).

4.5.2 Photometric Observations

We obtained high-speed photometric observations of J1614 at the McDonald Observatory over five consecutive nights in 2012 June for a total of nearly 15.4 hr of coverage. We divided the sky-subtracted light curves by the brightest comparison star in the field, SDSS J161433.39+191058.3 ($g = 14.3$ mag), to correct for transparency variations.

The top panel of Figure 4.8 shows a portion of a typical light curve for J1614, obtained on 2012 June 23, and includes the brightest comparison star in the field over the same period. The bottom panel of this figure shows a Fourier transform (FT) utilizing all $11{,}075$ light curve points collected thus far. We display the $4\langle \mathrm{A} \rangle$ significance line at the bottom of Figure 4.8, calculated from the average amplitude, $\langle \mathrm{A} \rangle$, of an FT within a 1000 μHz region in steps of 200 μHz, after pre-whitening by the two highest-amplitude periodicities.

The pulse shape of J1614 appears quite sinusoidal, and is well described by two nearby periods at 1262.67 and 1184.11 s. The amplitudes of these periods are identified in Table 4.4. For more realistic estimates, the cited errors are not formal least-squares errors to the data but rather the product of 10^5 Monte Carlo simulations of perturbed data using the software package Period04 (Lenz & Breger 2005). The signal-to-noise calculation is based on the amplitude of the variability as compared to the average amplitude of a 1000 μHz box centered around that variability, after pre-whitening by the two highest-amplitude periodicities.

It is possible that f_1 and f_2 are consecutive radial modes, in which case the

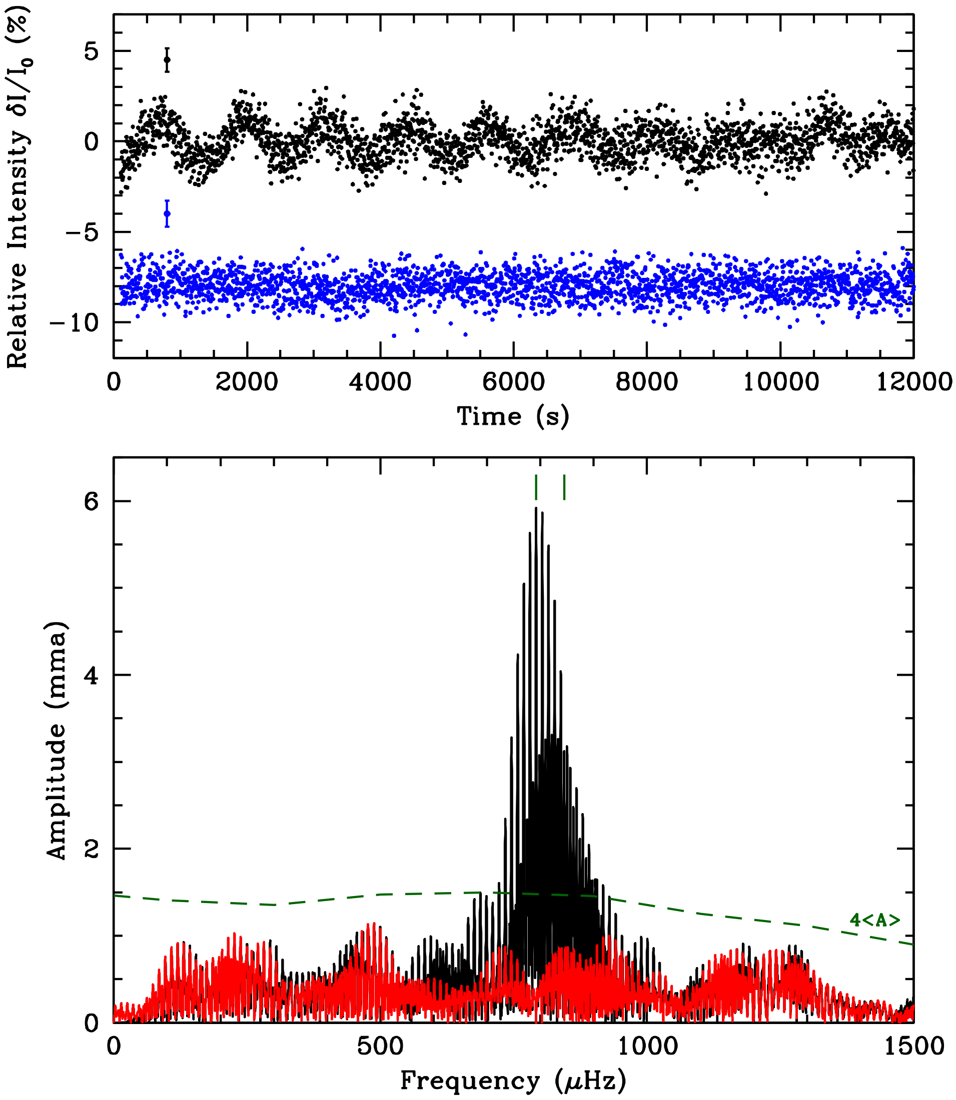

Figure 4.8 The top panel shows high-speed photometry of J1614 from a representative run on 2012 June 23. The brightest comparison star is shown in blue, offset by −8%. Average point-by-point photometric errors are also shown. The bottom panel shows a Fourier transform of our entire data set to date, some 15.4 hr of observations in 2012 June. We also display in red the Fourier transform of the residuals after prewhitening by the two periods listed in Table 4.4, and mark those periods with green tick marks at the top of the panel. We mark the $4\langle A\rangle$ significance level, described in the text, as a dashed green line.

Table 4.4. Frequency Solution for SDSS J1614+1912

ID	Period (s)	Frequency (μHz)	Amplitude (mma)	S/N
f_1	1262.668 ± 0.041	791.974 ± 0.026	5.94 ± 0.11	16.0
f_2	1184.106 ± 0.064	844.519 ± 0.045	3.20 ± 0.10	8.6

difference in their periods, 78.56 s, could probe the forward mean period spacing, which is a sensitive function of the overall WD mass. (We note that Córsico et al. 2012b find that low-mass WDs reach the asymptotic limit for mean period spacing for only high radial order, $k > 25$. For reference, they find an asymptotic mean period of 94.3 s for a 0.20 $M_{\odot}$, 8860 K He-core WD.)

The models of Córsico et al. (2012b) provide a useful context for the observed periodicities: Their 8889 K, 0.22 $M_{\odot}$ He-core WD model, which has a relatively thick hydrogen layer ($M_{\rm H}/M_{*} = 10^{-2.78}$), shows an $\ell = 1, k = 11$ g-mode at 1196.07 s and an $\ell = 1, k = 12$ g-mode at 1274.67 s. In addition, we find an excellent match of these two periods to their 8850 K, 0.303 $M_{\odot}$ model, in which the $\ell = 1, k = 14$ and $\ell = 1, k = 15$ g-modes occur at 1196.07 s and 1274.66 s, respectively, and differ by 78.60 s.

It is also possible that the 52.5 μHz difference between these two oscillations could be explained by a rotational splitting from a single mode in the star (Hansen et al. 1977). Such a splitting could arise from a 16.9 hr rotation rate if the 1184 s mode is an $\ell = 1$ mode, assuming roughly solid-body rotation. However, such an interpretation would predict three evenly spaced frequencies in the data. We find only two. These two periodicities are therefore likely independent modes in the star.

4.6 SDSS J222859.93+362359.6 (J2228)

4.6.1 Spectroscopic Observations

We targeted J2228 based on a single classification spectrum published in Brown et al. (2012). A preliminary fit to the spectrum of this $g = 16.9$ mag WD from the FLWO 1.5 m telescope using the FAST spectrograph found $T_{\rm eff} = 8590 \pm 540$ K and $\log g = 5.64 \pm 0.12$. We have obtained 30 additional spectra using the FLWO 1.5 m telescope and two additional spectra using the Blue Channel Spectrograph (Schmidt et al. 1989) on the 6.5m MMT.

4.6.1.1 Atmospheric Parameters

As with J1614, we have co-added our spectroscopic observations to determine the atmospheric parameters of the primary ELM WD visible in J2228. Our model atmosphere fitting is identical to that as described in Section 4.5.1.1.

Our final fit to the co-added MMT spectrum of J2228 is shown in Figure 4.9 and yields $T_{\rm eff} = 7870 \pm 120$ K and $\log g = 6.03 \pm 0.08$. This corresponds to a mass of ~0.16 $M_{\odot}$ using the He-core WD models of Panei et al. (2007). Similarly, a fit to our 31 FAST spectra, which has lower S/N, finds $T_{\rm eff} = 7990 \pm 190$ K and $\log g$ $= 6.25 \pm 0.15$.

In addition to the Balmer series, the Ca II K line is also observed in the spectra of J2228 (see the deep absorption feature at 3933 Å in Figure 4.10, as well as the absorption in the blue wing of the Hϵ line seen in Figure 4.9). We have previously seen strong Ca lines in very low-surface-gravity WDs ($\log g < 6.0$). These metal lines typically phase with the ELM WD radial velocity and are thus not interstellar (e.g. Hermes et al. 2013d, Brown et al. 2013, Kaplan et al. 2013). For the purposes of this analysis, we simply exclude the wavelength range where that metal line is present so that it does not affect either the normalization of the individual Balmer

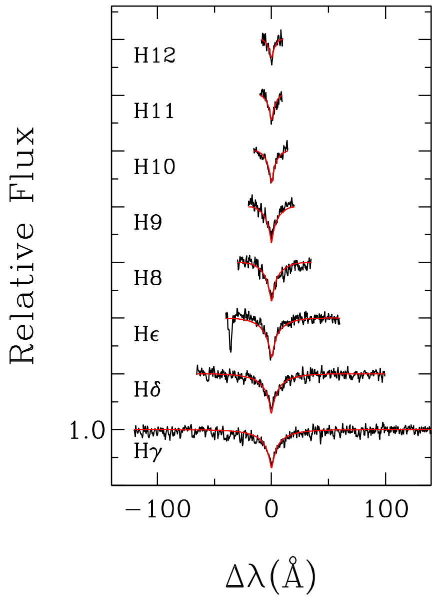

Figure 4.9 The summed spectrum of J2228, with a model fit to the Hγ−H12 lines of the Balmer series derived from the spectroscopic method. We have excluded the region of the deep Ca absorption in the blue wing of the Hϵ line. This model derives the primary parameters in Section 4.6.1.1.

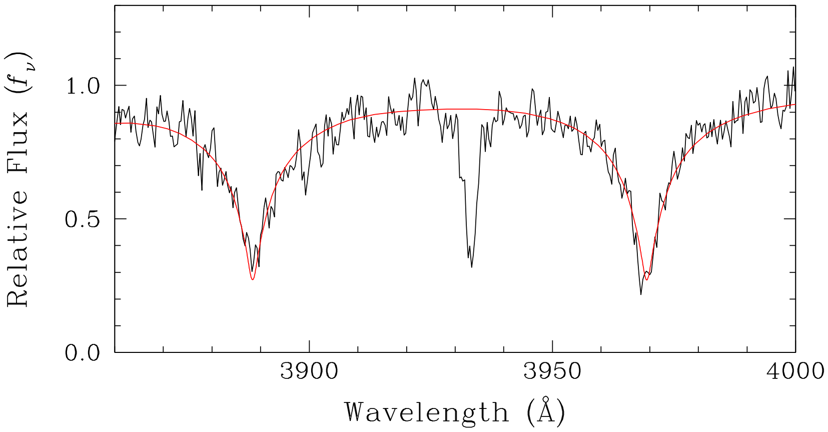

Figure 4.10 A zoomed in portion from 3800−4000 Å of the summed spectra of J2228 from our MMT observations. The deep absorption feature at 3933 Å, between H8 (left) and Hϵ (right) corresponds to the Ca II K line and is most likely in the atmosphere of this ELM WD. The best model atmosphere, shown in detail in Figure 4.9, is over-plotted in red.

lines nor the actual fits themselves. However, the presence of Ca in the atmosphere of this WD may introduce a systematic effect on the derived atmospheric parameters.

4.6.1.2 Radial Velocity Observations

As with J1614, we do not detect any significant radial velocity variability in our observations of J2228. Again, the r.m.s. scatter gives us an upper limit on the RV semi-amplitude: $K < 28$ km s^{-1}. The systemic velocity is $\gamma = -52.5 \pm 4.7$ km s^{-1}.

If the inclination is $i > 30°$, we can put an upper limit on the companion mass of $M_2 < 0.06\ M_\odot$ if the orbital period is 7 hr (see Section 4.5.1.2). Similarly, the companion would have less mass than $M_2 < 0.26\ M_\odot$ if the inclination is $i > 10°$. If the system inclination is randomly oriented, there is a $< 2\%$ probability that the inclination is $i < 10°$. If a binary companion remains around J2228, it likely has low mass.

4.6.2 Photometric Observations

Our high-speed photometric observations of J2228 were obtained and reduced in an identical manner as those described in Section 4.5.2. We divided the sky-subtracted light curves by the sum of three brighter comparison stars in the field: SDSS J222904.91+362454.1 ($g = 15.4$ mag), SDSS J222859.80+362532.3 ($g = 15.8$ mag), and SDSS J222902.31+362351.5 ($g = 16.2$ mag).

We first observed J2228 over three consecutive nights in 2011 November, but the star went behind the Sun before we could confirm variability. All told, we obtained more than 25.7 hr of photometric observations spread over nearly 10 months. A full journal of observations can be found in Table 4.8.

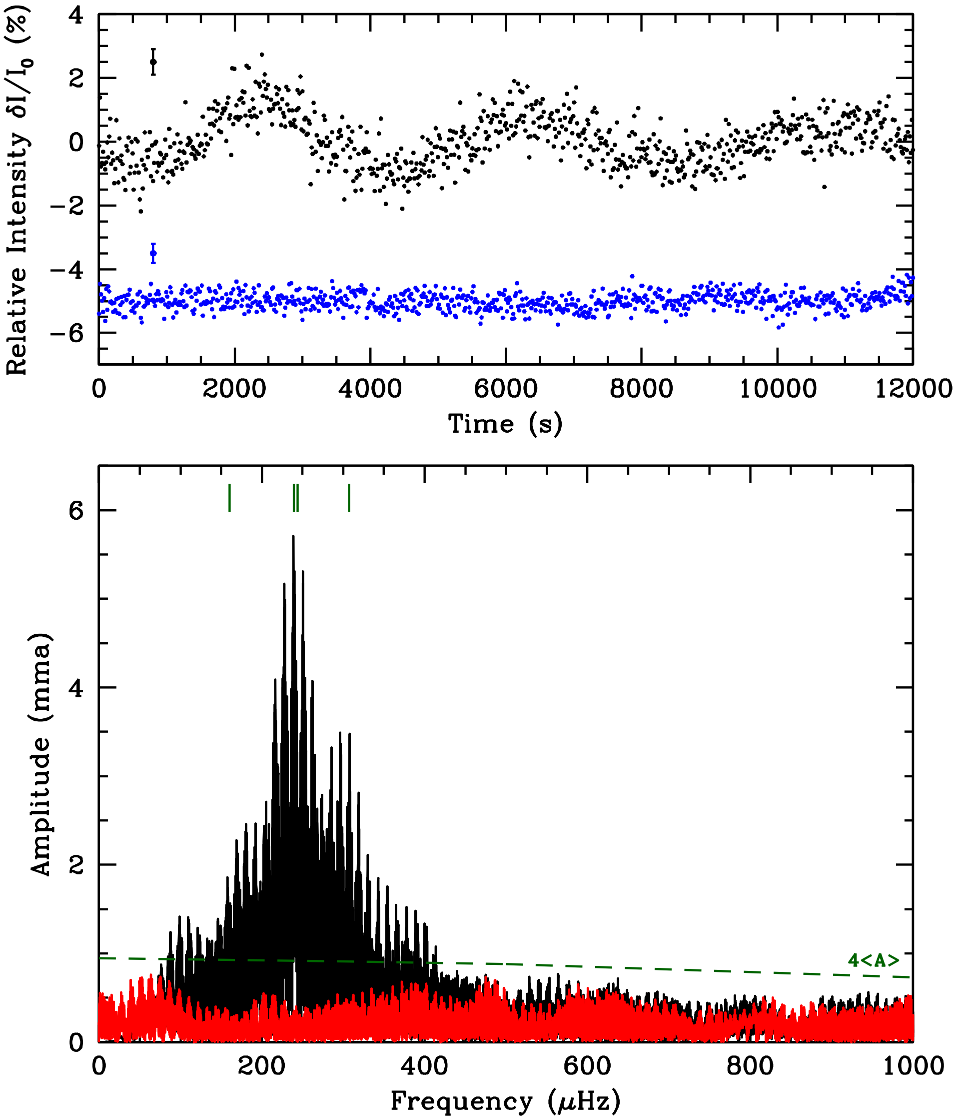

Figure 4.11 The top panel shows high-speed photometry of J2228 from a representative run on 2012 Sep 20. The brightest comparison star is shown in blue, offset by −5%. Average point-by-point photometric errors are also shown. The bottom panel shows a Fourier transform of our entire data set to date, some 25.7 hr of observations from 2011 November to 2012 September. We also display in red the Fourier transform of the residuals after prewhitening by the highest-amplitude periods listed in Table 4.5 and mark those periods with green tick marks at the top of the panel. We mark the 4<A> significance level, described in the text, as a dashed green line.

The top panel of Figure 4.11 shows a portion of a typical light curve for J2228, obtained on 2012 Sep 20, and includes the brightest comparison star in the field over the same run. The bottom panel of this figure shows a Fourier transform (FT) utilizing all 9327 light curve points collected thus far. We display the $4\langle \mathrm{A} \rangle$ significance line at the bottom of Figure 4.11, calculated from the average amplitude of an FT within a 1000 μHz region in steps of 200 μHz, after pre-whitening by the four highest-amplitude periodicities identified in Family 1 of Table 4.5.

We identify these periods by taking an initial Fourier transform of the data. We iteratively pre-whiten by the highest amplitude peak and take a Fourier transform of the residuals, until there are no peaks above 4 times the average amplitude over the initial Fourier transform out to the Nyquist frequency. As before, the cited errors are not formal least-squares errors to the data but rather the product of 10^5 Monte Carlo simulations, and the S/N calculation is performed identically to that in J1614.

Because our coverage is so sparse over nearly 10 months, we have computed two families of frequency solutions in Table 4.5. Family I comes from our entire data set, spanning 2011 November to 2012 September, and is the set of periods that have been pre-whitened to display the red residual Fourier transform in Figure 4.11. Family II uses only our 2012 September data, 16.6 hr of coverage in good conditions over five nights, and has a considerably cleaner spectral window.

There is evidence for a formally significant peak at $10{,}075.1$ s (2.8 hr). However, this periodicity is quite close to the length of a typical run on this object, and may be an artifact from differential transparency variations. We have tested this hypothesis by reducing a star with a similar magnitude to J2228 in the field, SDSS J222901.52+362426.5 ($g = 16.9$); one formally significant peak shows up in the FT of that star at a similarly long period, 8999 s. We have therefore not included the

$10{,}075.1$ s period in J2228 in our frequency solution. There are no other significant periodicities out to 2000 μHz in the FT of this nearby, similarly bright comparison star.

In addition to the multiple long-period modes excited in J2228, we see low-amplitude but significant evidence for variability at 120.411 s (see Figure 4.12, zoomed into more detail in Figure 4.13). As with the other higher-amplitude periodicities in J2228, we have computed the probability these detections are real by computing the False Alarm Probability, using the formalism described in Kepler (1993). We find that all periodicities, including f_5 at 120.411 s, have a FAP $> 99.9\%$. (We note that f_5 is close to the 119.667 s periodic drive error of the 2.1 m Otto Struve telescope. However, we see no evidence at all for a 120.411 s periodicity in the comparison star of comparable magnitude. We have also systematically increased the radius of the aperture used for our light curve extraction, each by 4 pixels from our optimal aperture, and continue to see a significant peak at 120.406 s with S/N$= 4.3$. We therefore consider this periodicity intrinsic to J2228.)

This 120.4 s oscillation is too short to be explained as a g-mode pulsation without invoking implausibly high values of the spherical harmonic degree, $\ell \geq 3$. Neither is it a nonlinear combination frequency of any low-frequency modes observed (Brickhill 1992). Instead, we propose that this variability is caused by acoustic or pressure (p-mode) pulsations driven to observability in J2228.

Two independent groups have recently published low-mass white dwarf models, and each predict both g- and p-mode pulsational instabilities in ELM WDs. For the g-mode pulsations, Córsico et al. (2012b) found that only higher-radial-order $\ell = 1$ ($k \geq 9$) were unstable, and thus they predict $\ell = 1$ pulsation periods $\Pi > 1100$ s. This is consistent with observed distribution of long-period variability in the pulsating ELM white dwarfs discovered so far (Hermes et al. 2012c, 2013d).

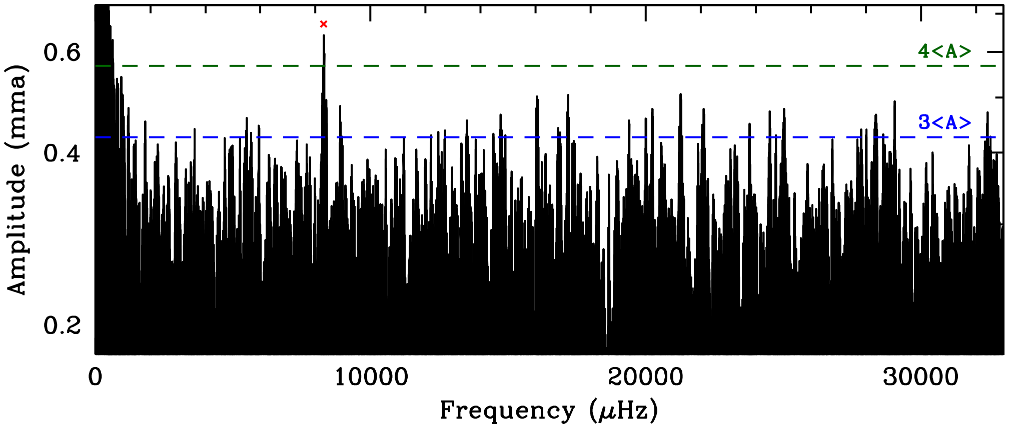

Figure 4.12 A Fourier transform of our entire data set for J2228 out to the Nyquist frequency. The low-frequency region shown in the bottom panel of Figure 4.11 is mostly off-scale, but this figure shows the significant variability marked with a red X around 8305 μHz (120.4 s). We show this region of interest in more detail in Figure 4.13. The dashed blue and green lines show the $3\langle\mathrm{A}\rangle$ and $4\langle\mathrm{A}\rangle$ lines, respectively.

Similarly, Van Grootel et al. (2013) found that only $k \geq 4$ g-modes were unstable in their non-adiabatic models, suggesting mode periods in excess of $\Pi > 500$ s. Thus, the shorter-period optical variability in J1112 is best explained as pressure (p-mode) pulsations.

This is not the first detection of short-period, possible p-mode pulsations in an ELM WD. J1112, a $\log g = 6.36 \pm 0.06$ WD, shows significant evidence for variability at 134.275 s and 107.56 s, at similar amplitudes of 0.44 and 0.38 mma, respectively (Hermes et al. 2013d). J1112 and J2228 are the two lowest surface-gravity pulsating WDs known, which should make them more conducive to exhibit p-mode pulsations at higher amplitudes, since they can allow for a smaller ratio of horizontal to vertical displacement on the surface.

Córsico et al. (2012b) found $\ell = 1, k = 1$ p-modes with periods of roughly 109 s for their 0.17 $M_{\odot}$ models, qualitatively similar to this 120.4 s oscillation, espe-

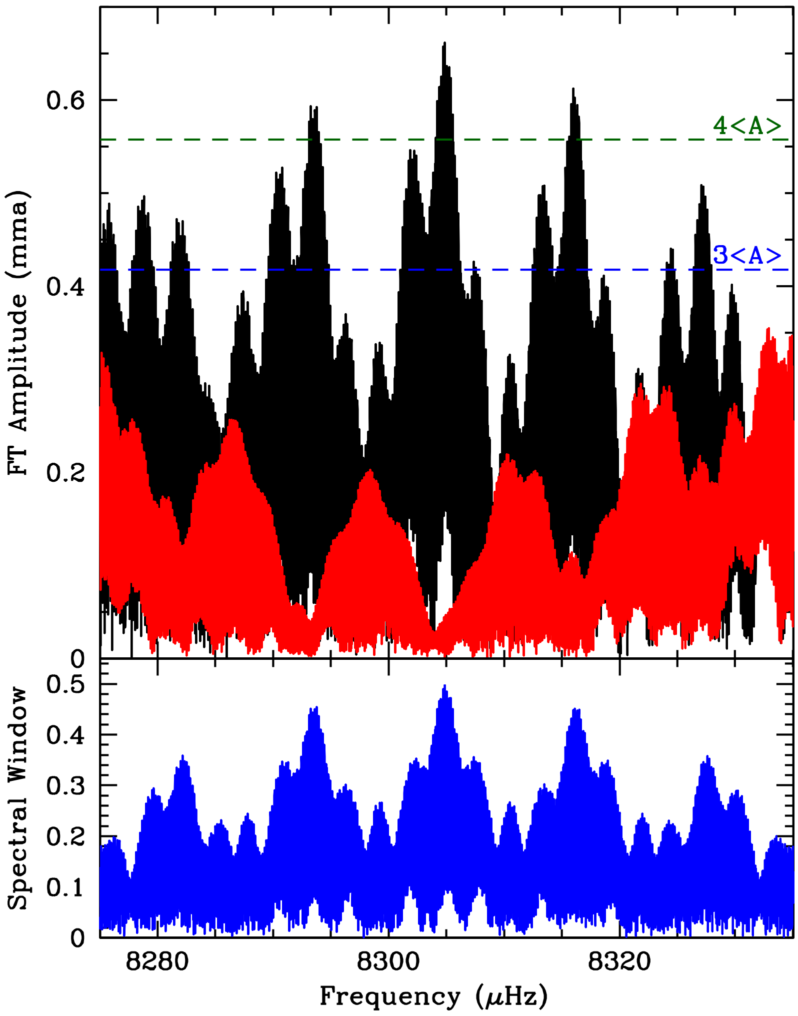

Figure 4.13 A zoom of the high-frequency region in the FT of J2228 that displays evidence for short-period variability, potential p-mode pulsations at 120.4 s. The original FT using all our data is shown in black, and the red shows the residuals after pre-whitening by the highest-amplitude peak. The dashed green and blue lines show the $4\langle \mathrm{A} \rangle$ and $3\langle \mathrm{A} \rangle$ significance lines, respectively. The lower panel shows the spectral window in blue centered around 8304.89 μHz.

Table 4.5. Frequency Solutions for SDSS J2228+3623

ID	Period (s)	Frequency (μHz)	Amplitude (mma)	S/N
		Family I: All Data		
f_1	4181.067 ± 0.005	239.1734 ± 0.0003	6.12 ± 0.13	24.8
f_2	3252.420 ± 0.008	307.4634 ± 0.0008	2.52 ± 0.14	10.5
f_3	6228.90 ± 0.18	160.542 ± 0.005	1.64 ± 0.16	6.6
f_4	4096.851 ± 0.022	244.0899 ± 0.0013	1.35 ± 0.16	6.0
f_5	120.411 ± 0.003	8304.89 ± 0.19	0.67 ± 0.12	4.8
		Family II: Only 2012 Sep Data		
f_1	4178.43 ± 0.85	239.325 ± 0.049	6.47 ± 0.18	23.0
f_2	3253 ± 82	307.4 ± 7.7	2.60 ± 0.43	9.5
f_3	6235 ± 490	160 ± 13	1.87 ± 0.32	6.8
f_4	3901.9 ± 4.5	256.29 ± 0.29	1.20 ± 0.18	4.3
f_5	120.411 ± 0.004	8304.87 ± 0.31	0.69 ± 0.15	3.9

cially considering J2228 likely has lower mass than 0.17 $M_{\odot}$.

4.7 Discussion

4.7.1 Ensemble Properties of Pulsating ELM WDs

We can begin to put the first five pulsating putatively He-core ELM WDs into context with the 150 previously known DAVs with probable CO-cores by comparing some ensemble properties of both. While we have not yet matched the observed periods in these pulsating ELM WDs to full asteroseismic models, we can begin to assess some of their observed properties.

Previous studies of the known DAVs have shown convincingly an observed increase in the periods of excited modes with lower effective temperatures (Mukadam et al. 2006). This is an expected consequence of cooler DAVs having deeper convection zones, which in turn lengthens the thermal timescale, most important for driving mode instabilities. Empirically, Mukadam et al. (2006) showed there was a roughly linear increase in the weighted mean period (WMP) of DAVs with decreasing effective temperature.

This trend holds true with the pulsating ELM WDs, which have significantly cooler temperatures and longer periods than their CO-core brethren. Table 4.6 shows the WMPs of the known He-core DAVs, as well as the range of periods observed, which extends up to 6229 s in J2228, the coolest DAV known to date. The long periods also make sense qualitatively in the context of low-mass WDs, since the period of pulsation modes roughly scales with the dynamical timescale for the whole star, $\Pi \propto \rho^{-1/2}$.

We are extremely interested in finding pulsation periods that are consecutive radial overtones, since the asymptotic period spacings of g-modes are a direct probe of the overall mass of the star. We expect that low-mass pulsating WDs will have relatively high mean period spacings. For the relevant He-core WD models, Córsico et al. (2012b) find that 0.17 $M_{\odot}$ WDs have dipole forward period spacings of roughly 104 s, compared to period spacings of 64 s for a 0.45 $M_{\odot}$ He-core WD. Similarly, Steinfadt et al. (2010a) find an 89 s mean period spacing for a 0.17 $M_{\odot}$ WD.

The rich and relatively simple pulsation spectrum of J1112 offers an excellent opportunity to search for consecutive radial overtones. The two shortest-period g-mode pulsations in this star, at 1884.6 s and 1792.9 s, differ by 91.7 s. If these are $\ell = 1$ modes of consecutive radial order, this would be excellent direct confirmation that this is indeed a roughly 0.17 $M_{\odot}$ He-core WD. However, a full asteroseismic investigation is warranted to confirm that these are indeed consecutive

Table 4.6. Properties of the Five Known Pulsating ELM WDs

Property	Value	Property	Value
SDSS J184037.78+642312.3			
$T_{\rm eff}$	9390 ± 140 K	$\log g$	6.49 ± 0.06
Mass	~0.17 $M_\odot$	g-band	18.8 mag
Periods	$2094 - 4890$ s	WMP	3722 s
$P_{\rm orb}$	4.5912 ± 0.001 hr	M_2	$> 0.64\ M_\odot$
SDSS J111215.82+111745.0			
$T_{\rm eff}$	9590 ± 140 K	$\log g$	6.36 ± 0.06
Mass	~0.17 $M_\odot$	g-band	16.2 mag
Periods	$107.6 - 2855$ s	WMP	2288 s
$P_{\rm orb}$	4.1395 ± 0.0002 hr	M_2	$> 0.14\ M_\odot$
SDSS J151826.68+065813.2			
$T_{\rm eff}$	9900 ± 140 K	$\log g$	6.80 ± 0.05
Mass	~0.23 $M_\odot$	g-band	17.5 mag
Periods	$1335 - 3848$ s	WMP	2404 s
$P_{\rm orb}$	14.624 ± 0.001 hr	M_2	$> 0.61\ M_\odot$
SDSS J161431.28+191219.4			
$T_{\rm eff}$	8800 ± 170 K	$\log g$	6.66 ± 0.14
Mass	~0.20 $M_\odot$	g-band	16.4 mag
Periods	$1184 - 1263$ s	WMP	1235 s
$P_{\rm orb}$	$\cdots$	M_2	$\cdots$
SDSS J222859.93+362359.6			
$T_{\rm eff}$	7870 ± 120 K	$\log g$	6.03 ± 0.08
Mass	~0.16 $M_\odot$	g-band	16.9 mag
Periods	$120.4 - 6229$ s	WMP	4958 s
$P_{\rm orb}$	$\cdots$	M_2	$\cdots$

modes. That hinges on constructing enough He-core WD models with sufficiently different hydrogen layer masses, if these models do indeed produce different hydrogen layer masses for a given overall mass.

Additionally, J1112 (relatively sinusoidal) and J1518 (extremely nonlinear) offer strongly contrasting pulse shapes. It has been suggested that the large nonlinear distortions in the emergent flux are due to the changing depth of the star's convection zone during a pulsation cycle (Brickhill 1992, Wu 2001, Montgomery 2005). If this is the case, the method of Montgomery et al. (2010) could be used on J1518 to infer the thermal response timescale and thereby the average depth of the convection zone in this highly non-sinusoidal DAV. Distortions in the light curve may also be the result of other processes, such as the nonlinear response of the emergent flux to temperature perturbations (Fontaine & Brassard 2008).

These pulsating ELM WDs lie in a new region of the classical ZZ Ceti instability strip, extending the strip to much cooler and lower surface gravity WDs. We have used our new temperature and surface gravity determinations described in Section 4.3.1.1 to characterize our five new ELM WDs. This means we have also updated the atmospheric parameters for J1840, the first pulsating ELM WD discovered. These values can be found in Table 4.6.

4.7.2 The Extended DAV Instability Strip

Aside from their variability, the DAVs discovered to date appear to be otherwise normal WDs, and are therefore believed to be a natural phase in the evolution for all DAs. Although some DAs within the empirical instability strip have been observed not to vary to decent limits (Kepler & Nelan 1993, Mukadam et al. 2004), follow-up observations have shown that some of these stars really do pulsate at low amplitude (Castanheira et al. 2007). Higher-quality optical and UV data have also moved some of these non-variable interlopers out of the instability strip (Bergeron et al. 1995). Thus, it is currently believed that the ZZ Ceti instability strip is pure, such that all DA WDs will at some point pass through it and pulsate (Fontaine et al. 1982, 1985, Bergeron et al. 2004). Much work has been devoted to empirically mapping the ZZ Ceti instability strip, which runs in temperature from roughly $12300-10800$ K for standard $\log g$ = 8.0 WDs (Koester & Holberg 2001, Bergeron et al. 2004, Mukadam et al. 2004, Gianninas et al. 2005, 2006, Mukadam et al. 2006). There is also a dependence on surface gravity, such that WDs with lower surface gravities pulsate at lower effective temperatures. This trend has been observed for WDs with masses from 1.1 $M_{\odot}$ down to 0.5 $M_{\odot}$.

The blue edge of the ZZ Ceti instability strip, where pulsations are turning on, has been successfully estimated by both convective period arguments (Brickhill 1991) and full non-adiabatic calculations (Winget et al. 1982, Brassard & Fontaine 1999, Van Grootel et al. 2012). A slightly more efficient prescription for convection has to be assumed, by increasing the value of the mixing-length theory parameter ML2/α, to make the theory match the observed blue edge, which was most recently mapped empirically by Gianninas et al. (2011).

However, estimating the temperature in which pulsations should shut down has remained a challenge. Modern non-adiabatic calculations do not predict a red edge until around 5600 K (Van Grootel et al. 2012), more than 5000 K cooler than the empirical red edge (Kanaan et al. 2002, Gianninas et al. 2011). Hansen et al. (1985) argue that a surface reflection criterion can be enforced to limit the maximum mode period, which may push a theoretical red edge to hotter temperatures, nearer what is observed (Van Grootel et al. 2013).

Our discovery of pulsating ELM WDs provides an exciting new opportunity to explore the nature of the physics of WD pulsations to much lower masses.

We can compare the five pulsating ELM WDs to the previously known DAVs by placing them in an extended instability strip, shown in Figure 4.14. Doing so, we discover there are at least six ELM WDs that have been observed extensively and do not show significant evidence for variability of at least 1% relative amplitude with temperatures and surface gravities between the newfound ELM DAV J2228 and the other four known pulsating ELM WDs. We have excellent limits on the lack of variability in four of these six, ruling out pulsations to at least 0.3% amplitude.

We have put limits on three of these new non-detections, detailed in Table 4.7. We note that Steinfadt et al. (2012) previously observed PSR 1012+5307, but we have put much more stringent limits on a lack of variability on this faint ELM WD with 7 hr of observations in excellent conditions.

The other three interlopers have been detailed in previous studies. SDSS J0822+2753 is a $T_{\rm eff} = 8880 \pm 60$ K, $\log g = 6.44 \pm 0.11$ WD observed not to vary to 0.2% (Hermes et al. 2012c). SDSS J1443+1509 is a $T_{\rm eff} = 8810 \pm 320$ K, $\log g = 6.32 \pm 0.07$ WD with exquisite limits on lack of variability, to < 0.1% (Hermes et al. 2013d). Finally, NLTT 11748 is the $T_{\rm eff} = 8540 \pm 50$ K, $\log g = 6.20 \pm 0.15$ primary WD in an eclipsing WD+WD binary (Steinfadt et al. 2010b). It was shown by Steinfadt et al. (2012) not to vary out of eclipse to at least 0.5%. We have obtained an additional 8 hr of photometry of NLTT 11748 out of eclipse at McDonald Observatory and can independently rule out variability to at least 0.3%.

The discovery of pulsations in J2228, which is considerably cooler than at least a half-dozen other photometrically constant ELM WDs, questions the purity of the extended ZZ Ceti instability strip for He-core WDs. However, there is no a priori reason to expect the ELM WD instability strip to be pure; evolution through a specific temperature-gravity region is not established for the ELM WDs, and they

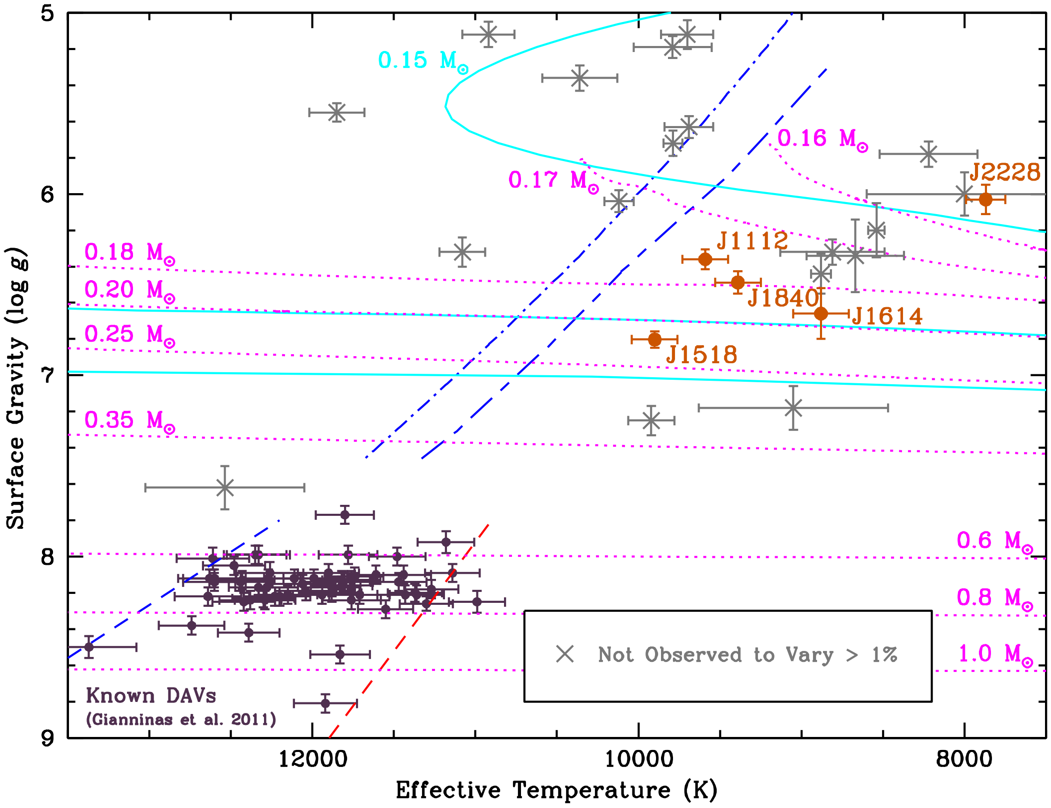

Figure 4.14 The extended ZZ Ceti instability strip. We show 56 CO-core DAVs characterized in a consistent way by Gianninas et al. (2011) as purple dots, and mark the five known pulsating ELM WDs in burnt orange. We denote an extrapolated theoretical blue edge for the low-mass ZZ Ceti instability strip; this dashed-dotted blue line is described in the text. We also include as a big-dashed-little-dashed blue line the theoretical blue edge for low-mass DAVs from Van Grootel et al. (2013). We mark the empirical blue- and red-edges for CO-core DAVs from Gianninas et al. (2011) as dashed blue and red lines, respectively. Objects not observed to vary to at least greater than 10 mma (1%) are marked with an X. We include three new WDs not observed to vary, listed in Table 4.7; the others were detailed in Steinfadt et al. (2012), Hermes et al. (2012c, 2013d), Antoniadis et al. (2013). Cooling models for different WD masses are included as dotted and solid lines, and described in the text.

may not all cool through the instability strip in as simple a manner as the CO-core DAVs.

To illustrate this, we have plotted the evolution of several different WD masses through the effective temperatures and surface gravities in Figure 4.14. We plot the 0.16 $M_{\odot}$, 0.17 $M_{\odot}$, 0.18 $M_{\odot}$, 0.20 $M_{\odot}$, 0.25 $M_{\odot}$, and 0.35 $M_{\odot}$ He-core models of Panei et al. (2007) as dotted magenta lines. We have also used the stellar evolution code MESA (Paxton et al. 2011, 2013) to model the evolution of 0.15 $M_{\odot}$, 0.20 $M_{\odot}$, and 0.25 $M_{\odot}$ He-core WDs, shown as solid cyan lines in Figure 4.14. For reference, we have also included 0.6 $M_{\odot}$, 0.8 $M_{\odot}$, and 1.0 $M_{\odot}$ C/O-core cooling tracks (Holberg & Bergeron 2006, Kowalski & Saumon 2006, Tremblay et al. 2011).

Where the lowest-mass WD models enter this diagram depends on how we artificially remove mass from the models, and there is a very noticeable discrepancy between the 0.16 $M_{\odot}$ Panei et al. (2007) WD models and our 0.15 $M_{\odot}$ WD models using MESA. As an added complication, except for the lowest-mass ELM WDs (below roughly 0.18 $M_{\odot}$), recurrent hydrogen shell flashes cause the ELM WD to loop many times through this diagram, further confusing the picture (e.g., Panei et al. 2007, Steinfadt et al. 2010a).

It is therefore not entirely surprising to find non-variable ELM WDs between J2228 and the four warmer pulsating ELM WDs. Further empirical exploration of the entire ELM WD instability strip offers a unique opportunity to constrain the binary and stellar ELM WD models, especially the regimes in which late thermal pulses occur in thick hydrogen layers for ELM WDs.

In contrast to the confusion along the red edge, the theoretical and empirical blue edge is relatively more straightforward. Following Brickhill (1991) and Goldreich & Wu (1999), we use the criterion that $P_{\rm max} \sim 2\pi\tau_{\rm C}$ for the longest period mode that is excited, where $P_{\rm max}$ is the mode period and the timescale $\tau_{\rm C}$ describes the heat capacity of the convection zone as a function of the local photospheric flux, which we compute from a grid of models[2]. Using the traditional value of $P_{\rm max} = 100\,{\rm s}$, we find that the convection parameters ML2/$\alpha = 1.5$ provide a good match to the blue edge for the normal-mass DAVs, but that extrapolating this relation to the pulsating ELM WDs yields a blue edge which is somewhat hotter than the observations (see the dotted blue line in Figure 4.14). The models of Córsico et al. (2012b) find that only g-mode periods greater than ~1000 s are excited, but using this criterion only moves the blue edge a small amount closer to the location of the observed pulsators (about 130 K for a given surface gravity). It is possible there are additional mechanisms at work that move the blue edge to cooler temperatures. Using a less efficient prescription for convection, such as ML2/$\alpha = 1.0$, will shift the blue edge to cooler temperatures, as seen in Van Grootel et al. 2013, whose blue edge we include in Figure 4.14. We are also still dominated by small number statistics, and perhaps we have simply not yet found any hotter pulsating low-mass WDs. It remains difficult to predict a theoretical red edge for even the classical C/O-core DAVs, so we have not extended it to low-mass WDs, and instead provide a portion of the red-edge established by Gianninas et al. (2011).

We now include in Figure 4.14 the newly discovered WD companion to a massive pulsar PSR 0348+0432, which has $T_{\rm eff}$ = 10,120 ± 90 K and $\log g = 6.04 \pm 0.06$, putting it very close to our theoretical blue edge. This ELM WD is photometrically constant in the g-band to a limit of roughly 7 mmag (Antoniadis et al. 2013).

We continue to search for new pulsating ELM WDs, but there is also utility in constraining the regions of parameter space where WDs are not observed

---

[2] Note that $\tau_{\rm C} \approx 4\tau_{\rm th}$, where $\tau_{\rm th}$ is the thermal timescale at the base of the convection zone. The average value of τ_C is often denoted as τ_0.

Table 4.7. Observed Low-Mass DAV Candidates and Null Results

Object	g-SDSS (mag)	$T_{\rm eff}$ (K)	$\log g$ (cm s^{-1})	Reference	Det. Limit %
SDSS J012549.37+461920.1	15.8	9050 ± 580	7.18 ± 0.12	Brown et al. (2012)	0.3
SDSS J011210.25+183503.74	17.3	9690 ± 150	5.63 ± 0.06	Brown et al. (2012)	0.1
SDSS J070216.21+111009.0	16.1	8800 ± 600	6.00 ± 0.12	Brown et al. (2012)	0.3
SDSS J082212.57+275307.4	18.3	8880 ± 60	6.44 ± 0.11	Kilic et al. (2010)	0.2
SDSS J090052.04+023413.8	18.0	8220 ± 300	5.78 ± 0.07	Brown et al. (2012)	0.4
SDSS J091709.55+463821.8	18.7	11850 ± 170	5.55 ± 0.05	Kilic et al. (2007)	0.3
PSR J101233.42+530702.8	19.6	8670 ± 300	6.34 ± 0.20	Callanan et al. (1998)	0.7
SDSS J122822.84+542752.92	19.6	9921 ± 143	7.25 ± 0.08	Eisenstein et al. (2006)	0.7
SDSS J123316.20+160204.6	19.8	10920 ± 160	5.12 ± 0.07	Brown et al. (2010)	0.9
SDSS J144342.74+150938.6	18.6	8810 ± 320	6.32 ± 0.07	Brown et al. (2012)	0.1
SDSS J174140.49+652638.7	18.4	9790 ± 240	5.19 ± 0.06	Brown et al. (2012)	0.3
SDSS J210308.80-002748.89	18.5	9788 ± 59	5.72 ± 0.07	Kilic et al. (2012)	0.2
SDSS J211921.96-001825.8	20.0	10360 ± 230	5.36 ± 0.07	Brown et al. (2010)	0.6
SDSS J221928.48+120418.6	17.7	9700 ± 160	5.12 ± 0.08	Brown et al. (2012)	0.3

to vary. We have put limits on the lack of variability in 14 ELM WDs, detailed in Table 4.7. Our limits on SDSS J144342.74+150938.6 are particularly stringent since we observed its field for more than 7.2 hr; one of the comparison stars we used, SDSS J144347.31+150841.9, turned out to be variable, most likely a δ-Scuti star, dominated by a 3.46-hr pulsation period. We construct an updated empirical instability strip using the three new pulsators and more than a dozen low-mass WDs not observed to vary, shown in Figure 4.14.

4.7.3 Acoustic (p-mode) Pulsations in WDs

As with the C/O-core DAVs that have been known for more than 40 years, the dominant optical variability in these ELM WDs is consistent with surface temperature variations caused by non-radial g-mode pulsations driven to observability by a hydrogen partial ionization zone. However, in J1112 and J2228, we also see the first evidence for short-period p-mode pulsations in a WD. These p-modes offer a tantalizing opportunity to probe the interior of an ELM WD in a complimentary way to the g-modes also present.

Pulsation calculations have long shown that WDs of all masses should be unstable to p-mode pulsations (e.g. Saio et al. 1983, Starrfield et al. 1983, Hansen et al. 1985). However, despite exhaustive searches (e.g. Robinson 1984, Kawaler et al. 1994, Silvotti et al. 2011), no such high-frequency modes have ever been observed in a WD. Discovery of p-mode pulsations in ELM WDs could suggest that these pulsation models are indeed valid, but that the amplitudes of these oscillations are simply too small to detect with significance in the more massive DAVs. This is likely due to the fact that the ratio of vertical to horizontal displacement in a typical 0.6 $M_{\odot}$ CO-core white dwarf is about one part in 1,000, which suggests the p-mode amplitudes should be orders of magnitude smaller than g-mode amplitudes in normal DAVs. The ELM WDs have up to 1000 times lower surface gravities, and thus this ratio is significantly reduced.

In the context of hot B subdwarf stars (sdBs), it is not entirely surprising to find ELM WDs with observable p-mode pulsations. Variable hot B subdwarf stars (sdBVs), especially of the EC 14026 or V361 Hya class, are observed to vary with p-mode pulsations (e.g. Kilkenny et al. 1997, Charpinet et al. 1997). These sdBVs are qualitatively quite similar to ELM WDs, with He-cores and similar surface gravities, $5.2 < \log g < 6.1$, although they are typically much hotter, with $T_{\mathrm{eff}} >$ 28,000 K, and more massive, with canonical masses ~0.45 $M_{\odot}$. Their pulsation periods are most often in the range $120 - 300$ s (Kilkenny 2007), quite similar to the variability in J1112. Many sdBVs are hybrid pulsators, showing both p- and g-mode pulsations.

The presence of hybrid g- and p-mode pulsations in ELM WDs offers an opportunity to probe these He-core WDs in fundamentally different ways, since the p-modes likely have low radial order and propagate in a different region of the star than g-modes. Additional p-mode pulsations will also more accurately constrain future asteroseismic fits to these pulsating WDs.

Still, we must be careful to rule out all other possibilities before declaring the short-period instabilities in J1112 as bona-fide p-modes. The low-order p-modes calculated by Córsico et al. (2012b) range from $109 - 7.5$ s for their $1 < k < 29$ models of a 0.17 $M_{\odot}$ He-core WD, slightly shorter than the 134.3 s periodicity in J1112. However, since that work finds that g-modes with periods shorter than 1100 s are stable to pulsations, p-mode pulsations remain the most likely explanation for the short-period variability in J1112. (It also remains possible that the 134.3 s periodicity is a radial fundamental mode for the star.)

4.7.4 Conclusions

We have discovered the first five pulsating ELM WDs, which are both the coolest and lowest-mass WDs known to pulsate. These objects offer, for the first time, an opportunity to explore the interior of a putative He-core WD using asteroseismology.

Asteroseismology of ELM WDs will help constrain the thickness of the surface hydrogen layers in these low-mass WDs. There are several millisecond pulsars with ELM WD companions, and the cooling ages of such companions can be used to calibrate the spin-down ages of these pulsars. However, current evolutionary models for ELM WDs are relatively unconstrained. For masses $M > 0.18$ $M_{\odot}$, diffusion-induced hydrogen-shell flashes take place, which yield small hydrogen envelopes (Althaus et al. 2001, Panei et al. 2007, Kilic et al. 2010). The models with $M \leq 0.17$ $M_{\odot}$ do not experience thermonuclear flashes. As a result, they have massive hydrogen envelopes, larger radii, lower surface gravities, and they are predicted to evolve much more slowly compared to more massive WDs. If enough modes are excited to observability, we hope to directly constrain the hydrogen layer mass.

A plethora of excited modes would also allow for measuring the mean period spacing, which is a sensitive function of the mass of the star, and is also slightly dependent on the core mass fraction. The models of Steinfadt et al. (2010a) found a mean period spacing of ~ 89 s for $\ell = 1$ g-modes of a 0.17 $M_{\odot}$ ELM WD, about a factor of two larger than the observed 47 ± 12 s period spacing for $\ell = 1$ g-modes in the cool C/O-core counterpart G29-38 (Kleinman et al. 1998).

We do expect these non-radial pulsators to be multi-periodic even if just one pulsation mode and its non-linear harmonics are amplified to observability: three of them are in relatively close binaries with an unseen companion. This companion will influence the light curve in many ways (see Chapter 2). The companion may induce a relatively low-amplitude Doppler beaming signal at the orbital period given the primary's effective temperature and the radial-velocity amplitude (Shporer et al. 2010). The companion may also induce tidal distortions on the primary, depending on the radius of the ELM WD, as seen in many other ELM WDs (Kilic et al. 2011c, Brown et al. 2011c, Hermes et al. 2012c).

The companion's effect on the rotation period is perhaps more significant. For example, the ~ 1.7 Gyr cooling age of J1840 (Panei et al. 2007) may be longer than the synchronization timescale for such a short-period, 4.6-hr binary (e.g., Claret et al. 1995). If so, and the ELM WD is rotating at the orbital period of 4.6 hr, then non-radial pulsations will be subsequently subject to rotational splittings determined by their modal degree. For example, if the 225 μHz mode is an $\ell = 1$ mode, a 4.6 hr rotation rate would cause it to be split by about 30 μHz, assuming solid-body rotation (Unno et al. 1989). However, synchronization is not a guarantee: Recent *Kepler* observations of a close sdB+dM binary found the primary rotating much slower than the ~ 9.5 hr orbital period (Pablo et al. 2012). An analysis of the rotational splittings in the pulsations of J1840 will test tidal synchronization in this system, thereby probing the rigidness of this ELM WD.

We also hope to use the nonlinearities in the light curve of two of these ELM WDs, J1840 and J1518, to constrain the size of the convection zone of this WD (e.g., Montgomery 2005, Montgomery et al. 2010). Since ELM WDs exist in a completely new regime of parameter space than do typical C/O core WDs, this analysis will provide important independent constraints on the structure of their outer layers, as well as providing a measure of the convective efficiency in this new regime.

We note, finally, that the driving mechanism for pulsations is not completely settled for these objects. It is natural to assume that the same mechanism of convective driving that operates in the C/O-core DAVs (Brickhill 1991, Wu 1998, Goldreich & Wu 1999) is also responsible for the pulsations of low-mass WDs. This mechanism is based on the assumption that the convective turnover timescale for a fluid element, $t_{\rm to}$, is much smaller than the oscillation periods, Π_i. For the $\log g \sim 8$ DAVs, $t_{\rm to} \sim 0.1$–1 sec and $\Pi_i \sim 100$–1000 sec, so $t_{\rm to} \ll \Pi_i$ is satisfied.

To estimate how this timescale scales with g we note that $t_{\rm to} \sim l/v$, where l is the mixing length and v is the velocity of the convective fluid elements. Employing a simplified version of mixing length theory (ignoring radiative losses) we find that $v \propto (gF/\rho)^{1/3}$, where F is the stellar flux and ρ is the mass density at the base of the star's surface convection zone (Mihalas 1978). Taking the mixing length as a factor of order one times a pressure scale height, we find $l \sim c_s^2/g \propto T/g$. Putting these results together we find $t_{\rm to} \propto T(\rho/F)^{1/3} g^{-4/3} \sim g^{-4/3}$. Thus, a $\log g \sim 6$ object would have $t_{\rm to} \sim$ 50–500 sec. In order for convective driving to operate, $\Pi_i \gg t_{\rm to}$ is required. Perhaps this is at least a partial explanation for the very long period (> 4000 s) seen in this pulsator. It may also set a lower limit to periods in this DAV of ~ 500–1000 s, although more detailed models will be needed to confirm this. Another potential source of driving is the ϵ mechanism, i.e., driving due to the modulation of H burning in the envelope. However, the timescale for such a mechanism is probably too short to explain the observed photometric variability (Van Grootel et al. 2013).

We hope that a multi-site, globally coordinated Whole Earth Telescope run on J1518 (e.g. Nather et al. 1990), carried out in 2013 April and May but too late for inclusion in this dissertation, will shed considerable light on these pulsating ELM WDs.

Table 4.8. Journal of photometric observations.

Run	UT Date	Length (hr)	Seeing ($''$)	Exp. (s)
	SDSS J1840+6423			
A2490	2011 Oct 25	3.4	1.6	15
A2494	2011 Oct 26	0.9	1.4	15
A2498	2011 Oct 27	1.4	1.6	15
A2643	2012 Apr 14	0.7	2.0	15
A2654	2012 Apr 18	3.1	1.8	15
A2657	2012 Apr 19	3.0	1.8	15
A2683	2012 Jun 17	4.4	1.6	15
A2685	2012 Jun 18	5.0	1.7	15
A2687	2012 Jun 19	4.3	2.1	15
A2696	2012 Jun 23	3.6	1.9	15
A2704	2012 Jul 12	0.7	1.1	15
A2706	2012 Jul 13	2.5	1.4	15
	Overall	33.0	1.7	
	SDSS J1112+1117			
A2568	2012 Jan 21	1.9	3.3	5
A2571	2012 Jan 22	1.3	2.2	10
A2574	2012 Jan 23	0.8	2.0	5
A2577	2012 Jan 24	2.2	1.3	10
A2578	2012 Jan 25	2.5	3.4	10
A2581	2012 Jan 27	6.5	3.0	5
A2586	2012 Jan 29	2.6	1.7	5
A2588	2012 Jan 30	3.2	2.0	5
A2590	2012 Jan 31	3.0	1.2	5
A2594	2012 Feb 1	3.5	2.1	5
A2597	2012 Feb 2	2.6	1.9	10
A2600	2012 Feb 3	2.8	1.5	5
A2605	2012 Feb 15	3.9	1.6	10
A2607	2012 Feb 16	2.4	1.8	10
A2611	2012 Feb 19	5.0	2.1	10
A2614	2012 Feb 20	2.9	1.8	10
A2616	2012 Mar 12	2.4	2.4	5
A2618	2012 Mar 13	2.9	1.4	10
A2621	2012 Mar 14	3.6	1.4	10
A2638	2012 Mar 17	3.1	2.5	10
A2641	2012 Apr 14	1.9	3.3	5
A2656	2012 Apr 19	3.7	2.0	5
A2659	2012 Apr 20	2.2	1.5	5
A2662	2012 Apr 21	1.7	1.3	5
A2675	2012 Apr 24	1.7	1.1	5
	Overall	70.2	2.0	

Table 4.8—Continued

Run	UT Date	Length (hr)	Seeing ($''$)	Exp. (s)
	SDSS J1518+0658			
A2626	2012 Mar 15	0.7	3.3	5
A2634	2012 Mar 16	2.2	2.2	10
A2639	2012 Mar 17	3.4	3.4	10
A2647	2012 Apr 16	4.9	1.7	5
A2650	2012 Apr 17	1.7	2.0	5
A2660	2012 Apr 20	1.7	1.2	5
A2664	2012 Apr 21	3.9	1.9	10
A2673	2012 Apr 23	0.7	1.5	5
A2676	2012 Apr 24	0.4	1.6	10
A2684	2012 Jun 18	2.7	2.1	10
A2686	2012 Jun 19	2.9	1.8	10
A2688	2012 Jun 20	2.3	2.4	5
A2705	2012 Jul 13	3.1	1.3	5
	Overall	32.2	2.0	
	SDSS J1614+1912			
A2690	2012 Jun 21	2.6	1.7	5
A2692	2012 Jun 22	2.0	1.8	5
A2695	2012 Jun 23	3.7	1.2	5
A2697	2012 Jun 24	3.5	1.4	5
A2699	2012 Jun 25	3.6	1.3	5
	Overall	15.4	1.5	
	SDSS J2228+3623			
A2521	2011 Nov 28	3.5	1.5	10
A2524	2011 Nov 29	1.6	2.5	10
A2528	2011 Nov 30	1.9	2.2	10
A2707	2012 Jul 13	2.3	1.1	5
A2710	2012 Sep 17	2.8	2.4	10
A2719	2012 Sep 20	6.4	1.6	15
A2721	2012 Sep 21	7.4	1.4	10
	Overall	25.9	1.8	

Chapter 5

Discovery of an Ultramassive Pulsating White Dwarf

We announce the discovery of the most massive pulsating DA (hydrogen-atmosphere) white dwarf (WD) ever discovered, GD 518. Model atmosphere fits to the optical spectrum of this star show it is a $12{,}030 \pm 210$ K WD with a $\log g$ $= 9.08 \pm 0.06$, which corresponds to a mass of 1.20 ± 0.03 $M_{\odot}$. Stellar evolution models indicate that the progenitor of such a high-mass WD endured a stable carbon-burning phase, producing an oxygen-neon-core WD. The discovery of pulsations in GD 518 thus offers the first opportunity to probe the interior of a WD with a possible oxygen-neon core. Such a massive WD should also be significantly crystallized at this temperature. The star exhibits multi-periodic luminosity variations at timescales ranging from roughly $425 - 595$ s and amplitudes up to 0.7%, consistent in period and amplitude with the observed variability of typical ZZ Ceti stars, which exhibit non-radial g-mode pulsations driven by a hydrogen partial ionization zone. Successfully unraveling both the total mass and core composition of GD 518 provides a unique opportunity to investigate intermediate-mass stellar evolution, and can possibly place an upper limit to the mass of a carbon-oxygen-core WD, which in turn constrains SNe Ia progenitor systems.[1]

---

[1] *Significant portions of this chapter have been previously published as:* J. J. Hermes, S. O. Kepler, Barbara G. Castanheira, A. Gianninas, D. E. Winget, M. H. Montgomery, Warren R. Brown, and Samuel T. Harrold, *The Astrophysical Journal*, **771**, L2 (2013)

5.1 Introduction

White dwarf (WD) stars are stellar remnants composed almost entirely of the inert byproducts of previous nuclear reactions; they are the burnt-out cores of stars with initial masses below about $8.0 \pm 1.5\ M_\odot$ (Smartt et al. 2009, Williams et al. 2009).

The majority of WDs have an overall mass near $\sim$0.6 $M_\odot$ (Falcon et al. 2010, Tremblay et al. 2011, Kleinman et al. 2013). WDs near this canonical mass are expected to harbor remnant carbon-oxygen (CO) cores after core hydrogen burning and subsequent helium burning. However, an isolated progenitor star with an initial mass larger than about 7 $M_\odot$ will reach sufficiently high temperature to achieve stable carbon burning, and may possibly end up as an ultramassive WD with an oxygen-neon (ONe) or oxygen-neon-magnesium (ONeMg) core, if the progenitor had insufficient conditions to start further nuclear burning and detonate as a Type II supernova (Nomoto 1984).

Garcia-Berro et al. (1997) found that a 9 $M_\odot$ progenitor model undergoes repeated carbon-burning shell flashes when its core exceeds $\sim$1.05 $M_\odot$, ultimately ending up as a WD with an ONe core, although rotation may also play a role in the outcome of an intermediate-mass progenitor (Dominguez et al. 1996). We note that there are other possible formation channels for ultramassive WDs, most importantly binary evolution, specifically the merger of double-degenerate systems (Segretain et al. 1997, Marsh et al. 1997, Liebert et al. 2005, García-Berro et al. 2012).

A handful of ultramassive WDs ($\geq 1.2\ M_\odot$) have been found in nature. Vennes & Kawka (2008) have reviewed the evidence for ultramassive WDs and find much of it compelling. However, since we cannot see below the photosphere of these WDs, our understanding of their interiors is essentially superficial.

Direct evidence that ultramassive WDs harbor ONe cores comes from heavy isotope anomalies found in classical novae, which match predicted abundances from explosive nucleosynthesis on massive WDs with ONeMg cores (Gehrz et al. 1998). Additionally, two oxygen-rich WDs were recently discovered in the Sloan Digital Sky Survey (Gänsicke et al. 2010). These WDs are likely exposed ONe cores, as the observed O/C abundance ratio indicates a very low overall carbon mass fraction, a prediction for some of the most massive progenitors avoiding core collapse (Iben et al. 1997).

A more direct test of ultramassive WD core composition would be to find a massive WD undergoing pulsations. Asteroseismology offers the unique opportunity to use these pulsations to probe below the photosphere and into the interior of stars, and has had numerous successful applications with WDs (see reviews by Winget & Kepler 2008, Fontaine & Brassard 2008, Althaus et al. 2010). We have thus engaged in a search for pulsations in massive WDs in or near the DAV (or ZZ Ceti) instability strip, a region for which WDs with hydrogen-dominated atmospheres have the appropriate temperature to develop a hydrogen partial ionization zone, which in turn drives global pulsations. That search has already yielded multiple new massive DAVs (Kepler et al. 2012, Castanheira et al. 2013) after the 1.1 $M_{\odot}$ BPM 37093 discovered by Kanaan et al. (1992).

Here we report a new success in that search: The discovery of the most massive pulsating WD known, GD 518. Model fits to the optical spectrum first reported by Gianninas et al. (2011) show this is a $T_{\mathrm{eff}} = 12{,}030 \pm 210$ K WD with $\log g = 9.08 \pm 0.06$, which would correspond to a mass of 1.20 ± 0.03 $M_{\odot}$ using the ONe WD models of Althaus et al. (2005) or a mass of 1.23 ± 0.02 $M_{\odot}$ using the CO WD models of Wood (1995).

In this paper we present our discovery of pulsations in GD 518. In Sections 5.2 and 5.3 we outline our observations and analysis. We conclude with a discussion of the impact of this finding in Section 5.4.

5.2 Observations

We targeted GD 518 (WD J165915.11+661033.3) as a candidate ultramassive pulsating white dwarf based on model atmosphere fits to its optical spectrum. The object was first classified in Gianninas et al. (2011). Evolutionary models by Althaus et al. (2007) suggest that such a WD has a cooling age of roughly 1.7 Gyr and an absolute V-band magnitude of 13.6 mag, which indicates that GD 518 (g=17.2 mag) is roughly 53 pc from Earth.

We display the optical spectrum analyzed by Gianninas et al. (2011) in Figure 5.1. The spectrum was obtained in 2009 March using the 2.3 m telescope at Steward Observatory, equipped with the Boller & Chivens spectrograph at a resolution of ∼6 Å FWHM, covering a wavelength range from roughly $3700 - 5200$ Å. A more detailed explanation of the observations, models, and fitting can be found in Sections $2 - 4$ of Gianninas et al. (2011).

We obtained additional spectroscopy from the FLWO 1.5 m telescope in 2013 April using the FAST spectrograph (Fabricant et al. 1998). These observations, four 20-min exposures at a resolution of 1.7 Å FWHM, cover a wavelength range from $3600-5500$ Å. Using the same models and fitting method as in Gianninas et al. (2011), we confirm that this WD has a very high surface gravity. Although this new summed spectrum is much lower signal-to-noise (S/N∼15), our fits formally yield $T_{\rm eff} = 12{,}100 \pm 370$ K and $\log g = 9.00 \pm 0.09$, which agree with the previous determination within the stated uncertainties. We thus adopt the primary parameters derived from the higher quality (S/N∼55) spectrum analyzed in Gianninas et al. (2011), displayed in Figure 5.1.

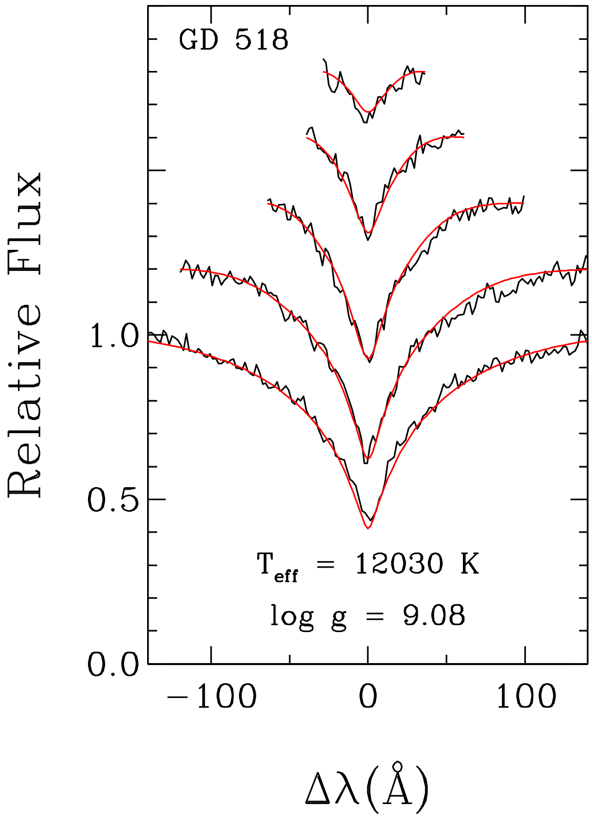

Figure 5.1 The individual Balmer line profiles (black) of GD 518. The lines range from Hβ (bottom) to H8 (top), each offset by a factor of 0.2 in relative flux. The model fits (red), first reported by Gianninas et al. (2011), derive the atmosphere parameters and show this is a high-surface-gravity WD, with $\log g = 9.08 \pm 0.06$. This corresponds to a mass of $1.20 \pm 0.03\ M_{\odot}$.

A $12{,}030$ K temperature puts GD 518 inside an extrapolated empirical instability strip for DAVs of high mass (Castanheira et al. 2013). In fact, Gianninas et al. (2011) noted that GD 518 was a "most intriguing" candidate to target for possible pulsations.

We obtained time-series photometric observations of GD 518 at the McDonald Observatory over nine nights in 2013 March, eight of them consecutive, and five nights in 2013 April, for a total of more than 42.9 hr of coverage over 33 nights. A full journal of observations can be found in Table 5.1. We used the Argos instrument, a frame-transfer CCD mounted at the prime focus of the 2.1m Otto Struve telescope (Nather & Mukadam 2004), to obtain $5 - 10$ s exposures on this $g = 17.2$ mag WD. The seeing averaged 2.0″ and conditions were generally fair. Observations were obtained through a 3mm BG40 filter to reduce sky noise.

The raw science frames were calibrated by dark subtraction and flat-fielding. We performed weighted aperture photometry on the calibrated frames using the external IRAF package *ccd_hsp* written by Antonio Kanaan (the reduction method is outlined in Kanaan et al. 2002). We divided the sky-subtracted light curves by the sum of the three nearest brighter comparison stars in the field to correct for transparency variations, and applied a timing correction to each observation to account for the motion of the Earth around the barycenter of the solar system (Stumpff 1980, Thompson & Mullally 2009).

The top panel of Figure 5.2 shows the light curve of GD 518 from 2013 March 16. A two-frequency solution to this 3.0-hr run finds variability at 441.36 ± 0.66 s (6.5 ± 0.4 mma[1]) and 514.1 ± 2.4 s (2.5 ± 0.4 mma).

The bottom panel of Figure 5.2 shows a Fourier transform (FT) for our entire

---

[1] 1 mma = 0.1% relative amplitude

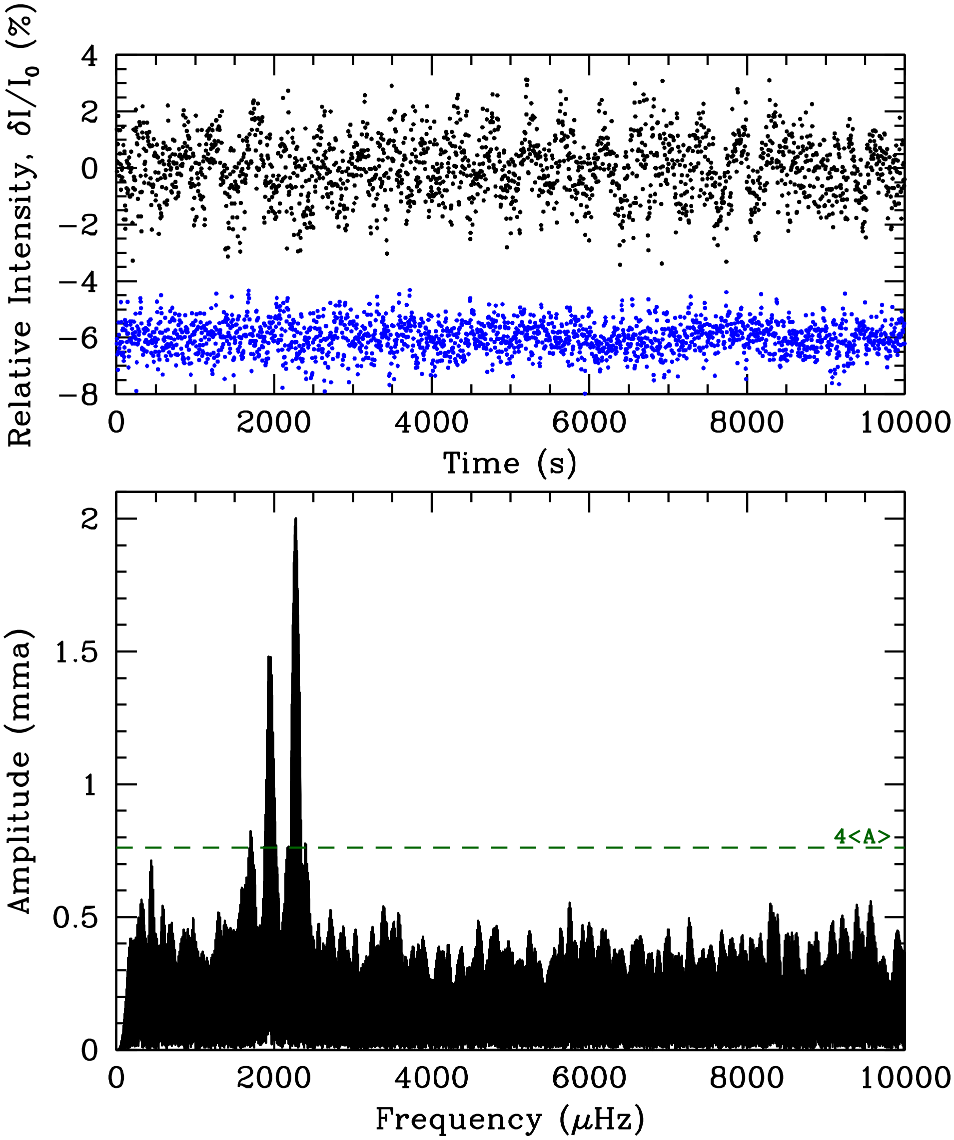

Figure 5.2 The top panel shows high-speed photometry of GD 518, this a portion from 2013 March 16. The brightest comparison star is shown in blue, offset by −6%. For both we have co-added the data by two points, slightly smoothing the light curve. The bottom panel shows a Fourier transform of our entire data set to date, some 29,985 points taken during more than 42.9 hr of observations in 2013 March and 2013 April. We mark the $4\langle A\rangle$ reference, described in the text, as a dashed green line.

data set, some $29{,}985$ points from more than 42.9 hr of observations in 2013 March and 2013 April. We display the $4\langle\mathrm{A}\rangle$ reference line, calculated from the average amplitude, $\langle\mathrm{A}\rangle$, of the FT of the entire dataset from 0 to $10{,}000$ μHz.

5.3 Light Curve Analysis

The optical light curve of GD 518 shows low-amplitude but statistically significant variability at multiple periods, ranging from roughly $425-595$ s, with amplitudes that can reach up to 0.7% over a single night of observations. This can be seen by eye in the top panel of Figure 5.2, as well as in the FT of our entire data set in the bottom panel of that same figure.

We have attempted to identify the periodicities present in the star, which will form the basis for future asteroseismic modeling. Complicating our analysis, however, is the fact that the amplitudes (and perhaps frequencies) of the observed variability are not consistent from night-to-night. In fact, the FT for a few nights had no significant peaks above 1.5 mma. We have included the period (P_+) and amplitude (A_+) of the highest peaks for each night in Table 5.1.

There is thus some strong frequency and/or amplitude modulation occurring in GD 518 acting on the timescale of days, perhaps caused by beating of closely spaced periodicities or perhaps due to a physical mechanism in the star. We have therefore broken up the data into different subsets of minimum length allowed by the frequency splitting in the overall frequency solution: the first five nights (10 Mar 2013 – 14 Mar 2013), the second five nights (15 Mar 2013 – 19 Mar 2013), and the final nine nights (4 Apr 2013 – 12 Apr 2013).

We present a frequency solution for each subset in Table 5.2. It was determined by computing an FT, then a nonlinear least-squares fit on the frequency with the highest amplitude, then prewhitening by that frequency until there are no peaks above a $4\langle\mathrm{A}\rangle$ significance line, which came from the average amplitude of an FT from 0 to $10{,}000$ μHz of the unprewhitened data. We have included the 508 s periodicity in the solution for our first subset even though it is not above $4\langle\mathrm{A}\rangle$, based on its presence in other subsets. For more realistic estimates, the quoted uncertainties in Table 5.2 are not formal least-squares uncertainties to the data but rather the product of 1000 Monte Carlo simulations of perturbed data using the software package Period04 (Lenz & Breger 2005).

We calculate the chance these detections are real by computing the False Alarm Probability (FAP) using the formalism described in Kepler (1993). We find that all periodicities in each subset have a FAP $> 99.9\%$ except for f_2 in the first subset, which has a FAP of 91.0%.

Computing a full frequency solution for our entire dataset, using the same method as we have for each subset, yields 12 formally significant frequencies, many of which are quite closely spaced (see the bottom panel of Table 5.2). Since we observe large-scale amplitude changes over the course of days, we have chosen not to adopt these 12 frequencies as a formal solution, because we cannot confirm the coherence of each periodicity. Some frequencies may represent sampling artifacts or frequency drifting rather than truly excited modes in the star. Still, we include these 12 frequencies in Table 5.2 since our full dataset allows us to detect low-amplitude features that may be additional independent periods. Every periodicity in the frequency solution for the entire dataset has a FAP $> 99.9\%$ except for f_6, which has a 99.8% FAP.

We calculate a more conservative overall frequency solution by fitting a Lorentzian function to the three significant bands of power for the FT of each of the three subsets, shown in Figure 5.3. We adopt the mean of the centroids, weighted by their full width at half maximum, as the overall frequency solution in Table 5.2,

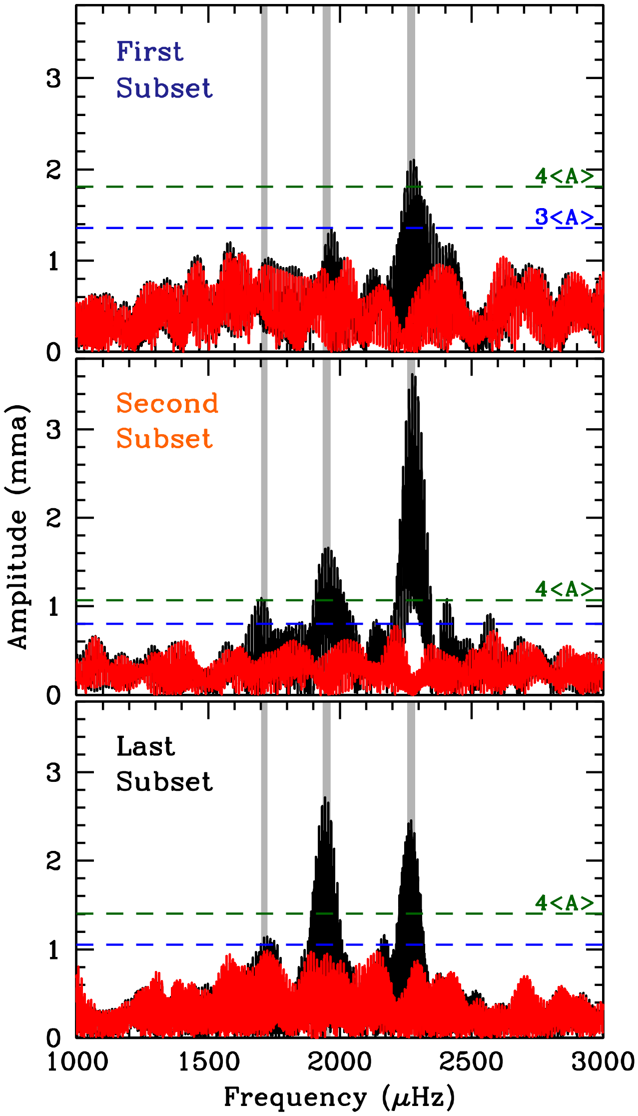

Figure 5.3 Fourier transforms, in black, of the light curves of our first five nights of data (top panel), our second five nights of data (middle panel) and our last nine nights of data (bottom panel). The frequency solutions for each subset are described in Table 5.2. In each case we also display in red the Fourier transform of the residuals after pre-whitening by the significant frequencies. We mark the $4\langle A\rangle$ and $3\langle A\rangle$ significance lines as dashed green and blue lines, respectively. The vertical gray lines show the 1σ uncertainties for the overall frequency solution adopted in Table 5.2.

with the uncertainty determined by the standard deviation of the three measurements.

Figure 5.3 shows the Fourier analysis for each subset. We display the original FT for that subset in black, overlaid with the FT prewhitened by the frequencies marked as significant in Table 5.2. It is evident that the amplitudes of the variability near 440 s and 513 s (2270 and 1949 μHz, respectively) change significantly, even over the timescale of a few days.

5.4 Discussion and Conclusions

We have discovered pulsations in GD 518, which is to date the most massive pulsating WD known. This star has a mass of roughly 1.2 $M_{\odot}$, derived from model fits to its pressure-broadened Balmer lines. The object offers the best opportunity, to date, to explore the interior of a possible ONe-core WD using asteroseismology.

Since our best current evidence on the high-mass nature of GD 518 rests on its optical spectrum, we have been careful to ensure that this WD truly has high surface gravity. Masses of WDs derived from the spectroscopic method, as we have here with GD 518, show an unphysical upturn in derived surface gravity for effective temperatures below $11{,}500$ K (Koester et al. 2009, e.g.). However, the models used to calculate the surface gravity of GD 518 include improved Stark broadening profiles with non-ideal gas effects, which have slightly moderated this upturn (Tremblay et al. 2011, Kleinman et al. 2013). A full 3D treatment of convection for a WD atmosphere near $12{,}000$ K and $\log g = 9.0$ shows that corrections to the 1D models we have used for this spectroscopic analysis do not diverge by more than $0.1 - 0.15$ dex (Pier-Emmanuel Tremblay 2013, private communication). Additionally, we do not observe evidence for splitting of the Balmer lines caused by a high surface magnetic field, which can sometimes be confused as a high-surface-gravity

WD (Kepler et al. 2013).

Fits to follow-up spectroscopy on GD 518 agree with the high surface gravity first reported in Gianninas et al. (2011), which confirms a high-mass interpretation for this WD. Additionally, the star is in the footprint of the SDSS, and matching $ugriz$ colors with synthetic models[2] suggests this is an ultramassive WD (Holberg & Bergeron 2006, Kowalski & Saumon 2006, Tremblay et al. 2011). Obtaining a parallax distance to GD 518 will help settle its mass.

There is theoretical support to expect that it will be possible to distinguish the core composition of a massive WD. Córsico et al. (2004) explored the adiabatic pulsational properties of massive WDs and found several noticeable differences between CO-core models and ONe-core models of a $1.05\ M_{\odot}$ WD, the only mass they calculated. Their ONe-core models were characterized by strong deviations in their forward period spacing, and the mean period spacing for their ONe models was noticeably larger than the mean period spacing for their CO-core modes. Additionally, the pulsation modes in their ONe-core models had consistently lower kinetic energies than those in the CO-core models.

However, the reason they found lower kinetic energies (and larger period spacings) for pulsations in their ONe-core models is that those ONe-core models were significantly more crystallized ($> 90\%$ by mass) at the same temperature, $11{,}810$ K, than their CO-core models (~50% by mass). Crystallization occurs when the Coulomb energy between neighboring ions becomes more than two orders of magnitude larger than the thermal energy of the ions in the WD core, and is a naturally occurring stage of WDs as they cool (Salpeter 1961, D'Antona & Mazzitelli 1990). A 1.2 $M_{\odot}$ WD should be significantly more crystallized at a similar tem-

---

[2] http://www.astro.umontreal.ca/~bergeron/CoolingModels

perature than a 1.05 $M_\odot$ WD. We expect that pulsation energy would be largely excluded from the interior crystallized mass.

With less of the stellar material participating in the global pulsations, it is conceivable that the oscillations have less mode inertia, and can vary on shorter timescales relative to the pulsation periods. Indeed, we observe large amplitude changes in this massive WD (see Figure 5.3), which may be a consequence of its large crystallized mass fraction. This relatively short-term amplitude modulation, especially in which pulsation amplitudes fall below detectability, has been seen before in other massive pulsating WDs, notably BPM 37093 and SDSS J005047.60-002316.9 (Kanaan et al. 2005, Castanheira et al. 2010). As the highest-mass pulsating WD ever discovered, GD 518 will provide rich insight into the physics of crystallization, as initiated by studies of BPM 37093 (Metcalfe et al. 2004).

However, the degeneracy in parameters caused by crystallization will pose a significant challenge to finding a robust asteroseismic differentiation of the core composition of GD 518. We expect to need a significant number of observed independent pulsation modes in order to overcome the many free parameters in our asteroseismic fits. Still, we are encouraged by the number of independent periods we have already determined (at least three) with a relatively short, single-site campaign.

It is possible that the three highest-amplitude periods we observe — at 440.2 ± 1.5 s, 513.2 ± 2.4 s, and 583.7 ± 1.5 s — are of the same spherical degree (ℓ), since they are spaced by roughly 73.0 s and 70.5 s, respectively. They are unlikely consecutive radial orders. The 90% crystallized 1.15 $M_\odot$ CO-core models of Montgomery & Winget (1999) find mean period spacings for $\ell = 2$ modes of $15-25$ s, depending on the hydrogen layer mass. Likewise, Córsico et al. (2004) expect period spacings of roughly 20 s for $\ell = 2$ modes of a 1.05 $M_\odot$ ONe-core model. Period spacings for $\ell = 1$ modes should be $\sqrt{3}$ times longer.

Aside from the imprint the core chemical profile makes on the pulsation spectrum, the core composition also affects the rate of cooling for a WD. This is a consequence of the fact that the cooling time of a WD is inversely proportional to the mean atomic weight of the ions in the core. In some cases we can directly measure this cooling rate by monitoring, long-term, the rate of period change of stable pulsation modes in a DAV (e.g., Kepler et al. 2005, Mukadam et al. 2013). Measuring the rate of period change of any coherent modes will allow another direct test of core composition for this ultramassive WD, albeit a longer-term endeavor.

Successfully unraveling both the overall mass and the core composition of GD 518 will constrain intermediate-mass stellar evolution. It also provides an opportunity to put an upper limit on the primary in a SNe Ia progenitor system, which theory predicts is a CO-core WD, since an ONeMg-core WD is expected to collapse due to electron capture before detonation as a Type Ia supernova (Nomoto 1984, 1987).

Table 5.1. Journal of photometric observations.

UT Date	Length (hr)	Seeing ($''$)	Exp. (s)	$P_+[A_+]$ (s)[(mma)]
2013 Mar 10	3.1	3.9	10	437.6[4.9]
2013 Mar 12	3.0	2.2	5	437.6[2.0]
2013 Mar 13	3.0	1.7	5	418.4[1.8]
2013 Mar 14	2.3	1.4	5	438.0[4.3]
2013 Mar 15	2.5	1.7	5	441.0[3.8]
2013 Mar 16	3.0	1.8	5	441.4[6.5]
2013 Mar 17	3.4	1.9	5	439.9[6.2]
2013 Mar 18	3.5	2.2	5	438.5[4.6]
2013 Mar 19	2.9	1.5	5	437.0[4.1]
2013 Apr 4	3.6	1.8	5	440.0[5.4]
2013 Apr 6	4.4	2.0	5	441.1[3.7]
2013 Apr 7	3.1	1.4	5	524.2[1.6]
2013 Apr 9	2.6	2.5	5	519.1[3.6]
2013 Apr 12	2.9	1.7	5	514.2[4.3]

Table 5.2. Frequency solution for GD 518

ID	Period (s)	Frequency (μHz)	Amplitude (mma)
Overall Frequency Solution			
f_1	440.2 ± 1.5	2271.7 ± 7.6	
f_2	513.2 ± 2.4	1948.6 ± 9.2	
f_3	583.7 ± 1.5	1713.3 ± 4.5	
Using First Five Nights (10 Mar – 14 Mar)			
f_{1a}	438.47 ± 0.64	2280.7 ± 3.3	2.92 ± 0.44
f_{1b}	438.098 ± 0.057	2282.59 ± 0.30	2.24 ± 0.48
f_2	508.2 ± 1.5	1967.9 ± 5.9	1.30 ± 0.29
Using Second Five Nights (15 Mar – 19 Mar)			
f_{1a}	439.6 ± 4.5	2275 ± 24	4.05 ± 0.57
f_{1b}	438.89 ± 0.16	2278.45 ± 0.82	2.57 ± 0.24
f_{1c}	440.26 ± 0.25	2271.4 ± 1.3	2.42 ± 0.39
f_{2a}	511.3 ± 2.9	1956 ± 11	2.0 ± 1.3
f_{2b}	509.405 ± 0.099	1963.08 ± 0.38	1.8 ± 1.6
f_3	518.99 ± 0.14	1926.82 ± 0.52	1.49 ± 0.37
f_4	592 ± 33	1690 ± 95	1.24 ± 0.49
Using Last Nine Nights (4 Apr – 12 Apr)			
f_1	519.238 ± 0.043	1925.90 ± 0.16	2.51 ± 0.48
f_{2a}	441.244 ± 0.046	2266.32 ± 0.23	2.38 ± 0.41
f_{2b}	440.156 ± 0.062	2271.92 ± 0.32	2.12 ± 0.40
f_3	512.6 ± 5.3	1951 ± 20	1.63 ± 0.47
Using All Data (10 Mar – 12 Apr)			
f_{1a}	442.12 ± 0.42	2261.8 ± 2.1	2.38 ± 0.73
f_{1b}	441.15 ± 0.17	2266.81 ± 0.88	2.36 ± 0.72
f_{1c}	439.5 ± 1.4	2275.5 ± 7.3	1.94 ± 0.53
f_2	519.2 ± 1.8	1925.9 ± 6.7	1.55 ± 0.59
f_{1d}	440.59 ± 0.47	2269.7 ± 2.4	1.21 ± 0.52
f_{3a}	511.455 ± 0.009	1955.207 ± 0.035	1.21 ± 0.26
f_{3b}	510.824 ± 0.008	1957.622 ± 0.032	1.13 ± 0.18
f_{1e}	437.79 ± 0.13	2284.20 ± 0.67	1.13 ± 0.46
f_{4a}	503.800 ± 0.010	1984.914 ± 0.040	0.95 ± 0.23
f_{4b}	501.44 ± 0.50	1994.3 ± 2.0	0.93 ± 0.24
f_5	426.71 ± 0.86	2343.5 ± 4.7	0.81 ± 0.34
f_6	587.25 ± 0.96	1702.8 ± 2.8	0.78 ± 0.24

Chapter 6

A New Timescale for Period Change in the Pulsating DA White Dwarf WD 0111+0018

We report the most rapid rate of period change measured to date for a pulsating DA (hydrogen atmosphere) white dwarf (WD), observed in the 292.9 s mode of WD 0111+0018. The observed period change, faster than 10^{-12} s s^{-1}, exceeds by more than two orders of magnitude the expected rate from cooling alone for this class of slow and simply evolving pulsating WDs. This result indicates the presence of an additional timescale for period evolution in these pulsating objects. We also measure the rates of period change of nonlinear combination frequencies and show that they share the evolutionary characteristics of their parent modes, confirming that these combination frequencies are not independent modes but rather artifacts of some nonlinear distortion in the outer layers of the star.[1]

6.1 Introduction

White dwarf (WD) stars represent the final evolutionary stage of all single low-mass stars, and are thus representative of the future of the majority of stars in our Galaxy. They are primarily composed of the inert by-products of hydrogen and helium fusion, and their evolution is dictated by the rate at which these carbon and oxygen ions lose their residual thermal energy (Mestel 1952). This cooling takes

---

[1] *Significant portions of this chapter have been previously published as:* J. J. Hermes, M. H. Montgomery, Fergal Mullally, D. E. Winget, and A. Bischoff-Kim, *The Astrophysical Journal*, **766**, 42 (2013)

billions of years.

However, we can witness this cooling on human timescales by watching the WDs that pulsate. These variable stars come in several classes, based on their dominant atmospheric composition (their strong surface gravity and rapid gravitational settling leads to chemically homogenous photospheres). Here we will restrict our discussion to the coolest class of such pulsators: the hydrogen-atmosphere DAV (or ZZ Ceti) stars, found in an instability strip between $10{,}800 - 12{,}300$ K for standard $\log g = 8.0$ (Koester & Holberg 2001, Bergeron et al. 2004, Mukadam et al. 2004, Gianninas et al. 2005, 2006, Mukadam et al. 2006).

Aside from their variability, which is brought on by a hydrogen partial-ionization zone in the star's non-degenerate atmosphere, DAVs appear to be normal WDs. They are therefore believed to be representative of evolution for all DA WDs (Robinson 1979, Fontaine et al. 1985, Bergeron et al. 2004). Cooling from neutrino emission is expected to be negligible for DA WDs within the ZZ Ceti instability strip (Winget et al. 2004), and their evolution should be dominated by radiative surface emission.

The C/O-core DAVs undergo multi-periodic, non-radial g-mode pulsations with periods between roughly $100 - 1400$ s. Seismology using these g-mode pulsations has enabled us to constrain the mass, core and envelope composition, rotation rate, and the behavior of convection in these objects (see reviews by Winget & Kepler 2008, Fontaine & Brassard 2008 and Althaus et al. 2010). These modes are often stable in period and amplitude, especially for the hot DAVs (hDAVs) near the blue-edge of the ZZ Ceti instability strip. hDAVs are expected to show an extremely slow period drift caused by the gradual cooling of the star.

Two of the longest-studied hDAVs are G117-B15A and ZZ Ceti itself (also referred to as R548), which have been observed since the early 1970s. Both show considerable stability in their largest-amplitude modes. The rate of change of period with time, dP/dt, of the dominant 215.2 s mode in G117-B15A has been measured to be $(4.19 \pm 0.73) \times 10^{-15}$ s s^{-1} (Kepler 2012). R548 has been observed since 1970, but more sparingly: For the 213.1 s periodicity in R548, Mukadam et al. (2013) determine a dP/dt = $(3.3 \pm 1.1) \times 10^{-15}$ s s^{-1}. These values have taken decades of observations, and are in line with theoretical predictions of rates of period change from cooling alone in DAVs of $dP/dt < 10^{-14}$ s s^{-1} (Bradley et al. 1992, Bischoff-Kim et al. 2008, Córsico et al. 2012a).

After more than nine years of monitoring, we have found evidence for an hDAV that has a rate of period change inconsistent with cooling alone. The period change in the highest-amplitude periodicity for that star, SDSS J011100.63+001807.2 (hereafter WD 0111+0018; $g = 18.7$ mag), exceeds 10^{-12} s s^{-1}. This observed rate of change of period with time is several orders of magnitude faster than predicted from cooling alone for this 11810 K WD. It therefore signifies some physical process operating on a considerably shorter timescale.

In this paper we present our observations of period evolution in the four highest-amplitude periodicities present in WD 0111+0018. In Sections 2 and 3 we outline our observations and analysis, and we reserve Sections 4 and 5 for a discussion of possible explanations for this rapid period change and our conclusions.

6.2 Time-Series Photometric Observations

Mukadam et al. (2004) discovered pulsations in WD 0111+0018, resulting from a search for variable DAs. The WD was initially targeted as a result of model atmosphere fits to spectra from the Sloan Digital Sky Survey: with $T_{\rm eff}$ = $11{,}510 \pm 110$ K and $\log g$ = 8.26 ± 0.06, the object was predicted and confirmed to be a DAV within the ZZ Ceti instability strip.

Using new treatments of line broadening theory, Tremblay et al. (2011) refined the temperature and surface gravity of WD 0111+0018 to $T_{\rm eff}$ = $11{,}810 \pm 190$ K and $\log g$ = 8.17 ± 0.07, which corresponds to a mass of $M_{\rm WD} = 0.71 \pm 0.04\ M_{\odot}$ and a cooling age of 510 Myr.

Including the initial discovery observations in early 2003, the White Dwarf Group at the University of Texas at Austin has logged a total of more than 136 hr of observations of WD 0111+0018 on 39 separate nights. As the journal of observations in Table 6.2 indicates, the data span more than nine years. One motivation for these observations was to use the stable pulsation modes of hDAVs as precise clocks, searching for evidence of planetary companions by looking for periodic variations in the pulse arrival times (Winget et al. 2003, Mullally et al. 2008). The project has also effectively opened a window on new evolutionary timescales for more than a dozen hDAVs, including WD 0111+0018.

All of our data on WD 0111+0018, more than $33{,}100$ images, have been taken using the same instrument (Argos, a frame-transfer CCD; see Nather & Mukadam 2004) with the same filter (a 3 mm *BG40*, to reduce sky noise) on the same telescope (the 2.1m Otto Struve at McDonald Observatory), allowing for an especially coherent data set. Depending on the conditions, we have used $10 - 30$ s exposures, as indicated in Table 6.2.

The raw science frames are calibrated by dark subtraction and flat-fielding. We perform weighted, circular, aperture photometry on the calibrated frames using the external IRAF package *ccd_hsp* written by Antonio Kanaan (the reduction method is outlined in Kanaan et al. 2002 and Mullally et al. 2005). We divided the sky-subtracted light curves using two bright comparison stars in the field, SDSS J011055.57+001850.6 ($g = 15.0$ mag) and SDSS J011056.17+001955.8 ($g = 16.2$ mag), to correct for transparency variations. Using the WQED software suite

Table 6.1. Mode periods and observed rates of period change in WD 0111+0018

Mode	t_0 (BJD$_{\mathrm{TDB}}$)	P_0 (s)	Amplitude (%)	dP/dt (10^{-12} s s^{-1})
f_1	2452666.562825(21)	292.944305(9)	2.573	4.280(42)
f_2	2452666.562314(31)	255.663971(2)	1.428	0.340(58)
$2f_1$	2452666.562701(42)	146.472153(3)	0.633	2.075(44)
$f_1 + f_2$	2452666.562624(29)	136.518707(5)	0.730	1.109(30)

(Thompson & Mullally 2009), we fit and subtract out a low-order polynomial (at the timescale of several hours) to each run to remove any long-term trend caused by atmospheric extinction, and apply a timing correction to each observation to account for the motion of the Earth around the barycenter of the solar system (Stumpff 1980).

6.3 Light Curve Analysis

6.3.1 The Pulsation Spectrum of WD 0111+0018

The light curve of WD 0111+0018 features modulation at four distinct periodicities between $100 - 300$ s, which can be well-resolved in a 3-hr run in good conditions (see Figure 6.1). In order to most accurately identify these four periods, we begin by computing a Fourier transform of our entire data set. Using these results as an initial guess, we then perform a nonlinear least-squares fit for the frequency, amplitude, and phase of the four periodicities present.

This allows us to isolate an initial estimate of the periods of the four highest-amplitude pulsations present in WD 0111+0018, which we use to construct an initial $(O - C)$ diagram. The amplitudes for these four periodicities never fall below 0.5%; the amplitudes listed in Table 6.1 are weighted-mean amplitudes using each subgroup.

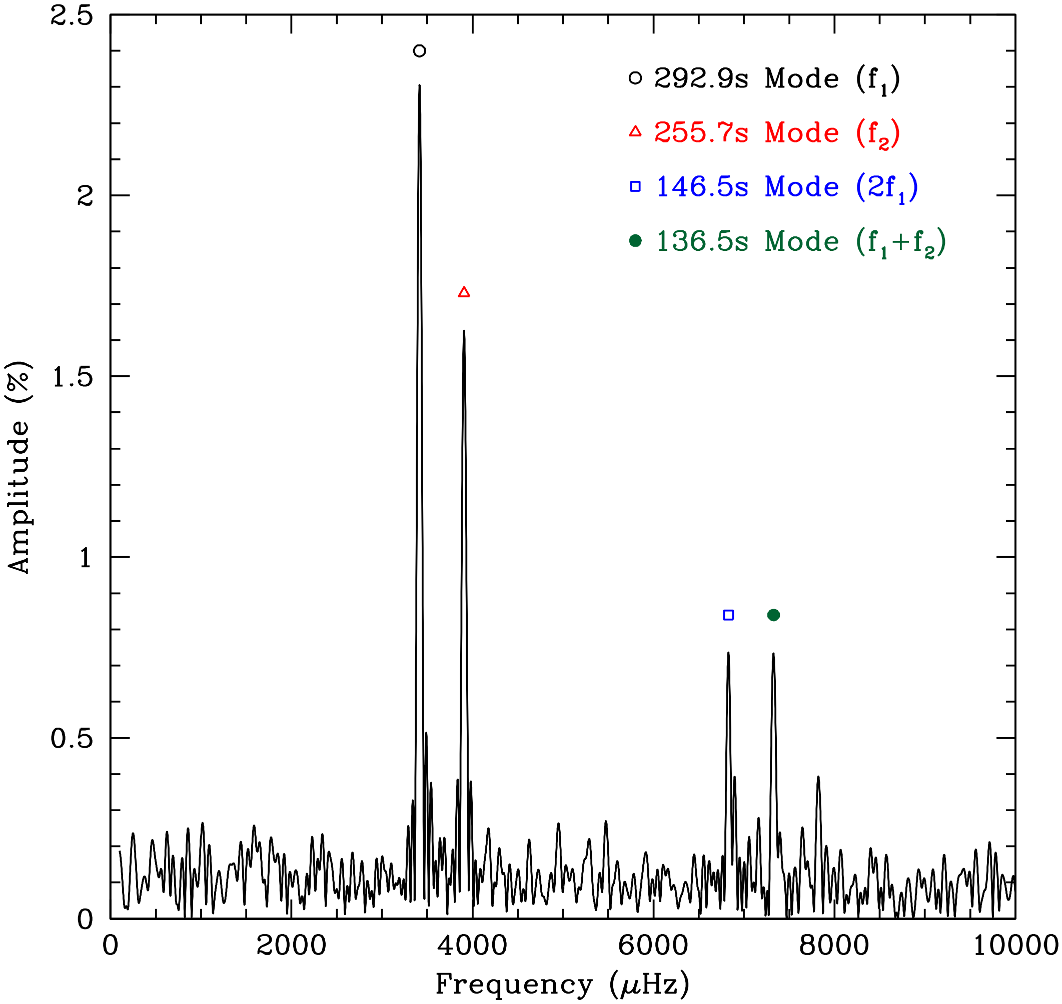

Figure 6.1 The pulsation spectrum of WD 0111+0018 for a typical run, this on 15 Sep 2009. A Fourier transform of this 5.5-hr run illustrates that the four periodicities of interest, seen marked, can be resolved in a single night.

We perform this analysis independently for all 18 subgroups of our data. The subgroups are created by combining data from as many contiguous nights as possible; no combined subgroup spans more than two weeks. These subgroups have been identified in Table 6.2. In each case, the periods we determine for each subgroup match the periods we have found for the entire data set, within the uncertainties.

We fix these periods and compute a simultaneous linear least-squares fit for each subgroup to create an $(O-C)$ diagram. Thus, the uncertainties in our $(O-C)$ diagrams represent formal uncertainties on the least-squares fit for the phase on at least one—and as many as three—nights of data, separated by as many as 10 days.

We will refer to the two highest-amplitude periodicities as the parent modes f_1 and f_2, and the two smaller-amplitude periodicities $2f_1$ and $f_1 + f_2$ as the combination frequencies, such that the frequency for $2f_1$ is (within the uncertainty) exactly twice the frequency of f_1 and the frequency for $f_1 + f_2$ is the sum of the frequencies of f_1 and f_2. We will discuss in more detail these combination frequencies and how they arise in Section 6.4.1.

Additionally, we note the presence of an additional combination frequency $2f_2$ at 127.8 s, visible but not labeled in Figure 6.1. In fact, we detect at least five additional nonlinear combination frequencies. Using all of our light curves from 2009 to early 2012 to detect as many combination frequencies as possible, we find: $f_1 = 2.739(29)$%, $f_2 = 1.526(31)$%, $2f_1 = 0.472(27)$%, $f_1 + f_2 = 0.732(28)$%, $2f_2 = 0.193(25)$%, $3f_1 = 0.143(44)$%, $2f_1 + f_2 = 0.295(98)$%, $f_1 + 2f_2 = 0.147(44)$%, $3f_2 = 0.068(28)$%. However, the amplitudes of most of the combination frequencies are too low to produce an $(O-C)$ diagram for all subgroups, so we do not include them in the $(O-C)$ analysis.

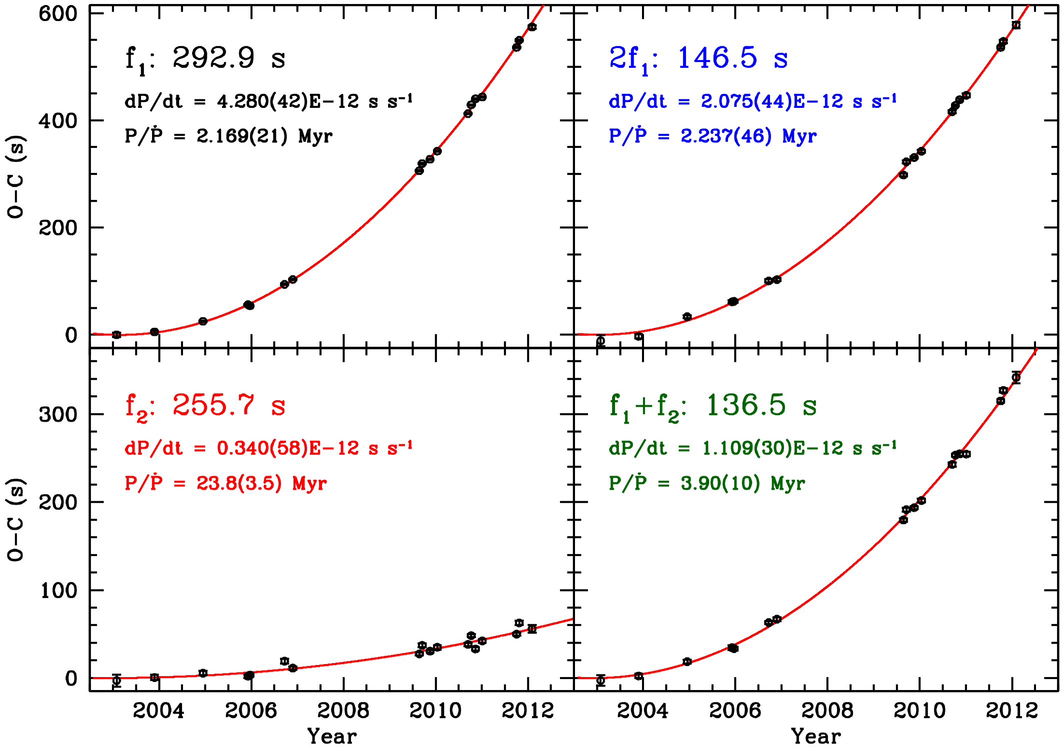

Figure 6.2 $(O - C)$ diagrams for the four highest-amplitude periodicities present in WD 0111+0018. The f_1 and $2f_1$ $(O - C)$ diagrams are nearly identical, which strongly suggests that nonlinear combination frequencies in DAVs are not independent pulsation modes but are directly tied to their parent modes. A best-fit parabola yields a rate of change of period with time: See Table 6.1 for full solutions.

6.3.2 Constructing an $(O - C)$ Diagram

We demonstrate a secular change in the pulsation periods of WD 0111+0018 by constructing $(O - C)$ diagrams, where we compare the observed time of maximum for a pulsation (O) to when we expect such a maximum assuming that the pulsation obeys a constant period (C).

Following Kepler et al. (1991), if the pulsation period is changing slowly with time, we can expand the observed time of maximum of the Eth pulse, t_E, in a

Taylor series around E_0:

$$t_{max}\mid_E = \ t_{max}\mid_{E_0} + \frac{dt_{max}}{dE}\mid_{E_0}(E-E_0)+\frac{1}{2}\frac{d^2t_{max}}{dE^2}\mid_{E_0}(E-E_0)^2+\ ...$$

where the epoch is $E = t/P$ and the change in arrival time with epoch, dt/dE, is the period, P. If we drop all terms higher than second order (assuming that $\ddot{P}$ is negligible), we arrive at the classic $(O - C)$ equation

$$O\ -\ C = \Delta t_0 +\ \Delta P_0\, E + \frac{1}{2}P_0\dot{P}E^2 \tag{6.1}$$

where t_0 is the time of first maximum, Δt_0 is the uncertainty in this time, P_0 is the pulsation period at this time of first maximum and ΔP_0 is the error in the observed period. Thus, any secular change in the period, dP/dt, will cause a parabolic curvature in an $(O - C)$ diagram.

We construct an initial $(O - C)$ diagram using the periods identified in Section 6.3.1. We then iteratively adjust t_0 and P_0 by the zeroth- and first-order terms from our best second-order fit until the adjustments are smaller than the uncertainty in these terms; these uncertainties result from the covariance matrix. Our recomputed, final $(O - C)$ diagrams use these final ephemera and periods, which can be found for each mode in Table 6.1. The final $(O - C)$ diagrams are shown in Figure 6.2. Table 6.3 presents the times of maximum from each subset of our observations.

6.3.3 Observed Rates of Period Change

Mullally et al. (2008) published an $(O-C)$ diagram of f_1 in WD 0111+0018, noting the large curvature but urging caution given the sparse coverage. Still, a rather high rate of change of period with time was observed: $(3.87 \pm 0.43) \times 10^{-12}$ s s^{-1}.

We have added another 86 hr of observations, more than doubling the coverage, and confirm this large trend in the $(O - C)$ diagram of f_1. We have additionally been able to make $(O - C)$ diagrams for three other periodicities. These diagrams can be found in Figure 6.2.

Using Equation 2, a best-fit parabola to each $(O - C)$ diagram yields a rate of change of period with time. We list these results in Table 6.1. Our results for f_1 actually fall within the errors of the Mullally et al. (2008) result, at $(4.280 \pm 0.042) \times 10^{-12}$ s s^{-1} (or 0.135 ± 0.001 ms yr^{-1}). We also strongly establish the need for a second-order fit rather than a first-order fit to the 18 data points: The best second-order fit for the $(O - C)$ diagram of f_1 has $\chi^2 = 145$ (15 degrees of freedom, or d.o.f.), whereas the best linear fit has $\chi^2 = 10292$ (16 d.o.f.).

Although the $(O - C)$ diagrams for WD 0111+0018 appear parabolic, as we would expect if the pulsations periods were changing secularly, we would also like to establish the timescale of variability if these observed trends are instead periodic in nature, since a portion of a sinusoid can mimic a parabola. For f_1 we find that the data can be well fit by a sinusoid with a 101 year period and a 3931 s $(O - C)$ amplitude, with a $\chi^2 = 142$ (15 d.o.f.). However, we will only continue our analysis in the framework of a secular period change.

In the future, a third-order fit including the acceleration in the period change may be needed to best represent the data. This would enter the $(O - C)$ equation as

$$O \; - \; C = \Delta t_0 + \, \Delta P_0 \, E + \frac{1}{2} P_0 \dot{P} E^2 + \, \frac{1}{6} (\ddot{P} P_0^2 + \dot{P}^2 P_0) E^3$$

Currently, a third-order polynomial fit to the $(O - C)$ diagram of f_1 has $\chi^2 = 143$ (14 d.o.f.), which reduces to a value still slightly higher than that for a second-order fit. The best third-order fit would correspond to $\ddot{P} = (-2.3 \pm 1.4) \times 10^{-21}$ s s^{-2}, with a second-order term corresponding to $dP/dt = (4.65 \pm 0.23) \times 10^{-12}$ s s^{-1}.

We have also attempted a direct measurement of dP/dt by computing a nonlinear least-squares fit to find the period for each subgroup. A best-fit line to these periods over time yields a rate of change of period with time. Unfortunately, there is simply not enough data for this direct measurement. The best result comes for f_1, where we determine $dP/dt = (5.5 \pm 6.8) \times 10^{-12}$ s s^{-1}, consistent with the $(O - C)$ value but not yet significant.

The other independent parent mode in WD 0111+0018, f_2, shows a much slower period change than f_1. Still, it is significantly faster than predicted by cooling theory, with a best-fit parabola that corresponds to $(3.40 \pm 0.58) \times 10^{-13}$ s s^{-1} (or 0.011 ± 0.002 ms yr^{-1}). In this case, a second-order fit is only marginally better than a linear fit: The best-fit parabola has $\chi^2 = 93.8$ (15 d.o.f.), whereas the best-fit straight line has $\chi^2 = 128.7$ (16 d.o.f.).

Noise can cause scatter about a straight line in an $(O - C)$ diagram, especially over a relatively short baseline (e.g., Kepler et al. 1991). Since a bad period can cause a dominant linear term, we caution that the rate of change of the f_2 periodicity may still be somewhat slower than the value cited in Table 6.1 if the period we use for our $(O - C)$ diagrams is off by as little as 0.06 ms. Therefore, we recommend that our value be construed as an upper limit on the rate of change of period with time of f_2. As with the other parent mode, we also investigated the best periodic rather than secular fit, and found a sinusoid with a 9540 year period and 3051490 s $(O - C)$ amplitude, with a $\chi^2 = 93.8$ (15 d.o.f.). (If such a trend were from an external companion, it would require a 10.8 $M_\odot$ unseen companion at 401 AU.)

A Monte Carlo simulation of the uncertainties using the software package Period04 (Lenz & Breger 2005) indicates that our formal least-squares uncertainties on the phases used to construct the $(O-C)$ diagrams are underestimated by at most

10%. Thus, the scatter about our residuals (evident by the large χ^2_{red} quoted above for the second-order fits, e.g. $\chi^2_{\mathrm{red}} = 9.7$ for f_1) may not be entirely the result of underestimated uncertainties. The deviation about the residuals is consistent with the observed scatter in other long-studied DAVs, such as G117-B15A (see Figure 2 of Kepler et al. 2005).

We have investigated the stability of the four highest-amplitude periodicities in WD 0111+0018 by plotting the amplitudes of each determined by a linear least-squares fit to each subgroup, using the periods in Table 6.1. This result is shown in Figure 6.3. It is meaningful since all observations were obtained and reduced in an identical manner. We have also marked the weighted mean amplitude for each mode with dotted lines.

There are considerable deviations about this mean compared to the formal uncertainties, such that only the periodicity at $2f_1$ has a constant amplitude in a statistically meaningful way. While the amplitudes of the f_1 and f_2 modes do not appear constant over our entire data set, the deviations from the mean do not appear coherent, and cannot explain the large-scale parabolic changes we observe in observed times-of-maxima.

Finally, in line with the original intentions of this data set, we have investigated whether periodic changes in the times of maxima can explain the scatter observed about the residuals after subtracting the dominant parabolic terms. This scatter might reveal the presence of an unseen companion. However, a Fourier transform of all four $(O - C)$ residuals, after subtracting the dominant parabolic terms identified in Figure 6.2, show no peaks above twice the mean noise level of 1.5 s. We can thus conservatively rule out the presence of any companion more massive than Jupiter at a current orbit between $2 - 10$ AU; the scatter is predominantly incoherent and cannot currently be attributed to an unseen companion.

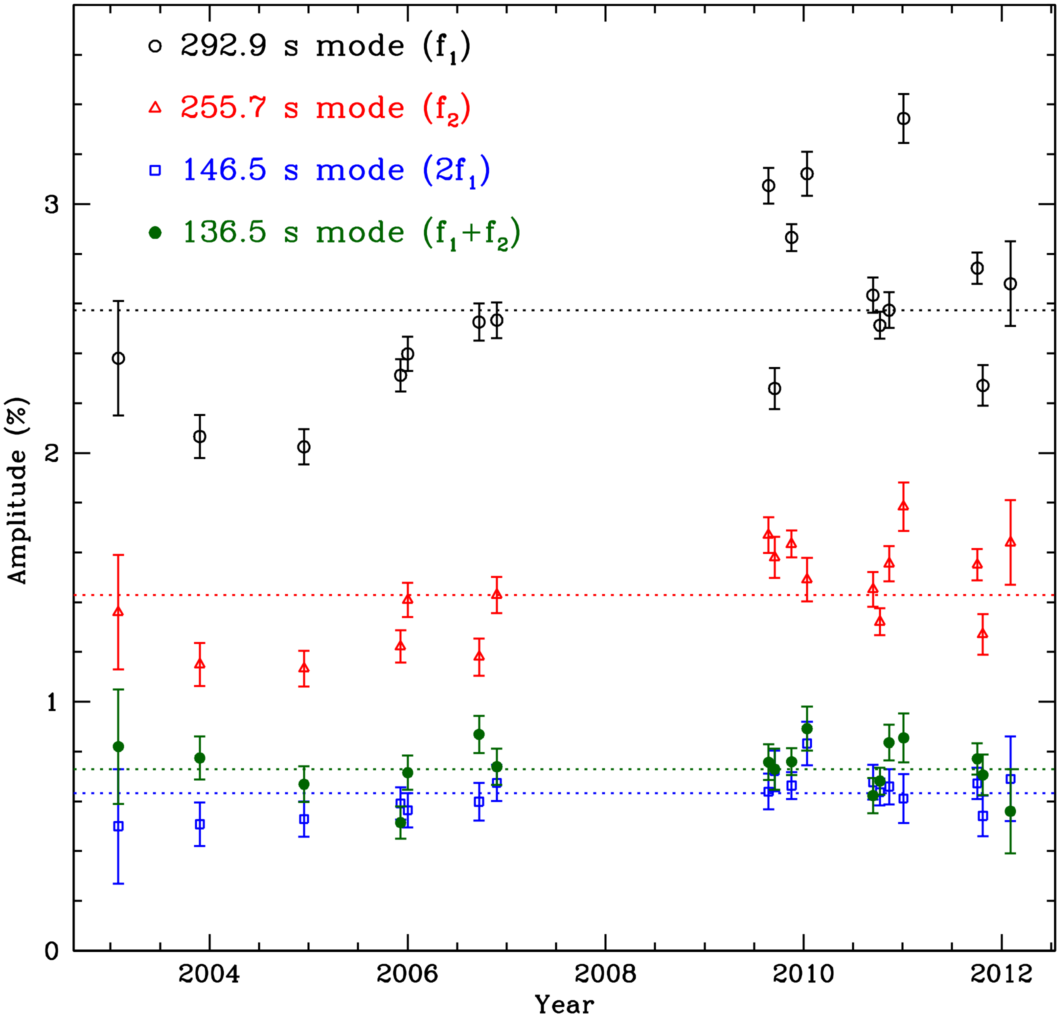

Figure 6.3 The amplitude evolution of WD 0111+0018 over nine years of observations. The dotted lines represent the weighted mean amplitude over the entire data set, shown in Table 6.1. While our data show that the amplitudes are not stable over the entire data set, they rule out a large-scale amplitude increase as the cause of the large trends in the $(O - C)$ diagrams shown in Figure 6.2.

6.4 Discussion

6.4.1 Nonlinear Combination Frequencies

Before focusing on the rapid rates of period change, we first draw attention to the observation that dP/dt for the $2f_1$ and $f_1 + f_2$ combination frequencies evolve exactly in lockstep with their parent modes. For example, we expect the $2f_1$ combination frequency to have half the rate of change of period with time of its parent mode, since $2f_1$ has half the period. We expect $(2.140 \pm 0.042) \times 10^{-12}$ s s^{-1} and in fact observe $(2.075 \pm 0.044) \times 10^{-12}$ s s^{-1}, in excellent agreement.

The $f_1 + f_2$ combination frequency is a bit more complicated, given it is a sum of the parent frequencies and not an integer ratio. We expect its rate of change of period with time to be

$$\frac{dP_3}{dt} = \frac{P_3^2}{P_1^2}\frac{dP_1}{dt} + \frac{P_3^2}{P_2^2}\frac{dP_2}{dt} \tag{6.2}$$

where $P_1 = {f_1}^{-1}$, $P_2 = {f_2}^{-1}$, and $P_3 = (f_1 + f_2)^{-1}$. We thus expect a rate of $(1.027 \pm 0.099) \times 10^{-12}$ s s^{-1} and in fact observe $(1.109 \pm 0.030) \times 10^{-12}$ s s^{-1}. As with $2f_1$, our observed rates match the predictions exactly within the errors.

This lends convincing evidence that these nonlinear combination frequencies are not independent modes themselves, but rather artifacts of some nonlinear distortion in the outer layers of the star. They are thus directly tied to the parent modes, and evolve at exactly the same rate as these parent modes. This is an important result that convincingly demonstrates the nonlinear nature of these signals.

In fact, an extensive theory explaining the creation of nonlinear combination frequencies in DAVs was introduced by Brickhill (1992). He attributed the nonlinearities to the changing thickness of the star's convection zone, which acts to distort a linear input signal. Physically, local surface temperature variations lead to changes in the depth of the convection zone, which both absorb and release energy. Because this process is so sensitive to temperature ($\propto T^{-90}$ for a DAV; Montgomery 2005), these variations in the depth of the convection zone lead to nonlinear effects in the observed light curve. An alternate explanation that may play a role for the hottest DAVs is given by Brassard et al. (1995) and Fontaine & Brassard (2008). They invoke the nonlinear response of the flux observed in a passband to the temperature (i.e., the "T^4" nonlinearity). Regardless of the source of these nonlinearities, our result confirms that the phase evolution of these combination frequencies mirrors that of their parent modes. These combination frequencies are thus directly tied to their parent modes.

The presence of nonlinear combination frequencies may also be useful in identifying the spherical degree (ℓ) and azimuthal order (m) of the parent modes. In an investigation of eight DAVs, Yeates et al. (2005) found that the amplitudes of combination frequencies are too large to be created by the T^4 nonlinearity, and are probably due to the higher-order temperature dependence of the convection zone. They employed the formalism of Wu (2001), who derived an analytical expression for the amplitudes of the combination frequencies in the context of the Brickhill framework of a depth-varying convection zone. Using the ratio of the amplitudes of the parent and combination frequencies, Yeates et al. derived constraints on the ℓ and m value of the parent mode.

With the same goal in mind, we have used our own code to automatically search for combinations of ℓ and m that best fit the observed amplitudes in WD 0111+0018. This code uses a genetic algorithm to efficiently sample parameter space; see §4.1 of Provencal et al. (2012) for more details. We run this algorithm 1000 times so that we obtain 1000 estimates of the best-fit parameters.

The method of Wu (2001) is only applicable to second-order combinations,

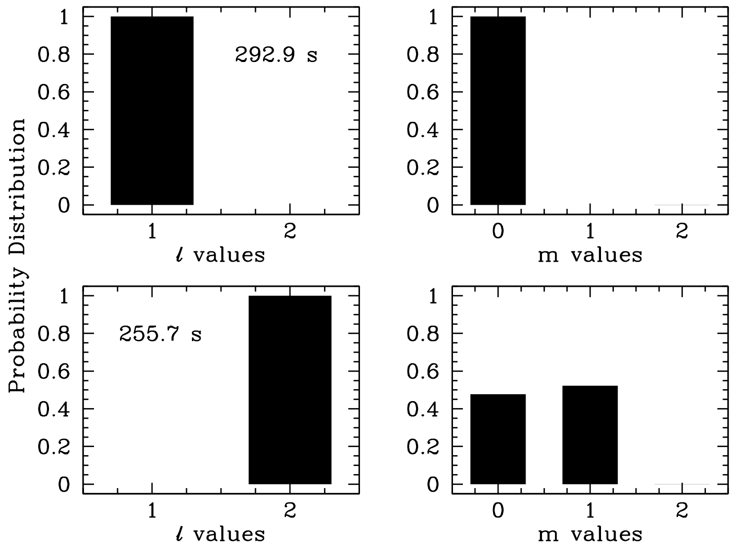

Figure 6.4 A probability distribution of ℓ and m values for the best 7% of fits using the amplitude ratio of the nonlinear combination frequencies to the parent modes, a method similar to the one used in Yeates et al. (2005). The amplitude ratios for the 292.9 s mode, f_1, are best explained by an $\ell = 1$, $m = 0$ mode (top two panels). The amplitude ratios for the 255.7 s mode, f_2, indicate this is an $\ell = 2$ mode, although there is more ambiguity about the azimuthal order of this mode (bottom panels).

i.e., $2f_1$ or $f_1 + f_2$ but not $3f_1$. Even with just three independent combination amplitudes we are able to find constraints. Consistently, we best reproduce the observed amplitude ratios (we have used the amplitudes of the 2009-2012 group, provided in Section 6.3.1) when we allow the f_1 parent mode at 292.9 s to be an $\ell = 1$, $m = 0$ mode. We also find the f_2 parent mode at 255.7 s to be an $\ell = 2$, $m = 0, \pm 1$ mode. This is shown in Figure 6.4, where we plot the distribution of the top 7% of fits with the lowest χ^2, interpreting this as a probability distribution for the identifications.

In addition, we have implemented the convective nonlinear light curve fitting code of Montgomery (2005) and Montgomery et al. (2010) to generate a synthetic light curve based on the parent modes in WD 0111+0018. This method investigates the time-averaged thermal response time of the convection zone, τ_c, which relates to the mass and depth of the convection zone. In principle, it should be superior to the perturbative method of Wu (2001) in that it makes use of all higher-order amplitudes and their phases. These nonlinear fits produce estimates for the ℓ and m values of the parent modes, the time-averaged convective timescale τ_0, the temperature sensitivity exponent N, and the inclination of the pulsation axis to our line of sight θ.

Fitting our light curves from the 2011b subgroup, we find an identical match to our previous method. The 292.9 s mode is best represented by an $\ell = 1$, $m = 0$ mode and the f_2 parent mode at 255.7 s best fits as an $\ell = 2$, $m = \pm 1$ mode. Additionally, these fits find $\tau_0 = 137.8 \pm 11.8$ s, $N = -82.0 \pm 3.6$, and $\theta = 34.6 \pm 2.5°$.

We thus adopt an interpretation that f_1 is an $m = 0$ dipole ($\ell = 1$) mode and f_2 is a quadropole ($\ell = 2$) mode. The constraints on the azimuthal order of f_2 are less conclusive. We will use this information to help constrain our asteroseismic models, which will in turn inform our attempts at understanding the observed dP/dt.

6.4.2 Expected Rates of Period Change

We can immediately rule out the possibility that an unseen external body is vigorously tugging WD 0111+0018 away from our line of sight, causing a light-travel time effect that is manifest as the increasing delay in pulse arrival times: Rapid space motion would affect all modes identically, and the periodic modulation in the mode f_2 is more than an order of magnitude slower than that of f_1, as we found in Section 6.3.3. We must be observing a phenomenon internal to the WD.

We expect cooling to be the dominant evolutionary effect of an isolated DAV, and this cooling timescale should have a direct effect on the period evolution of modes in a pulsating WD. To first order, as a WD cools it becomes more degenerate. This causes a decrease in the square of the Brunt-Väisälä frequency, N^2. The Brunt-Väisälä frequency is essentially the oscillatory frequency of an adiabatic fluid displacement in a convectively stable medium. In the limit of low temperature and complete degeneracy, where pressure does not depend on temperature, a displaced fluid element would remain in pressure and density equilibrium with its surroundings. It would stay put and thus have zero oscillatory motion — and thus a zero N^2. Thus, N^2 decreases with increasing degeneracy, and therefore decreasing temperature (see Kim 2007).

The period of a g-mode pulsation is inversely proportional to the Brunt-Väisälä frequency (Unno et al. 1989). Therefore, cooling will cause a secular increase in a pulsation period with time, which can be estimated from the cooling timescale predicted from Mestel theory, as well as full evolutionary models. Predicted rates of period change for DAVs undergoing simple cooling are of order 10^{-15} s s^{-1}; we find observational evidence to support this timescale from observations of G117-B15A and R548 (Kepler 2012, Mukadam et al. 2013). The 215.2 s mode in G117-B15A and the 213.1 s mode in R548 are most likely either an $\ell = 1, k = 1$ mode or a $\ell = 1, k = 2$ mode, depending on the adopted hydrogen layer mass (Bischoff-Kim et al. 2008, Romero et al. 2012).

We note that the work of monitoring long-term phase evolution of DAVs requires a mode coherent in amplitude and phase. This is usually not the case for the cooler DAVs, which evidence strong amplitude modulation and a corresponding lack of stability in phase (e.g. Kleinman et al. 1998, Dolez et al. 2006). One cool DAV has, for at least a brief time, shown enough phase coherence to create a meaningful

$(O - C)$ diagram: The 615.2 s mode in G29-38 (Kleinman 1995), which showed a coherent but extremely rapid phase change, more than 200 s over less than three months of monitoring in 1988 (Winget et al. 1990). There is also evidence that the 274.8 s mode in R548 has a $dP/dt > 10^{-13}$ s s^{-1} (Mukadam et al. 2003), and that the 270.5 s and 304.1 modes in G117-B15A have $dP/dt > 3 \times 10^{-14}$ s s^{-1} (Kepler et al. 2005). Still, most modes in DAVs observed to date simply do not show enough coherence to create stable $(O - C)$ diagrams.

WD stars with heavier cores should cool faster than those that are lighter. Indeed, spectral fits show that WD 0111+0018, at $\simeq 0.71\ M_{\odot}$, is slightly more massive than G117-B15A and R548, which are between 0.59 – 0.60 $M_{\odot}$. Still, even a 1.4 $M_{\odot}$ Fe-core WD would have a dP/dt from cooling of less than 9×10^{-15} s s^{-1} if the WD has $T_{\rm eff} = 11800$ K (Bradley et al. 1992).

Our observed rate of change of period with time for f_1 in WD 0111+0018 exceeds 10^{-12} s s^{-1}, more than two orders of magnitude faster than predicted from cooling alone. It is also more than an order of magnitude faster than expected from an avoided crossing (Bradley & Winget 1991) or by invoking excess cooling from exotic particles such as axions (Bischoff-Kim et al. 2008, Córsico et al. 2012a). We thus interpret this discovery as evidence of an additional physical timescale acting on the evolution of the pulsation periods in WD 0111+0018.

6.4.3 Asteroseismology of WD 0111+0018

Both the 292.9 s and 255.7 s modes of WD 0111+0018 likely probe different regions of the star, so mode identification (specifically the radial order, k) would yield further insight into understanding these anomalous rates of period change. Unfortunately, asteroseismology is made more difficult by the presence of just two independent modes; there are far more free parameters than observations.

Still, we have attempted to match the observed periods to adiabatic pulsation models with some assumptions and the constraints provided by our spectroscopic mass and temperature determinations. Our two best matches to the observed periods have the following properties:

Solution 1: f_1 is an $\ell = 1$, $k = 5$ mode ($m = 0$ occurs at 293.4 s), while f_2 is an $\ell = 2$, $k = 8$ mode ($m = 0$ occurs at 255.0 s). This WD model has a stellar mass of 0.710 $M_{\odot}$, an effective temperature $T_{\rm eff} = 11630$ K, a He envelope mass of $M_{\rm He}/M_{*} = 10^{-2.1}$, and a H envelope mass of $M_{\rm H}/M_{*} = 10^{-4.5}$.

Solution 2: f_1 is an $\ell = 2$, $k = 10$ mode ($m = 0$ occurs at 293.7 s), while f_2 is an $\ell = 2$, $k = 8$ mode ($m = 0$ occurs at 255.0 s). This WD model has a stellar mass of 0.720 $M_{\odot}$, an effective temperature $T_{\rm eff} = 11610$ K, a He envelope mass of $M_{\rm He}/M_{*} = 10^{-2.0}$, and a H envelope mass of $M_{\rm H}/M_{*} = 10^{-4.5}$.

Additionally, we can use our spectroscopic constraints to explore the models of Romero et al. (2012) of a 0.705 $M_{\odot}$, 11,810 K WD with a thick ($10^{-4.445}$ $M_{\star}$) hydrogen layer mass. Similarly, we find that the 292.9 s mode is either an $\ell = 2, k = 10$ or $\ell = 1, k = 5$ mode. The 255.7 s mode is either an $\ell = 2, k = 8$ or $\ell = 1, k = 4$ mode. We caution that because these solutions are consistent does not imply they are correct — our assumptions may not indeed be valid. But these solutions will help inform our analysis of what could be causing the rapid period change in WD 0111+0018.

Using our spherical degree (ℓ) identifications described in Section 6.4.1, we can break the degeneracy in f_1 and suggest that the 292.9 s periodicity represents an $\ell = 1, k = 5$ mode, while the the 255.7 s periodicity is an $\ell = 2, k = 8$ mode. In order to visualize how each such mode samples the star, we have included a propagation diagram in Figure 6.5. We have marked where a $\sim$250 s and a $\sim$300 s g-mode for different ℓ values would probe the star (where $\sigma^2 < N^2, L_{\ell}^2$).

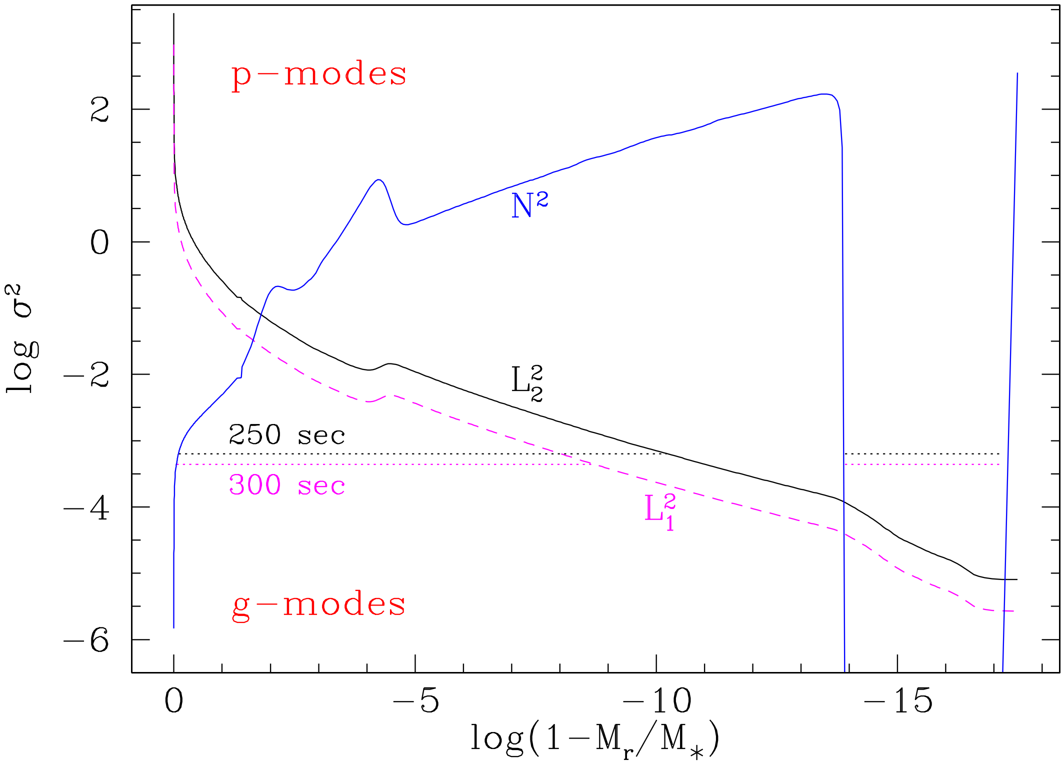

Figure 6.5 A propagation diagram for a representative asteroseismic fit, a WD model with stellar mass 0.710 $M_\odot$, an effective temperature $T_{\rm eff}$ = 11630 K, a He envelope mass of $M_{\rm He}/M_* = 10^{-2.1}$, and a H envelope mass of $M_{\rm H}/M_* = 10^{-4.5}$. The run of the Brunt-Väisälä frequency is shown in blue. The run of the Lamb (acoustic) frequency for an $\ell = 1$ mode is shown as a dashed magenta line, while the Lamb frequency for an $\ell = 2$ mode is shown as a solid black line. The horizontal axis is in fractional mass units; the surface is to the far right, while the center is to the far left. The base of the convection zone can be seen as the sharp drop in N^2 around $(1 - M_{\rm r}/M_*) \simeq 10^{-14}$.

However, an even more informative display of how each mode could probe the star differently can be found in Figure 6.6. Here we plot, as a function of the "normalized buoyancy radius" (see Montgomery et al. 2003), the weight functions for N^2 (see Equation 8c of Kawaler et al. 1985) for our best identifications of the modes in WD 0111+0018. The weight function essentially shows where in the star an excited pulsation is most resonant; it shows the sensitivity of a mode's period to changes in the equilibrium model.

Immediately evident from this exercise is that the majority of the energy of the 292.9 s mode, f_1, is located in the He layer or the region of the He-H transition. Conversely, nearly all the energy of the 255.7 s mode, f_2, is resonant much deeper in the star, inside the C/O-He transition. This suggests that the 255.7 s mode energy is predominantly resonant inside the core, while the 292.9 s mode samples significantly more of the surface layers of the star. The 255.7 s mode would therefore be much less sensitive to changes in the outer regions of the WD.

6.4.4 Additional Mechanisms for Rapid Period Change

Given the insensitivity of the 255.7 s mode to changes in the outer layer of the star, one possibility for the new timescale represented by the fast rate of change of period with time in WD 0111+0018 involves a change in the surface layers of the star at a rate much faster than from cooling alone but much slower than the timescales associated with the pulsations themselves. For instance, the depth of the convection zone of the WD could change gradually, perhaps as a result of a change in the global magnetic field of the WD. We have seen evidence for rapid changes in the pulsation profile of WDs in the past: especially notable is the so-called "sforzando" event seen in GD 358 in 1996, in which this DBV changed from a highly multi-periodic pulsation spectrum to a higher-amplitude, monoperiodic

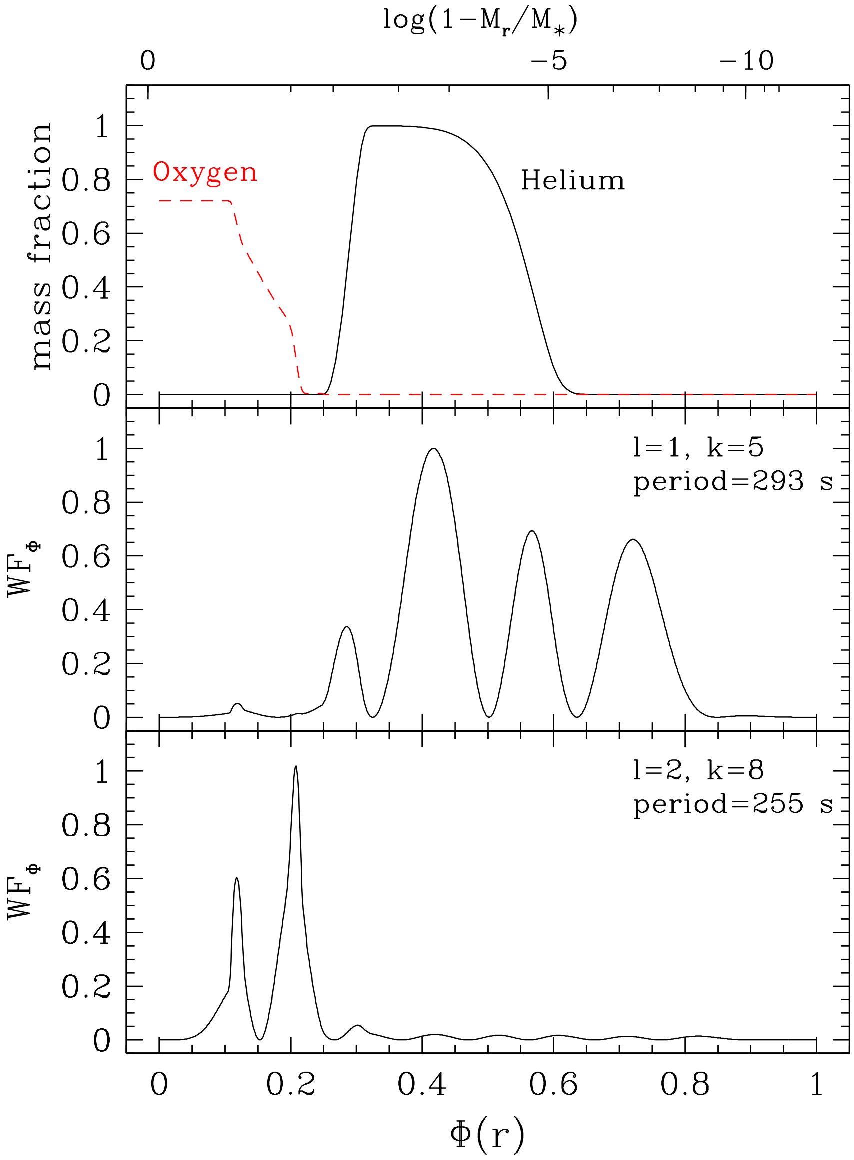

Figure 6.6 We can investigate how each pulsation samples the star by plotting a weight function (WF_Φ) for each mode. The top panel shows the chemical transition zones as a function of depth in the star. The bottom two panels show the weight functions for our best models (which are only marginally constrained) to represent f_1 and f_2, respectively. All plots are shown as a function of the "normalized buoyancy radius," $\Phi(\mathrm{r})$, described in Montgomery et al. (2003), where 0 is the center and 1 is the surface of the WD. The corresponding mass fraction is shown at the top of this figure.

pulse shape, indicating a rapid thinning of the convection zone during this event (Provencal et al. 2009, Montgomery et al. 2010).

We have investigated the plausibility of this scenario by comparing two slightly different theoretical models. Both model WDs have identical masses (0.71 $M_{\odot}$), effective temperatures (11810 K), and chemical profiles. However, we have changed the efficiency of convection by varying the mixing length parameter: in our initial model we use ML2/α=1.23 and in the other we use ML2/α=1.12. This effectively, albeit superficially, causes the second model to have a slightly thinner convection zone.

We take the difference of the periods computed by the first model with the periods from the second to estimate the effect these changes would have on different modes. We find that even the shortest period $\ell = 1, k = 1$ pulsations would change in mode period by more than 1 ms from one model to the next. This result can reproduce the observed rates of period change in WD 0111+0018 if the timescale of this change in the depth of the convection zone acts on the order a few decades.

One way to perturb the overall depth of the convection zone is to introduce a gradual change in the global magnetic field strength. In fact, increasing the global magnetic field from 0 G to 1 kG would effectively change the depth of the convection zone by the same amount as changing the convective efficiency from ML2/α=1.23 to ML2/α=1.12 (Montgomery & Vishniac, in preparation). It is possible then that the rapid period change we observe in WD 0111+0018 could be related to a secular (or long-term periodic) change in the strength of the magnetic field in the star. If this is indeed a byproduct of a stellar cycle, we might expect our heretofore secular increase to at some point turn over or in fact become discontinuous when the magnetic cycle changes course. Future observations of WD 0111+0018 will help constrain this hypothesis.

Another mechanism that could affect one mode differently than another, in the way we see in WD 0111+0018, is a changing rotation rate. Rotation will act to break spherical symmetry, splitting non-radial pulsations into $(2\ell + 1)$ azimuthal components that would normally be degenerate with the $m = 0$ component (Hansen et al. 1977). However, if the rotation rate were somehow to change (a spin-up or spin-down), only the $m \neq 0$ components would be affected. If f_1 is an $m = \pm 1$ mode and f_2 is an $m = 0$ mode, a changing rotation rate could explain the large difference in rates of period change between the two.

Our observed rate of change of period with time for f_1 would require the rotation of the WD to change at a rate $|\dot{P}_{\rm rot}| > 0.3$ s yr^{-1}. Such a rapid change would require a tremendous reservoir of angular momentum to redistribute, and some place to deposit this energy. This appears especially unlikely given the observational result that the hot pulsating white dwarf PG1159-035 rotates as a solid body through more than 97.5% of its mass, indicating that WDs have very little angular momentum, even at $T_{\rm eff} > 80{,}000$ K (Charpinet et al. 2009).

Unfortunately, we do not observe any other multiplet components for f_1 or f_2, making it difficult to definitively rule out this rotational effect[2]. But our results from the convective light curve fitting discussed in Section 6.4.1 did yield predictions for the m value of each mode: $m = 0$ for f_1 and $m = 0, \pm 1$ for f_2. This contradicts the values needed to invoke a changing rotation rate to explain the different rates of period change between these modes.

Some additional effects intrinsic to the star that could cause phase varia-

---

[2] Due to inclination effects, it is not uncommon to see an $m = \pm 1$ component of a rotationally split multiplet and not the $m = 0$ central component. This is well illustrated for different ℓ,m values in Figure 1 of Brassard et al. (1995). It is also possible that only one component of a multiplet is excited.

tions include linear interference (such as beating of closely spaced modes), nonlinear interactions with other modes (such as mode coupling) and a precession of the rotation axis with our line of sight (Winget et al. 1990). Each of these cases would simultaneously affect the amplitude of a given mode. Since we do not see evidence of the amplitudes evolving identically with the phase (comparing Figure 6.2 with Figure 6.3), none of these are likely responsible for the inferred high rates of period change in WD 0111+0018.

6.5 Conclusions

As part of a search for substellar companions to isolated WDs, we have discovered a DAV, WD 0111+0018, with an unexpectedly fast rate of change of period with time. We see this anomalously high rate reflected in not only the highest-amplitude mode in the star at 292.9 s but also the two nonlinear combination frequencies that sample this parent mode. All three periodicities are changing at a rate faster than 10^{-12} s s^{-1}, more than two orders of magnitude more quickly than expected from cooling alone in a DAV.

The pulsation period of the other parent mode at 255.7 s is increasing at a rate at least an order of magnitude more slowly, which allows us to rule out an extrinsic source of this rapid period change. Instead we are likely observing a physical phenomena intrinsic to the star acting on a timescale we have not yet observed in a DAV.

This discovery indicates that our understanding of the expected rates of period change for the slow and simply evolving DAVs is far from complete. It also complicates, in a macroscopic sense, our ability to infer the contributions of exotic weakly interacting particles such as axions to anomalies in the rate of change of period with time of DAVs.

We have attempted to use the nonlinear combination frequencies present in this star as probes of the spherical degree of the two parent modes. Using convective light curve fitting (Montgomery 2005), we find that the 292.9 s mode is best represented as an $\ell = 1$, $m = 0$ mode and that the f_2 parent mode at 255.7 s best fits as an $\ell = 2$, $m = \pm 1$ mode. This identification, if confirmed, would rule out a changing rotation rate as the explanation of the rapid period change in the 292.9 s mode.

Guided by the spherical degrees we identify by this convective light curve fitting we have found a best-fit asteroseismic model, which is admittedly poorly constrained. Still, this exercise suggests that f_1 is an $\ell = 1, k = 5$ mode and f_2 is an $\ell = 2, k = 8$ mode. We construct a weight function, and show that this solution for f_2 is almost entirely resonant inside the core, and is thus much less sensitive than f_1 to changes in the outer regions of the WD.

We discuss a scenario where a gradual thinning of the convection zone could be responsible for the rapid rates of period change observed in this DAV. This thinning could be caused by increasing the global magnetic field by less than 1 kG over a decade. Such a hypothesis is hard to test empirically, although if this magnetic field change is related to a stellar magnetic activity cycle, we would expect an eventual turnover or discontinuity in the observed $(O - C)$ diagram.

Independent of the cause of this unexpected period change, we have for the first time shown that the evolution of nonlinear combination frequencies in a DAV matches the evolution of their parent modes. This behavior confirms that these combination frequencies are not independent pulsation modes but rather artifacts from some nonlinear distortion occurring in the star.

Table 6.2. Journal of observations.

Subgroup	UT Date	Length (hr)	Seeing ($''$)	Exp. (s)
2003a	27 Jan 2003	1.5	2.3	15
	02 Feb 2003	0.9	1.6	20
2004a	20 Nov 2003	2.9	2.3	15
	30 Nov 2003	3.0	2.4	15
2005a	12 Dec 2004	5.0	2.5	15
	14 Dec 2004	4.2	2.7	15
	16 Dec 2004	3.4	1.4	15
2006a	03 Dec 2005	3.5	1.8	15
	06 Dec 2005	5.4	1.5	15
2006b	30 Dec 2005	3.4	2.0	15
	31 Dec 2005	2.8	2.0	15
	03 Jan 2006	2.6	1.6	15
2007a	19 Sep 2006	3.1	1.5	15
	22 Sep 2006	2.7	1.7	15
2007b	25 Nov 2006	6.1	1.3	10
2010a	23 Aug 2009	2.2	1.6	15
	24 Aug 2009	4.2	1.4	15
2010b	15 Sep 2009	5.5	1.5	15
2010c	11 Nov 2009	3.5	1.6	15
	17 Nov 2009	3.7	2.7	30
	21 Nov 2009	7.4	1.6	30
2010d	12 Jan 2010	3.3	2.1	15
	13 Jan 2010	3.6	1.8	15
2011a	12 Sep 2010	3.6	1.1	15
	13 Sep 2010	6.0	1.6	15
2011b	07 Oct 2010	4.5	1.3	15
	08 Oct 2010	4.3	1.6	15
	09 Oct 2010	5.3	1.3	15
2011c	10 Nov 2010	1.7	1.8	15
	11 Nov 2010	3.1	1.3	15
2011d	02 Jan 2011	2.8	3.0	20
	04 Jan 2011	4.1	1.6	15
	05 Jan 2011	1.7	1.7	20
2012a	02 Oct 2011	3.8	1.2	15
	03 Oct 2011	2.6	1.2	15
2012b	23 Oct 2011	4.5	1.5	15
2012c	01 Feb 2012	1.2	1.4	15
	02 Feb 2012	1.2	2.5	15
	03 Feb 2012	1.8	2.1	15

Table 6.3. Observed times of maximum in WD 0111+0018

	Time of Maximum ($\mathrm{BJD_{TDB}}$)	Epoch	$(O-C)$ (s)	σ (s)
f_1	2452668.431022	551	-0.11	4.41
	2452968.919383	89176	5.29	1.96
	2453353.385279	202569	25.11	1.62
	2453709.441810	307583	56.14	1.30
	2453725.336726	312271	53.99	1.34
	2453999.274020	393065	94.00	1.38
	2454064.667839	412352	103.15	1.33
	2455067.170353	708026	305.96	1.09
	2455089.880472	714724	319.29	1.69
	2455152.022733	733052	327.43	0.87
	2455209.164001	749905	342.55	1.31
	2455452.386565	821640	412.39	1.24
	2455477.944792	829178	429.02	1.00
	2455511.887808	839189	440.13	1.29
	2455565.211171	854916	443.63	1.37
	2455837.226626	935143	536.16	1.07
	2455857.749832	941196	549.35	1.67
	2455959.724574	971272	574.11	2.94
f_2	2452668.432414	632	-2.94	6.75
	2452968.917516	102179	0.57	3.07
	2453353.384106	232107	5.55	2.53
	2453709.440530	352434	1.93	2.15
	2453725.333732	357805	3.46	2.00
	2453999.273126	450381	19.25	2.58
	2454064.668563	472481	11.27	2.06
	2455067.167424	811269	27.44	1.75
	2455089.875468	818943	37.12	2.11
	2455152.018898	839944	30.44	1.34
	2455209.158663	859254	34.84	2.40
	2455452.382727	941450	38.19	1.96
	2455477.937402	950086	48.08	1.66
	2455511.880763	961557	33.06	1.86
	2455565.206336	979578	42.18	2.23
	2455837.222237	1071504	49.81	1.65
	2455857.743562	1078439	62.61	2.60
	2455959.716124	1112900	55.88	4.21
$2f_1$	2452668.432466	1103	-11.08	10.53
	2452968.917468	178351	-3.06	3.98
	2453353.385256	405138	33.60	3.11
	2453709.441750	615166	61.32	2.54
	2453725.336700	624542	62.18	2.86
	2453999.273975	786130	100.45	2.92
	2454064.669411	824705	102.78	2.50
	2455067.170145	1416052	297.94	2.62
	2455089.878699	1429447	322.50	2.64
	2455152.022654	1466104	330.52	1.89
	2455209.163883	1499810	342.33	2.46

Table 6.3—Continued

	Time of Maximum ($\mathrm{BJD}_{\mathrm{TDB}}$)	Epoch	$(O-C)$ (s)	σ (s)
	2455452.386495	1643280	416.25	2.40
	2455477.942967	1658355	427.70	1.97
	2455511.885977	1678377	438.32	2.51
	2455565.211093	1709832	446.75	3.74
	2455837.228208	1870287	536.15	2.18
	2455857.747999	1882391	547.15	3.50
	2455959.722809	1942543	577.84	5.71
$f_1 + f_2$	2452668.431822	1183	-2.87	5.98
	2452968.918406	191355	2.36	2.44
	2453353.384661	434676	18.53	2.29
	2453709.441119	660017	34.57	2.73
	2453725.335107	670076	33.47	2.10
	2453999.273507	843446	62.98	1.87
	2454064.668225	884833	66.87	2.13
	2455067.168742	1519295	179.62	2.06
	2455089.877753	1533667	191.35	2.44
	2455152.020653	1572996	193.66	1.54
	2455209.162674	1609160	201.74	2.14
	2455452.384498	1763090	242.81	2.44
	2455477.940796	1779264	253.35	1.72
	2455511.884039	1800746	254.73	1.85
	2455565.210077	1834495	254.55	2.49
	2455837.225881	2006648	315.02	1.77
	2455857.746487	2019635	326.94	2.50
	2455959.720129	2084172	341.82	6.59

Chapter 7

Conclusions and Future Work

This dissertation has been a detailed observational exploration of optical variability in extremely low-mass (ELM; $M \leq 0.25\ M_{\odot}$) white dwarf (WD) stars, and I have been incredibly fortunate to work with a class of stars with such an immediate and wide-ranging need for high-speed photometric monitoring. These collected works have enabled swift and considerable progress on constraining some of the fundamental properties of low-mass white dwarfs and their environments, and have generated considerable excitement in both the binary evolution and stellar pulsation communities. Still, there remains considerable work to be done.

7.1 Discussion of Results

We presented in Chapter 2 high-speed photometry of 20 low-mass WDs in compact binaries with unseen companions, all of which have orbital periods less than 4 hr. These observations further constrain the physical and binary parameters of some of the most compact detached binary systems ever found.

At least eight of these compact systems show high-amplitude tidal distortions from their massive, unseen companions, and at least 10 systems show the special relativistic Doppler beaming effect. In 2011, before this work began, not a single tidally distorted WDs was known. We have leveraged the discovery of the first eight WDs with ellipsoidal variations to constrain the mass-radius relationship for He-core WDs with masses below 0.2 $M_{\odot}$. We find that these low-mass

WDs all have radii exceeding 0.05 $R_\odot$, consistent with He-core WD models. Matching the derived surface gravities obtained from spectroscopic observations to the amplitude of the ellipsoidal variations, we have also been able to put marginal constraints on the system inclination, which in turn constrains the unseen companion in these compact binary systems. The shortest-period binaries are strong sources of gravitational wave radiation, and we expect to use the time-of-minimum of those that display ellipsoidal variations to detect orbital decay from these waves, which carry away orbital angular momentum.

For the most compact of these systems, the signature of orbital decay will be readily observable on short timescales. Indeed, for the most compact detached WD system known, J0651+2844, we have already detected and measured this signature. This 12.75-min displays both primary and secondary eclipses, which allow us to constrain the radii of both WDs and provide an excellent clock of the orbital period. The low-mass primary is a 0.26 ± 0.04 $M_\odot$ WD with a radius of 0.0371 ± 0.0012 $R_\odot$. Given the derived inclination of 84.4 ± 2.3 degrees from the eclipses and the mass function, we determine that the much fainter secondary is a 0.50 ± 0.04 $M_\odot$ WD with a radius of 0.0142 ± 0.0010 $R_\odot$. By measuring the changing mid-eclipse times we have shown that the orbit is decaying at a rate of $(-8.9 \pm 1.0) \times 10^{-12}$ s s^{-1} (or -0.28 ± 0.03 ms yr^{-1}), in line with the expected decay from general relativity. This marks the cleanest indirect detection of gravitational waves using visible light.

The work presented here also includes the discovery of the first five pulsating ELM WDs, which presents the first opportunity to explore the interior structure of a putatively He-core WD that never initiated core helium burning. Spectral fits indicate these are both the coolest and lowest-mass pulsating WDs ever found. All have effective temperatures below $10{,}000$ K and masses below 0.25 $M_\odot$, establishing these putatively He-core WDs as a cooler class of pulsating hydrogen-atmosphere WDs (DAVs). These stars exhibit long-period variability consistent with non-radial g-mode pulsations; these are not tidally induced pulsations and are so far best explained by the same hydrogen partial-ionization driving mechanism at work in classic C/O-core DAVs. The two lowest-mass ELM WDs also exhibit lower-amplitude, short-period variability that is likely evidence for hybrid acoustic (p-mode) pulsations, which provide an exciting opportunity to probe this WD in a complimentary way. This marks the first evidence for p-mode pulsations ever observed in a pulsating WD, after having been predicted more than 30 years ago. Asteroseismology will go a long way in confirming that these low-mass WDs indeed have helium cores, and can also probe the star's hydrogen layer mass and rotation rate, which in turn constrains hypothesized residual hydrogen burning and tidal synchronization, since we have detected close, unseen companions for at least three of these systems.

In tandem with the discovery of pulsations in low-mass, He-core WDs and given the prospect asteroseismology holds for discerning the interior composition of these stars, we have searched for pulsations in very massive WDs ($M \geq 1.0$ $M_{\odot}$), as well. This search has yielded the most massive pulsating WD ever found, GD 518, a 1.2 $M_{\odot}$ WD which may have a highly crystallized oxygen-neon (ONe) core. We see evidence for multi-periodic luminosity variations at timescales ranging from roughly $425 - 595$ s and amplitudes up to 0.7% in this star, although the pulsations do not appear especially coherent from night to night. This could be an observable consequence of the WD being highly crystallized; we expect that pulsation energy would be largely excluded from any interior crystallized mass, so it is conceivable that the oscillations in this crystallized WD have less mode inertia and can vary on shorter timescales relative to the pulsation periods than is usually the case in canonical-mass, 0.6 $M_{\odot}$ CO-core WDs. This dissertation work has thus uncovered both the lowest- and highest-mass pulsating WDs, objects at each extremum that will shed considerable light on the late stages of binary and stellar evolution.

In addition to the discovery of pulsations in low- and high-mass WDs, we have also extended observations of hot, CO-core DAVs as part of a planet search using the arrival times of stable pulsation modes in these stars. One star in this sample, WD 0111+0018, shows an anomalously rapid rate of period change in its highest-amplitude mode that is incompatible with simple Mestel cooling of an isolated WD. This is the most rapid rate of period change ever observed in a DAV, $dP/dt > 4 \times 10^{-12}$ s s^{-1}, well in excess of the theoretically predicted rate of period change from cooling alone for an $11{,}810$ K WD, which is not expected to exceed 10^{-14} s s^{-1}. This likely signifies the discovery of a new physical timescale, intermediate between growth-times and cooling times, in the evolution of DAVs.

Finally, we present in the Appendix an exciting consequence of our extensive observing time at McDonald Observatory: the discovery of the first DAV in the *Kepler* field. The spacecraft obtained nearly 1.5 yr of near-continuous ($> 90\%$ duty cycle) observations every minute on this WD, marking the most extensive coverage of any DAV ever obtained.

7.2 Future Work

This dissertation highlights discoveries that have extended the scope of previous work and opened up fertile new fields of investigation. In some cases it is the first of many steps on the path toward detailed exploration of exciting new physics.

Most significantly, our refinement of the orbital period in the 12.75-min J0651+2844 has the potential to position this system as the best-constrained verification binary for future space-based gravitational wave detectors such as *eLISA*.

It is possible that this wonderful binary will be the source of the first directly detected gravitational waves. It is the second-strongest gravitational wave source known in the mHz regime, for which space-based detectors will be most sensitive, and it is by far the cleanest strong gravitational wave source, since both stars are currently detached. We have an estimate of the orbital period currently good to a fraction of a millisecond, which will give us an excellent test frequency at which to tune future gravitational wave detectors. Given current design specifics, *eLISA* would detect the gravitational wave strain ($h \sim 10^{-22}$) from J0651+2844 within its first week of operation.

In addition, J0651+2844 provides an excellent opportunity to explore the effect of tides on compact, merging binary systems. On the timescale of a few years or less it will be possible to measure any mismatch between the observed rate of orbital decay and the rate predicted solely by the emission of gravitational radiation. We expect that these tides will act as a torque to spin-up the WDs if the system is synchronized, further robbing the orbit of angular momentum and increasing the rate of orbital period decay. The degree to which this tidal torquing influences the orbital evolution depends on the effective tidal locking, which is determined by the physical structure of the low-mass WD. This effect could increase the rate of period decay by at least 5% if the system is synchronized, depending on the heretofore unconstrained efficiency of depositing that energy in a 0.26 $M_{\odot}$ WD. Continued monitoring of this unique 12.75-min system will make for an unprecedented laboratory for testing tidal effects in merging compact binaries.

While J0651+2844 was the first system with a low-mass WD for which we could detect the orbital decay from gravitational wave radiation, there are two other exciting systems that can be monitored to make a similar measurement. Instead of timing the mid-eclipses, it is possible to monitor the time-of-arrival of the minima of the ellipsoidal variations of the 39.1-min binary J0106$-$1000 and the 88.0-min binary J1741+6526 to observe the effects of gravitational radiation on the orbital period and thus the period of the ellipsoidal variations. Using the ephemeris established in this dissertation, it may be possible to detect the spin-up of the tidal bulge within a decade given further photometric observations.

In addition to continued photometry of our compact binaries, there is ample justification for more detailed follow-up observations of the new pulsating WDs discovered in the course of this dissertation. Further photometric monitoring will better constrain the periods of variability present, and discover any additional lower-amplitude oscillations. A huge leap forward is enabled by coordinated global, multi-site coverage using tools like the Whole Earth Telescope (WET, Nather et al. 1990).

We have already taken the first step along this path; I will lead analysis of a recent WET campaign on the third pulsating ELM WD found, J1518, which displays high-amplitude, non-sinusoidal, multi-mode variability. This relatively bright ($g = 17.4$ mag) WD was observed for nearly two months in 2013 April/May as the primary target of XCOV29, the 29th WET campaign. We amassed nearly 54 days of coverage from 19 different sites, yielding a better than 40% duty cycle. This WET data was obtained too late to be fully reduced and analyzed for this dissertation, but will be an immediate focus after my defense. Figure 7.1 shows a preliminary comparison of this WET campaign to our discovery data from McDonald Observatory. In fact, this was the first data taken using a share of the McDonald Observatory site time on the Las Cumbres Observatory Global Telescope network, from their 1.0m nodes at Cerro Tololo Inter-American Observatory and at the South African Astronomical Observatory. Such multi-site, near-continuous observations will help clean up the spectral windows caused by gapped coverage during our

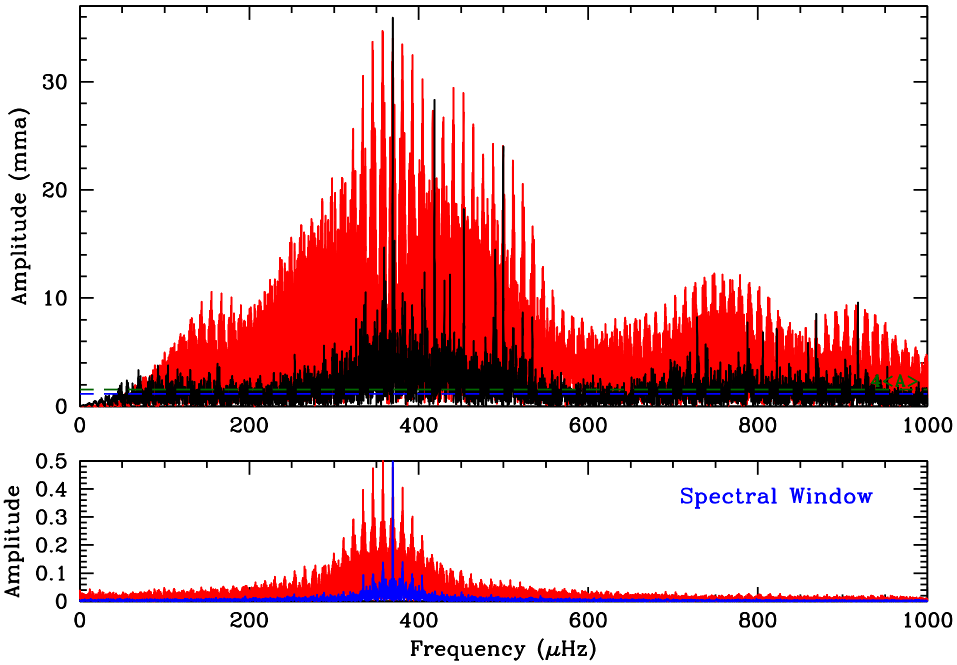

Figure 7.1 A comparison of the Fourier transforms of our single-site discovery observations of J1518 (red) and our subsequent Whole Earth Telescope campaign on the same star (black). The discovery photometry was spread over four months with roughly 1% duty cycle, while the WET data spans roughly two months with better than 40% duty cycle. The spectral window of the discovery data is shown in the bottom panel in red; the much improved WET spectral window is shown in blue.

discovery observations from McDonald Observatory, and will shed considerable light on the true periods of variability in these pulsating WDs.

The immediate next step will demand that theory catch up with observations by building a sufficiently robust suite of He-core models required to match the observed pulsation periods. Fortunately, our discovery of pulsations in ELM WDs has re-motivated theorists to consider pulsation models of He-core WDs extending beyond the pioneering work of Steinfadt et al. (2010b); this has already yielded interesting new results from the Argentinian group (Córsico et al. 2012b) and the extended Montreal group (Van Grootel et al. 2012). The Texas group continues to explore the pulsation properties of He-core WDs, and we will use the open-source stellar evolution code MESA to explore these properties. The fruits of some of these early MESA models can be found in Figure 4.14 of Chapter 4, but theoretical results remain unreliable until we can converge on an effective way to artificially but realistically lose mass from the ELM WD progenitors. Sufficient He-core WD models are needed in order to compare the observed periods to theory so that we may perform a full asteroseismic analysis of our stars.

A similar future awaits GD 518, the probable ONe-core WD we discovered in 2013 March. Very few models exist of such a massive WD, but the potential for this star to constrain both intermediate-mass stellar evolution *and* Supernova Ia progenitor systems will likely accelerate theoretical investigation of the pulsation properties of 1.2 $M_{\odot}$ WDs. In many ways, the work has only begun by discovering pulsations in this ultramassive WD.

Appendices

Appendix A

Details of Argos Observations and Reductions

Time-series photometry is the backbone of this observational dissertation. For handy reference, this appendix outlines the observing and reduction methods used for the vast majority of this work at McDonald Observatory. Even more details can be found in the Argos observing manual[1], "Observing Variable White Dwarfs with Argos/Raptor," which I have worked to update and maintain.

Our observations begin with the Argos instrument, a frame-transfer CCD mounted at the prime focus of the 2.1m Otto Struve telescope (Nather & Mukadam 2004). Argos[2] features a 512×512 back-illuminated, thermoelectrically cooled chip. Nearly all observations are obtained with 1×1 binning, which incurs a read noise of approximately 4 e^- r.m.s. At prime focus (f/3.9) our field of view is 2.8 arcmin on each side; our 13 μm $\times$ 13 μm pixels have an image scale of 3.05 pixels arcsec^{-1}. There is substantial dark current ($1 - 2$ ADU s^{-1} pixel^{-1}) since we run the CCD at -30 C. Observations have all been obtained through a 3mm blue-bandpass BG40 filter, which blocks much of the red light contributed by sky noise but lets through photons from our hotter WDs.

We obtain 30 dark frames at the start of the night, with the exposure lengths

---

[1] http://www.as.utexas.edu/mcdonald/facilities/2.1m/Argos-WhiteDwarfPulsations.pdf

[2] In 2011 December the original Argos camera head was destroyed in an unfortunate accident. An exact replica from Chris Clemens, Raptor, has since taken its place, although we still use the original Argos controller box, which was not harmed in the accident. I will continue to refer to this instrument setup as "Argos" throughout this work, even though all observations from 2012 January were technically obtained with the "Raptor" camera head.

we plan to use that night. We obtain dome flats, using a flat lamp controlled by a variac in order to keep our counts at $20{,}000 - 30{,}000$ ADU pixel^{-1} (the chip has 1% linearity below $40{,}000$ ADU and saturates at $65{,}000$ ADU). Our raw science frames are calibrated by dark subtraction and flat-fielding.

We perform weighted aperture photometry on the calibrated frames using the external IRAF package *ccd_hsp* written by Antonio Kanaan (Kanaan et al. 2002); apertures are extracted with radii ranging from $3 - 14$ pixels, in 1 pixel steps. Using the software package WQED, we divide the sky-subtracted light curves by the sum of the brighter comparison stars in the field of view to correct for transparency variations, and apply a timing correction to each observation to account for the motion of the Earth around the barycenter of the solar system (Stumpff 1980, Thompson & Mullally 2009).

In order to find the optimal aperture size, we reduce each aperture, and choose the aperture that minimizes the formal uncertainties resulting from a linear-least squares fit at the known period of variability. If the object is not known to vary, we choose the aperture with the smallest r.m.s. scatter in the light curve. Choosing the smallest appropriate aperture minimizes sky noise, which can add significantly to the noise budget for the faintest stars in our sample. For example, a 4 pixel aperture was chosen for run A2487 on J0106−1000, a $g = 19.8$ mag WD+WD binary. Over-estimating the aperture by a factor of two, using an 8-pixel radius, introduces more than 60% larger uncertainties in a linear least-squares fit at the signal of interest, 19.6 min. The difference can be fully appreciated in Figure A.1. Similarly, for run A2620 on the significantly brighter, $g = 17.4$ mag WD0751−0141 a 4-pixel aperture yields the best results. An 8 pixel aperture has just 15% larger formal uncertainties in the signal of interest at 57.6 min. For the faintest targets, aperture selection is key for optimal results.

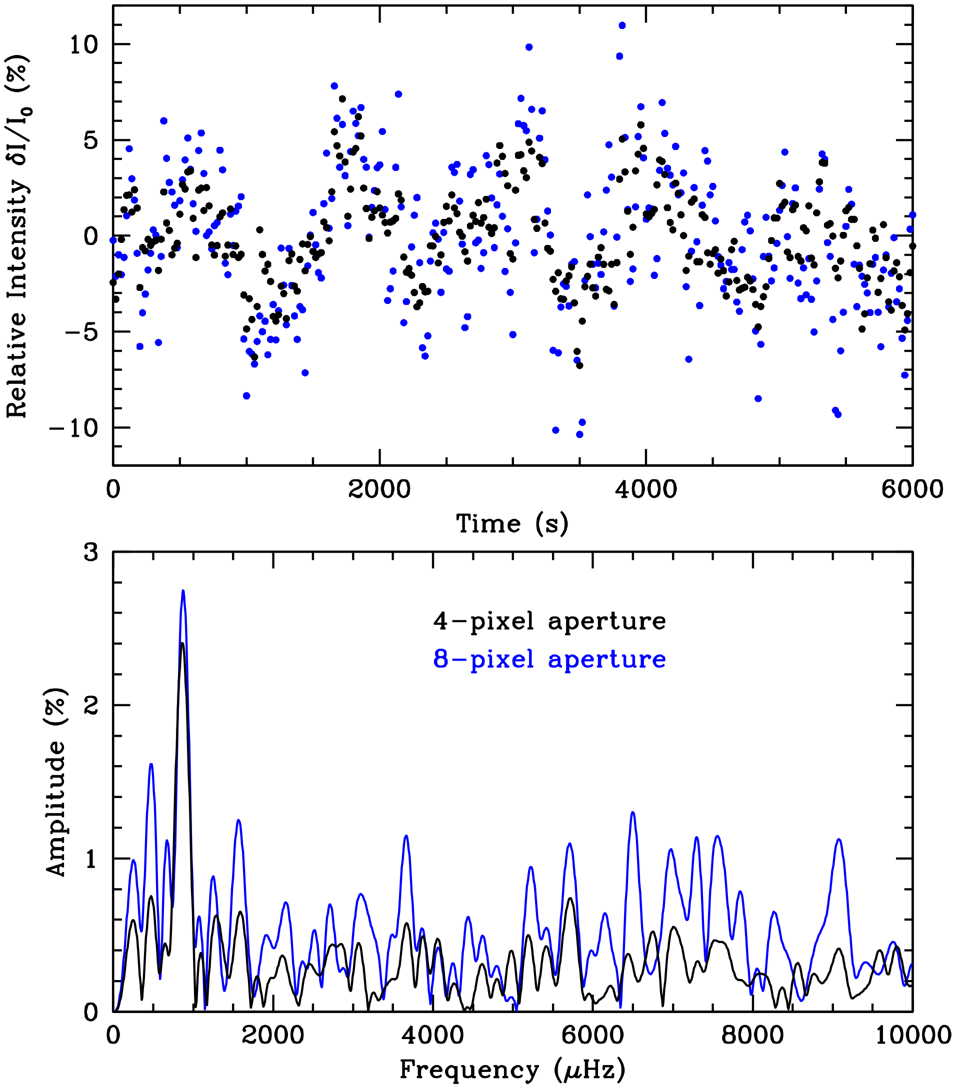

Figure A.1 An illustration of the utility in finding the optimal aperture for faint objects when observing with Argos. Here we compare the full reductions for J0106−1000, a $g = 19.8$ mag WD+WD binary with 1.77% ellipsoidal variations peaking every 19.6 min, using an aperture with a 4-pixel radius, the optimal choice shown in black, and an 8-pixel aperture, which is a factor of two too large and shown in blue. The point-to-point scatter is much greater with the larger aperture (2.3% for 4-px versus 3.7% for 8-px), as can be seen in the light curve in the top panel. The Fourier transform for both, shown in the bottom panel, is also considerably noisier for the larger aperture. This run, A2487, was taken on 2011 October 24.

Appendix B

Discovery of a ZZ Ceti in the Kepler Mission Field

We report the discovery of the first identified pulsating DA white dwarf in the field of the *Kepler* mission, WD J1916+3938 (*Kepler* ID 4552982). This ZZ Ceti star was first identified through ground-based, time-series photometry, and follow-up spectroscopy confirm it is a hydrogen-atmosphere white dwarf with $T_{\rm eff}$ = $11{,}130 \pm 120$ K and $\log g$ = 8.34 ± 0.06, placing it within the empirical ZZ Ceti instability strip. The object shows up to 0.5% amplitude variability at several periods between $800 - 1450$ s. Extended *Kepler* observations of WD J1916+3938 could yield the best lightcurve, to-date, of any pulsating white dwarf, allowing us to directly study the interior of an evolved object representative of the fate of the majority of stars in our Galaxy.[1]

B.1 Introduction

Hydrogen atmosphere (DA) white dwarf stars account for more than 80% of all spectroscopically identified WDs (Eisenstein et al. 2006). When these objects cool to around $12{,}500$ K, the hydrogen in their non-degenerate atmosphere forms a partial ionization zone, impeding energy transport and leading to global g-mode oscillations. It is believed that all DA white dwarf stars with carbon/oxygen cores undergo such pulsations when they reach the appropriate temperature (Castan-

---

[1] *Significant portions of this chapter have been previously published as:* J. J. Hermes, Fergal Mullally, R. H. Østensen, Kurtis A. Williams, John Telting, John Southworth, S. Bloemen, Steve B. Howell, Mark Everett, and D. E. Winget, *The Astrophysical Journal*, **741**, L16 (2011)

heira et al. 2007), allowing us to probe a stellar population representative of the fate of most stars in our Galaxy, including our Sun.

Asteroseismology provides a unique opportunity to investigate the internal structure of these stars (see reviews by Winget & Kepler 2008, Fontaine & Brassard 2008). Given enough observed modes, we can put accurate estimates on the overall stellar mass, hydrogen and helium layer masses, internal chemical transition zones, magnetic field strength, and rotation rate. Performing asteroseismology on a WD benefits from its degenerate interior, which makes its structure less complicated than for stars still undergoing fusion.

In an effort to reduce aliasing caused by gaps in the data, much effort has been expended to obtain uninterrupted time-series observations of these variable DA (DAV) stars (also known as ZZ Ceti stars), using the Whole Earth Telescope (Nather et al. 1990). However, these ground-based campaigns rarely extend beyond a few weeks, fundamentally limited by weather and moonlight, not to mention the availability of telescope time.

Space-based photometry has revolutionized the extended coverage of stars. The *Kepler* spacecraft was launched in March 2009, and while its primary mission is to detect Earth-sized planets around Sun-like stars, its extensive light curves are transforming many fields in asteroseismology. The spacecraft stares at some 156,000 stars and has the capability to monitor 512 objects with one-minute cadence. Month-long observations typically yield a duty cycle of more than 97% with micromagnitude precision, depending on the brightness of the target.

Despite an expansive search (Østensen et al. 2010, 2011b) in which 17 compact objects were targeted by *Kepler* as potential pulsating white dwarf stars, none were observed to vary above the 4σ detection limit. One DAV candidate, KIC10420021, was monitored for 7 months and is stable to at least 60 parts-per-million (ppm). *Ke-*

pler has monitored a uniquely variable DA, but that system is best explained by a magnetic spin-modulated WD model, not by pulsations (Holberg & Howell 2011). However, as part of a recent auxiliary search, Østensen et al. (2011a) announced the successful detection of the first pulsating WD in the *Kepler* field, a V777 Her star. It was quite a fortuitous discovery, as this was just the second DB found in the field and has a *Kepler* magnitude of $Kp = 18.46$.

Using facilities at the McDonald Observatory in west Texas, we have discovered the first ZZ Ceti star in the *Kepler* field, WD J191643.83+393849.7 (*Kepler* ID 4552982, hereafter WD J1916+3938). This object has a *Kepler* magnitude of $Kp = 17.85$ (Brown et al. 2011b). Previous *Kepler* observations of such faint, blue objects have reached better than 130 ppm (0.013%) precision with just one month's worth of data. Extended short-cadence *Kepler* observations will provide a detailed look at the pulsation spectrum of this cool ZZ Ceti star.

B.2 High-Speed Photometric Observations

B.2.1 Selection and Time-Series Photometry

Potential pulsating WDs in the *Kepler* field were selected from a recent list of high reduced proper motion stars in the SuperCOSMOS Sky Survey (Rowell & Hambly 2011). From their catalog of roughly 10,000 candidate WDs, we found 20 that actually fell on *Kepler* CCDs. Five of those had already been surveyed by *Kepler* and found not to vary (Østensen et al. 2010, 2011b).

One of the remaining 15, WD J1916+3938, fell in the footprint of the POSS-II survey, and showed $(B-R)$, $(R-I)$ colors extremely close to values for a typical ZZ Ceti star, so it was targeted for time-series photometric observations. The discovery observations were taken at the McDonald Observatory using the Argos instrument, a frame-transfer CCD mounted at the prime focus of the 2.1m Otto Struve telescope

(Nather & Mukadam 2004). Data were obtained through a 3mm BG40 filter to reduce sky noise.

Photometric observations were carried out over 6 nights in May 2011, for a total of more than 21 hours of coverage. Exposure times ranged from 5 to 15 seconds, depending on seeing and cloud conditions.

We performed weighted, circular aperture photometry on the calibrated frames using the external IRAF package *ccd_hsp* written by Antonio Kanaan. We divided the sky-subtracted light curves using at least 3 brighter comparison stars in the field to allow for fluctuations in seeing and cloud cover. Using the WQED software suite (Thompson & Mullally 2009), we fit a second-order polynomial to the data to remove the long-term trend caused by atmospheric extinction, and applied a timing correction to each observation to account for the motion of the Earth around the barycenter of the solar system.

Figure B.1 shows a representative light curve, smoothed by a four-point moving average window for visualization purposes with the brightest comparison star offset below.

B.2.2 Ground-Based Light Curve Analysis

We performed a Fourier transform of the entire data set, 7454 points spread over nearly a month for a duty cycle of 3.1% (Figure B.2). This FT extends to the Nyquist frequency for *Kepler* short-cadence observations; there is nothing above the 4σ threshold for higher frequencies. The window function is quite messy, as there are variably spaced gaps in the data.

While *Kepler* will allow us to improve our determination of the periodicities present in this star, we attempt to identify the periods present in all our May 2011 data. Table B.1 lists the highest seven peaks, all with power above four times the

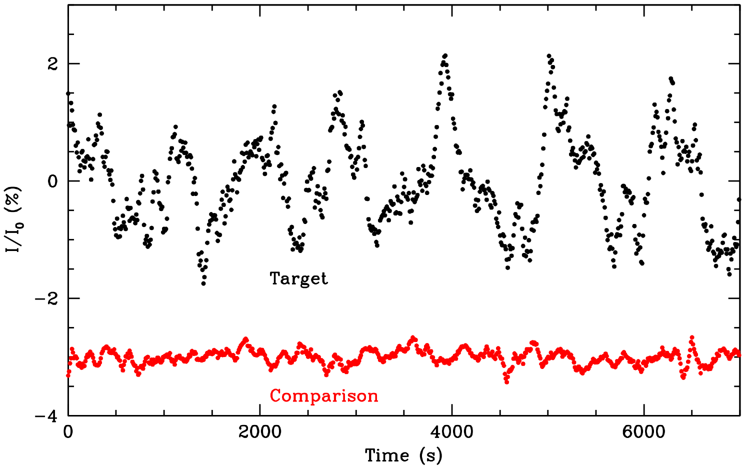

Figure B.1 A portion of the lightcurve for WD J1916+3938, taken on 2011 May 11, that has been smoothed by a four-point moving average. The red, offset lightcurve is of the brightest comparison star in the field.

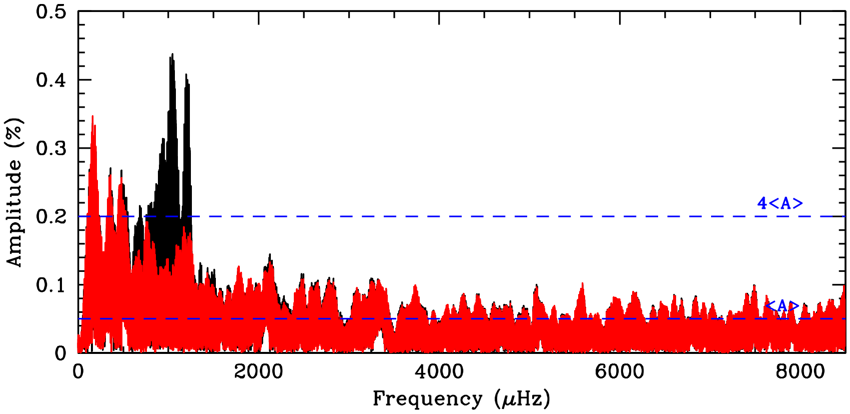

Figure B.2 A Fourier transform of our May 2011 data on WD J1916+3938. The red transform has been computed after prewhitening by the seven periodicities listed in Table B.1, which removes all peaks above four times the mean FT level, σ. We have ignored the low-frequency peaks in this FT, with periods longer than 2,000 s, which are likely to be noise from variability in the Earth's atmosphere.

Table B.1 Frequencies present in WD J1916+3938 from May $3-31$.

ID	Freq. (μHz)	Period (s)	Amp. (%)
f_1	1032.1	968.9	0.44
f_2	1213.7	823.9	0.38
f_3	1070.1	934.5	0.36
f_4	1198.9	834.1	0.32
f_5	918.3	1089.0	0.25
f_6	696.0	1436.7	0.24
f_7	854.8	1169.9	0.23

mean FT level. The large aliasing present makes it nearly impossible to determine, with much certainty, the true periods in this short, ground-based data set, so we have omitted the formal least-squares errors. It appears this star has several excited modes between $800-1450$ s, although the amplitudes appear unstable from night to night. There is consistently power well above the noise around 970 s and 820 s each night, although the level of excitation appears inconsistent.

For comparison sake, we also took an FT of all the data for the brightest comparison star in the field. The average amplitude over all frequency space is 0.03%, the same level as our formal least-squares amplitude errors.

B.3 Spectroscopic Analysis

B.3.1 Spectroscopic Observations

Excitement among the *Kepler* compact object community, specifically Working Group 11 within the Kepler Asteroseismic Science Consortium (KASC), led to multiple spectroscopic follow-ups, and WD J1916+3938 was observed using 4 different telescopes, especially after our first spectrum from the Nordic Optical Telescope (NOT) confirmed the object as a DA within the ZZ Ceti instability strip.

Table B.2 Spectroscopically determined parameters.

Instrument	Date Observed	Coverage (Å)	$T_{\rm eff}$ (K)	$\log g$ (dex)
NOT/ALFOSC	2011-05-22	3850–6850	11,152 ± 80	8.24 ± 0.06
CAHA/TWIN	2011-06-17	3500–5450/ 5700–6790	11,116 ± 139	8.36 ± 0.09
HET/LRS	2011-06-14	4300–7200	11,104 ± 150	9.51 ± 0.43
KPNO/RCS	2011-06-09	3650–5120	11,115 ± 92	8.43 ± 0.05
Adopted			**11,130 ± 120**	**8.34 ± 0.06**

Fits to these observations were used to derive an effective temperature and surface gravity.

Observations using the 9.2m Hobby-Eberly Telescope (HET) at McDonald Observatory were carried out with the Marcario Low Resolution Spectrograph (LRS) using its g2_2.0 setup. The observations using the 2.6m NOT at Roque de los Muchachos Observatory were done in low-resolution with the ALFOSC spectrograph and its grism #7. The observations using the 3.5m telescope at Calar Alto Observatory (CAHA) were done in medium-resolution with the TWIN spectrograph, using grating T06 for the red arm and grating T12 for the blue arm. Finally, the observations using the 4m Mayall Telescope at Kitt Peak National Observatory (KPNO) were done in low-resolution with the R-C CCD Spectrograph. Each spectral image and flux standard were reduced using standard long-slit IRAF routines.

The KPNO spectrum of WD J1916+3938, showing the Balmer lines Hβ through H9, can be seen in Figure B.3. Overplotted is the best-fit DA model spectrum.

We have fit model grid spectra to each of these observations, using the procedure outlined in Bergeron et al. (1992). The WD models used for the spectroscopic fitting were kindly provided by Detlev Koester and are described in Koester (2010). Balmer lines in the models were calculated with the modified Stark broad-

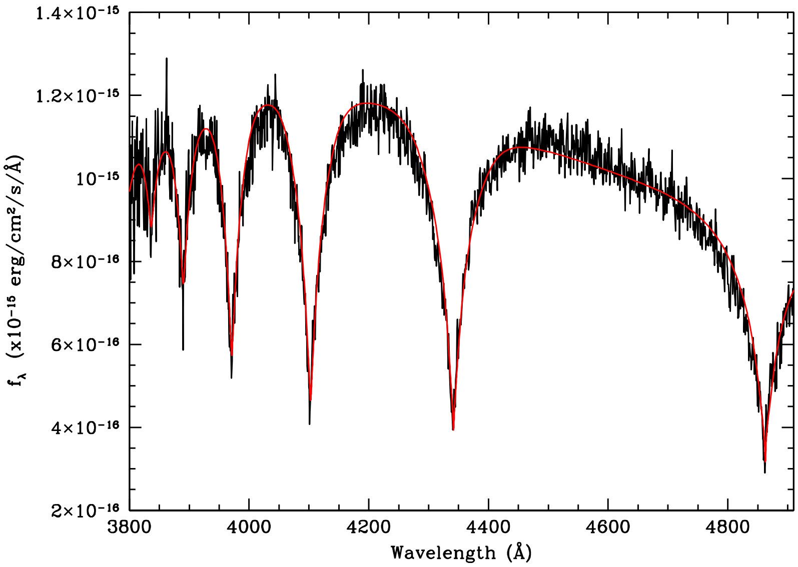

Figure B.3 The KPNO spectrum of WD J1916+3938, showing the Balmer lines Hβ through H9. Overplotted in red is the best-fit DA model spectrum.

ening profiles of Tremblay & Bergeron (2009), kindly made available by the authors, and use the mixing length prescription ML2/α=0.6. Table B.2 lists the best fits to the observations. Using a weighted mean of all four determinations, we adopt a best value of $T_{\rm eff}$ = $11{,}130 \pm 120$ K and $\log g$ = 8.34 ± 0.06. This places the object within the empirical ZZ Ceti instability strip.

B.3.2 Implications

ZZ Ceti stars at the hotter, blue edge of the instability strip tend to pulsate with short period (100 – 300 s) modes that have shown to be extremely stable in period and amplitude. Such stars have been the focus of work to detect an evolutionary rate of period change of these modes (e.g., Kepler et al. 2005, Mukadam et al. 2009). However, the ZZ Ceti stars near the cooler, red edge of the instability strip with effective temperatures near $11{,}000$ K typically feature much longer periods (> 600 s) and have more excited modes. These pulsations are typically unstable in amplitude and phase.

Spectroscopic fits show that WD J1916+3938 has an effective temperature that places it in the cooler region of the ZZ Ceti instability strip. This result is duly confirmed by our time-series photometric observations. WD J1916+3938 shows long-period oscillations — its weighted mean period (Mukadam et al. 2006) lies around 1003 s — that do not appear stable in amplitude. For example, during the runs from May $27 - 29$, the power observed in the mode near 824 s went from (0.66 ± 0.06)% to (0.88 ± 0.05)% to (0.43 ± 0.05)%, respectively.

Many modes in other cool ZZ Ceti stars have amplitudes that grow and decay in a way that cannot be explained by beating (e.g., Kleinman et al. 1998), so we expect the same is true with this star. The opportunity for nearly continuous *Kepler* observations of this amplitude modulation may afford us a completely new insight into the growth and decay of mode amplitudes, opening a new window into how these objects behave on a variety of timescales inaccessible from the ground.

B.4 Discussion and Conclusion

We have discovered just the second pulsating white dwarf in the *Kepler* field, and the first ZZ Ceti star suitable for *Kepler* monitoring. Several modes appear to be excited from 800 – 1450 s, with a fractional amplitude of up to 0.5%. Spectroscopic fits yield an effective temperature of $11{,}130 \pm 120$ K and a surface gravity of $\log g = 8.34 \pm 0.06$, which corresponds to a mass of $0.82 \pm 0.04\ M_{\odot}$ from the evolutionary models of Wood (1990). This spectroscopic temperature puts it on the cool, red edge of the ZZ Ceti instability strip, where pulsations may begin shutting down.

Submitted for *Kepler* observations through KASC, the spacecraft is scheduled to commence short-cadence observations on this ZZ Ceti pulsator in October 2011 (Q11). By virtue of its impressive duty cycle, we anticipate that extended *Kepler* observations will yield the best lightcurve, to date, of any pulsating white dwarf, even those that are more than four magnitudes brighter.

The lightcurves can be analyzed from a variety of asteroseismic angles. With enough modes, we will be able to put an accurate constraint on the overall mass of the WD. Perhaps more importantly, we may also extract an accurate estimate for the hydrogen layer mass, which controls the rate at which this star cools. This hydrogen mass fraction has been constrained through asteroseismology in fewer than a dozen DA WDs (Dolez et al. 2006), although Castanheira & Kepler (2009) attempted to derive the parameter from the few modes present in an ensemble of 83 ZZ Ceti stars. Uncertainties in this parameter is imprinted as scatter in the white dwarf luminosity function, which is used in cosmochronology to put an estimate on the age of the Galaxy (e.g., Winget et al. 1987, Harris et al. 2006).

The sensitivity of *Kepler* observations may also allow us to see a wealth of low-amplitude multiplet structure. Previous ground-based campaigns on cool ZZ Ceti stars, such as G29-38, have revealed instability in the amplitude of these multiplets (Kleinman et al. 1998). Extended *Kepler* coverage will allow us to observe how the amplitudes of all modes in this star change with time.

ZZ Ceti stars often exhibit some nonlinear combination frequencies, which are believed to arise from convective driving (e.g., Brickhill 1992, Wu 2001). If observable, these combination frequencies may be used to identify the spherical degree of the parent modes (Yeates et al. 2005). With an ideal *Kepler* lightcurve, we would be able to compare this mode identification with the ℓ values as determined from the period spacings. Pulse-shape fitting of properly identified modes may also be used to constrain some of the convective parameters in this star, especially the depth of the convection zone (Montgomery et al. 2010).

For now, though, we eagerly await the unrivaled staring competition *Kepler* will have with this cool ZZ Ceti star.

Bibliography

Althaus, L. G., Córsico, A. H., Isern, J., & García-Berro, E. 2010, A&A Rev., 18, 471

Althaus, L. G., García-Berro, E., Isern, J., & Córsico, A. H. 2005, A&A, 441, 689

Althaus, L. G., García-Berro, E., Isern, J., Córsico, A. H., & Rohrmann, R. D. 2007, A&A, 465, 249

Althaus, L. G., Serenelli, A. M., & Benvenuto, O. G. 2001, MNRAS, 324, 617

Amaro-Seoane, P., Aoudia, S., Babak, S., Binétruy, P., Berti, E., Bohé, A., Caprini, C., Colpi, M., Cornish, N. J., Danzmann, K., Dufaux, J.-F., Gair, J., Jennrich, O., Jetzer, P., Klein, A., Lang, R. N., Lobo, A., Littenberg, T., McWilliams, S. T., Nelemans, G., Petiteau, A., Porter, E. K., Schutz, B. F., Sesana, A., Stebbins, R., Sumner, T., Vallisneri, M., Vitale, S., Volonteri, M., & Ward, H. 2012, ArXiv e-prints

Antoniadis, J., Freire, P. C. C., Wex, N., Tauris, T. M., Lynch, R. S., van Kerkwijk, M. H., Kramer, M., Bassa, C., Dhillon, V. S., Driebe, T., Hessels, J. W. T., Kaspi, V. M., Kondratiev, V. I., Langer, N., Marsh, T. R., McLaughlin, M. A., Pennucci, T. T., Ransom, S. M., Stairs, I. H., van Leeuwen, J., Verbiest, J. P. W., & Whelan, D. G. 2013, Science, 340, 448

Benacquista, M. J. 2011, ApJ, 740, L54

Bergeron, P., Fontaine, G., Billères, M., Boudreault, S., & Green, E. M. 2004, ApJ, 600, 404

Bergeron, P., Saffer, R. A., & Liebert, J. 1992, ApJ, 394, 228

Bergeron, P., Wesemael, F., Dufour, P., Beauchamp, A., Hunter, C., Saffer, R. A., Gianninas, A., Ruiz, M. T., Limoges, M.-M., Dufour, P., Fontaine, G., & Liebert, J. 2011, ApJ, 737, 28

Bergeron, P., Wesemael, F., Lamontagne, R., Fontaine, G., Saffer, R. A., & Allard, N. F. 1995, ApJ, 449, 258

Bischoff-Kim, A., Montgomery, M. H., & Winget, D. E. 2008, ApJ, 675, 1505

Bradley, P. A. & Winget, D. E. 1991, ApJS, 75, 463

Bradley, P. A., Winget, D. E., & Wood, M. A. 1992, ApJ, 391, L33

Brassard, P. & Fontaine, G. 1999, in Astronomical Society of the Pacific Conference Series, Vol. 173, Stellar Structure: Theory and Test of Connective Energy Transport, ed. A. Gimenez, E. F. Guinan, & B. Montesinos, 329

Brassard, P., Fontaine, G., & Wesemael, F. 1995, ApJS, 96, 545

Breton, R. P., Rappaport, S. A., van Kerkwijk, M. H., & Carter, J. A. 2012, ApJ, 748, 115

Brickhill, A. J. 1991, MNRAS, 251, 673

—. 1992, MNRAS, 259, 519

Brown, J. M., Kilic, M., Brown, W. R., & Kenyon, S. J. 2011a, ApJ, 730, 67

Brown, T. M., Latham, D. W., Everett, M. E., & Esquerdo, G. A. 2011b, AJ, 142, 112

Brown, W. R., Kilic, M., Allende Prieto, C., Gianninas, A., & Kenyon, S. J. 2013, ApJ, 769, 66

Brown, W. R., Kilic, M., Allende Prieto, C., & Kenyon, S. J. 2010, ApJ, 723, 1072

—. 2012, ApJ, 744, 142

Brown, W. R., Kilic, M., Hermes, J. J., Allende Prieto, C., Kenyon, S. J., & Winget, D. E. 2011c, ApJ, 737, L23

Burgay, M., D'Amico, N., Possenti, A., Manchester, R. N., Lyne, A. G., Joshi, B. C., McLaughlin, M. A., Kramer, M., Sarkissian, J. M., Camilo, F., Kalogera, V., Kim, C., & Lorimer, D. R. 2003, Nature, 426, 531

Callanan, P. J., Garnavich, P. M., & Koester, D. 1998, MNRAS, 298, 207

Carter, J. A., Rappaport, S., & Fabrycky, D. 2011, ApJ, 728, 139

Castanheira, B. G. & Kepler, S. O. 2009, MNRAS, 396, 1709

Castanheira, B. G., Kepler, S. O., Costa, A. F. M., Giovannini, O., Robinson, E. L., Winget, D. E., Kleinman, S. J., Nitta, A., Eisenstein, D., Koester, D., & Santos, M. G. 2007, A&A, 462, 989

Castanheira, B. G., Kepler, S. O., Kleinman, S. J., Nitta, A., & Fraga, L. 2010, MNRAS, 405, 2561

—. 2013, MNRAS, 430, 50

Cepa, J., Aguiar, M., Escalera, V. G., Gonzalez-Serrano, I., Joven-Alvarez, E., Peraza, L., Rasilla, J. L., Rodriguez-Ramos, L. F., Gonzalez, J. J., Cobos Duenas, F. J., Sanchez, B., Tejada, C., Bland-Hawthorn, J., Militello, C., & Rosa, F. 2000, in Society of Photo-Optical Instrumentation Engineers (SPIE) Conference Series, Vol. 4008, Society of Photo-Optical Instrumentation Engineers (SPIE) Conference Series, ed. M. Iye & A. F. Moorwood, 623–631

Cepa, J., Aguiar-Gonzalez, M., Bland-Hawthorn, J., Castaneda, H., Cobos, F. J., Correa, S., Espejo, C., Fragoso-Lopez, A. B., Fuentes, F. J., Gigante, J. V., Gonzalez, J. J., Gonzalez-Escalera, V., Gonzalez-Serrano, J. I., Joven-Alvarez, E., Lopez-Ruiz, J.-C., Militello, C., Cano, L. P., Perez, A., Perez, J., Rasilla, J. L., Sanchez, B., & Tejada, C. 2003, in Society of Photo-Optical Instrumentation Engineers (SPIE) Conference Series, Vol. 4841, Society of Photo-Optical Instrumentation Engineers (SPIE) Conference Series, ed. M. Iye & A. F. M. Moorwood, 1739–1749

Charpinet, S., Fontaine, G., & Brassard, P. 2009, Nature, 461, 501

Charpinet, S., Fontaine, G., Brassard, P., Chayer, P., Rogers, F. J., Iglesias, C. A., & Dorman, B. 1997, ApJ, 483, L123

Claret, A., Gimenez, A., & Cunha, N. C. S. 1995, A&A, 299, 724

Córsico, A. H., Althaus, L. G., Miller Bertolami, M. M., Romero, A. D., García-Berro, E., Isern, J., & Kepler, S. O. 2012a, MNRAS, 424, 2792

Córsico, A. H., García-Berro, E., Althaus, L. G., & Isern, J. 2004, A&A, 427, 923

Córsico, A. H., Romero, A. D., Althaus, L. G., & Hermes, J. J. 2012b, A&A, 547, A96

D'Antona, F. & Mazzitelli, I. 1990, ARA&A, 28, 139

Dolez, N., Vauclair, G., Kleinman, S. J., Chevreton, M., Fu, J. N., Solheim, J.-E., González Perez, J. M., Ulla, A., Fraga, L., Kanaan, A., Reed, M., Kawaler, S., O'Brien, M. S., Metcalfe, T. S., Nather, R. E., Sanwal, D., Klumpe, E. W., Mukadam, A., Wood, M. A., Ahrens, T. J., Silvestri, N., Sullivan, D., Sullivan, T., Jiang, X. J., Xu, D. W., Ashoka, B. N., Leibowitz, E., Ibbetson, P., Ofek, E., Kilkenny, D., Meištas, E. G., Alisauskas, D., Janulis, R., Kalytis, R., Moskalik, P., Zola, S., Krzesinski, J., Ogloza, W., Handler, G., Silvotti, R., & Bernabei, S. 2006, A&A, 446, 237

Dominguez, I., Straniero, O., Tornambe, A., & Isern, J. 1996, ApJ, 472, 783

Eastman, J., Siverd, R., & Gaudi, B. S. 2010, PASP, 122, 935

Eddington, A. S. 1924, MNRAS, 84, 308

Eggleton, P. P. 1983, ApJ, 268, 368

Eisenstein, D. J., Liebert, J., Harris, H. C., Kleinman, S. J., Nitta, A., Silvestri, N., Anderson, S. A., Barentine, J. C., Brewington, H. J., Brinkmann, J., Harvanek, M., Krzesiński, J., Neilsen, Jr., E. H., Long, D., Schneider, D. P., & Snedden, S. A. 2006, ApJS, 167, 40

Everett, M. E. & Howell, S. B. 2001, PASP, 113, 1428

Fabricant, D., Cheimets, P., Caldwell, N., & Geary, J. 1998, PASP, 110, 79

Falcon, R. E., Winget, D. E., Montgomery, M. H., & Williams, K. A. 2010, ApJ, 712, 585

Fontaine, G., Bergeron, P., Lacombe, P., Lamontagne, R., & Talon, A. 1985, AJ, 90, 1094

Fontaine, G. & Brassard, P. 2008, PASP, 120, 1043

Fontaine, G., Lacombe, P., McGraw, J. T., Dearborn, D. S. P., & Gustafson, J. 1982, ApJ, 258, 651

Fowler, R. H. 1926, MNRAS, 87, 114

Fruchter, A. S., Gunn, J. E., Lauer, T. R., & Dressler, A. 1988, Nature, 334, 686

Fuller, J. & Lai, D. 2012, MNRAS, 421, 426

Gänsicke, B. T., Koester, D., Girven, J., Marsh, T. R., & Steeghs, D. 2010, Science, 327, 188

García-Berro, E., Lorén-Aguilar, P., Aznar-Siguán, G., Torres, S., Camacho, J., Althaus, L. G., Córsico, A. H., Külebi, B., & Isern, J. 2012, ApJ, 749, 25

Garcia-Berro, E., Ritossa, C., & Iben, Jr., I. 1997, ApJ, 485, 765

Gehrz, R. D., Truran, J. W., Williams, R. E., & Starrfield, S. 1998, PASP, 110, 3

Gianninas, A., Bergeron, P., & Fontaine, G. 2005, ApJ, 631, 1100

—. 2006, AJ, 132, 831

Gianninas, A., Bergeron, P., & Ruiz, M. T. 2011, ApJ, 743, 138

Gianninas, A., Strickland, B. D., Kilic, M., & Bergeron, P. 2013, ApJ, 766, 3

Goldreich, P. & Wu, Y. 1999, ApJ, 511, 904

Haberl, F. & Motch, C. 1995, A&A, 297, L37

Hansen, C. J., Cox, J. P., & van Horn, H. M. 1977, ApJ, 217, 151

Hansen, C. J., Winget, D. E., & Kawaler, S. D. 1985, ApJ, 297, 544

Harris, H. C., Munn, J. A., Kilic, M., Liebert, J., Williams, K. A., von Hippel, T., Levine, S. E., Monet, D. G., Eisenstein, D. J., Kleinman, S. J., Metcalfe, T. S., Nitta, A., Winget, D. E., Brinkmann, J., Fukugita, M., Knapp, G. R., Lupton, R. H., Smith, J. A., & Schneider, D. P. 2006, AJ, 131, 571

Hermes, J. J., Kepler, S. O., Castanheira, B., Gianninas, A., Winget, D. E., Montgomery, M. H., Brown, W. R., & Harrold, S. T. 2013a, ApJ, accepted

Hermes, J. J., Kilic, M., Brown, W. R., Montgomery, M. H., & Winget, D. E. 2012a, ApJ, 749, 42

Hermes, J. J., Kilic, M., Brown, W. R., Winget, D. E., Allende Prieto, C., Gianninas, A., Mukadam, A. S., Cabrera-Lavers, A., & Kenyon, S. J. 2012b, ApJ, 757, L21

Hermes, J. J., Montgomery, M. H., Gianninas, A., Harrold, S. T., Winget, D. E., Brown, W. R., Bell, K. J., Kenyon, S. J., & Kilic, M. 2013b, MNRAS, in prep.

Hermes, J. J., Montgomery, M. H., Mullally, F., Winget, D. E., & Bischoff-Kim, A. 2013c, ApJ, 766, 42

Hermes, J. J., Montgomery, M. H., Winget, D. E., Brown, W. R., Gianninas, A., Kilic, M., Kenyon, S. J., Bell, K. J., & Harrold, S. T. 2013d, ApJ, 765, 102

Hermes, J. J., Montgomery, M. H., Winget, D. E., Brown, W. R., Kilic, M., & Kenyon, S. J. 2012c, ApJ, 750, L28

Hermes, J. J., Mullally, F., Østensen, R. H., Williams, K. A., Telting, J., Southworth, J., Bloemen, S., Howell, S. B., Everett, M., & Winget, D. E. 2011, ApJ, 741, L16

Hermes, J. J., Mullally, F., Winget, D. E., Montgomery, M. H., Miller, G. F., & Ellis, J. L. 2010, in American Institute of Physics Conference Series, Vol. 1273, American Institute of Physics Conference Series, ed. K. Werner & T. Rauch, 446–449

Holberg, J. B. & Bergeron, P. 2006, AJ, 132, 1221

Holberg, J. B. & Howell, S. B. 2011, AJ, 142, 62

Hook, I. M., Jørgensen, I., Allington-Smith, J. R., Davies, R. L., Metcalfe, N., Murowinski, R. G., & Crampton, D. 2004, PASP, 116, 425

Iben, Jr., I., Ritossa, C., & Garcia-Berro, E. 1997, ApJ, 489, 772

Israel, G. L., Hummel, W., Covino, S., Campana, S., Appenzeller, I., Gässler, W., Mantel, K.-H., Marconi, G., Mauche, C. W., Munari, U., Negueruela, I., Nicklas, H., Rupprecht, G., Smart, R. L., Stahl, O., & Stella, L. 2002, A&A, 386, L13

Israel, G. L., Panzera, M. R., Campana, S., Lazzati, D., Covino, S., Tagliaferri, G., & Stella, L. 1999, A&A, 349, L1

Kanaan, A., Kepler, S. O., Giovannini, O., & Diaz, M. 1992, ApJ, 390, L89

Kanaan, A., Kepler, S. O., & Winget, D. E. 2002, A&A, 389, 896

Kanaan, A., Nitta, A., Winget, D. E., Kepler, S. O., Montgomery, M. H., Metcalfe, T. S., Oliveira, H., Fraga, L., da Costa, A. F. M., Costa, J. E. S., Castanheira, B. G., Giovannini, O., Nather, R. E., Mukadam, A., Kawaler, S. D., O'Brien, M. S., Reed, M. D., Kleinman, S. J., Provencal, J. L., Watson, T. K., Kilkenny, D., Sullivan, D. J., Sullivan, T., Shobbrook, B., Jiang, X. J., Ashoka, B. N., Seetha, S., Leibowitz, E., Ibbetson, P., Mendelson, H., Meištas, E. G., Kalytis, R., Movedauskas, D., O'Donoghue, D., Buckley, D., Martinez, P., van Wyk, F., Stobie, R., Marang, F., van Zyl, L., Ogloza, W., Krzesinski, J., Zola, S., Moskalik, P., Breger, M., Stankov, A., Silvotti, R., Piccioni, A., Vauclair, G., Dolez, N., Chevreton, M., Deetjen, J., Dreizler, S., Schuh, S., Gonzalez Perez, J. M., Østensen, R., Ulla, A., Manteiga, M., Suarez, O., Burleigh, M. R., & Barstow, M. A. 2005, A&A, 432, 219

Kaplan, D. L., Bhalerao, V. B., van Kerkwijk, M. H., Koester, D., Kulkarni, S. R., & Stovall, K. 2013, ApJ, 765, 158

Kawaler, S. D. 1987, in Lecture Notes in Physics, Berlin Springer Verlag, Vol. 274, Stellar Pulsation, ed. A. N. Cox, W. M. Sparks, & S. G. Starrfield, 367–370

Kawaler, S. D., Bond, H. E., Sherbert, L. E., & Watson, T. K. 1994, AJ, 107, 298

Kawaler, S. D., Winget, D. E., & Hansen, C. J. 1985, ApJ, 295, 547

Kenyon, S. J. & Garcia, M. R. 1986, AJ, 91, 125

Kepler, S. O. 1993, Baltic Astronomy, 2, 515

Kepler, S. O. 2012, in Astronomical Society of the Pacific Conference Series, Vol. 462, Progress in Solar/Stellar Physics with Helio- and Asteroseismology, ed. H. Shibahashi, M. Takata, & A. E. Lynas-Gray, 322

Kepler, S. O., Costa, J. E. S., Castanheira, B. G., Winget, D. E., Mullally, F., Nather, R. E., Kilic, M., von Hippel, T., Mukadam, A. S., & Sullivan, D. J. 2005, ApJ, 634, 1311

Kepler, S. O. & Nelan, E. P. 1993, AJ, 105, 608

Kepler, S. O., Pelisoli, I., Jordan, S., Kleinman, S. J., Koester, D., Külebi, B., Peçanha, V., Castanheira, B. G., Nitta, A., Costa, J. E. S., Winget, D. E., Kanaan, A., & Fraga, L. 2013, MNRAS, 429, 2934

Kepler, S. O., Pelisoli, I., Peçanha, V., Costa, J. E. S., Fraga, L., Hermes, J. J., Winget, D. E., Castanheira, B., Córsico, A. H., Romero, A. D., Althaus, L., Kleinman, S. J., Nitta, A., Koester, D., Külebi, B., Jordan, S., & Kanaan, A. 2012, ApJ, 757, 177

Kepler, S. O., Winget, D. E., Nather, R. E., Bradley, P. A., Grauer, A. D., Fontaine, G., Bergeron, P., Vauclair, G., Claver, C. F., Marar, T. M. K., Seetha, S., Ashoka, B. N., Mazeh, T., Leibowitz, E., Dolez, N., Chevreton, M., Barstow, M. A., Clemens, J. C., Kleinman, S. J., Sansom, A. E., Tweedy, R. W., Kanaan, A., Hine, B. P., Provencal, J. L., Wesemael, F., Wood, M. A., Brassard, P., Solheim, J.-E., & Emanuelsen, P.-I. 1991, ApJ, 378, L45

Kilic, M., Allende Prieto, C., Brown, W. R., Agüeros, M. A., Kenyon, S. J., & Camilo, F. 2010, ApJ, 721, L158

Kilic, M., Allende Prieto, C., Brown, W. R., & Koester, D. 2007, ApJ, 660, 1451

Kilic, M., Brown, W. R., Allende Prieto, C., Agüeros, M. A., Heinke, C., & Kenyon, S. J. 2011a, ApJ, 727, 3

Kilic, M., Brown, W. R., Allende Prieto, C., Kenyon, S. J., Heinke, C. O., Agüeros, M. A., & Kleinman, S. J. 2012, ApJ, 751, 141

Kilic, M., Brown, W. R., Hermes, J. J., Allende Prieto, C., Kenyon, S. J., Winget, D. E., & Winget, K. I. 2011b, MNRAS, 418, L157

Kilic, M., Brown, W. R., Kenyon, S. J., Allende Prieto, C., Andrews, J., Kleinman, S. J., Winget, K. I., Winget, D. E., & Hermes, J. J. 2011c, MNRAS, 413, L101

Kilkenny, D. 2007, Communications in Asteroseismology, 150, 234

Kilkenny, D., Koen, C., O'Donoghue, D., & Stobie, R. S. 1997, MNRAS, 285, 640

Kim, A. 2007, PhD thesis, The University of Texas at Austin

Kleinman, S. J. 1995, PhD thesis, THE UNIVERSITY OF TEXAS AT AUSTIN.

Kleinman, S. J., Kepler, S. O., Koester, D., Pelisoli, I., Peçanha, V., Nitta, A., Costa, J. E. S., Krzesinski, J., Dufour, P., Lachapelle, F.-R., Bergeron, P., Yip, C.-W., Harris, H. C., Eisenstein, D. J., Althaus, L., & Córsico, A. 2013, ApJS, 204, 5

Kleinman, S. J., Nather, R. E., Winget, D. E., Clemens, J. C., Bradley, P. A., Kanaan, A., Provencal, J. L., Claver, C. F., Watson, T. K., Yanagida, K., Nitta, A., Dixson, J. S., Wood, M. A., Grauer, A. D., Hine, B. P., Fontaine, G., Liebert, J., Sullivan, D. J., Wickramasinghe, D. T., Achilleos, N., Marar, T. M. K., Seetha, S., Ashoka,

B. N., Meistas, E., Leibowitz, E. M., Moskalik, P., Krzesinski, J., Solheim, J.-E., Bruvold, A., O'Donoghue, D., Kurtz, D. W., Warner, B., Martinez, P., Vauclair, G., Dolez, N., Chevreton, M., Barstow, M. A., Kepler, S. O., Giovannini, O., Augusteijn, T., Hansen, C. J., & Kawaler, S. D. 1998, ApJ, 495, 424

Koester, D. 2008, ArXiv: 0812.0482

—. 2010, Mem. Soc. Astron. Italiana, 81, 921

Koester, D. & Holberg, J. B. 2001, in Astronomical Society of the Pacific Conference Series, Vol. 226, 12th European Workshop on White Dwarfs, ed. J. L. Provencal, H. L. Shipman, J. MacDonald, & S. Goodchild, 299

Koester, D., Kepler, S. O., Kleinman, S. J., & Nitta, A. 2009, Journal of Physics Conference Series, 172, 012006

Koester, D. & Werner, K., eds. 1995, Lecture Notes in Physics, Berlin Springer Verlag, Vol. 443, White Dwarfs

Kopal, Z. 1959, Close binary systems

Kowalski, P. M. & Saumon, D. 2006, ApJ, 651, L137

Landau, L. D. & Lifshitz, E. M. 1975, The classical theory of fields

Landolt, A. U. 1968, ApJ, 153, 151

Lenz, P. & Breger, M. 2005, Communications in Asteroseismology, 146, 53

Liebert, J., Bergeron, P., & Holberg, J. B. 2005, ApJS, 156, 47

Lyutikov, M. & Thompson, C. 2005, ApJ, 634, 1223

Marsh, M. C., Barstow, M. A., Buckley, D. A., Burleigh, M. R., Holberg, J. B., Koester, D., O'Donoghue, D., Penny, A. J., & Sansom, A. E. 1997, MNRAS, 287, 705

Marsh, T. R. 2001, MNRAS, 324, 547

Marsh, T. R., Dhillon, V. S., & Duck, S. R. 1995, MNRAS, 275, 828

Marsh, T. R., Nelemans, G., & Steeghs, D. 2004, MNRAS, 350, 113

Maxted, P. F. L., Anderson, D. R., Burleigh, M. R., Collier Cameron, A., Heber, U., Gänsicke, B. T., Geier, S., Kupfer, T., Marsh, T. R., Nelemans, G., O'Toole, S. J., Østensen, R. H., Smalley, B., & West, R. G. 2011, MNRAS, 418, 1156

Mazeh, T. & Faigler, S. 2010, A&A, 521, L59

Mestel, L. 1952, MNRAS, 112, 583

Metcalfe, T. S., Montgomery, M. H., & Kanaan, A. 2004, ApJ, 605, L133

Mihalas, D. 1978, Stellar atmospheres /2nd edition/

Montgomery, M. H. 2005, ApJ, 633, 1142

Montgomery, M. H., Metcalfe, T. S., & Winget, D. E. 2003, MNRAS, 344, 657

Montgomery, M. H., Provencal, J. L., Kanaan, A., Mukadam, A. S., Thompson, S. E., Dalessio, J., Shipman, H. L., Winget, D. E., Kepler, S. O., & Koester, D. 2010, ApJ, 716, 84

Montgomery, M. H. & Winget, D. E. 1999, ApJ, 526, 976

Morris, S. L. & Naftilan, S. A. 1993, ApJ, 419, 344

Mukadam, A. S., Bischoff-Kim, A., Fraser, O., Córsico, A. H., Montgomery, M. H., Kepler, S. O., Romero, A. D., Winget, D. E., Hermes, J. J., Riecken, T. S., Kronberg, M. E., Winget, K. I., Falcon, R. E., Chandler, D. W., Kuehne, J. W., Sullivan, D. J., Reaves, D., von Hippel, T., Mullally, F., Shipman, H., Thompson, S. E., Silvestri, N. M., & Hynes, R. I. 2013, ApJ, 771, 17

Mukadam, A. S., Kepler, S. O., Winget, D. E., Nather, R. E., Kilic, M., Mullally, F., von Hippel, T., Kleinman, S. J., Nitta, A., Guzik, J. A., Bradley, P. A., Matthews, J., Sekiguchi, K., Sullivan, D. J., Sullivan, T., Shobbrook, R. R., Birch, P., Jiang, X. J., Xu, D. W., Joshi, S., Ashoka, B. N., Ibbetson, P., Leibowitz, E., Ofek, E. O., Meištas, E. G., Janulis, R., Ališauskas, D., Kalytis, R., Handler, G., Kilkenny, D., O'Donoghue, D., Kurtz, D. W., Müller, M., Moskalik, P., Ogłoza, W., Zoła, S., Krzesiński, J., Johannessen, F., Gonzalez-Perez, J. M., Solheim, J.-E., Silvotti, R., Bernabei, S., Vauclair, G., Dolez, N., Fu, J. N., Chevreton, M., Manteiga, M., Suárez, O., Ulla, A., Cunha, M. S., Metcalfe, T. S., Kanaan, A., Fraga, L., Costa, A. F. M., Giovannini, O., Fontaine, G., Bergeron, P., O'Brien, M. S., Sanwal, D., Wood, M. A., Ahrens, T. J., Silvestri, N., Klumpe, E. W., Kawaler, S. D., Riddle, R., Reed, M. D., & Watson, T. K. 2003, ApJ, 594, 961

Mukadam, A. S., Kim, A., Fraser, O., Winget, D. E., Kepler, S. O., Sullivan, D. J., Reaves, D., Robinson, E. L., von Hippel, T., Mullally, F., Shipman, H., Thompson, S. E., Silvestri, N. M., & Hynes, R. I. 2009, Journal of Physics Conference Series, 172, 012074

Mukadam, A. S., Montgomery, M. H., Winget, D. E., Kepler, S. O., & Clemens, J. C. 2006, ApJ, 640, 956

Mukadam, A. S., Owen, R., Mannery, E., MacDonald, N., Williams, B., Stauffer, F., & Miller, C. 2011, PASP, 123, 1423

Mukadam, A. S., Winget, D. E., von Hippel, T., Montgomery, M. H., Kepler, S. O., & Costa, A. F. M. 2004, ApJ, 612, 1052

Mullally, F., Badenes, C., Thompson, S. E., & Lupton, R. 2009, ApJ, 707, L51

Mullally, F., Thompson, S. E., Castanheira, B. G., Winget, D. E., Kepler, S. O., Eisenstein, D. J., Kleinman, S. J., & Nitta, A. 2005, ApJ, 625, 966

Mullally, F., Winget, D. E., De Gennaro, S., Jeffery, E., Thompson, S. E., Chandler, D., & Kepler, S. O. 2008, ApJ, 676, 573

Nather, R. E. & Mukadam, A. S. 2004, ApJ, 605, 846

Nather, R. E., Winget, D. E., Clemens, J. C., Hansen, C. J., & Hine, B. P. 1990, ApJ, 361, 309

Nauenberg, M. 1972, ApJ, 175, 417

Nomoto, K. 1984, ApJ, 277, 791

—. 1987, ApJ, 322, 206

Østensen, R. H., Bloemen, S., Vučković, M., Aerts, C., Oreiro, R., Kinemuchi, K., Still, M., & Koester, D. 2011a, ApJ, 736, L39

Østensen, R. H., Silvotti, R., Charpinet, S., Oreiro, R., Bloemen, S., Baran, A. S., Reed, M. D., Kawaler, S. D., Telting, J. H., Green, E. M., O'Toole, S. J., Aerts, C., Gänsicke, B. T., Marsh, T. R., Breedt, E., Heber, U., Koester, D., Quint, A. C., Kurtz, D. W., Rodríguez-López, C., Vučković, M., Ottosen, T. A., Frimann, S., Somero, A., Wilson, P. A., Thygesen, A. O., Lindberg, J. E., Kjeldsen, H., Christensen-Dalsgaard, J., Allen, C., McCauliff, S., & Middour, C. K. 2011b, MNRAS, 414, 2860

Østensen, R. H., Silvotti, R., Charpinet, S., Oreiro, R., Handler, G., Green, E. M., Bloemen, S., Heber, U., Gänsicke, B. T., Marsh, T. R., Kurtz, D. W., Telting, J. H., Reed, M. D., Kawaler, S. D., Aerts, C., Rodríguez-López, C., Vučković, M., Ottosen, T. A., Liimets, T., Quint, A. C., Van Grootel, V., Randall, S. K., Gilliland, R. L., Kjeldsen, H., Christensen-Dalsgaard, J., Borucki, W. J., Koch, D., & Quintana, E. V. 2010, MNRAS, 409, 1470

Pablo, H., Kawaler, S. D., Reed, M. D., Bloemen, S., Charpinet, S., Hu, H., Telting, J., Østensen, R. H., Baran, A. S., Green, E. M., Hermes, J. J., Barclay, T., O'Toole, S. J., Mullally, F., Kurtz, D. W., Christensen-Dalsgaard, J., Caldwell, D. A., Christiansen, J. L., & Kinemuchi, K. 2012, MNRAS, 422, 1343

Panei, J. A., Althaus, L. G., Chen, X., & Han, Z. 2007, MNRAS, 382, 779

Parsons, S. G., Marsh, T. R., Gänsicke, B. T., Drake, A. J., & Koester, D. 2011, ApJ, 735, L30

Paxton, B., Bildsten, L., Dotter, A., Herwig, F., Lesaffre, P., & Timmes, F. 2011, ApJS, 192, 3

Paxton, B., Cantiello, M., Arras, P., Bildsten, L., Brown, E. F., Dotter, A., Mankovich, C., Montgomery, M. H., Stello, D., Timmes, F. X., & Townsend, R. 2013, ArXiv e-prints

Piro, A. L. 2011, ApJ, 740, L53

Provencal, J. L., Montgomery, M. H., Kanaan, A., Shipman, H. L., Childers, D., Baran, A., Kepler, S. O., Reed, M., Zhou, A., Eggen, J., Watson, T. K., Winget, D. E., Thompson, S. E., Riaz, B., Nitta, A., Kleinman, S. J., Crowe, R., Slivkoff, J., Sherard, P., Purves, N., Binder, P., Knight, R., Kim, S. ., Chen, W.-P., Yang, M., Lin, H. C., Lin, C. C., Chen, C. W., Jiang, X. J., Sergeev, A. V., Mkrtichian, D., Andreev, M., Janulis, R., Siwak, M., Zola, S., Koziel, D., Stachowski, G., Paparo, M., Bognar, Z., Handler, G., Lorenz, D., Steininger, B., Beck, P., Nagel, T., Kusterer, D., Hoffman, A., Reiff, E., Kowalski, R., Vauclair, G., Charpinet, S., Chevreton, M., Solheim, J. E., Pakstiene, E., Fraga, L., & Dalessio, J. 2009, ApJ, 693, 564

Provencal, J. L., Montgomery, M. H., Kanaan, A., Thompson, S. E., Dalessio, J., Shipman, H. L., Childers, D., Clemens, J. C., Rosen, R., Henrique, P., Bischoff-Kim, A., Strickland, W., Chandler, D., Walter, B., Watson, T. K., Castanheira, B., Wang, S., Handler, G., Wood, M., Vennes, S., Nemeth, P., Kepler, S. O., Reed, M., Nitta, A., Kleinman, S. J., Brown, T., Kim, S.-L., Sullivan, D., Chen, W. P., Yang, M., Shih, C. Y., Jiang, X. J., Sergeev, A. V., Maksim, A., Janulis, R., Baliyan, K. S., Vats, H. O., Zola, S., Baran, A., Winiarski, M., Ogloza, W., Paparo, M., Bognar, Z., Papics, P., Kilkenny, D., Sefako, R., Buckley, D., Loaring, N., Kniazev, A., Silvotti, R., Galleti, S., Nagel, T., Vauclair, G., Dolez, N., Fremy, J. R., Perez, J., Almenara, J. M., & Fraga, L. 2012, ApJ, 751, 91

Robinson, E. L. 1979, in IAU Colloq. 53: White Dwarfs and Variable Degenerate Stars, ed. H. M. van Horn & V. Weidemann, 343–358

Robinson, E. L. & Shafter, A. W. 1987, ApJ, 322, 296

Robinson, R. L. 1984, AJ, 89, 1732

Roelofs, G. H. A., Rau, A., Marsh, T. R., Steeghs, D., Groot, P. J., & Nelemans, G. 2010, ApJ, 711, L138

Romero, A. D., Córsico, A. H., Althaus, L. G., Kepler, S. O., Castanheira, B. G., & Miller Bertolami, M. M. 2012, MNRAS, 420, 1462

Rowe, J. F., Borucki, W. J., Koch, D., Howell, S. B., Basri, G., Batalha, N., Brown, T. M., Caldwell, D., Cochran, W. D., Dunham, E., Dupree, A. K., Fortney, J. J., Gautier, III, T. N., Gilliland, R. L., Jenkins, J., Latham, D. W., Lissauer, J. J., Marcy, G., Monet, D. G., Sasselov, D., & Welsh, W. F. 2010, ApJ, 713, L150

Rowell, N. & Hambly, N. C. 2011, MNRAS, 417, 93

Saio, H., Winget, D. E., & Robinson, E. L. 1983, ApJ, 265, 982

Salpeter, E. E. 1961, ApJ, 134, 669

Schmidt, G. D., Weymann, R. J., & Foltz, C. B. 1989, PASP, 101, 713

Segretain, L., Chabrier, G., & Mochkovitch, R. 1997, ApJ, 481, 355

Serenelli, A. M., Althaus, L. G., Rohrmann, R. D., & Benvenuto, O. G. 2002, MNRAS, 337, 1091

Shklovskii, I. S. 1970, Soviet Ast., 13, 562

Shporer, A., Kaplan, D. L., Steinfadt, J. D. R., Bildsten, L., Howell, S. B., & Mazeh, T. 2010, ApJ, 725, L200

Silvotti, R., Fontaine, G., Pavlov, M., Marsh, T. R., Dhillon, V. S., Littlefair, S. P., & Getman, F. 2011, A&A, 525, A64

Sirko, E. & Paczyński, B. 2003, ApJ, 592, 1217

Smartt, S. J., Eldridge, J. J., Crockett, R. M., & Maund, J. R. 2009, MNRAS, 395, 1409

Southworth, J., Maxted, P. F. L., & Smalley, B. 2004, MNRAS, 351, 1277

Southworth, J., Smalley, B., Maxted, P. F. L., Claret, A., & Etzel, P. B. 2005, MNRAS, 363, 529

Starrfield, S., Cox, A. N., Hodson, S. W., & Clancy, S. P. 1983, ApJ, 269, 645

Steeghs, D., Marsh, T. R., Barros, S. C. C., Nelemans, G., Groot, P. J., Roelofs, G. H. A., Ramsay, G., & Cropper, M. 2006, ApJ, 649, 382

Steinfadt, J. D. R., Bildsten, L., & Arras, P. 2010a, ApJ, 718, 441

Steinfadt, J. D. R., Bildsten, L., Kaplan, D. L., Fulton, B. J., Howell, S. B., Marsh, T. R., Ofek, E. O., & Shporer, A. 2012, PASP, 124, 1

Steinfadt, J. D. R., Kaplan, D. L., Shporer, A., Bildsten, L., & Howell, S. B. 2010b, ApJ, 716, L146

Stella, L., Priedhorsky, W., & White, N. E. 1987, ApJ, 312, L17

Stetson, P. B. 1987, PASP, 99, 191

Stumpff, P. 1980, A&AS, 41, 1

Thompson, S. E. & Mullally, F. 2009, Journal of Physics Conference Series, 172, 012081

Tremblay, P.-E. & Bergeron, P. 2009, ApJ, 696, 1755

Tremblay, P.-E., Bergeron, P., & Gianninas, A. 2011, ApJ, 730, 128

Tremblay, P.-E., Bergeron, P., Kalirai, J. S., & Gianninas, A. 2010, ApJ, 712, 1345

Unno, W., Osaki, Y., Ando, H., Saio, H., & Shibahashi, H. 1989, Nonradial oscillations of stars

van den Broek, D., Nelemans, G., Dan, M., & Rosswog, S. 2012, MNRAS, 425, L24

Van Grootel, V., Dupret, M.-A., Fontaine, G., Brassard, P., Grigahcène, A., & Quirion, P.-O. 2012, A&A, 539, A87

Van Grootel, V., Fontaine, G., Brassard, P., & Dupret, M.-A. 2013, ApJ, 762, 57

van Kerkwijk, M. H., Rappaport, S. A., Breton, R. P., Justham, S., Podsiadlowski, P., & Han, Z. 2010, ApJ, 715, 51

Vennes, S. & Kawka, A. 2008, MNRAS, 389, 1367

Vennes, S., Thorstensen, J. R., Kawka, A., Németh, P., Skinner, J. N., Pigulski, A., Steampsacute, licki, M., Kołaczkowski, Z., & Śródka, P. 2011, ApJ, 737, L16

Warner, B. & Woudt, P. A. 2002, PASP, 114, 129

Williams, K. A., Bolte, M., & Koester, D. 2009, ApJ, 693, 355

Winget, D. E., Cochran, W. D., Endl, M., Kanaan, A., Kepler, S. O., Mukadam, A., Mullally, F., Nather, R. E., Reaves, D., Slaughter, D., Sullivan, D. J., & von Hippel, T. 2003, in Astronomical Society of the Pacific Conference Series, Vol. 294, Scientific Frontiers in Research on Extrasolar Planets, ed. D. Deming & S. Seager, 59–64

Winget, D. E., Hansen, C. J., Liebert, J., van Horn, H. M., Fontaine, G., Nather, R. E., Kepler, S. O., & Lamb, D. Q. 1987, ApJ, 315, L77

Winget, D. E. & Kepler, S. O. 2008, ARA&A, 46, 157

Winget, D. E., Nather, R. E., Clemens, J. C., Provencal, J., Kleinman, S. J., Bradley, P. A., Wood, M. A., Claver, C. F., Robinson, E. L., Grauer, A. D., Hine, B. P., Fontaine, G., Achilleos, N., Marar, T. M. K., Seetha, S., Ashoka, B. N., O'Donoghue, D., Warner, B., Kurtz, D. W., Martinez, P., Vauclair, G., Chevreton, M., Kanaan, A., Kepler, S. O., Augusteijn, T., van Paradijs, J., Hansen, C. J., & Liebert, J. 1990, ApJ, 357, 630

Winget, D. E., Sullivan, D. J., Metcalfe, T. S., Kawaler, S. D., & Montgomery, M. H. 2004, ApJ, 602, L109

Winget, D. E., van Horn, H. M., Tassoul, M., Fontaine, G., Hansen, C. J., & Carroll, B. W. 1982, ApJ, 252, L65

Wood, M. A. 1990, PhD thesis, Texas Univ., Austin.

Wood, M. A. 1995, in Lecture Notes in Physics, Berlin Springer Verlag, Vol. 443, White Dwarfs, ed. D. Koester & K. Werner, 41

Wu, Y. 1998, PhD thesis, California Institute of Technology

—. 2001, MNRAS, 323, 248

Yeates, C. M., Clemens, J. C., Thompson, S. E., & Mullally, F. 2005, ApJ, 635, 1239

Zucker, S., Mazeh, T., & Alexander, T. 2007, ApJ, 670, 1326

Vita

JJ Hermes was born on May 8, 1984 in Houston, TX, and grew up an Astros fan, although this had no bearing on his eventual career path. He attended high school at St. Paul's School in Covington, LA, but returned to Texas as an undergraduate to attend the University of Texas at Austin. There he served as editor-in-chief of *The Daily Texan* from 2006 June to 2007 May. In 2007 May he received Bachelor's degrees in physics and astronomy, then moved to Washington, D.C. to work as a reporter for *The Chronicle of Higher Education*, covering federal education policy, analyzing earmarks for colleges and universities, and generally muckraking. He returned to the University of Texas at Austin in 2008 August as a graduate student in astronomy. From 2009 August to 2013 April he spent nearly 1 in 5 nights at the McDonald Observatory, basking in the thrill of discovery while learning to cope with isolation. Thanks to the meticulous record-keeping of Joel Green, he can report a .727/.727/1.621 slash line in 66 plate appearances with the Ultra-Deep Fielders, the astronomy department's softball team (though he posted an 11.57 ERA through 21 innings). He finds beauty in the violent stillness of the night sky.

Permanent address: 6409 Canterbury Court
Ft. Worth, Texas 76132

This dissertation was typeset with LaTeX by the author.